UNIVERSITY OF CAPE TOWN
IYUNIVESITHI YASEKAPA • UNIVERSITEIT VAN KAAPSTAD
Department of Mechanical Engineering

The use of cellular materials to alleviate the damage from blast-induced fragments

Nzudzanyo Ranwaha

Dissertation presented for the degree Master of Science in Engineering in the Department of Mechanical Engineering, University of Cape Town.

BISRU

BLAST IMPACT AND SURVIVABILITY RESEARCH UNIT

January 2014

DECLARATION

- I know the meaning of plagiarism and declare that all of the work in the dissertation, save for that which is properly acknowledged, is my own.
- I used the Vancouver convention for citing and referencing. Each significant contribution to, and quotation in, this thesis report from the work(s) of other people has been attributed, and has been cited and referenced.
- I empower the university to reproduce for the purpose of research either the whole or any portion of the contents in any manner whatsoever.

Signed by candidate

SIGNATURE: _____

DATE: 24/01/2014

ABSTRACT

This study aims to understand how different cellular materials mitigate the damage that is caused by a blast-induced fragment. In the experimental arrangement, a front plate is subjected to localised blast load to release a "controlled" fragment (cap) to impact a similar plate positioned 190mm apart. A cylindrical charge of Plastic Explosive 4 (PE4) of different diameters (27mm, 36mm and 43mm) and masses ranging from 7g to 11g are used to create fragments of different sizes and masses propelled at different velocities to impact the rear plate. Both front and rear plates are made from 1.6mm thick mild steel sheet with an exposed circular area of 106mm diameter. Tests are carried out with and without energy absorbing materials to investigate the protective performance of the different materials investigated by means of the mode of failure and maximum deflection of the rear plate.

The different energy absorbing cellular materials investigated in this study include aluminium foam, aluminium honeycomb, balsa wood, Corecell M-80 foam, Divinycell H200 PVC foam and rigid polyurethane 200 foam. The 40mm thick energy absorbing materials are 106mm in diameter (same size as the exposed plate area) are placed in front of the rear plate. Additional experiments are carried out in three further test series to investigate different parametric conditions:-

- *Effect of the thickness of the energy absorbing materials*

  Three energy absorbing materials – balsa wood, Divinycell foam and polyurethane foam – are investigated and tested at 60mm. In these experiments, the charge has a constant diameter of 36mm and varying charge masses (ranging from 7g to 11g) to induce fragments of different speeds.

- *Effect of different layering arrangement of the energy absorbing materials*

  These tests are carried out using different layering configurations of polyurethane foam with combined thickness of 40mm. The layer arrangements include one 40mm thick disc, two 20mm thick discs and four 10mm thick discs of 10mm. In these experiments, the charge has a constant diameter of 36mm and varying charge masses (ranging from 7g to 11g) to induce fragments of different speeds.

- *Effect of size and speed of blast-induced fragment*

  In this series of experiments, three charge diameters (27mm, 36mm and 43mm) with different masses of explosive are used to induce fragments of at different speeds and masses with essentially identical kinetic energies.

The speed and mass of the fragment are observed to vary greatly for a given charge mass and charge diameter. In most cases, the failure of rear plates is characterised by large inelastic deflection. In some cases, at higher charge masses and without energy absorbing materials, the rear plates fails with due to thinning or partial tearing in the central region or full tearing (secondary capping). In some rare cases the rear plate fails due to sliced tearing with little deflection as a result of side impact of the fragment due to rotation.

The different energy absorbing materials show different failure modes upon fragment impact. Aluminium foams are perforated with a compressed plug sheared from the material. The layers of aluminium honeycomb are observed to bend during perforation. Balsa wood loses small lumps of wood and cracking is observed along the grain. Corecell foam shows scorch marks, in addition to soot deposits from the blast. Divinycell foam undergoes cross-cracking around the perforation tunnel which is propagated obliquely through the thickness of the foam layers. In some cases the fragment is tightly wedged in the hardened and densified Divinycell foam absorber. Polyurethane foam generally crushes into powder and loses the highest fraction of its original mass of any studied energy absorbing materials.

Overall, Divinycell foam provides the best damage mitigation whilst Corecell foam provides the least. Increasing the thickness of the absorber improves damage mitigation at lower fragment kinetic energies but the improvement tends to decrease with increasing kinetic energy. Varying the layer arrangement of polyurethane foam does not affect the damage mitigation. When different sized fragments are released within a narrow band of kinetic energy, the smallest fragment (having the highest impact speed) impart the greatest damage to the rear plate whilst the largest fragment – which has the lowest speed – imparts the least damage.

ACKNOWLEDGEMENTS

First of all, I would like to thank the almighty God, by whose grace I have completed this thesis project successfully, and without whom, I am absolutely nothing. I also wish to acknowledge my loving parents and siblings who have supported me throughout my studies.

I would like to also thank my supervisor, Dr. Steeve Chung Kim Yuen, who has been an unbelievable source of support and guidance. Having worked with him in my undergraduate project and now my MSc. project, he has helped me to be more competent in my research, personal management and to be more professional. I would also like to thank Prof. Gerald Nurick, who has given extremely helpful feedback and given me advice on how I can improve my project structure and has been very supportive and empathetic in the hardest of times for me, personally. A big 'thank you' also goes to Thomas Baby, Lloyd Zacharias, Batlile Mofokeng, Jean-Eudes Niollet and Guy Cunliffe who physically helped with some of the tests. I also extend thanks to the rest of the BISRU colleagues and staff, who helped me to see where I can improve during the progress of my thesis.

My gratitude also goes to the technical staff of the Mechanical Engineering workshop; Mr. Glen Newins, Mr. Horst Emrich, Mr. Hubert Tomlinson and everyone who helped in any way through purchasing of products, cutting of specimen, advice and other ways of administering student support. In addition, I also appreciate the help I got from the Centre of Materials Engineering (CME) staff; particularly Mrs. Penny Park-Ross, who helped me in carrying out quasi-static testing. I would like to also deeply acknowledge Peter Slattery of *Aerothane Applications* who selflessly provided me with all the polyurethane foam I needed for my tests.

Last but not least, I also appreciate the support and encouragement from my friends; Todani Khorombi, Khuthadzo Ndwambi, Ndanganeni Muthadi, Peter Irungu, Zwivhuya Mulibana, Joseph Lithudzha, and a very special mention to Lesedi Thuto Mogotsi. You are very special people to me.

DEDICATION

Having acknowledged all those who made important contributions towards completion of this project, I would like to specially dedicate any positive results that comes out of this dissertation to the family into which I was born.

To my amazing and supportive father Fhedzisani Frentch Rańwaha whose leadership and love has been invaluable to our family, to my strong and beautiful mother Azwifarwi Martha Rańwaha who has remained strong and gets stronger as I successfully submit this work, to my wonderful sisters Tsireledzo Rańwaha, Zwivhuya Rańwaha, Nḓivho Rańwaha and Hakhakhi Rańwaha; all of you have been with me from the time I started this degree and have supported me through my lows and shared my joys with me. I really thank God for all of you.

The work in this study is dedicated to all of you. Thank you. I love you.

TABLE OF CONTENTS

DECLARATION i

ABSTRACT ii

ACKNOWLEDGEMENTS v

DEDICATION vi

TABLE OF CONTENTS vii

LIST OF FIGURES xiv

LIST OF TABLES xxvii

ACRONYMS xxx

NOMENCLATURE xxxi

GLOSSARY xxxvi

1. INTRODUCTION 1

2. LITERATURE REVIEW 5

2.1. REVIEW ON BLAST LOADING AND FRAGMENTATION 5

2.1.1. Overview of detonation explosions in air 5

2.1.2. Structural Response to Blast Loading 9

2.1.2.1. Uniform Blast Loads 9

2.1.2.2. Localised Blast Loads 17

2.1.3. Fragmentation 21

2.1.3.1. Ways of fragmentation and release of fragments 22

2.1.3.2. Capping (Mode IIc) 27

2.1.3.3. Impact and damage by fragments 31

2.1.4. Theory on locally blast loaded plates 34

2.1.4.1. Theoretical background on localised blast loading and capping 34

2.1.4.2. Theoretical background on plate response to fragment impact 35

2.2. REVIEW ON IMPACT ENERGY ABSORPTION AND ENERGY ABSORBERS 40

2.2.1. Importance of energy absorption during impact: A general outline 40

2.2.2. Absorption of energy from a ballistic fragment 41

2.2.3. Energy absorbers 42

2.2.3.1. Fibre reinforced composites 42

2.2.3.2. Cellular materials 44

2.2.3.3. Ceramic materials 55

2.2.3.4. Magnetorheological (MR) and shear-thickening (ST) fluids 56

2.2.3.5. Micro-architectured lattice structures: Trusses 57

2.2.3.6. Corrugated board 59

2.2.4. Summary of considered energy absorbers 60

3. EXPERIMENTAL DETAILS 62

3.1. Setup for blast testing 62

3.1.1. The ballistic pendulum 62

3.1.2. Experimental rig arrangement 66

3.1.2.1. System without energy absorbers 66

3.1.2.2. System with Energy Absorbers 68

3.1.3. Speed Trap System 71

3.1.3.1. Wire-break speed trap system 71

3.2. Explosive charge details 75

3.3. Test plate details 76

3.4. Energy absorbing materials 79

3.4.1. Material characterisation of the energy absorbers 79

3.4.2. Energy absorbers used in blast testing 85

3.5. Experimental plan for the blast tests 87

3.5.1. Tests with no energy absorbers 87

3.5.2. Effect of the thickness of the energy absorbing materials 88

3.5.3. Effect of different layering arrangements of the energy absorbing materials 89

3.5.4. Effects of size and speed of a fragment 90

3.5.5. Repeat tests 91

3.6. Measurements and Test notations 92

3.6.1. Determining the speed of the fragment 93

3.6.2. Fragment diameter 93

3.6.3. Measuring the mass of the fragment 95

3.6.4. Rear plate maximum deflection 95

3.6.5. Material loss from the energy absorber 96

3.6.6. Notations used to describe the blast tests 97

4. EXPERIMENTAL OBSERVATIONS AND RESULTS 99

4.1. Front plate 99

4.2. Fragment characteristics 102

4.3. General observations on rear plate failure 104

4.3.1. Inelastic deflection (Mode I) 104

4.3.2. Inelastic deformation with thinning around the centre (Mode Itc) 105

4.3.2.1. Perimetral thinning 105

4.3.2.2. Chordal thinning 106

4.3.3. Inelastic deflection with partial tearing (early Mode II*c) 107

4.3.3.1. Perimetral small partial tearing 107

4.3.3.2. Chordal small partial tearing 108

4.3.4. Inelastic deflection with large partial tearing (advanced Mode II*c) 109

4.3.5. Inelastic deflection with full tearing of central region (Mode IIc) 110

4.4. Tests with no energy absorbers protecting the rear plate 111

4.5. Tests with the rear plates protected by energy absorbers 114

4.5.1. Tests with 40mm thick energy absorbers protecting the rear plate 114

4.5.1.1. Aluminium foam 114

4.5.1.2. Aluminium honeycomb 116

4.5.1.3. Balsa wood 119

4.5.1.4. Corecell foam 122

4.5.1.5. Divinycell foam 124

4.5.1.6. Polyurethane foam 128

4.5.1.7. Summary 130

4.5.2. Tests with 60mm thick energy absorbers protecting the rear plate 133

4.5.3. Effect of varying the layering arrangements of energy absorbers 137

4.5.4. Effect of size and speed of a fragment 141

5. ANALYSIS AND DISCUSSIONS OF RESULTS 147

5.1. Effects of the blast on the front plate 147

5.1.1. Impulse from the blast 147

5.1.2. Theoretical prediction of maximum front plate deflection just before capping 151

5.2. Kinetics of the fragment 153

5.2.1. Mass of the fragments 153

5.2.2. Speed of the fragments 154

5.2.3. Momentum of the fragments 157

5.2.4. Kinetic energy of the fragments 160

5.3. Damage on rear plate without energy absorbers 165

5.3.1. Variation of plate separation distance without energy absorbers 165

5.3.2. Rear plate tearing limits under unprotected impact 167

5.3.3. Theoretical analysis 168

5.3.3.1. Dimensionless analysis – Zhao's response number 168

5.3.3.2. Theoretical prediction of rear plate deflection 170

5.3.3.3. Theoretical prediction of critical perforation energy 172

5.4. Damage of rear plate protected by 40mm thick absorbers 173

5.4.1. Aluminium foam 173

5.4.2. Aluminium honeycomb 174

5.4.3. Balsa wood 175

5.4.4. Corecell foam 176

5.4.5. Divinycell foam 177

5.4.6. Polyurethane foam 178

5.4.7. Summary 179

5.5. Damage of rear plate protected by 60mm thick absorbers 184

5.6. Effect of varying layering arrangements of energy absorbers 192

5.7. Effect of size and speed of a fragment 193

6. CONCLUSIONS 195

7. RECOMMENDATIONS 203

8. REFERENCES 204

A. Appendix A – INFRA-RED SPEED TRAP CONCEPT 216

B. Appendix B – MATERIAL CHARACTERISATION 218

B.1. Tensile tests on mild steel 218

B.2. Quasi-static compression on energy absorbing materials 222

C. Appendix C – BALLISTIC PENDULUM THEORY 229

D. Appendix D – CHALLENGES IN THEORETICAL ANALYSIS 236

E. Appendix E – DRAWINGS 238

LIST OF FIGURES

Figure 2-1 : Pressure distribution against distance for detonation blast for different points in time [9] 7

Figure 2-2 : Pressure vs. time history of an ideal blast wave [8] 7

Figure 2-3 : Temperature profiles for a detonation blast over distance for different points in time [9] 8

Figure 2-4 : Explosive layout in a two-ring concentric circle annulus [13] 10

Figure 2-5: Schematic showing conditions for a blast load to be uniform for a circular target [45] 11

Figure 2-6: Photograph showing localisation of blasts on plates for varying stand-off distances 12

Figure 2-7 : Schematic showing loading condition for localised and uniform blasts on test plates [24] 13

Figure 2-8 : Schematic of Mode I failure for blast loaded clamped beams and plates [11] 14

Figure 2-9 : Schematic of Mode II failure for blast loaded clamped beams and plates [11] 14

Figure 2-10 : Schematic of Mode III failure for blast loaded clamped beams and plates [11] 15

Figure 2-11 : Typical 'global dome' Mode I plate deflection under uniform blast loading [27] 16

Figure 2-12 : Plate deflection profile under localised loading [24] 18

Figure 2-13: Picture of a series of plates subjected to localised blast loading, showing various failure modes [19] 19

Figure 2-14: Pre-capping relationship between inflection diameter (ID), Burn diameter (BD) against load diameter (LD) - as well as post-capping relationship between cap diameter (CD) and load diameter [19] 20

Figure 2-15: A typical munition casing of a missle [50] 22

Figure 2-16: Section through a munition casing showing the genesis of fragmentation [51] 23

Figure 2-17: Steel plate deformed by blast wave but perforated by fragments from the munition casing [32] 24

Figure 2-18 : Simulation of spallation due to projectile impact [57] 26

Figure 2-19 : Schematic showing capping failure on a plate 29

Figure 2-20 : Schematic of experimental setup for the studies conducted by Nurick et al. [39,40] 30

Figure 2-21 : Picture showing capping failure on front face with fragment welded onto the back face [39] 31

Figure 2-22: Common failure responses of intermediate and thin plates struck by projectiles [63] 33

Figure 2-23: Graph used to determine a plate's deflection under impact from a fragment [8] 38

Figure 2-24 : Hemp fibre composite failure after impact by a fragment-simulating projectile (FSP) [83] 43

Figure 2-25 : Typical cellular material (polyurethane foam) Stress-Strain curve under quasi-static compression [111] 45

Figure 2-26: (a) Typical compressive stress of a cellular material and (b) its corresponding energy absorption efficiency curve [112] 47

Figure 2-27 : (a) Closed-cell Aluminium foam and (b) open-cell Aluminium foam 48

Figure 2-28 : Quasi-static failure mechanism of (a) Cymat and (b) ALPORAS aluminium foams [116] 49

Figure 2-29 : Stress vs strain curves for the several woods along (a) and across (b) the grain [90] (cited in [70]) 52

Figure 2-30 : Aluminium honeycomb (hexagonal cells) 53

Figure 2-31: Schematic of a honeycomb sandwich panel before impact (left) and after perforation by projectile [100] 54

Figure 2-32: Typical layout of a ceramic armour system [104] 56

Figure 2-33: Sandwich panels with lattice truss cores – (a) tetrahedral, (b) pyramidal and (c) Kagome lattices [127] 57

Figure 2-34: Photographs of sectioned aluminium alloy sandwich panels (pyramidal truss cores) subjected to impact velocities of (a) 280m/s and (b) 1222m/s from spherical steel projectiles [88] 59

Figure 2-35 : A typical multi-layered (triple) corrugated board 59

Figure 3-1: Schematic showing setup on the ballistic pendulum 64

Figure 3-2: Photograph showing set-up of the ballistic pendulum 65

Figure 3-3: (a) Dimensioned view and (b) CAD schematic of the experimental arrangement without energy absorber 67

Figure 3-4: (a) Dimensioned view and (b) CAD schematic of the experimental arrangement with energy absorbers 69

Figure 3-5: Photograph of the speed trap wooden block assembly..... 72

Figure 3-6: (a) Speed trap circuit box and (b) circuit diagram showing the connections between the circuit box and oscilloscope 73

Figure 3-7: Photograph showing the PE4 explosive charge setup used in the blast experiments 76

Figure 3-8: Engineering stress vs. strain curves for specimens taken from one of the sheets of mild steel (Sheet 1) 77

Figure 3-9: Photograph of all specimens subjected to quasi-static testing..... 80

Figure 3-10: Compressive stress vs. Strain for all materials tested quasi-statically (cross-head speed = 10mm/min)..... 82

Figure 3-11: Stress and energy absorption efficiency against strain for Divinycell foam compressed at 10mm/min..... 83

Figure 3-12: Photograph of all the materials used as energy absorbers during blast tests (40mm thick specimens shown) 85

Figure 3-13: Side view photograph of a typical fragment in the study – showing face and edge region 92

Figure 3-14: Typical oscilloscope voltage drop signals for the tests conducted during the study..... 93

Figure 3-15: Typical measurement of the diameter of the a fragment (ruler shown, in mm, is for scale) 94

Figure 3-16: Typical initial and post-impact states of an aluminium honeycomb energy absorber 96

Figure 4-1: Front test rig, with test plate exposed to a blast from an 11g, 36mm charge; showing how the petalled test plate wraps around the rear clamping plate 99

Figure 4-2: Photograph showing the failure of the front plates when charge mass increases for 27mm charge diameter (for tests NA00-2707-02, NA00-2708-01, NA00-2709-01 and NA00-2710-01) 100

Figure 4-3: Photograph showing the failure of the front plates when charge mass increases for 36mm charge diameter (for tests NA00-3607-02, NA00-3608-01, NA00-3609-02, NA00-3610-01 and NA00-3611-01) 101

Figure 4-4: Photograph showing the failure of the front plates when charge mass increases for 43mm charge diameter (for tests NA00-4307-02, NA00-4308-01, NA00-4309-01, NA00-4310-01 and NA00-4311-01) 101

Figure 4-5: Various states of the fragments after impact with the rear plates (ruler, in mm, is added for scale) 103

Figure 4-6: Photograph of a rear plate which fails by simple inelastic deflection (Mode I) after fragment impact 104

Figure 4-7: Photograph showing typical inelastic deflection with thinning around the impact region 105

Figure 4-8: Photograph of a rear plate showing failure by inelastic deflection with chordal thinning 106

Figure 4-9: Photograph of a rear plate showing failure by inelastic deflection with perimetral partial tearing (charge diameter = 36mm) 107

Figure 4-10: Photograph of inelastic deflection with chordal small partial tearing observed on rear plates, (a) when subjected to 27mm diameter charge, and (b), charge diameter is 36mm 108

Figure 4-11: Photograph of rear plate showing eccentric chordal partial tearing with little inelastic deflection. The maximum deflection cannot be defined in such a case (charge diameter = 43mm) 109

Figure 4-12: Photograph of large tearing of the rear plate (a) because of fragment perforation and (b) because of fusion of fragment onto the rear plate 110

Figure 4-13: Photograph of rear plates which have undergone secondary capping failure 111

Figure 4-14: Post impact for of aluminium foam under impact from a fragment released from the front plate by a 36mm diameter charge (showing sheared-off foam plug) 115

Figure 4-15: Entry, Exit and Sectioned views of 40mm thick aluminium foam subjected to increasing charge masses at 36mm charge diameter 115

Figure 4-16: Post impact state of aluminium honeycomb showing bending of the absorber layers and increasing opening from entry side to exit side 117

Figure 4-17: Entry, Exit and Sectioned views of 40mm thick aluminium honeycomb subjected to increasing charge masses at 36mm charge diameter 117

Figure 4-18: Post-impact state of 40mm thick balsa wood, showing material loss along the wood grain on the exit surface 119

Figure 4-19: Entry, Exit and Sectioned views of 40mm thick balsa wood subjected to charges of 36mm diameter 120

Figure 4-20: Corecell foam of 40mm thickness after impact - showing darkening of foam material in the fragment's path 122

Figure 4-21: Entry, Exit and Sectioned views of 40mm thick Corecell foam subjected to increasing charge masses at 36mm charge diameter 123

Figure 4-22: Photograph of a post impact state of 40mm thick Divinycell foam, showing the fragment wedged in 125

Figure 4-23 : Entry and Sectioned views of 40mm thick Divinycell foam, showing cross-cracks propagated through the thickness of the each foam disc 126

Figure 4-24: Entry, Exit and Sectioned views of 40mm thick Divinycell foam subjected to increasing charge masses at 36mm charge diameter 127

Figure 4-25: Photograph showing post-impact state of polyurethane foam while it is still in containment tube, showing powderised material 128

Figure 4-26: Entry, Exit and Sectioned views of 40mm thick polyurethane foam subjected to increasing charge masses at 36mm charge diameter 129

Figure 4-27: Entry, Exit and Sectioned views of the 40mm thick energy absorbers subjected to impacts from fragment released by 7g charge masses at 36mm charge diameter 131

Figure 4-28: Entry, Exit and Sectioned views of the 40mm thick energy absorbers subjected to impacts from fragment released by 11g charge masses at 36mm charge diameter 131

Figure 4-29: Entry, exit and sectioned views of 60mm thick energy absorbers subjected to fragment impact from 7g charge mass 135

Figure 4-30: Entry, exit and sectioned views of 60mm thick energy absorbers subjected to fragment impact from 11g charge mass 136

Figure 4-31: Entry, Exit and Sectioned views of 40mm thick single, double and quadruple-layered polyurethane foam subjected to 7g charge mass at 36mm charge diameter 137

Figure 4-32: Entry Entry, Exit and Sectioned views of 40mm thick single, double and quadruple-layered polyurethane foam subjected to 11g charge mass at 36mm charge diameter 138

Figure 4-33: Entry, Exit and Sectioned views of 40mm thick balsa wood subjected to impact by fragments with similar kinetic energies (Charge diameter = 27mm, 36mm & 43mm) 142

Figure 4-34: Entry, Exit and Sectioned views of 40mm thick Divinycell foam subjected to impact by fragments with close kinetic energies (Charge diameter = 27mm, 36mm & 43mm) 143

Figure 4-35: Entry, Exit and Sectioned views of 40mm thick polyurethane foam subjected to impact by fragments with close kinetic energies (Charge diameter = 27mm, 36mm & 43mm) 144

Figure 5-1: Impulse from the blast against varying charge mass for tests conducted using 27mm charge diameter 148

Figure 5-2: Impulse from the blast against varying charge mass for tests conducted using 36mm charge diameter 149

Figure 5-3: Impulse from the blast against varying charge mass for tests conducted using 43mm charge diameter 149

Figure 5-4: Impulse against varying charge mass for tests conducted using all three charge diameters 150

Figure 5-5: Measured fragment masses for all the fragments released by charges of the three tested diameters 153

Figure 5-6: Speed of the fragment, plotted against charge mass for tests conducted at 27mm charge diameter 154

Figure 5-7: Speed of the fragment, plotted against charge mass for tests conducted at 36mm charge diameter 155

Figure 5-8: Speed of the fragment, plotted against charge mass for tests conducted at 43mm charge diameter 157

Figure 5-9: Momentum of the fragment against charge mass for tests conducted at 27mm charge diameter 158

Figure 5-10: Momentum of the fragment against charge mass for tests conducted at 36mm charge diameter 159

Figure 5-11: Momentum of the fragment against charge mass for tests conducted at 43mm charge diameter 159

Figure 5-12: A generic ideal transition of trends from assumed momentum (linear) to a consequent kinetic energy trend 161

Figure 5-13: Kinetic energy of the fragment against charge mass for tests conducted at 27mm charge diameter 162

Figure 5-14: Kinetic energy of the fragment against charge mass for tests conducted at 36mm charge diameter 163

Figure 5-15: Kinetic energy of the fragment against charge mass for tests conducted at 43mm charge diameter 164

Figure 5-16: Rear plate deflection against fragment kinetic energy with no energy absorber at 150mm and 190mm plate separation 166

Figure 5-17: Rear plate deflection against fragment kinetic energy with no energy absorber - showing plate tearing points 167

Figure 5-18: Rear plate deflection to thickness ratio against Zhao's Response number for tests with no absorbers 169

Figure 5-19: Rear plate deflection against fragment kinetic energy for tests with 40mm thick aluminium foam 173

Figure 5-20: Rear plate deflection against fragment kinetic energy for tests with 40mm thick aluminium honeycomb 174

Figure 5-21: Rear plate deflection against fragment kinetic energy for tests with 40mm thick Balsa wood 175

Figure 5-22: Rear plate deflection against fragment kinetic energy for tests with 40mm thick Corecell foam 176

Figure 5-23: Rear plate deflection against fragment kinetic energy for tests with 40mm thick Divinycell foam 177

Figure 5-24: Rear plate deflection against fragment kinetic energy for tests with 40mm thick polyurethane foam 178

Figure 5-25: Comparative plot of rear plate deflection against fragment kinetic energy for all energy absorbers at 40mm thickness 179

Figure 5-26: Rear plate deflection against fragment kinetic energy for tests with 60mm thick Balsa wood 185

Figure 5-27: Change in rear plate deflection against kinetic energy when Balsa wood thickness increases to 60mm 186

Figure 5-28: Rear plate deflection against fragment kinetic energy for tests with 60mm thick Divinycell foam 187

Figure 5-29: Change in rear plate deflection against kinetic energy when Divinycell foam thickness increases to 60mm 188

Figure 5-30: Rear plate deflection against fragment kinetic energy for tests with 60mm thick polyurethane foam 189

Figure 5-31: Change in rear plate deflection against kinetic energy when polyurethane foam thickness increases to 60mm 190

Figure 5-32: Comparative plot of rear plate deflection against kinetic energy for the 60mm thick energy absorbers 191

Figure 5-33: Graph of rear plate deflection plotted against fragment kinetic energy, of the various polyurethane foam layering arrangements 192

Figure 5-34: Graph showing rear plate deflection under impact from difference sized fragments with close kinetic energies 193

Figure A-1: Threaded tube with two infra-red emitter-receiver pairs for velocity measurement 216

Figure B-1: Engineering Stress vs. Strain for all tests conducted on sheet 2 mild steel 219

Figure B-2: Engineering Stress vs. Strain for all tests conducted on sheet 3 mild steel 220

Figure B-3: Engineering Stress vs. Strain for all tests conducted on sheet 4 mild steel 220

Figure B-4: Engineering Stress vs. Strain for all tests conducted on sheet 5 mild steel 221

Figure B-5: Engineering Stress vs Strain for all tests conducted on sheet 6 mild steel..... 221

Figure B-6: Compressive stress vs. Strain for aluminium foam at different cross-head speeds 222

Figure B-7: Compressive stress vs. Strain for aluminium honeycomb 'A' at different cross-head speeds..... 222

Figure B-8: Compressive stress vs. Strain for aluminium honeycomb 'B' at different cross-head speeds 223

Figure B-9: Compressive stress vs. Strain for balsa wood at different cross-head speeds 223

Figure B-10: Compressive stress vs. Strain for Corecell A500 foam at different cross-head speeds 224

Figure B-11: Compressive stress vs. Strain for Corecell M80 foam at different cross-head speeds 224

Figure B-12: Compressive stress vs. Strain for corrugated board at different cross-head speeds 225

Figure B-13: Compressive stress vs. Strain for Divinycell H200 foam at different cross-head speeds 225

Figure B-14: Compressive stress vs. Strain for polystyrene foam at different cross-head speeds 226

Figure B-15: Compressive stress vs. Strain for polyurethane 80 foam at different cross-head speeds 226

Figure B-16: Compressive stress vs. Strain for polyurethane 200 'A' foam at different cross-head speeds..... 227

Figure B-17: Compressive stress vs. Strain for polyurethane 200 'B' foam at different cross-head speeds 227

Figure B-18: Compressive stress vs. Strain for RG5565 EVA foam at different cross-head speeds 228

Figure C-1: Simplified geometry and key dimensions of the ballistic pendulum 229

LIST OF TABLES

Table 2.1 : Summary of experimental details as carried out by Jacob [24] 11

Table 2.2: Summary of materials considered from literature and the ones used for quasi-static and fragment-impact testing 61

Table 3.1: Mass detail of components of the test rig 70

Table 3.2: Properties of PE4 75

Table 3.3: Selected properties of mild steel 78

Table 3.4: Mean dimensions, masses and densities for compression specimens 81

Table 3.5: Results on materials subjected to quasi-static compression testing 84

Table 3.6: Summary of all the energy absorbing material layer arrangements for each nominal thickness 86

Table 3.7: Details of parameters governing blast tests which occur with no energy absorbers 88

Table 3.8: Parameters for series of blast tests carried out with 40mm & 60mm thick absorbers (36mm charge diameter) 89

Table 3.9: Details of series of tests to investigate effects of different layering arrangements of energy absorbers 90

Table 3.10: Details of plan of series of tests to investigate effects of different size and speed of a fragment 91

Table 3.11: Notations used to describe the name of the energy absorber used for the various blast tests 97

Table 4.1: Summarised details of the released fragments from the blast tests 102

Table 4.2: Summary of results for tests in which no energy absorbers are used 113

Table 4.3: Summary of results for tests conducted with aluminium foam energy absorbers of 40mm thickness 116

Table 4.4: Summary of results for tests conducted with aluminium honeycomb energy absorbers of 40mm thickness 118

Table 4.5: Summary of results for tests conducted with balsa wood energy absorbers of 40mm thickness 121

Table 4.6: Summary of results for tests conducted with Corecell foam energy absorbers of 40mm thickness 124

Table 4.7: Summary of results for tests conducted with Divinycell foam energy absorbers of 40mm thickness 127

Table 4.8: Summary of results for tests conducted with polyurethane foam energy absorbers of 40mm thickness 130

Table 4.9: Summary of the general failure patterns of the energy absorbing materials (observed at 40mm thickness) 132

Table 4.10: Summary of results for tests conducted on balsa wood, Divinycell foam & polyurethane foam of 60mm thickness 134

Table 4.11: Summary of results for tests conducted on 40mm thick single, double and quadruple-layered polyurethane foam 140

Table 4.12: Summarised results for the test series where balsa wood, Divinycell foam and polyurethane foam are subjected to impact from different sized fragments (for investigations on close kinetic energies) 145

Table 5.1: Table showing the theoretical prediction of maximum front plate deflection before capping 152

Table 5.2: Relationship between dimensionless deflection and Zhao's Response number for different fragments 169

Table 5.3: Summary of predicted and measured rear plate deflection for tests carried out with no energy absorbers 171

Table 5.4: Comparisons between the critical perforation energy prediction and maximum experimental energy reported before perforation 172

Table 5.5: Decrease in calculated mean rear plate deflections at fragment kinetic energy intervals for 40mm thick absorbers compared to when no energy absorber is present 183

Table 6.1: Summary of the ranking of the protective performances of the various energy absorbers at 40mm thickness 200

Table B.1: : Detailed results of the quasi-static tensile tests performed on mild steel 218

Table C.1: Details of dimensions and masses of the ballistic pendulum 234

ACRONYMS

BISRU	Blast Impact and Survivability Research Unit
C4	Composition 4
CAD	Computer Aided Design
CME	Centre for Materials Engineering
EVA	Ethylene Vinyl Acetate
EVE	E-Glass Vinyl Ester
FEA	Finite Element Analysis
FSP	Fragment simulating projectile
IED	Improvised Explosive Device
PE4	Plastic Explosive 4
PVC	Polyvinylchloride
RDX	Research Development Explosive
SLM	Selective Laser Manufacturing
TNT	Trinitrotoluene
UHMwPE	Ultra-high molecular weight polyethylene

NOMENCLATURE

a	The constant in De Marre's equation
B	Breadth of the quasi-static compression specimen (m)
D	Constant in the Cowper-Symonds relation (s^{-1})
d	Plate Diameter (m)
d_c	Charge Diameter (m)
d_f	Fragment Diameter (m)
$\bar{d}_f$	Mean fragment Diameter (m)
E_{Abs}	Energy absorbed during quasi-static compression (J)
E_{cr}	Critical Energy for perforation (J)
E_{def}	Energy for deforming a plate (J)
E_f	Input energy from the fragment (J)
E_{in}	Input energy (J)
E_k	(Fragment) kinetic energy (J)
$\bar{E}_k$	Mean (fragment) kinetic energy (J)
$\sqrt{2E'}$	Gurney velocity (m/s)
H	Height of the quasi-static compression specimen (m)
h	Thickness of plate (m)

I	Impulse (N.s)
L	Length of the quasi-static compression specimen (m)
M	Mass of pendulum (kg)
M_{cas}	Mass of casing (kg)
m_{a0}	Mass of absorber before impact by the fragment (kg)
m_{a1}	Mass of absorber after impact by the fragment (kg)
m_c	Charge Mass (kg)
$m_c{}'$	1.2 x charge mass (kg)
m_f	Mass of fragment (kg)
$\overline{m}_f$	Mean fragment mass (kg)
m_{fp0}	Initial front plate mass (kg)
m_{fp1}	Final front plate mass (kg)
m_p	Mass of exposed area of the plate (kg)
p	Momentum (of the fragment) (Ns)
$\left(p_{pend}\right)_0$	Initial momentum of the pendulum (Ns)
p^*	Porosity of a cellular/porous material
q	Constant in the Cowper-Symonds relation
R	Plate Radius (m)
R_c	Explosive Charge Radius (m)

R_f	Radius of the fragment (m)
R_n	Zhao's Response number
SEA	Specific Energy Absorbed (J/kg) or (J/m^3)
SOD	Stand-Off Distance (m)
§	Literary 'section' symbol
§§	Used when reference is made to more than one 'section'
T	Time period of the pendulum (s)
Δt	Time differential in breaking the speed trap wire meshes (s)
v_{cr}	Critical initial plate deflection speed (for capping) (m/s)
v_f	Speed of fragment (m/s)
$\left(\overrightarrow{v_f}\right)_0$	Velocity of fragment on impact (m/s)
$\left(\overrightarrow{v_f}\right)_1$	Rebound velocity of fragment (m/s)
$\left(v_f\right)_{min}$	Minimum speed of fragment (m/s)
$\left(v_f\right)_{max}$	Maximum of fragment (m/s)
v_p	Initial plate deflection speed (m/s)
w_i	Arbitrary deflection on the plate deflection profile (m)
$\dot{x}_0$	Initial speed of the pendulum (m/s)
Δx_{mesh}	Distance between the two wire meshes of the speed-trap assembly (m)

Greek Symbols

α	Johnson's damage number
β	Damping constant
δ	(Rear) plate maximum deflection (m)
δ_0	Plate midpoint deflection just before cap fragment is ejected (m)
ε	Strain (m/m)
ε_d	Onset strain of densification (m/m)
ε_{fr}	Uniaxial fracture strain (m/m)
ε_{pk}	Strain at peak load (m/m)
$\dot{\varepsilon}$	Strain rate (s^{-1})
$\gamma(r)$	Shape function of the plate deflection profile
η	Energy absorption efficiency (%)
Φ_c	Dimensionless impulse/Damage number for circular plates
ρ	Density (of a monolithic material) (kg/m^3)
ρ^*	Density (of a cellular/porous material) (kg/m^3)
ρ^*/ρ	Relative density of a cellular or porous material
ρ_p	Density of the plate (kg/m^3)
σ_0	Static yield stress (Pa)
${\sigma_0}^1$	Dynamic yield stress (Pa)

σ_d	Damage stress (Pa)
σ_p	Yield stress of the plate (Pa)
σ_{pl}	Plateau stress (Pa)
ν	Poisson's ratio

GLOSSARY

Chordal thinning/tearing	Failure which is witnessed on a plate subjected to fragment impact in particular where the thinning/tearing occurs in an almost linear pattern adjacent to or through the point of maximum or potential maximum deflection
Incident motion	In projectile impact, the incident motion is the motion of the projectile as it initially approaches the target
Onset strain for densification	The compressive strain at which densification begins in a cellular material, lattice structure or any porous material under compression
Penetration	When impact from a projectile does not go all the way through the target but to a depth within its thickness
Perforation	When impact from a projectile completely punctures through the entire thickness of a target
Perimetral thinning/tearing	Failure which is witnessed on a plate subjected to localised blast or fragment impact where the thinning/tearing occurs in a perimetric pattern surrounding the point of maximum or potential maximum deflection (classic Mode Itc and Mode II*c)
Tunnel	During penetration or perforation of a structure by a projectile, the tunnel is the path in the structure that is opened by the projectile.

1. INTRODUCTION

Background

The world has witnessed a general increase in the use of improvised explosive devices (IED's) over the last few years. In a 25 month period from August 2010 to August 2012, almost 7,800 people were killed globally, and about 20,000 injured in IED incidents [1]. These casualties are in addition to damages caused to modes of transportation and various infrastructure. The numbers reported above are not inclusive of incidents reported in Afghanistan where, in the country alone, IED incidents rose from 9300 in 2009 to 17000 in 2012 [2]. Besides the effects of the explosive shock wave itself, secondary effects, which are considerable, are caused by the unleashing of fragments from the explosive casing and from surrounding structures, all propagated outwards from the point of detonation [3]. These fragments, unleashed at high velocities, can cause significant damage and casualties.

Besides the fragment hazard posed by terrorism or other forms of warfare, unforeseen operational incidents or design flaws in moving parts can also result in high speed fragments posing a threat to safety. This is perhaps exemplified by an accident caused by a turbine disk of an aeroplane engine which fractured, fragmented and punctured the fuselage of a Boeing 767 in a test run after an emergency-landing [4]. Design flaw, huge centrifugal forces may be attributed to the eventual failure and fracture of the disc. The effects of the event rendered the plane damaged beyond repair. During flight with passengers, such a case of fragmentation can prove to be catastrophic.

Whether it is in the field of war, from terrorist attacks, accidents that occur in a public, working, or industrial domains, there exists the hazard of damage or injuries caused by unforeseen or uncontrolled free-flying fragments. Ways of absorbing the kinetic energy from fragments to mitigate the damag effects need to be developed; and further insight into fragment induced damage is required.

Subject of the project

This study reports on an experimental investigation conducted on mild steel plates of 1.6mm thickness, and exposed circular areas of diameter 106mm. Plastic Explosive 4 (PE4) cylindrical charges are detonated locally on a front plate which fails in a Mode IIc failure mode (capping), ejecting a fragment from the central region to subsequently impact a rear plate. Three charge diameters of 27mm, 36mm and 43mm with mass ranging from 7g to 11g are used to produce the fragments. The fragment is characterised by means of its speed, measured by means of a speed trap, and its mass. The damage on the rear plate is noted by the mode of failure and quantified by means of deflection. Different energy absorbing cellular materials – Aluminium foam, aluminium honeycomb, balsa wood, Corecell foam, Divinycell (PVC) foam and polyurethane foam are place in front of the rear plate for damage mitigation. The change in failure mode and maximum deflection of the rear plate are used to assess the damage mitigation performance of the different energy absorbers.

Objectives of the project

The aim of this study is to investigate the use of cellular materials to mitigate damaged caused by a blast-induced fragment. The key aspects of the investigation are:

- Inducing Mode IIc (capping) failure on a circular mild steel plate by a localised blast from a cylindrical PE4 charge,
- Measuring the speed and the mass of the free-flying fragment,
- Observing the failure mode of the rear (impacted) plate and also by measuring the maximum deflection,
- Introducing different energy absorbing cellular materials – in different thicknesses and under varying test parameters – in front of the rear plate to subsequently mitigate damage to the plate,
- Assessing the protective performance of the absorber materials by assessing rear plate failure and observing how the absorber materials fail when subjected to fragment impact.

Report structure

The report is structured to include:

- Chapter 2 – Literature review
  - A review on literature pertaining to blast loading, fragmentation and impact onto structures.
  - A review on impact energy absorption and energy absorbers.

- Chapter 3 – Experimental details
  - Details are given on the different experimental arrangements to characterise different energy absorbing materials by means of quasi-static compression tests and the material of the test plates by means of quasi-static tensile experiments.
  - Details are also given on the structure of the blast tests – the testing rig, speed trap system, energy absorbers and measurement methods used in the experiments.

- Chapter 4 – Experimental Observations and Results
  - All phenomena which are found and observed during the experiments are discussed.
  - Furthermore, results which have been attained through measurements and calculations are presented in conjunction with the observations.
- Chapter 5 – Analysis and Discussions of Results
  - The experimental results which are presented in Chapter 4 are interpreted and discussed.
- Chapter 6 – Conclusions
  - The project is evaluated based on the objective of the study.
  - The results and observation of the tests, the accompanying analyses and discussions are summarised with conslusions.

- Chapter 7 – Recommendations
  - Based on the conclusions and challenges encountered during the project, recommendations are made for future studies.

- Chapter 8 – References
  - The external sources which are used and referred to in this project are listed.

- Appendices – Further details of auxiliary methods followed, results from material characterisation, calculations for the ballistic pendulum and drawings are included.

2. LITERATURE REVIEW

In this chapter, background information which has been acquired from various sources is discussed. The review includes concepts, principles, theories and past studies which have been reviewed to attain a comprehensive understanding of the background pertaining to this study.

The first section describes a review designed to obtain a better understanding of phenomena which relate to blast waves, localised blast loading, subsequent capping failure as a result of localised loading, the concept of fragmentation and the damage it can impart on structures. The second section gathers information on impact energy absorption as well as reviewing energy absorbers.

2.1. REVIEW ON BLAST LOADING AND FRAGMENTATION

2.1.1. Overview of detonation of explosions in air

An explosion can be described as a rapid, sudden and intense release of energy [5]. This energy discharge is primarily in form of heat, sound and light and it is mainly propagated through pressure waves. Explosions can be categorised into two main types; deflagrations and detonations [6]. A deflagration occurs in such a way that the blast wave from the reaction zone propagates outwards at a rate lower than the speed of sound in the medium in which the explosion is taking place. 'Reaction zone' refers to the region in the explosive where the chemical reaction which produces the explosion occurs.

During detonation, however, the blast wave – which is the pressure wave generated by the heating, chemical reaction and consequent expansion of the explosive gases (detonation products) – propagates outwards at supersonic speeds [6]. The relatively slow burning of gun powder is a good example of deflagration whereas explosives like Trinitrotoluene (TNT) and Plastic Explosive 4 (PE4) undergo rapid conversion of available chemical energy.

Detonation explosions are characterised by two phases [5]. The first phase of the explosion or blast is the detonation stage, where a detonator or booster may be needed [7]. The detonator sends a signal, in form of a pressure wave, - to start the detonation reaction. If the signal from the detonator, however, is not strong enough to initiate the reaction in the explosive material, a booster charge is required. The booster's is triggered by the signal from the detonator and it amplifies the signal from the detonator, i.e. booster explosive are more easily detonated than many primary explosives. This amplified shock wave signal has the strength to initiate the primary explosive detonation reaction [7].

The second stage of this process is the interaction of the generated blast wave with the surroundings [5]. Once the detonation reaction is initiated, the temperature at the point of detonation rises sharply and along with the initial detonation pressure causes the explosive to release its chemical energy. This resulting detonation products then expands and causes the surrounding medium to be compressed to a pressure that is significantly above the surrounding pressure. The maximum pressure, above the ambient pressure, is called peak side-on overpressure or just peak overpressure [8]. The compressed air is moved outwards and it thus gets propagated as a pressure wave, or a shock wave. The higher the peak overpressure generally means a higher shock wave speed [5]. The pressure distribution over distance at different times t_1, t_2 and t_3 (where $t_1 < t_2 < t_3$) from the point of detonation to the current shockwave front is illustrated in Figure 2-1. A pressure measurement can be conducted with a pressure gauge at anydistance from the point of detonation. The resulting pressure history (pressure vs. time) Is illustration in Figure 2-2 for an idealized representation of pressure versus time due to a blast wave.

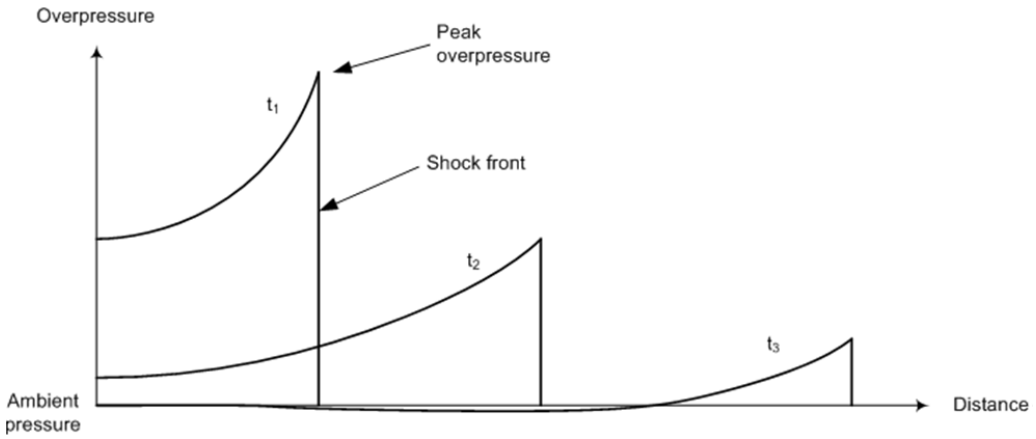

Figure 2-1 : Pressure distribution versus distance for detonation blast for different points in time [9]

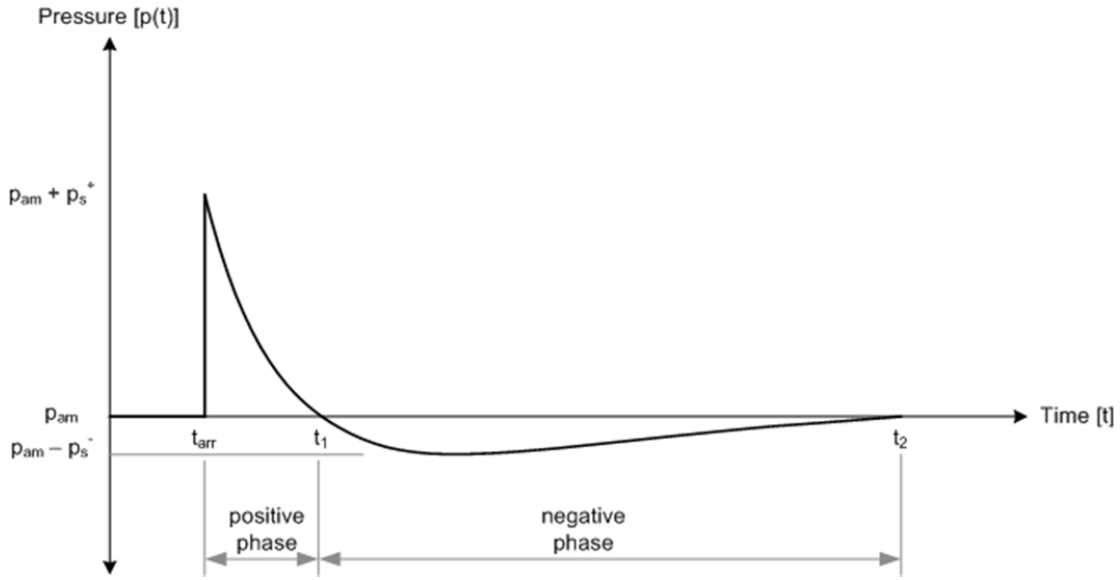

Figure 2-2 : Pressure versus time of an ideal blast wave [8]

If the detonation occurs at time 0, the blast wave propagates outwards and reaches an arbitrary point where the pressure is measured at the time of arrival (t_{arr}). At that time, the measured pressure rises above ambient pressure (p_{am}) and is referred to as peak overpressure ($p_{am} + p_s^+$). The pressure then exponentially decays to ambient at time t_1. After t_1, a negative phase occurs, with a reverse in gas flow due to the low pressure created by the over expanding gas. In the negative phase, the pressure drops below ambient and gradually rises until ambient pressure is again reached at time t_2 [10].

The temperature also increases instantaneously at the reaction zone and the outwards gas flow heats up the air that is compressed into a pressure wave. The temperature profile, from the point of detonation to the shock front, for the distinct points in time t_1, t_2 and t_3 after detonation (where $t_1 < t_2 < t_3$) is illustrated in Figure 2-3. The temperature is initially highest at the reaction zone (where distance = 0 on the horizontal axis) and decreases outwards to the shock front. The rate of this decrease in temperature drops with time (at t_2) until the temperature at the reaction zone drops to ambient pressure with the temperature at the shock front further decreasing but greater than ambient temperature (at t_3).

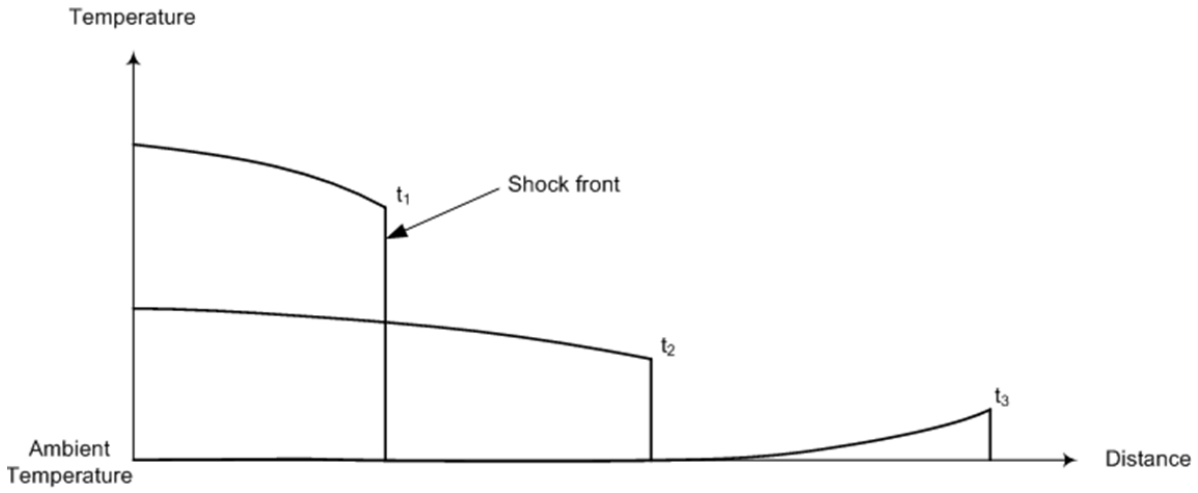

Figure 2-3 : Temperature profiles for an airblast over distance for different points in time [9]

2.1.2. Structural Response to Blast Loading

A blast can have damaging or destructive effects on obstacles within the proximity of its propagated pressure wave. This effect depends on explosive factors such as the type of explosive, the quantity, and its shape. The other influential parameters can be referred to as obstacle factors; which include the medium between the target and source of the blast, the stand-off distance and the level of confinement of the blast.

Structures made of various materials, of different geometries and boundary conditions have been studied under impulsive loads to understand the effects of blast loads. Studies have been carried out on structures like beams [11,12], circular plates [5,13-27], quadrangular plates [5,14,15,28-32], stiffened plates [33-36], V-shaped plates [37,38], square tubes [39,40], and composite panels [41-43]. In these studies, different blast load parameters are used to better understand how these structures respond to blast loads. While numerous studies on structures of various geometries have been carried out, this review \ emphasizes on circular plates.

2.1.2.1. Uniform Blast Loads

Overview

In case of flat structures, a uniform blast load is typically imparted as evenly distributed over the entire area of the target. Studies pertaining to structures exposed to uniform blasts have been carried out by a number of authors, including Nurick et al. [16,18,24,27,28,30,32,34,43], Xue & Hutchinson [44], Gupta [25] and Gharababaei & Darvizeh [26].

Bodner (cited by Nurick and Martin [13]) suggested using a formable explosive shaped into concentric annuli (rings) to achieve uniform loading on steel plates. Though the distance between the explosive and the target plate is small, forming the explosive into this ‘web’ configuration that follows the general shape of the target plate ensures that the impulse on it is uniformly distributed.

Nurick & Martin [13] defined the explosive layout for circular plates using a two-ring annular setup of the Metabel sheet explosive. The ratios of the radius of each of the explosive rings to the radius of the exposed area of the plate, using the two-ring annulus setup, are shown in the schematic in Figure 2-4.

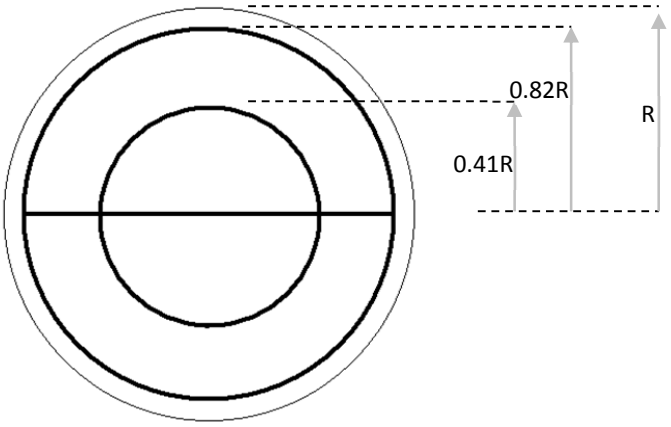

Figure 2-4 : Explosive layout in a two-ring concentric circle annulus [13]

A shortcoming of using the concentric ring method to impart uniform loading on a plate is that it is time-consuming to roll the explosive to the desired shape. Furthermore, the there is a minimum required thickness for the explosive to successfully detonate [15], i.e. a relatively large amount of explosive material may be consumed to achieve uniform loading.

Marchand and Alfawakhiri [45], suggested that for a load to be regarded as uniformly distributed over a target structure, the stand-off distance (SOD) should be greater that one half of the target's element width or height dimension. As illustrated in the schematic on Figure 2-5, this means that for a circular plate, the load is only uniform if:

$$SOD > R \qquad \text{Eq. 2-1}$$

Where SOD = Stand-off distance R = Plate Radius.

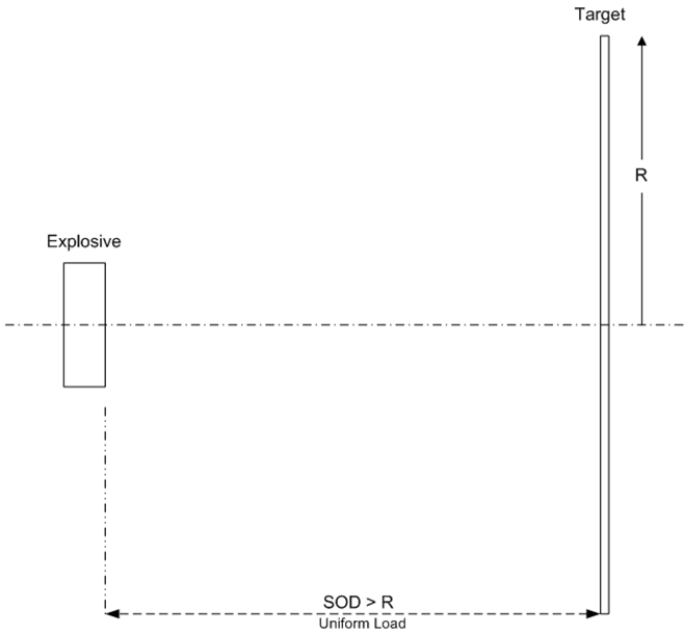

Figure 2-5: Schematic showing conditions for a blast load to be uniform for a circular target [45]

Investigations were carried out by Jacob et al. [24] to study the effects stand-off distance on the response of thin circular plates. In this study, mild steel plates had an exposed circular area of diameter 106mm. The details of the investigation are summarised in Table 2.1.

Table 2.1 : Summary of experimental details as carried out by Jacob [24]

Test Parameters	**Parameter Variations**
Plate thickness (mm)	1.9
Exposed diameter on plate (mm)	106
Stand-off distance (mm)	13, 25, 30, 40, 50, 75, 100, 150, 200, 250 & 300
Charge diameter (mm)	34
Charge mass (g)	4, 5, 7, 9, 11, 13 & 15

It was observed that between a SOD of 13mm and 40mm, the plate deformation shows a deflection profile where a central dome appears superimposed on a global dome, suggesting localised loading. The plate responses showed a transition from localised into uniform deformation between SODs of 50mm and 75mm. When the SOD is 100mm and greater, the loading effect on the plates appears to be essentially uniform in nature, evidenced by a simple global dome – as shown on the photograph in Figure 2-6.

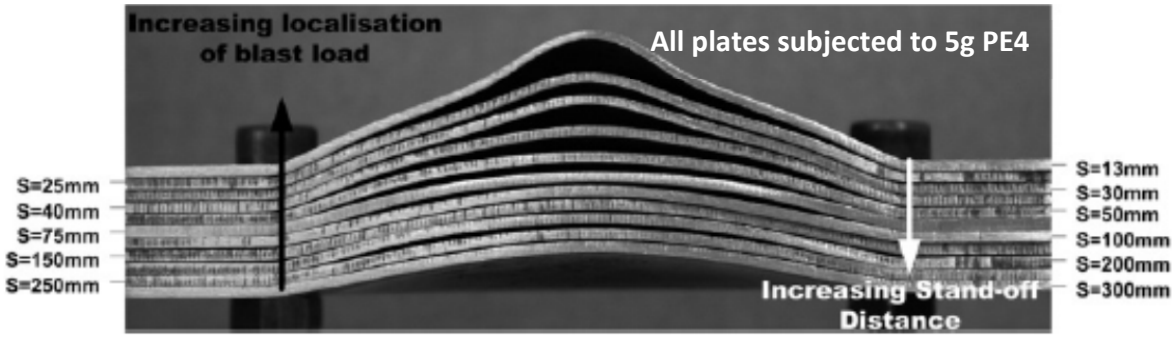

Figure 2-6: Photograph showing localisation of blasts on plates for varying stand-off distances

Moreover, it was suggested that for cylindrical charges, the relationship between the charge radius and the SOD is a prime indicator of whether a load is uniform or not [24]. In the suggested relationship, when the SOD is equal to or greater than the charge radius, the load can be assumed uniform, otherwise it is considered localised – as is shown in the schematic in Figure 2-7.

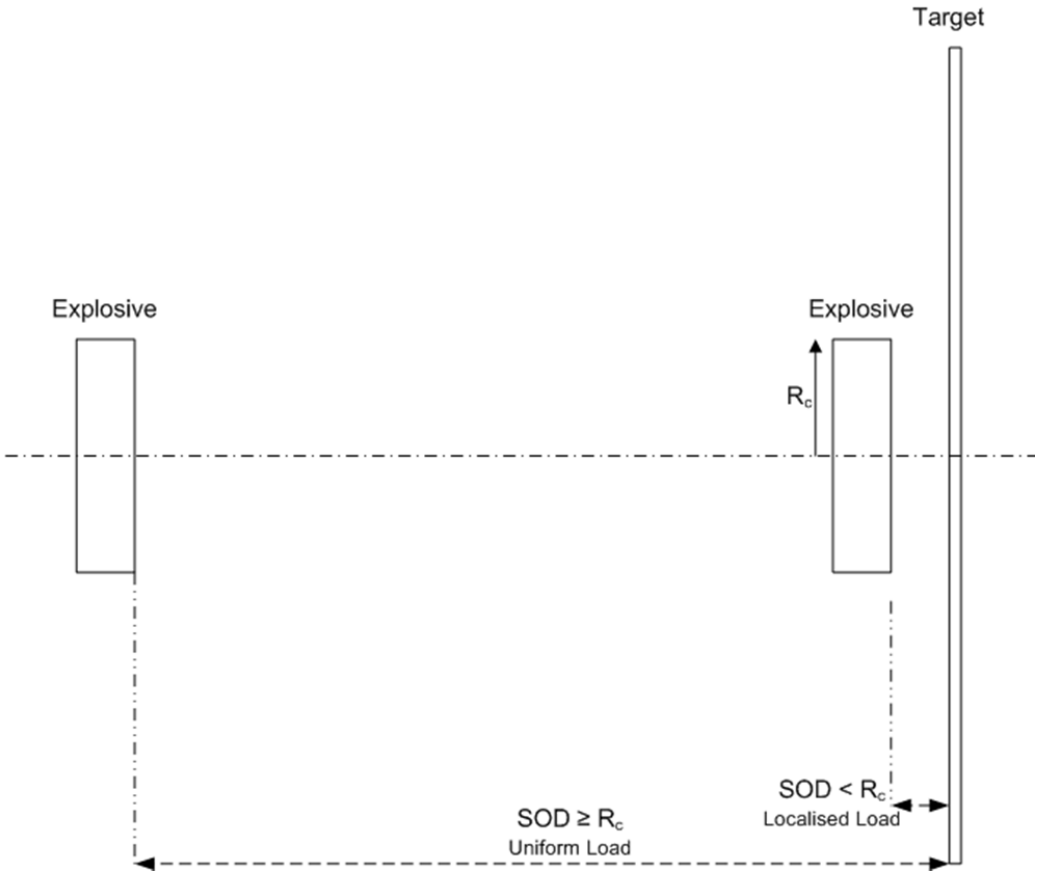

Figure 2-7 : Schematic showing loading condition for localised and uniform blasts on test plates [24]

General structural response to uniform loading

Menkes and Opat [11] defined three modes of failure for clamped beams which are subjected to uniform impulsive loads. Under these loads the beams fail by large inelastic deflection, large inelastic deflection with tearing in the boundary region, and also by failure through shearing at the boundary.

Mode I : Large inelastic deflection

This failure mode is characterised by a global uniform deformation of the beam clamped at the boundary, as depicted in Figure 2-8.

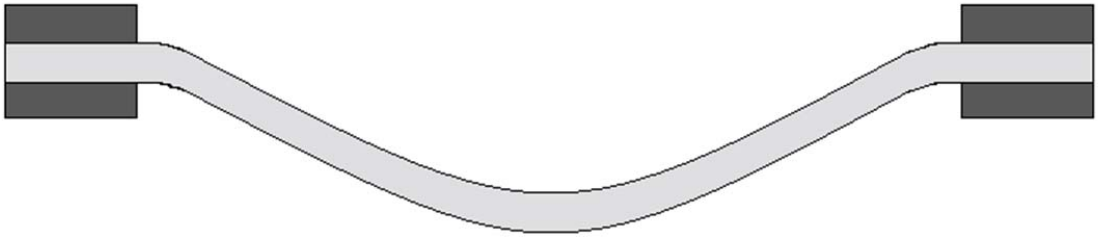

Figure 2-8 : Schematic of Mode I failure for blast loaded clamped beams and plates [11]

Mode II : Large inelastic deflection with tearing at the boundary

This mode of failure is typically observed at loads which are larger than loads which cause Mode I failure. This is characterised by a large inelastic global deflection with tearing at the fixation points, or boundary – as shown in the schematic Figure 2-9.

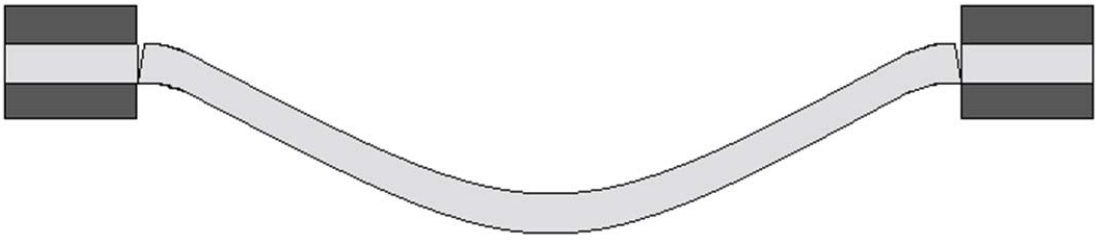

Figure 2-9 : Schematic of Mode II failure for blast loaded clamped beams and plates [11]

Mode III : Shear failure at the boundary

This failure mode is achieved by a further increase of load from Mode II and this increase induces shear failure, as illustrated in Figure 2-10.

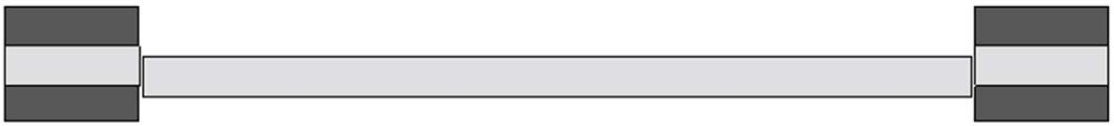

Figure 2-10 : Schematic of Mode III failure for blast loaded clamped beams and plates [11]

The aforementioned triad of modes of failure is a generalized view of how clamped beams or plates fail under impulsive loads. Depending on the localisation and intensity of the load, additional modes of failures were later derived from these parent modes of failure.

Plate failures for uniform loading

For plates subjected to uniformly distributed loads, modes of failures were comprehensively defined by Nurick et al. [18]**.** In these investigations – performed on circular plates – Nurick et al. [18] observed that the impulsive loads yielded variants of Mode I failure, in addition to Mode I itself viz. **Mode Ia** and **Mode Ib**. For uniform loading, a 'global dome' deflection profile is observed for Mode I failure, as can be seen in the sectioned plate profiles in Figure 2-11. Mode Ia failure refers to Mode I (large plastic deformation) with through thickness thinning or necking across a portion of the boundary. With increased impulse, Mode Ib was observed – which is Mode I with thinning across the *entire* boundary [18].

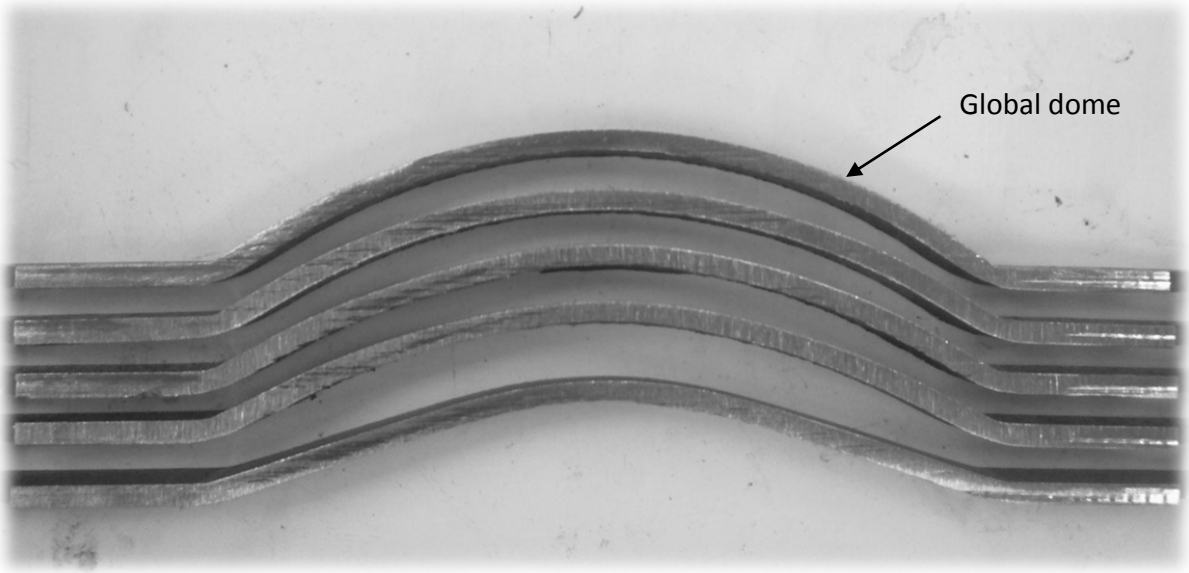

Figure 2-11 : Typical 'global dome' Mode I plate deflection under uniform blast loading [27]

Further findings by Nurick et al. [18] showed a transition from Mode Ib to Mode II*. This mode of failure is characterised by large inelastic deformation with tearing across part of the boundary. This is a form of Mode II, which, as described by Menkes and Opat [11], is inelastic deformation with complete tearing at the boundary.

2.1.2.2. Localised Blast Loads

Overview

A structure subjected to a localised blast load experiences a concentrated impulsive load on the target region that is closest tothe charge. The localisation of the impulse in the center region is generally greater than in the peripheral regions.

In investigations carried out by Jacob et al. [24], it was suggested that if the distance between the (cylindrical) charge and the target structure is less than the radius of the charge, then the load is deemed to be localised. This is shown on the illustrative schematic in Figure 2-7; a blast is deemed localised if:

$$SOD < R_c \qquad \text{Eq. 2-2}$$

Where *SOD* = Stand-off distance, R_c = Charge Radius

How plates fail under localised loads

For plates subjected to localised blast loads, investigations were carried by Nurick and Radford [19] to get derivative modes of failure from the principal modes defined in §2.1.2.1. In the investigations - amongst other observations - there were remarks on some of the modes of failures which were described by Menkes and Opat [11], namely:

- Mode I - Large inelastic deformation,
- Mode II - Inelastic deformation with complete tearing of the boundary.

When a plate subjected to localised loading fails in mode I, the region around its midpoint deflects differently from the area next to the boundary. There appear two domes – a global dome away from the plate midpoint, and a secondary dome lying atop the global dome at the central region as shown in Figure 2-12.

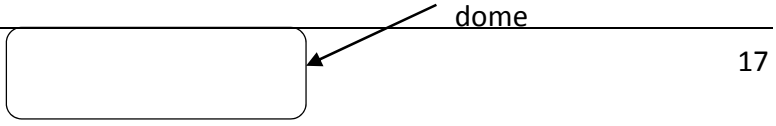

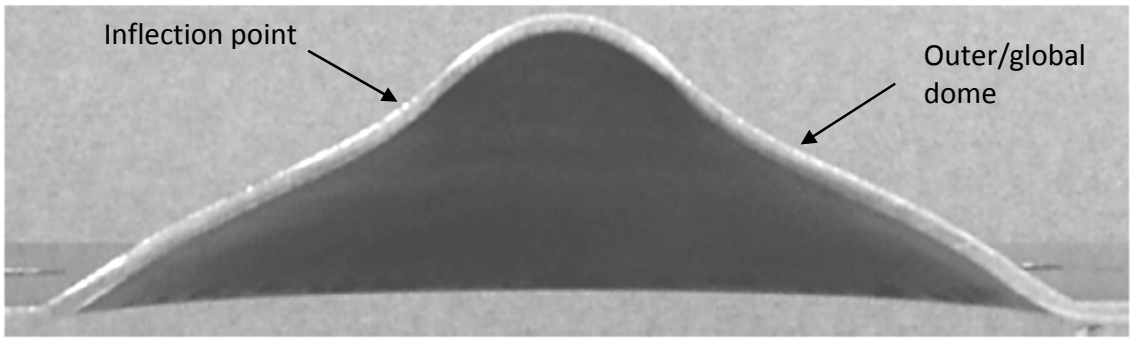

Figure 2-12 : Plate deflection profile under localised loading [24]

Nurick and Radford [19] also found additional modes of failure, shown in the plates shown in Figure 2-13, which evolve from the two aforementioned parent types:

- Mode Itc - Large inelastic deformation with thinning around the centre
- Mode Ib - Large inelastic deformation with thinning at the peripheral boundary
- Mode II*c – Inelastic deformation with partial tearing around the centre
- Mode IIc - Inelastic deformation with complete tearing around the centre (capping)

Failure by means of Mode IIc entails complete tearing around the central region and subsequent ejection of the fragment.It was also noticed that in addition to the aforesaid failure modes, plates can fail by petalling, which is a tearing of the central plate area with the torn area deforming into a petal-like form.

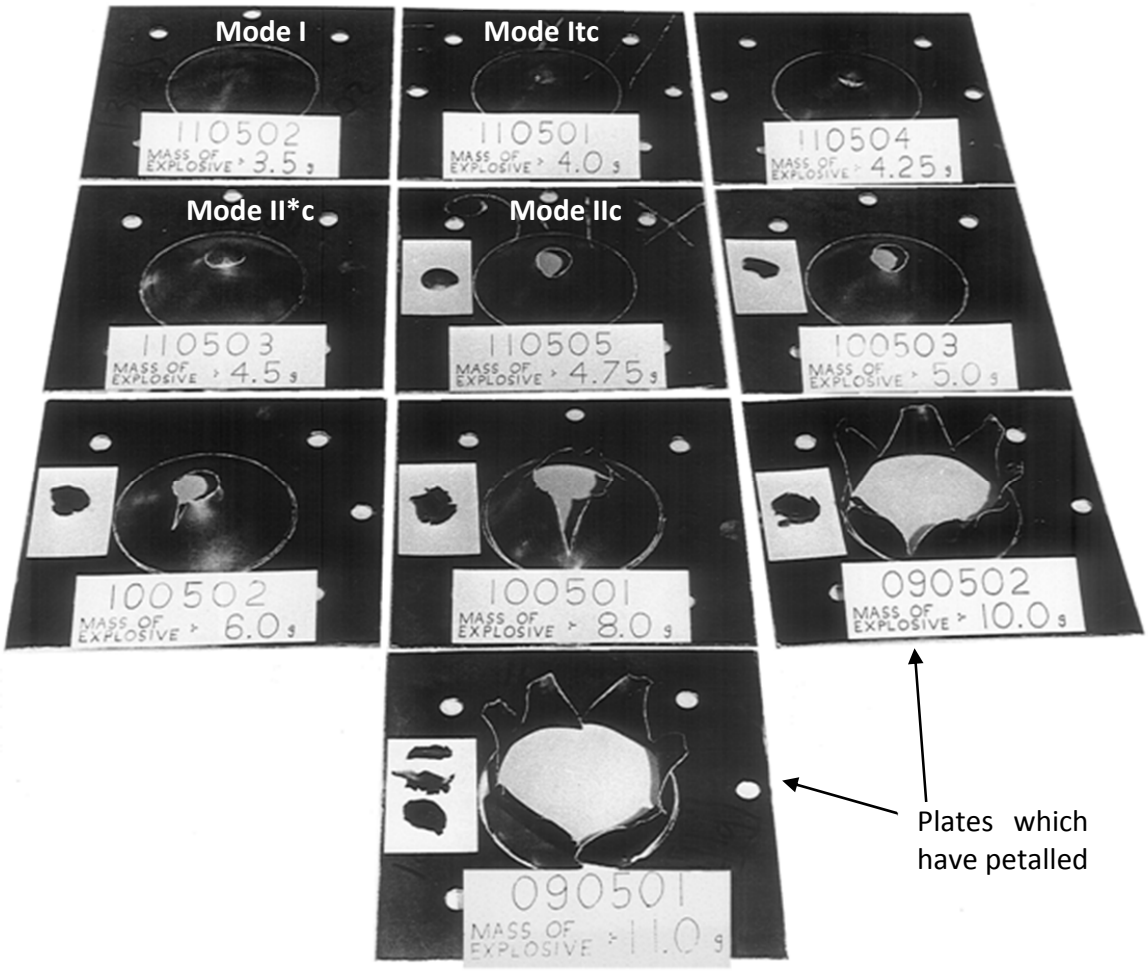

Figure 2-13: Picture of a series of plates subjected to localised blast loading, showing various failure modes [19]

Nurick and Radford [19], moreover, observed that there appears to be a proportional relationship between the load (charge) diameter and the inflection diameter - which is the diameter of the region on the plate where the local dome appears to blend into the global dome. A proportional relationship was also observed between the charge diameter and the diameter of the cap fragment, which is always smaller than the charge diameter. Another observed relationship was between charge diameter and the size of the discolouration of the loaded side of the plate due to the blast – also referred to as 'burn diameter'. The graph shown in Figure 2-14 represents the empirical relationships which were established [19].

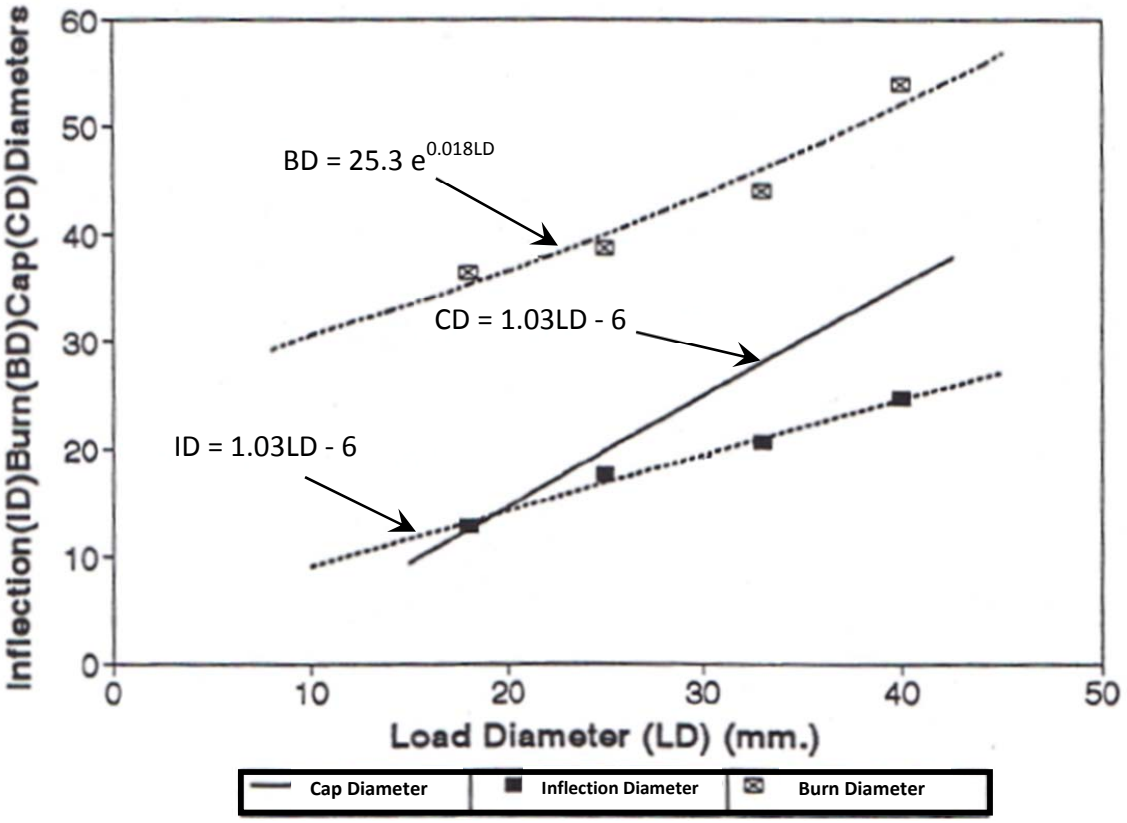

Figure 2-14: Pre-capping relationship between inflection diameter (ID), Burn diameter (BD) against load diameter (LD) - as well as post-capping relationship between cap diameter (CD) and load diameter [19]

2.1.3. Fragmentation

Fragmentation, as pertaining to the background and direct work covered for this study, is the dynamic unleashing of a fragment or fragments due to the propagation of a blast wave or a due to impact. These fragments are objects or bodies which are dynamically released or broken from any substrate on which the load of the blast wave or impact is imparted. Moreover, fragments can also be secondarily released or torn from a surrounding structure which is subjected to ballistic impact from an incident fragment.

Fragments can be released from the casing that surrounds an explosive charge, in cases of munitions that have casings to contain the explosive charge. As the charge goes off, the casing or container breaks into fragments which are accelerated outwards from the charge. Most such fragments are from portions of the case that are in contact with the charge. Fragments which are released this way are referred to as primary fragments [3].

Secondary fragments are released from a state in which they are not in contact with the charge but within the vicinity of its effect. These objects might be loose or might be broken off from the substrate onto which they are fixed. Once they are released, they have the potential to cause damage on any target (also referred to as 'receiver') they contact [3]. When any of these fragments are released, they move as projectiles as they are subjected to forces of gravity and aerodynamic forces (lift and drag). If the geometry of the fragment is such that the drag factor is considerably higher than the lift factor, then the fragment is called a drag-type fragment and if the force of lift on the fragment is greater or equal to the drag force, then the fragment is a lift-type fragment [3]. **Fragmentation can either occur accidentally or by design**.

2.1.3.1. Fragmentation and release of fragments

Fragmentation during rock blasting

In the mining industry or other processes which entail land excavation, rock blasting is a designed fragmentation process where masses of parent rocks are subjected to blast loads to break them into fragments of rocks which would then be transported from the site. Rock drilling is another form of desirable fragmentation in mines, where mineral host rocks are fragmented under dynamic impact loading. In the rock blasting and mining industries, numerous studies have been carried out, including prediction of explosive energy required for rock fragmentation to occur and prediction of the resulting fragmentation mode and fragment sizes [46-49].

Fragmentation of munition casings

Bombs and other commercial or improvised explosive devicess are usually located in a container referred to as a casing. The casing is designed such that as the explosive undergoes denotation, it breaks into many primary fragments which are propagated outwards. The sectioned view in Figure 2-15 shows the geometry and parts of a typical missile casing.

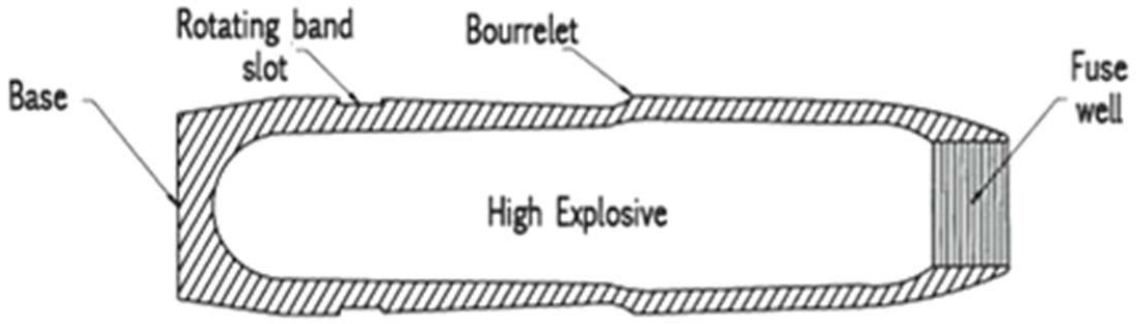

Figure 2-15: A typical munition casing of a missile [50]

When subjected to the internal load, imparted by the outward-propagating blast wave, the casing expands and cracks propagate from the outer surface to the inner surface because of the excessive external hoop stress. This is illustrated in Figure 2-16, which is a sectioned schematic of part of a casing. The Gurney model is used to estimate the initial fragment speed from the casing through Eq. 2-3 [50,51]

$$\left(v_f\right)_0 = \sqrt{2E'}\left[\frac{M_{cas}}{m_c{}'} + \frac{1}{2}\right]^{-1/2} \qquad \text{Eq. 2-3}$$

Where: $\sqrt{2E'}$ = Gurney velocity, $m_c{}'$ = 1.2 x charge mass, M_{cas} = Mass of casing

Numerical simulations reported by Glanville et al. [52,53] attempted to estimate the size distribution, speed distribution and directions of fragments after the shattering of munition casings following the blast from the contained explosive. Using the geometry and refined material properties of the casing, close agreement between the predictions by the model and experimental findings was achieved.

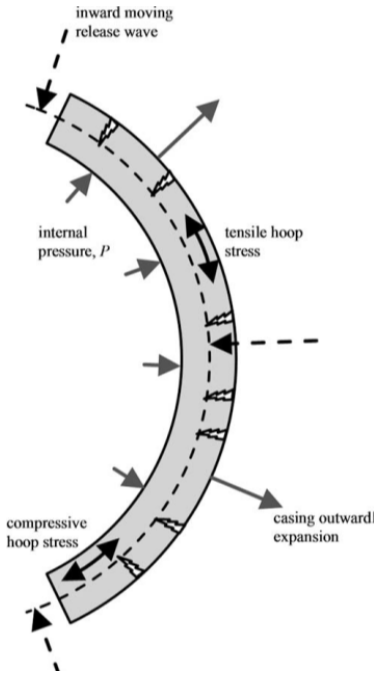

Figure 2-16: Section through a munition casing showing the genesis of fragmentation [51]

Figure 2-17 is a prime example of the potential effects of fragmentation of munition casings. In the study by Chung Kim Yuen et al. [32] where mild steel quadrangular plates were subjected to large scale blast loads as a result of detonation of large amount of ordnance in an outdoor testing site, some plates, like the one shown in Figure 2-17, were perforated by fragments from the casing of the explosive charge.

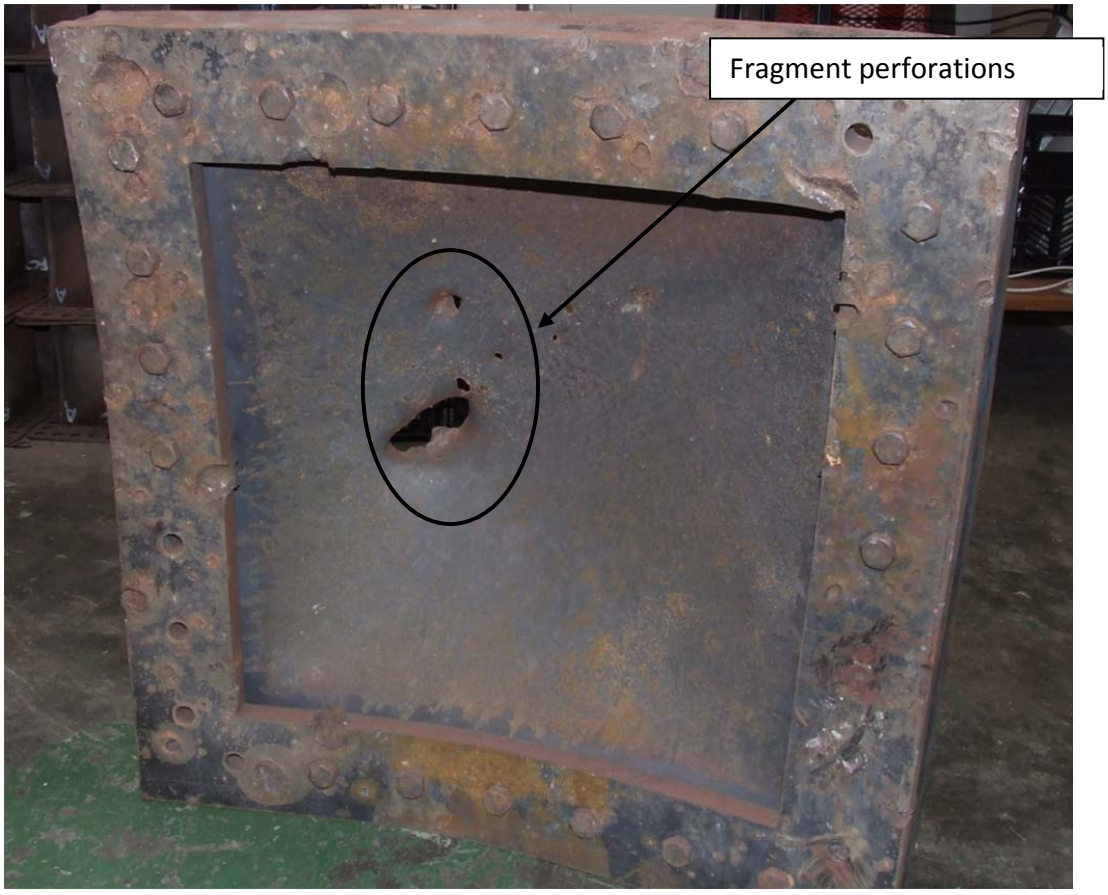

Figure 2-17: Steel plate deformed by blast wave but perforated by fragments from the munition casing [32]

Fragmentation by means of spallation

The formation of spall fragments can be due to the transmission of a dynamic load on a wall structure which results in fragmentation on the free (or back or exit) face. The load on the donor (or impact or entry) face might be a blast load. When the incident load is imparted on the donor face, rupturing or spall occurs at the free face resulting in the flying off of fragments [54].

Spallation occurs in two ways: direct spallation and scabbing [55]. Direct spallation occurs due to the compression wave that is initiated by the load on the impact face being propagated to the free face. A disengagement of spall fragments from the free face is subsequently caused by a reflected tensile wave emanating from the free face, fracturing and consequently fragmenting part of the surface. Scabbing may occur in reinforced concrete structures, in a similar initiation compressive wave as in direct spalling, except that the disengagement of the spalls occurs due to excessive flexural strains on reinforcing members [55]. The two phenomena are often confused in literature because of the similarity of the generation of the spall fragments [3]. A general case of spallation is illustrated in steps in the simulation depicted in Figure 2-18. In their experimental study, Wu et al. [56] subjected reinforced concrete wall to blast loads to categorise the fragment size distribution due to scabbing. Amongst other findings, it was found that the fragment sizes follow a Weibull distribution. Consequently, a better understanding was attained about scabbing and it could give rise to more scab resistant building walls being constructed [56].

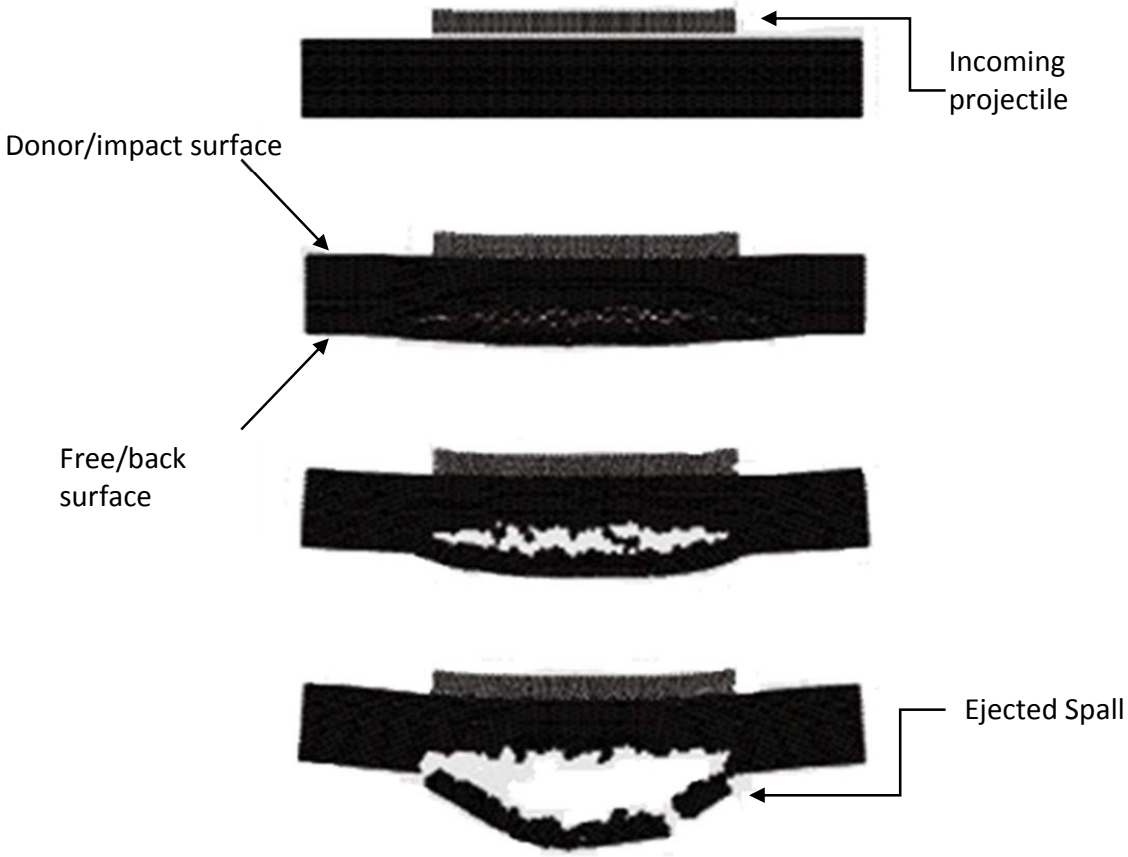

Figure 2-18 : Simulation of spallation due to projectile impact [57]

Unleashing of free (secondary) fragments

Whilst rock blasting, fragmentation of munition casings and spallation all entail disengagement of fragments from whole parent structures, fragmentation does not always occur by dynamic disengagement of fragments from a parent material As implied by the statement *"Secondary fragments are released from a state in which they are not in initial contact with the charge but within the vicinity of its effect"*, a blast wave can accelerate small rocks, small solids bodies and other loose debris within the environment in which the blast has initiated. As with other types of fragmentation, some of these fragments can be hurled by the blast at several hundreds to thousands of metres per second into the surrounding where they can come into contact with objects and cause damage or fatalities [3].

Thin metallic shells and plates to subjected to blast loading

Fragmentation of aluminium and steel spherical shells were studied prominently by Ivanov et al. [58] to investigate the initial fragment speed distributions. Between 2800 and 5000 fragments travelling between speeds of 2700m/s and 3000m/s were observed when various sizes of the spherical charges (66mm – 180mm diameter range) were detonated in shells of varying wall thicknesses with internal diameters of the shells equal to the diameters of the respective charges, i.e. fully contained charges.

As described in §2.1.2.1, plates subjected to uniform blast loading can fail by either Mode II (inelastic deflection with complete tearing at the boundary) or Mode III (shear failure at the boundary). In both cases a disc, emanating from the area exposed to the blast, is released from the plate. In their studies on mild steel circular plates subjected to uniform loading (100mm diameter and 1.6mm thickness), Teeling-Smith and Nurick [16] reported on, amongst other failure modes, Mode II and Mode III. Speeds of up to 423.7m/s were recorded for the ejected discs. This study was later extended to include square mild steel plates (89mm x 89mm exposed area and 1.6mm thickness) subjected to uniform loading by Nurick and Shave [30]. It was observed that the discs were ejected at maximum speeds of 281m/s in Mode II and 377m/s during Mode III failure. It was also confirmed through observations that the disc fragments did not all purely translate but also rotate [30].

Another form of fragmentation which has been reported on flat plates in literature is capping (Mode IIc) due to localised loading, as discussed in §2.1.2.2. **In this study, this mode of failure is used to achieve fragmentation and therefore it is discussed separately in §2.1.3.2.**

2.1.3.2. Capping (Mode IIc)

If the impulse imparted on a plate by a localised blast is great enough, the plate may fail by Mode IIc – which is complete tearing around the central region of the plate. The phenomenon is referred to as capping because of the cap-like fragment which is ejected from the central

region. Due to the more localised type of loading, this mode differs from the one that is characteristic of uniform loading where a plate is completely torn at its boundary, and is discharged as a fragmented disc in either Mode II or Mode III failure.

For localised loading, depending on the plate geometry and material properties, the impulse beyond which full tearing of a cap/fragment from the plate occurs is referred to as the critical impulse [39]. If the explosive exerts an impulse on the plate which exceeds the critical impulse, part of that impulse goes into deforming and tearing the fragment from the plate, and the remainder – known as the residual impulse - is imparted to the flying fragment [39]. The fragment that is released has a diameter that is marginally smaller than the diameter of the charge that is used [39].

Capping of plates subjected to localised loading

Figure 2-19 is a simplified schematic showing how a plate before being loaded by a localised blast and after ejection of a fragment from the central region. Different studies have been carried out to understand capping in terms of its genesis and method of fragment release to categorise its effects [5,18,21,23,39,40,59]. Wiehahn et al. [21] suggested a model which includes the temperature-dependant material properties – instead of just the stress-related properties – when attempting to better understand and predict the onset of capping and capping itself.

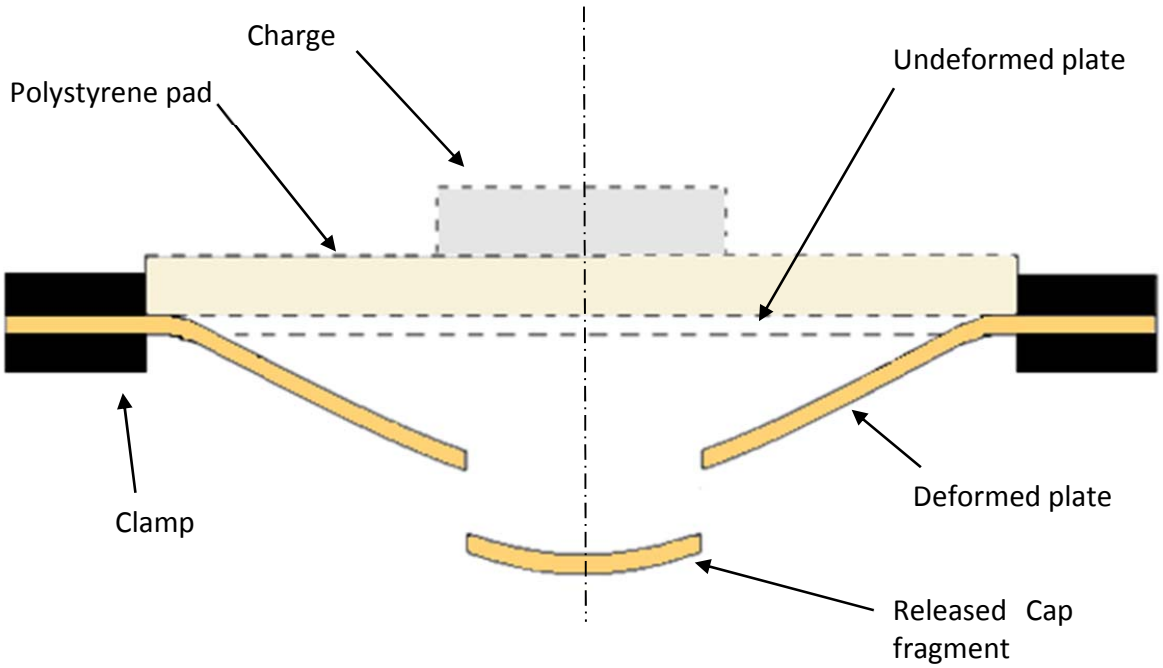

Figure 2-19 : Schematic showing capping failure on a plate

In a subsequent study by Chung Kim Yuen and Nurick [59] – it was also shown that there exist localised regions with increased temperature when thinning and the onset of capping occurs. Plastc strain in the thinning region causes the temperature to increase to more than 600°C. Due to the short duration of the blast and consequent adiabatic deformation process, the heat generated in the thinned area is not transferred to the surrounding region of the plate. The tearing mechanism of the fragment is not necessarily symmetrical, suggesting that there could be some rotating and translation when the fragment is released because of discrepancies/asymmetries in the blast load and inconsistency in material properties – particularly of mild steel [59].

Capping of tubes subjected to localised loading

There are few studies on external blast loading of tubular structures [60-62], and even fewer studies have been carried out on square tubes for the sole purpose of understanding capping failure and its effects. An experimental investigation by Nurick and Bryant [39] which is extended into a numerical model by Balden and Nurick [40] on square tubes (100mm x 100mm x 300mm with 2mm and 3mm wall thicknesses) to investigate the motion and damage caused by a fragment released from one of the faces onto the other. The two faces of the tube were assumed to be parallel rectangular plates.

In this square tub study, a cylindrical charge, 40mm in diameter, was placed at the middle of one of the faces of the tube, known as the front face, as depicted on the CAD schematic in Figure 2-20. After detonation, a fragment was torn from the front face and impacted to the back face. This fragment caused the back face to deform. For some large impulses, it was observed that the fragment impacts the rear face and is fused onto it in addition to the deformation. A photograph showing one of the square tubes with a fragmented front face and subsequent fusion of the fragment onto the back face is shown is shown in Figure 2-21.

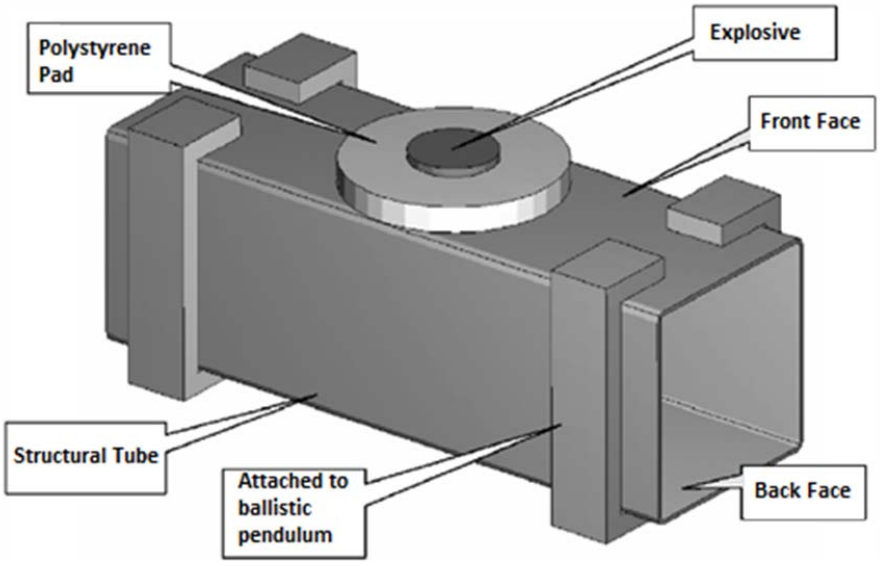

Figure 2-20 : Schematic of experimental setup for the studies conducted by Nurick et al. [39,40]

In the experimental studies by Nurick and Bryant [39], the speed of the fragments was not recorded. However, in the subsequent numerical simulation studies by Balden and Nurick [40], the predicted speeds of the fragments were as high as 835m/s.

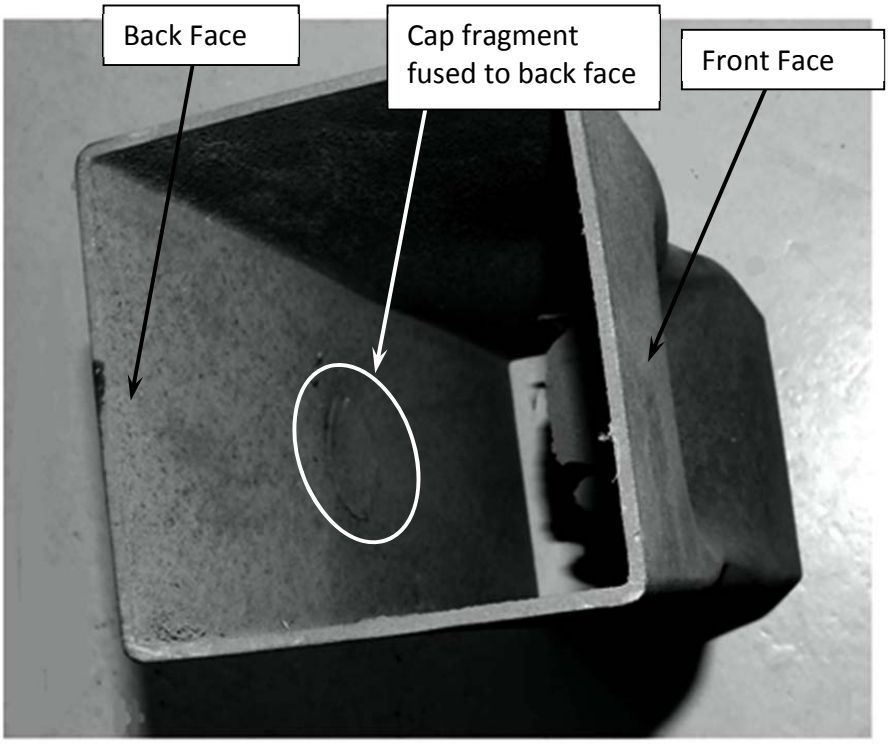

Figure 2-21 : Picture showing capping failure on front face with fragment welded onto the back face [39]

2.1.3.3. Impact and damage by fragments

When released, fragments behave as projectiles as they are subjected to aerodynamic and gravitational effects. When projectiles are fired at plates, the response of both the projectile and target depends on a number of factors, including material properties of both, incoming relative velocity of the projectile, method of support of the plate, the dimensions of the plate and the relative dimensions between the projectile and plate.

An important characteristic dimension for the plate, that has a bearing on the failure, is thickness. Zukas [63] defined four levels of plate thicknesses;

- Thin plates: they exhibit no stress response and failure difference across the thickness,
- Intermediate plates: The free face has a response throughout the penetrating process of the projectile,
- Thick plates: the boundary only has an effect on the penetration after some considerable penetration.
- Semi-infinite plates: the boundary has no effect on the penetration.

For thin and intermediate plates which are struck by a projectile, the principal failure responses, as reported by Zukas [63], are shown in Figure 2-22. For brittle materials, which have the compressive strength exceeding the tensile strength, cracks can form in the radial direction of the target plate during impact. For a blunt projectile, or one with a hemispherical impactor, approaching at a speed which is just below the speed required to cause perforation - also known as the ballistic limit - in that material, a 'plug' which has a similar diameter to that of the projectile may be sheared from the plate and ahead of the decelerating projectile [63].

For a thin plate, the stress waves in the radial direction are concentrated at the projectile tip. The forward motion of the projectile induces symmetric bending moments on the plate. If the projectile does not rebound off the plate, fracture may occur including perforation, and the plate fails in a peatling mode ,as plastic failure in the material is induced [63]. **It is important to note that the kind of projectiles shown in Figure 2-22 are well defined in geometry and the way in which the fragment strikes the target is through purely translation.**

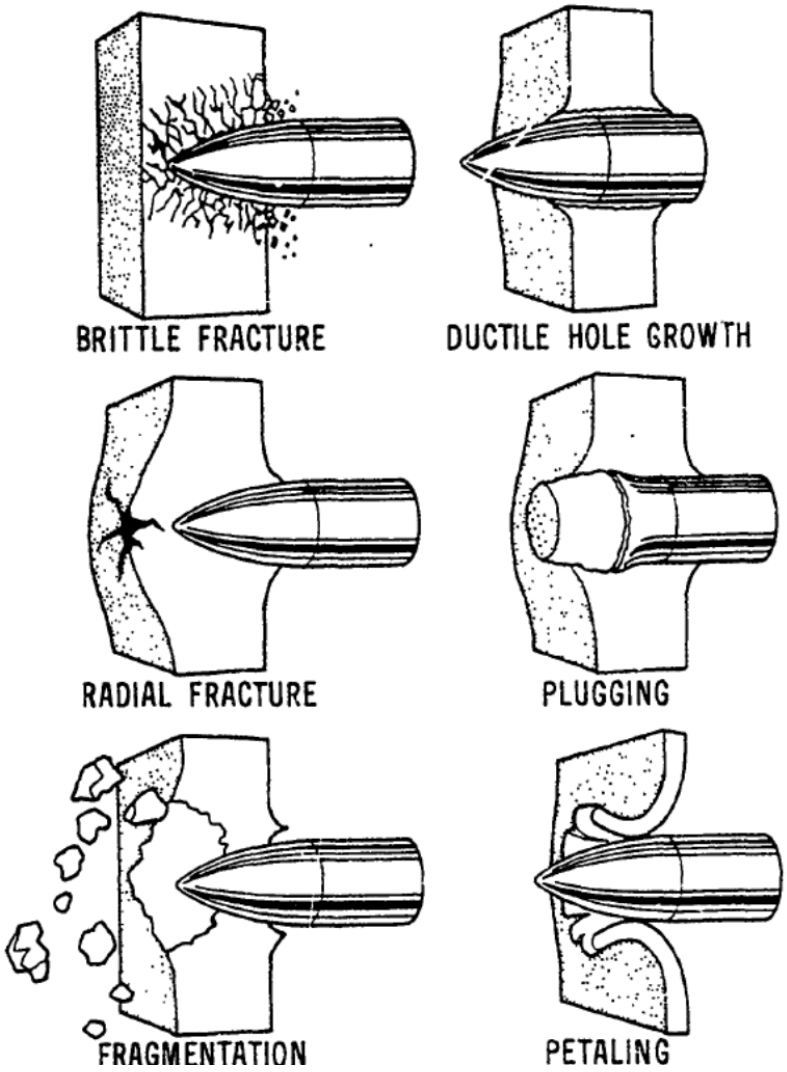

Figure 2-22: Common failure responses of intermediate and thin plates struck by projectiles [63]

2.1.4. Theory on locally blast loaded plates

2.1.4.1. Theoretical background on localised blast loading and capping

Experimental and theoretical insight into large deformations and tearing of locally blast loaded plates was undertaken by Wierzbicki and Nurick [17]. Wierzbicki [20] carried out studies, both from an analytical and numerical perspective, into the propagation of petalling on plates subjected to localised loading. For a plate that is subjected to a localised load, the impulse that is imparted on it can be expressed simply as:

$$I = m_p v_p \qquad \text{Eq. 2-4}$$

where : m_p = mass of the exposed area of the plate, v_p = initial plate deflection speed

Wierzbicki [20] affirmed that, during localised loading, for lower values of impulse, the mode of failure is restricted to dishing. This refers to the general shape of the plate after the blast, meaning either Mode I or a variant of Mode I. As the impulse increases, a point is reached when the impulse imparted to the plate causes the initial speed of the structure to reach a critical speed. Beyond this speed, the area on the plate around which the load is localised goes beyond necking and the impulse from the blast tears a fragment from the central region of the plate. The fragment that is released has a radius, R_f, which is smaller than the charge radius, R_c [5]. The mid-point deflection of the plate just before the cap is ejected, δ_0, is predicted by a relationship with the radius of ejected fragment and the fracture strain of the plate material, as described in Eq. 2-5.

$$\delta_0 = 2.47 R_f \sqrt{\varepsilon_{fr}} \qquad \text{Eq. 2-5}$$

where : ε_{fr} = Uniaxial fracture strain

2.1.4.2. Theoretical background on plate response to fragment impact

A dimensionless number or a damage number was proposed by Johnson [64] for metallic structures subjected to impact or impulsive loading in general:

$$\alpha = \frac{\rho {v_0}^2}{\sigma_d} \quad \text{Eq. 2-6}$$

where : α = Damage number, v_0 = impact velocity, ρ = density, σ_d = Damage stress

The damage stress can be approximated as the static yield stress (σ_0) of the material. To account for different loading conditions, thickness and area of the plate – all parameters which are not considered in the expression of the Johnson's damage number – Zhao [65] modified the damage number and suggested a "Response" number defined in Eq. 2-7;

$$R_n = \left(\frac{l}{h}\right)^2 \left(\frac{\rho {v_0}^2}{\sigma_0}\right) \quad \text{Eq. 2-7}$$

where : R_n= Response number, l= half length of plate *, h= plate thickness

*In the case of circular plates, the half length of the structure is the radius of the plate.

If a dynamic load (from a blast or impact) is imparted on a plate and only causes inelastic deflection of the plate (Mode I), the input energy (E_{in}) from the dynamic load is primarily converted to energy of deforming the plate (E_{def}), as shown in Eq. 2-8.

$$E_{in} = E_{def} \quad \text{Eq. 2-8}$$

If the load is from an impacting fragment, and the mass and the speed of the fragment are known, the input energy being transferred by the fragment to the deforming plate is the kinetic energy and it may be expressed as:

$$E_{in} = E_f = \frac{1}{2} m_f {v_f}^2 \qquad \text{Eq. 2-9}$$

where : E_f = Energy from the fragment, m_f = mass of the fragment

v_f = speed of the fragment

Teeling-Smith and Nurick [16], investigating circular plates subjected to uniform blast loading, assessed different methods to find the energy for deformation of the plate. It was found that the rigid-plastic model presented by Duffey [66] compares well with experimental results. The energy required for deforming the plate is described in Eq. 2-10.

$$E_{def} = \pi h \int_0^R \frac{{\sigma_0}^1}{(1 - \nu + \nu^2)^{1/2}} \left(\frac{\partial w_i}{\partial r}\right)^2 r dr \qquad \text{Eq. 2-10}$$

where ${\sigma_0}^1$ = dynamic yield stress, ν = poisson's ration of the plate, w_i is an arbitrary plate deflection, $w_i = \delta . \gamma(r)$ and δ is the maximum/midpoint deflection and $\gamma(r)$ is the shape function of the plate deflection profile.

The dynamic yield stress (${\sigma_0}^1$) from the Cowper-Symonds relation is used in Eq. 2-11 to account for the strain-rate sensitivity of the plate material. The value of dynamic yield stress during the dynamic loading is found according to a relationship suggested by Symonds and Wierzbicki [67] :

$$\frac{96421.8 I^2}{\sqrt{{\sigma_0}^1}} = 40 \left[\frac{{\sigma_0}^1}{\sigma_0} - 1\right]^5 \qquad \text{Eq. 2-11}$$

Eq. 2-11 can be rearranged into Eq. 2-12, in which the dynamic yield stress can thus be solved for iteratively.

$$\frac{I^4 96421.8^2}{{\sigma_0}^1}\left[\frac{{\sigma_0}^1}{\sigma_0}-1\right]^{-10}=1600 \qquad \text{Eq. 2-12}$$

where: I = Impulse from the load, σ_0 = static yield stress

If the plate is subjected to impact by a fragment, the impulse (as described in Eq. 2-13) that the fragment transmits to the plate is the change of its momentum in striking the plate. Therefore, the impulse parameter in Eq. 2-12 may be calculated as:

$$I = m_f\left[\left(\overrightarrow{v_f}\right)_0-\left(\overrightarrow{v_f}\right)_1\right] \qquad \text{Eq. 2-13}$$

where $\left(\overrightarrow{v_f}\right)_0$= impact velocity of the fragment, $\left(\overrightarrow{v_f}\right)_1$= its rebound velocity

Note* The velocities in this case are shown as vectors to account for the fact that the velocity of the fragment may not be normal to the plate, depending on how it strikes the plate.

For a structure like a flat plate undergoing plastic deformation under impact from a projectile, Baker et al [8] reported a relationship in which the deflection (δ) of the plate could be determined if the density of the fragment (ρ_f), the velocity (v_f), the radius (R_f), the density of the plate (ρ_p), the yield stress of the plate (σ_p), and thickness of the plate (h) are all known. The graph which shows that relation is shown in Figure 2-23.

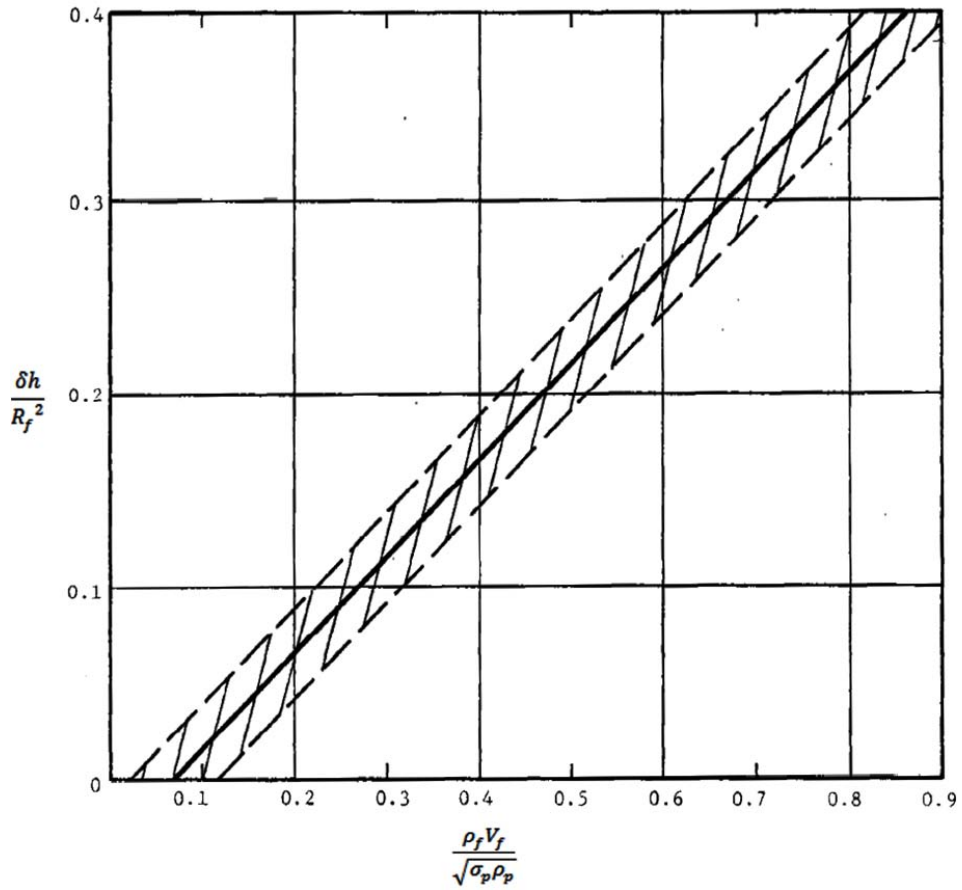

Figure 2-23: Graph used to determine a plate's deflection under impact from a fragment [8]

Since the curve relating the two expressions on the vertical and horizontal axis is a straight line, an equation can be generated by picking two points on the line and using simple algebra to find the equation of the relationship, since the exact equation is not defined by Baker et al. [3]. This results in the linear equation shown in Eq. 2-16.

$$\frac{\delta h}{{R_f}^2} = 0.5 \frac{\rho_f v_f}{\sqrt{\sigma_p \rho_p}} - 0.034 \qquad \text{Eq. 2-14}$$

If the plate deflection is to be made the subject of the formula, Eq. 2-14 can be re-arranged as:

$$\delta = \frac{{R_f}^2}{h}\left(0.5\frac{\rho_f v_f}{\sqrt{\sigma_p \rho_p}} - 0.034\right) \quad \text{Eq. 2-15}$$

If the kinetic energy of the fragment exceeds a critical value, the fragment perforates the plate structure. A number of empirical relationships have been established to determine the critical perforation energy for a hemispherical-head or flat-head projectile impacts a plate.

De Marre's equation, Eq 2-16, relates the carbon steel target thickness and fragment diameter, to the perforation energy by means of a constant 'a' [68].

$$E_{cr} = a.{d_f}^{1.5}.h^{1.4} \quad \text{Eq. 2-16}$$

Where d_f = diameter of fragment/projectile, h = target thickness, and the constant a is determined experimentally.

A similarl empirically equation – the BRL equation – is also reported for carbon steel targets under impact from a projectile/fragment.

$$E_{cr} = 1.44 \times 10^9.\left(d_f.h\right)^{1.5} \quad \text{Eq. 2-17}$$

In both cases, the velocity limits are not defined. In experiments to validate these empirical formulae, amongst others, tests conducted showed that the equations correlate reasonably well with the experimental data, with De Marre's equation most closely approximating the critical energy [69].

2.2. REVIEW OF IMPACT ENERGY ABSORPTION AND ENERGY ABSORBERS

A moving body is characterised by momentum and kinetic energy, based on its speed and mass. If the body comes into contact with a second body which is either static or has a component of velocity in an opposite direction to that of the first body then it will lose some or all of its kinetic energy. Some of the energy is lost in deformation of the first body, the second one, or both. In some applications and scenarios involving impact, it is important to mitigate the potential damage caused by the impact by absorbing the kinetic energy.

2.2.1. Importance of energy absorption during impact: A general outline

During impact, it is desirable that the kinetic energy from a moving body be absorbed not only gradually, but also optimally; particularly for the purpose of safety and protection. In the automotive industry more attention is being given to the safety of the driver and passengers during collision accidents. The chassis of a car is designed and built such that in a case of a collision, the kinetic energy is absorbed in an elongated duration to reduce the impulse or change in momentum that is experienced by the passengers as the car's front crumples. The greater the energy absorbed as the car deforms, the better the crashworthiness of the car [70]. To highlight the importance of energy absorption in this regard, numerous investigations pertaining to vehicle crashworthiness have been undertaken, where metal tubes, both square and circular, were loaded by both quasi-static and dynamic [71-77]. The tubes are used to represent the rails in the chassis of the vehicle which are designed to absorb impact by deforming. The use of guard-rails by the road-side is also useful in attenuating the kinetic energy from cars that accidentally impact guardrails [70].

Impact energy absorption is also useful in packaging; making sure that goods that are being transported from one point to another are well protected from incidents that involve being dropped. In some industrial areas, preventing pipe-whip damage during pipe breakage

occurring whilst the pipe is carrying fluids at high pressures can be attained by deploying an energy absorbent pipe-whip restraining system [70]. Personal safety can be increased by using energy absorbing materials like hard hats, bike helmets, safety shoes, bullet-proof vests which all contain materials which can absorb kinetic energy during impact.

In the abovementioned scenarios, energy absorption during impact is underlined as an important aspect. Thus materials and structures which can absorb energy are used The purpose of this project is to investigate ways in which different energy absorbing materials can be used to absorb impact energy from fragments.

2.2.2. Absorption of energy from a ballistic fragment

Projectiles like a bullet from a gun are well-defined in shape and consistent in terms of their release speed and flight pattern. Irregularly shaped projectiles like fragments released or torn from structures due to blast waves are not as simple to quanify in that regard. The damaging effect to which certain structures would be subjected to by fragment impact can be mitigated by introducing protective structures made from energy absorbing materials.

An energy absorbing material is different from an energy storage device in that the latter, after deformation due to the incident motion of the projectile, the device goes back to its original state and position and consequently subjects the incoming projectile to motion in the opposite direction [78] – an elastic spring is a good illustration. An energy absorber tends to dissipate the impact kinetic energy as it deforms beyond its elastic bounds.

In space travel, investigations have been made into finding suitable materials and material orientations for spacecraft walls [71]. This is particularly important because these walls have to protect the spacecraft's crucial parts inside and humans in cases of manned shuttles. The walls have to be able to withstand possible impact with meteors and other debris travelling at high speeds. Investigations carried out by Schonberg [79] were aimed at incorporating composite materials at different locations and arrangements in a multi-wall system to prevent complete perforation of the wall under high speed fragment impact.

2.2.3. Energy absorbers

During a blast or impact where an energy absorbing material is used to buffer the load, most of the kinetic energy absorbed from the incoming load is dissipated as energy of deformation in ensuring that the underlying target's absorber deforms beyond the elastic region [80] – either by ductile or brittle failure. A good energy absorbing material or structure, therefore, is one which absorbs a high level of energy from the incident impact or blast load and, as it undergoes failure, transmits as little residual energy as possible to the structure which the absorber is designed to protect.

Numerous materials have been used for the purpose of energy absorption when subjected to impact energy loading, particularly projectile impact. Typical materials investigated include fibre composites [81-83], adaptive materials like magnetorheological (MR) fluids and shear-thickening (ST) fluids [84-86], lattice structures like trusses [87-89], wood [90,91], foams [92-99], honeycombs [100-102] and ceramics [103-105]. Many of these structures are used as cores of sandwich panels. Sandwich panels are some of the most commonly used forms of composites in constructing impact resistant structures. These structures are advantageous as they combine the best energy absorbing material properties of the core (usually low weight and high energy absorption qualities) and the face sheet material (usually high bend resistance) [106]. For full perforation, an incoming projectile impacting the sandwich panel would perforate the sandwich panel in three phases; perforation of the front face, then of the core and then the back face.

2.2.3.1. Fibre reinforced composites

Composites are unique in that their various designs are all aimed at getting the best properties out of each of the constituent materials. Unlike metallic alloys which mix two metals to become one homogeneous alloy, composites remain heterogeneous when their constituent materials are combined. Composites, like fibre reinforced composites, contain fibres – natural or synthetic – which are arranged in a desired way within a matrix and stacked into material layers

comprising laminas [107]. The matrix keeps the reinforcing fibres or particulates in place in a fixed structure.

When subjected to impact, fibre composites fail, and hence absorb energy, by a number of processes, including fibre fracturing, fibre pullout, separation of fibre layers from each other (de-lamination), fibre-and-matrix de-bonding and matrix failure. The matrix used is usually brittle and the fibres used are also usually brittle. This serves to make the composite more stiff than it is ductile. Natural fibres like hemp and jute are more ductile than the more brittle synthetic fibres like glass and carbon fibres [108]. Wambua et al. [83] carried out studies on the response of natural fibre composites (flax, hemp and jute) to impact by fragment-simulating projectiles (FSP's). In their findings, flax exhibited the best ballistic performances. A photograph of one of the hemp specimens that has been perforated by the FSP is shown in Figure 2-24.

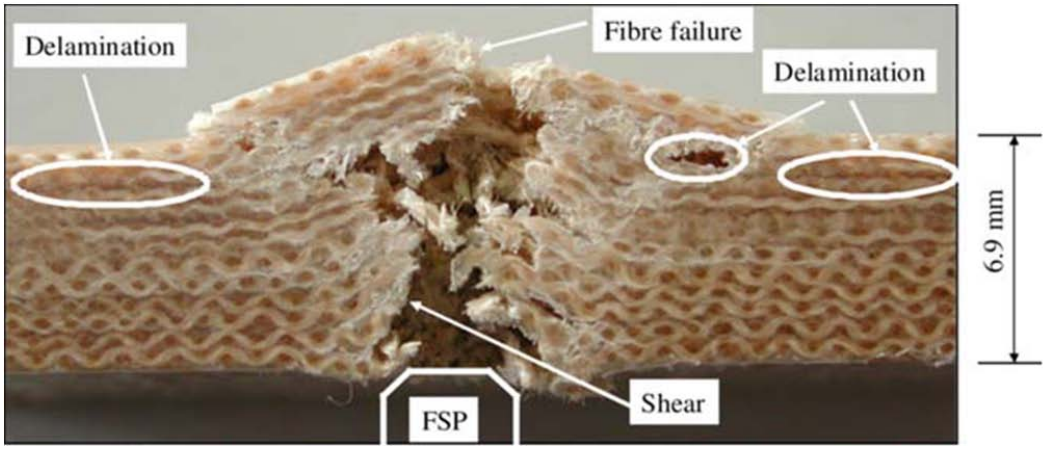

Figure 2-24 : Hemp fibre composite failure after impact by a fragment-simulating projectile (FSP) [83]

Synthetic fibre reinforced composites have received more attention in literature. Ultra-high molecular weight polyethylene (UHMwPE) fibre composites like Dyneema® have been tested in blast and impact loadings. Kandan et al. [109] reported that, compared to other synthetic fibre composites, one of the advantages of Dyneema under projectile shock loading is its nature of failing in shear and stretching of the fibre membranes, and geometry effect pull-out; which contributes to its superior strength and impact resistance.

2.2.3.2. Cellular materials

Gibson and Ashby [110] comprehensively studied the form and properties of cellular materials. These are solid materials which comprise cells in the structures. For some cellular materials like honeycombs, the cells are very uniform in their size and geometry whereas for foam materials, the cells do not have exactly the same volumetric sizes – even within the same materials. Some of these solids are isotropic whilst materials like honeycombs are anisotropic. For all cellular materials, the term 'relative density' is the fractional representation relating the density of the foam and the density of the material from which the foam has been made. This is denoted by ρ^*/ρ where ρ^* is the density of the material, whilst ρ is the density of the parent material [70]. A relative density of 0.15 or 15% means that 15% of the volume of the cellular material is made of its parent material whilst 85% is filled with air. Conversely, porosity is a term relating the volume of air in the cellular material to the total volume of the material [70].

$$porosity\ (p^*) = 1 - \frac{\rho^*}{\rho} \qquad \text{Eq. 2-18}$$

Under compression, cellular materials generally exhibit a great deal of ductility with the stress increasing at a slow rate over large strains – after the yield strain. This constant stress, referred to as plateau stress, can be observed after the elastic limit and before densification which occurs as the walls of the cells come into self contact. Figure 2-25 shows a typical foam compression stress against strain for polyurethane foam. Plateau stress is a good indicator of the energy absorption ability of the material – undergoing large strain at a small rise in stress.

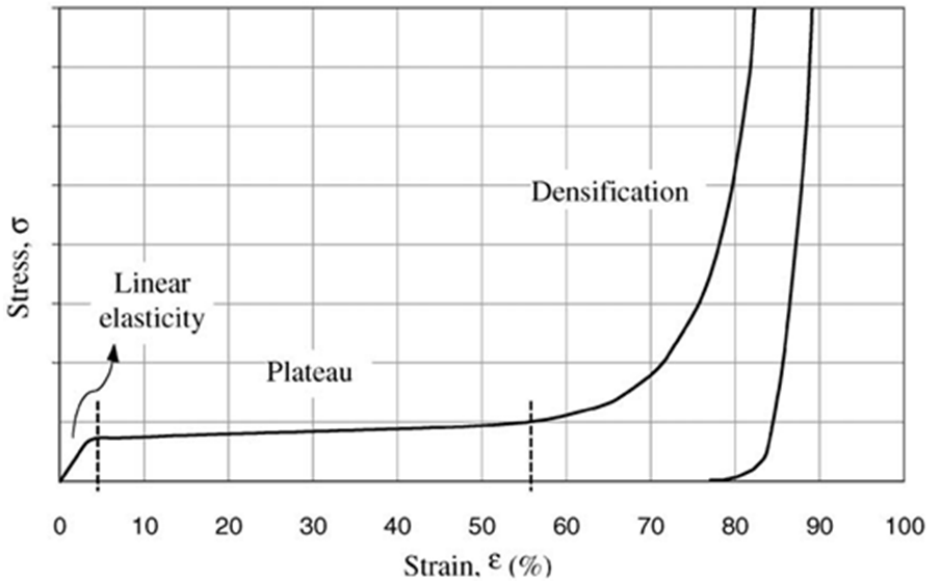

Figure 2-25 : Typical cellular material (polyurethane foam) Stress-Strain curve under quasi-static compression [111]

Beyond the onset strain of densification – which is also known as locking strain – the stress needed to compress the material further increases sharply and, consequently, the energy absorbing efficiency of the foam decreases considerably for additional straining. The onset of densification is therefore an important phenomenon to consider. However, to determine the onset of densification, it is often not obvious by visual means when one considers a stress-strain curve as shown in Figure 2-25. Li et al. [112] discussed that the most consistent way of determining the strain onset of densification is by using the energy efficiency method, which was suggested by Avalle et al. [111]. It is generally known that the energy absorbed by a material during straining to a certain strain value is the area under the stress-strain curve up to the said strain value.

$$E_{Abs} = \int_0^{\varepsilon} \sigma(\varepsilon) d\varepsilon \qquad \text{Eq. 2-26}$$

Energy absorption efficiency is defined as at a certain strain is the energy absorbed to that point divided by the stress at that point [111]. Using the absorbed energy as described in Eq. 2-26, the Energy absorption efficiency (η) can be found by using Eq. 2-27.

$$\eta = \frac{\int_0^{\varepsilon} \sigma(\varepsilon) d\varepsilon}{\sigma(\varepsilon)} \quad \text{Eq. 2-27}$$

The stress-strain curve or its raw data is thus required to determine the energy absorption efficiency. The onset strain of densification is known as the strain at which the energy absorption efficiency is at a maximum. Figure 2-26 shows a typical compressive stress vs. strain curve shown next to its corresponding energy absorption efficiency vs. strain curve. As can be noticed, the maximum efficiency is observed at a strain of 52% - which is also the onset strain of densification. **It is important to note that the method of maximum energy absorption efficiency can be applied to any porous material under compression when determining onset strain of densification, not only cellular materials.**

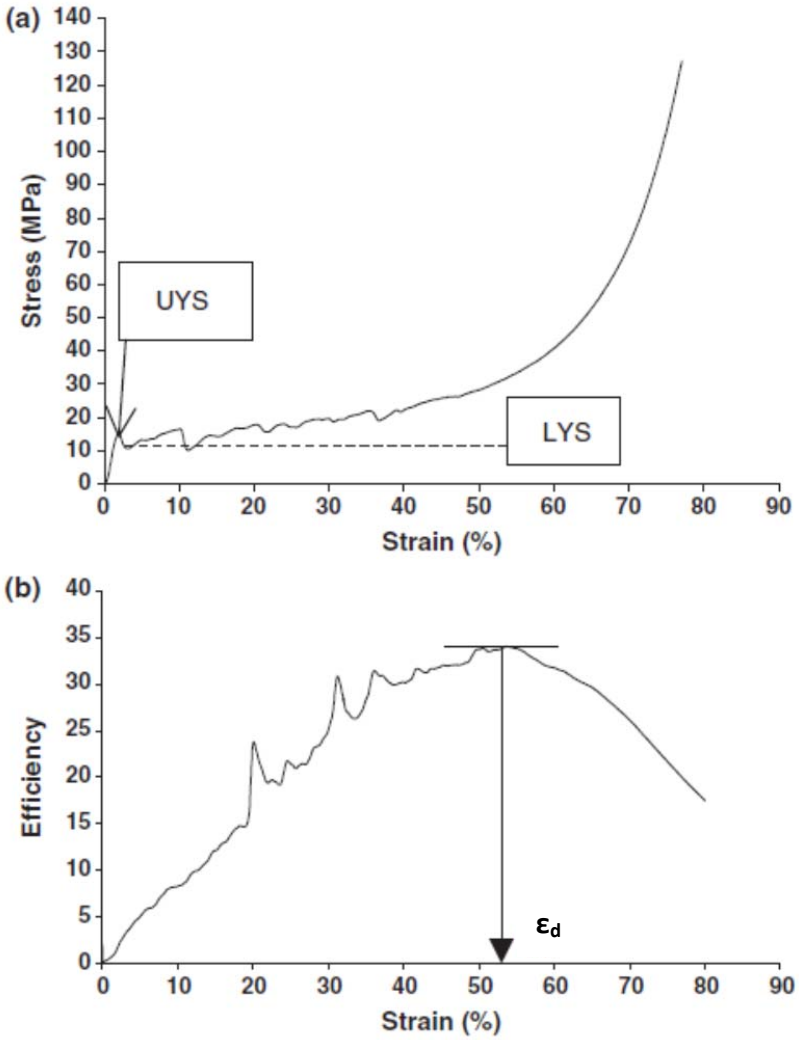

Figure 2-26: (a) Typical compressive stress of a cellular material and (b) its corresponding energy absorption efficiency curve [112]

Foams

Foams are a type of cellular materials which are produced by different processes from the parent material - from a liquid, solid gaseous or ionised form [113]. Foams can be classified as closed-cell and open cell. Open-cell foams are characterised by cells joined to each other at their edges only, whilst closed-cell foams comprise cells completely separated from each other by their walls. Figure 2-27 shows the two aforementioned kinds of foams. Good strength to weight and ductility are typical characteristics associated with foams.

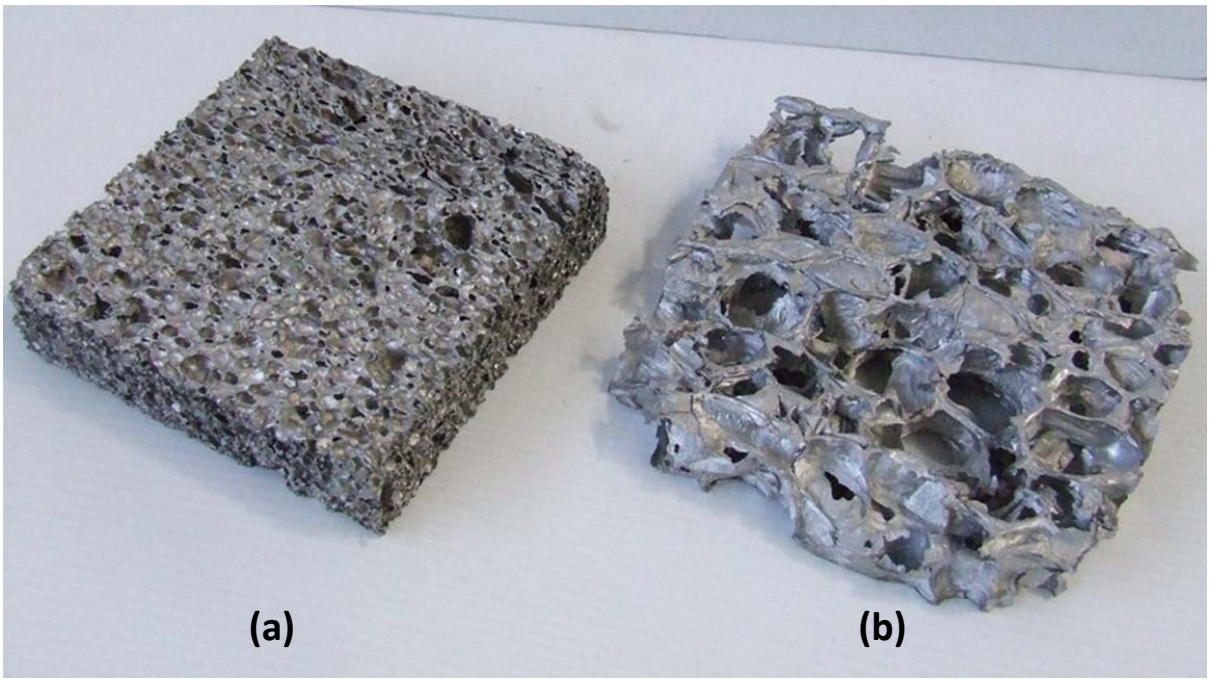

Figure 2-27 : (a) Closed-cell Aluminium foam and (b) open-cell Aluminium foam

Metallic foams

Although there have been studies carried out on other metallic materials in form of foams under different loading conditions [114,115], most quasi-static and dynamic tests on metallic foams are carried out on aluminium foam. Merrett [116], undertook investigations on the response of Cymat and ALPORAS closed-cell aluminium foams to quasi-static and dynamic compressive loading, and blast loading. Whilst Cymat foams exhibited some brittleness, particularly under quasi-static loading, ALPORAS foams were observed to fail in a more ductile

manner throughout the compressive cycle, as shown in Figure 2-28. Merrett [116] also subjected the two foam types to blast tests, with the two foams sandwiched between a deformable front plate and a rigid back plate. In the tests, it was found that Cymat foam deformed non-uniformly because of its non-uniformity of density and cell morphology. ALPORAS foam was observed to show more uniform response due to its homogeneous structure and uniform properties.

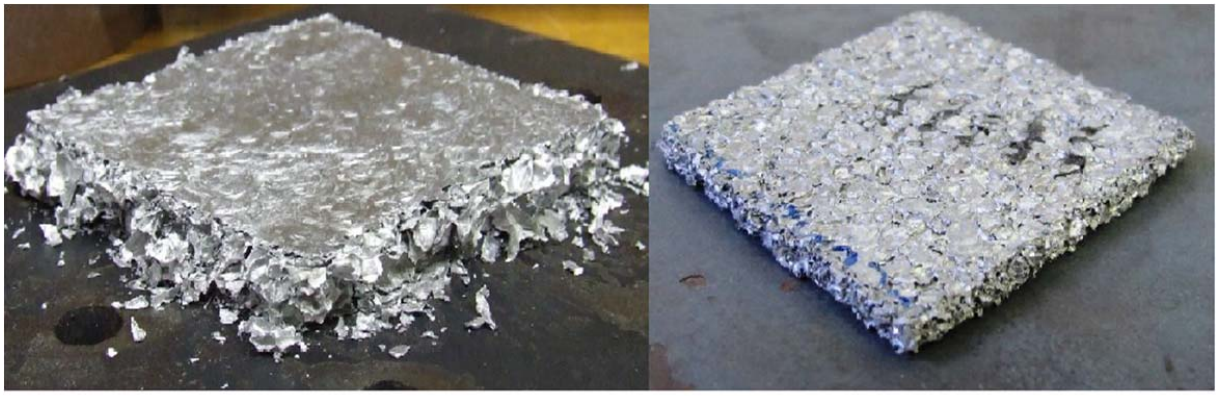

Figure 2-28 : Quasi-static failure mechanism of (a) Cymat and (b) ALPORAS aluminium foams [116]

Zhao et al. [92] investigated the perforation of sandwich panels made of aluminium foam between two aluminium alloy face sheets using a split Hopkinson pressure bar (SPHB) as the perforating agent. An advantage of this set up is the possibility to trace the force vs. displacement curves under both quasi-static and impact loading conditions. During penetration and perforation, the face sheets and the foam were both observed to be strain rate insensitive. In their studies, Hou et al. [93] subjected aluminium foam sandwich panels to ballistic impact by means of flat-nose, hemispherical-nose and conical-nose projectiles. For all the projectiles, it was found that the front face sheet fails by formation of a circular hole with insignificant deflection, whilst the core gets tunnelled during penetration or perforation. In cases of only penetration, observations showed that the foam material in front of the head of the projectile shows slight compression. The back face failed by delamination from the core, slight deflection and petalling. Moreover, it was found that the ballistic limit increases as the nose of the projectile becomes more blunt.

Polymeric foams

Polymeric foams – with their relative ease in formability, the variety of their synthetic geneses, and low weight – are widely studied when subjected to quasi-static and dynamic loading conditions. Wang et al. [94] carried out studies by subjecting sandwich panels comprising Corecell A300, A500 and A800 cores fused together between E-Glass vinyl ester (EVE) face sheets to shock loading. Observations showed that arranging the fusion of the cores in increasing density (A300 foam closest to the blast, fused to A500 foam which is fused to A800 foam) showed the highest level of blast mitigation as more compression was observed in the core. In a study by Song et al. [97], polystyrene foam was loaded in quasi-static and dynamic loading (at strain rates between 0.001 and 950/s) to investigate its behaviour at varying strain rates. It was observed that as strain rate increases, the elastic modulus and the crush stress of the polystyrene foam increase. Karagiozova et al. [117] investigated the blast attenuating capabilities of flexible sandwich panels with aluminium honeycomb cores (density 71 kg/m^3) and polystyrene foam cores of varying densities (16kg/m^3, 24 kg/m^3 and 32 kg/m^3). With its low plateau stress, polystyrene foam cores were generally observed to transmit stress from the deforming front sheet to the back sheet more easily than the honeycomb cores and thus showed lesser energy absorbing abilities.

Zaretsky et al. [96] subjected flexible polyurethane foam of density 409kg/m^3 to projectile impacts of speeds of up to 600m/s. One of the main findings was the fact that above an impact velocity of 43m/s, the polyurethane foam failed by crushing to powder, and there was also an irreversible heating effect on the foam. Ethylene vinyl acetate (EVA) foams, which are elastomeric in nature, have been tested for purpose of shoe soles in the shoe industry [98,99], but no investigation has been reported on their properties in dynamic loading.

Investigations were carried out by Kepler [118,119] on sandwich panels made of glass-fibre face sheets surrounding Divinycell H80 Polyvinylchloride (PVC) foam cores arranged in varying layering setups. These panels were subjected to quasi-static and impact loading from controlled indenters with different head geometries. It was shown that most of the energy dissipated from the indenter was lost in stretching of the face sheet material fibres, compression of the core as

the indenter passes through and friction between the two. A minority of the absorbed energy was attributed to de-lamination between the front face and the core, breaking of the brittle matrix that joins the face sheets with the core, cross- cracking of the core and de-bonding between the core and the back face due to plastic deformation [119]. The core cross-cracking, which is shearing in the core generally attributed to transverse impacts, was observed to propagate through the thickness of the foam core. It was more prevalent during impact testing.

Atas and Sevim [91] carried out tests on sandwich panels with PVC foams cores (density 62kg/m^3) and balsa wood cores (density 157kg/m^3). Drop weights were used to impact the panels which have E-Glass face sheets bonded using Epoxy resin to the cores. It was found that balsa wood is stiffer than PVC in impact but it debonds from the face sheets more easily than PVC.

Wood

Due to its cellular microstructure, wood is a natural cellular material [90], although in some literature it is also defined as a fibre reinforced composite due to the cellulose fibre aligned along the trunk in a matrix of lignin [107]. This natural fibre arrangement makes wood anisotropic – exhibiting different material properties and load response in the axial direction and transverse directions [90].

In an investigation into different types of wood under quasi-static and dynamic loading, Reid and Peng [90] studied the response of five species of wood; redwood, balsa wood, yellow pine, ekki and American oak with dynamic impact being varied between speeds of 30m/s and 300m/s. Under quasi-static loads, Figure 2-29 illustrates the responses of the different types of wood. The force vs. displacement curve (similar to the corresponding Stress-Strain curve) of wood is similar to that of typical cellular materials as there is a considerable stress plateau after initial crush occurs and before onset of densification is reached [90].

It can be observed from the force-displacement curves, particularly along the grain, that the plateau stress of Balsa wood is the lowest, whilst that of Oak is the highest, however, with a lower densification strain than that of Balsa wood. The area underneath a stress-strain curve

would represent the energy absorbed by the wood in the compression cycle, so a material of a lower plateau stress can absorb as much energy before densifying as a material that has a higher plateau stress but a lower onset strain of densification.

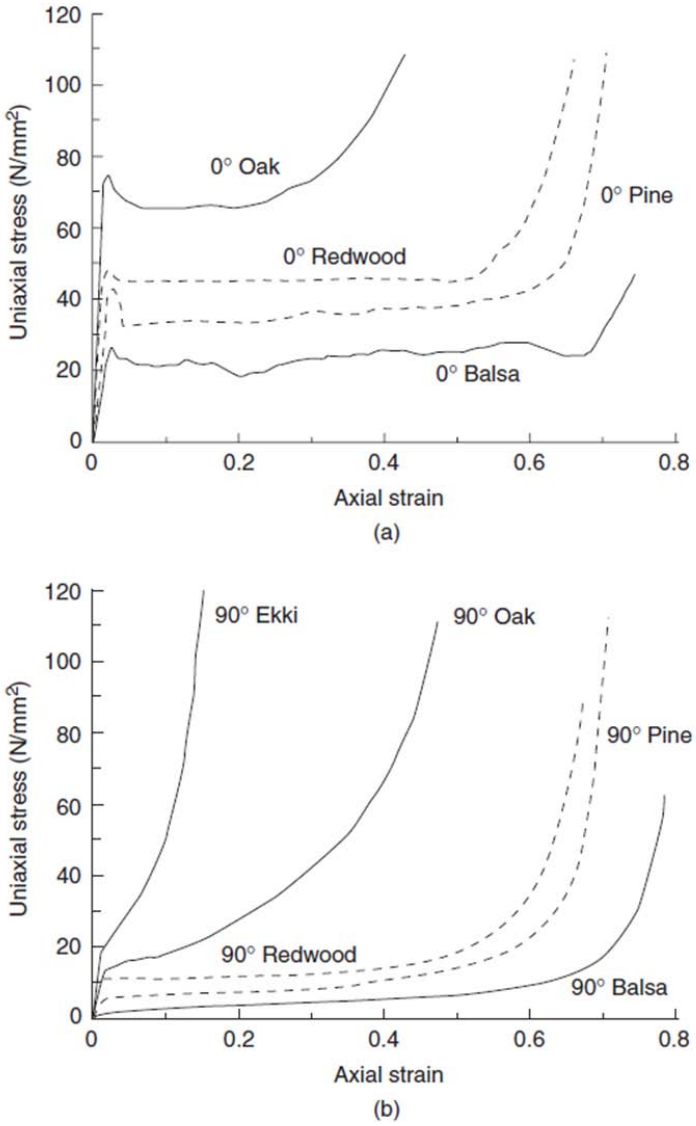

Figure 2-29 : Stress vs strain curves for the several woods along (a) and across (b) the grain [90] **(cited in** [70] **)**

Honeycombs

Aluminum Honeycombs are another type of cellular structure. It may be require for honeycombs to be enclosed within a tube to prevent buckling during axial loading or to be used as cores in sandwich panels to maximise energy absorbed [78]. As part of sandwich panels, honeycombs are widely used in the automotive, railway and aerospace industries [120]. Other honeycomb-types, like square honeycombs also exist, and use the same principles as hexagonal honeycombs. For hexagonal cell honeycombs, as shown in Figure 2-30, each cell is extruded in the direction normal to the hexagon plane.

Honeycombs are two dimensional and can be loaded in-plane and out-of-plane, unlike foams, which are effectively isotropic. If a load lies in the X-Y plane – as illustrated in Figure 2-30 – the load is said to be in-plane. If the honeycomb is loaded along the Z-axis the load is said to be out-of plane [70].

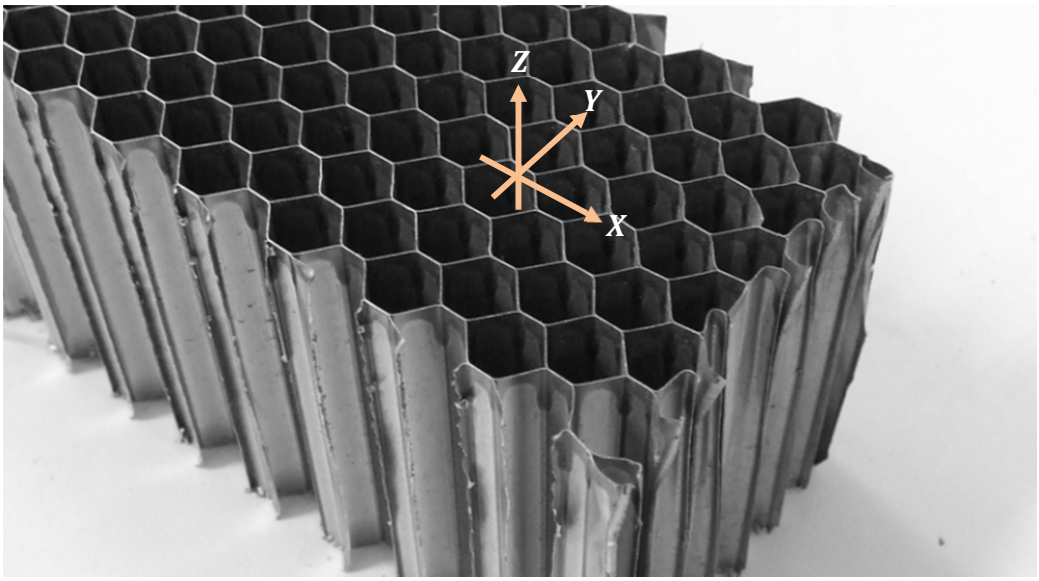

Figure 2-30 : Aluminium honeycomb (hexagonal cells)

The energy absorbing ability of honeycomb materials at high strain rates has been studied to a considerable extent for blast mitigation, particularly when the honeycomb is used as the sandwich panel core [121-123]. Blast tests on aluminium honeycomb cores were carried out by Chi et al. [121] where a blast load deformed a steel (front) face plate that deformed a sandwiched honeycomb core, transmitting the deformation to another (rear) face plate. It was observed that an increase in the honeycomb core thickness results in a decrease in the rear plate deformation.

Fatt and Park [100] carried out investigations for aluminium honeycomb materials subjected to out-of-plane projectile impact, as shown in Figure 2-31. It was observed that during perforation, the projectile is able to shear off a compressed plug of the sandwich panel (front sheet, core and back sheet) with some of the honeycomb core around the path of the projectile being compressed with debonding between the core and back sheet.

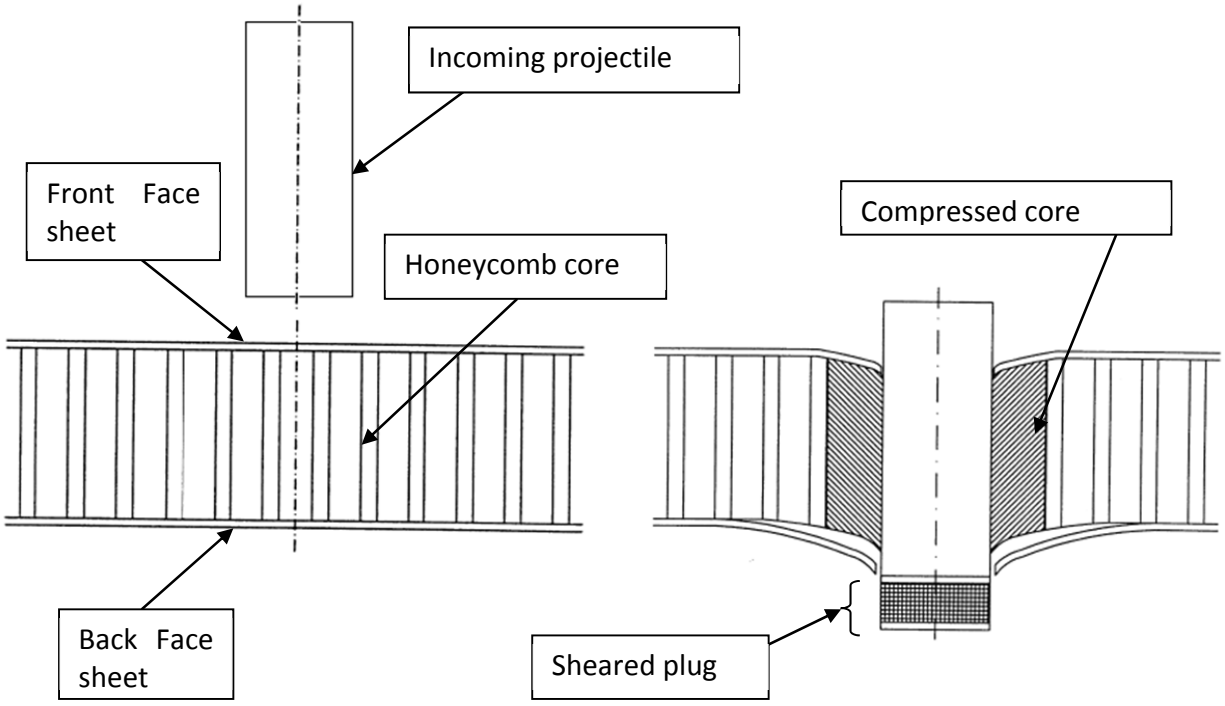

Figure 2-31: Schematic of a honeycomb sandwich panel before impact (left) and after perforation by projectile [100]

A drop impact study was carried out on paper honeycomb sandwich panels by Wang [101]. The cores were lined with *kraft* paper as well as corrugated board. It was observed that there is a linear relationship between the energy absorbed during impact and relative density of the honeycomb whilst the increasing of thickness of the core fluctuates the cushioning properties of the panel in that the advantage of increasing the core thickness decreases with increasing thickness until the advantage effectively disappears. The use of corrugated board as a liner was observed to improve the energy absorbing abilities of the panel. Honeycombs - square, circular or hexagonal - can be viewed as a collection of a number of tubes adjacent to each other. Tubes or cylindrical elements have been investigated of their energy absorbing abilities, with particular application of sacrificial materials – protecting structures from the effect of blast waves [102].

2.2.3.3. Ceramic materials

Ceramic materials are brittle and known for their insulation properties, lower density than steel, and possess superior impact energy absorption to metals [106]. Ceramic armour systems have been deployed for the main purpose of ballistic protection and have been tested under projectile impact in a few studies [103-105]. The test schematic shown in Figure 2-32 is from a study conducted by López-Puente et al [104]. It was observed that the ceramic armour system absorbs energy from the projectile by brittle failure of the ceramic layer, puncturing and delamination in the composite laminate and then inelastic deformation of the back plate.

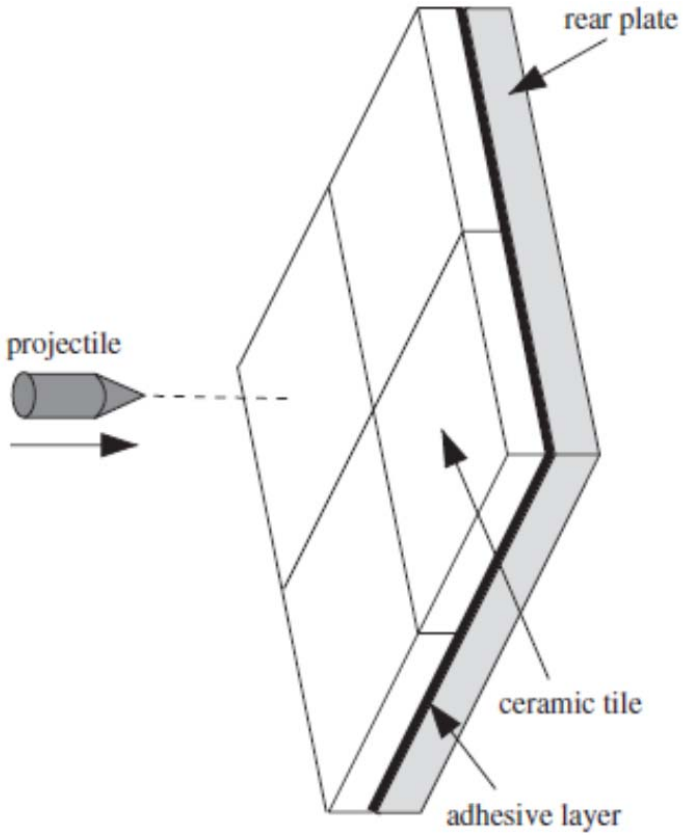

Figure 2-32: Typical layout of a ceramic armour system [104]

2.2.3.4. Magnetorheological (MR) and shear-thickening (ST) fluids

Kevlar is an aramid fibre that is well known for its use in soft body armour because of its good strength-to-weight ratio. Plain Kevlar, however, requires between 20 and 50 layers to absorb the energy from a typical bullet without perforation of the armour [124]. One of the solutions to this challenge is the introduction of adaptive fluids as part of the armour. ST fluids and MR fluids are the fluids used. ST fluids comprise small silica particles that make up a non-Newtonian fluid, that is a fluid that becomes extremely viscous when the stress in it increases suddenly [124]. Studies carried out by Lee et al. [86] made use of ST fluids to improve the ballistic performance of Kevlar armours.

MR fluids work with the same principle as shear thickening fluids but, rather than responding to increased stress by an increase in viscosity, they increase in viscosity through an activated magnetic field. The magnetic particles within the fluid line up with the activated field and the fluid becomes more resistant to impact [125]. The capability of MR fluids against impact, however, has been tested only at low velocities [84,85] and it is yet to be tested for high velocity impacts.

2.2.3.5. Micro-architectured lattice structures: Trusses

Trusses are forms of lattice structures made of struts that are joined to each other loosely or rigidly – much like a normal large scale engineering trusses. However, when they are scaled down to a level where they can be used as cores in sandwich panels, or as unbound lattice structures, for the purpose of impact energy absorption, they can be viewed, not just as structures, but as materials, which have their own inherent material properties [126]. Figure 2-33 shows three typical core structures made of trusses, as part of sandwich panels.

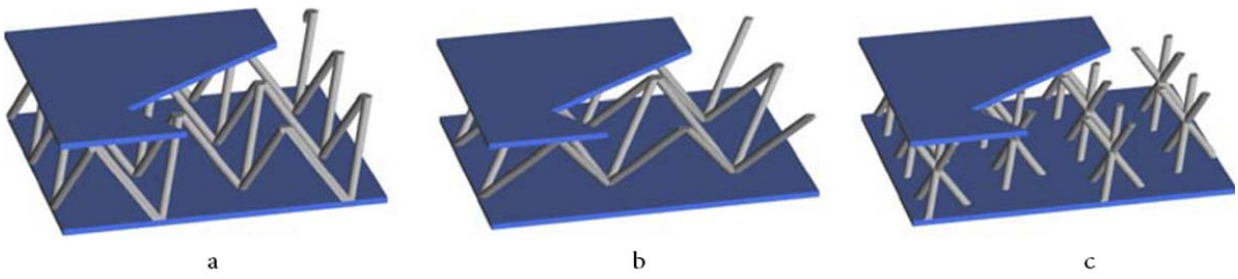

Figure 2-33: Sandwich panels with lattice truss cores – (a) tetrahedral, (b) pyramidal and (c) Kagome lattices [127]

Lattices, which behave akin to cellular materials, are easier to predict in terms of failure than foams, for example. This is because of the uniformity of the truss is pre-determined by the structure itself [126]. Numerous investigation pertaining to the response of lattice structures to loading have been carried out [88,127-131]. To get the maximum energy absorption, face sheets have been used to distribute the load evenly. An apparent challenge in the use of these micro-architectured structures is the fabrication of the lattices themselves. Tooled processes like punching have been used to fabricate some pyramidal lattice cores but they have a limit with regard to the manufacture of smaller lattices; Selective Laser Melting (SLM) has been used as an improvement to produce finer lattices with improved tolerances [131,132]. McKown et al. [131] tested sandwich panels – which have lattice cores produced using SLM method – to quasi-static and blast loads. In both loading conditions, the cores were observed to fail in a similar pattern, i.e. an increase in the yield stress of the core resulted in an increasing in the blast resistance of the sandwich panel.

Yungwirth et al. [88] carried out investigations on steel and aluminium alloy sandwich panels with pyramidal truss cores having equivalent geometries, and monolithic steel plates of an equivalent mass to the steel sandwich panels. The structures were subjected to impact from spherical steel projectiles with impact velocities varying from 250 to 1300m/s and it was observed that the monolithic plates and sandwich panels exhibited identical ballistic performances. Although the steel sandwich panels outperform the aluminium alloy counterpart on a per-volume basis, both the panels show similar failure patterns in that the front face sheet fails by ductile through hole enlargement and the rear plate fails by petalling [88]. Figure 2-34 shows two of the aluminium alloy sandwich panels perforated by the projectiles fired at speeds of 280m/s and 1222m/s.

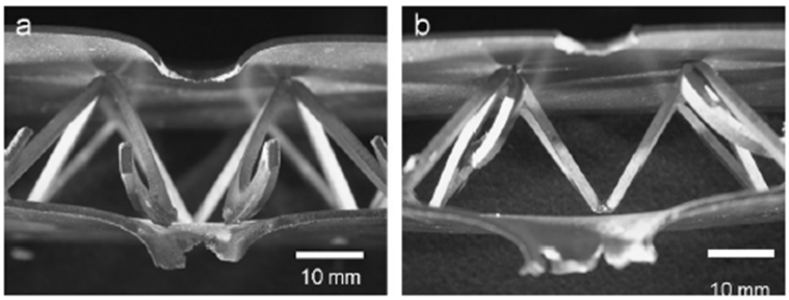

Figure 2-34: Photographs of sectioned aluminium alloy sandwich panels (pyramidal truss cores) subjected to impact velocities of (a) 280m/s and (b) 1222m/s from spherical steel projectiles [88]

2.2.3.6. Corrugated board

One of the commonly used materials in the packaging industry is corrugated board, also known as corrugated cardboard or corrugated fibre-board. This material is essentially a sandwich panel which has a structural corrugated core between two outer plies – in cases of single-layered fibre-board. Corrugated boards have three principal directions, machine-direction (MD), cross direction (CD) and a third mutually perpendicular z-direction. A typical multi-layered corrugated board is shown in Figure 2-35. As the number of flute layers (the corrugated structures) increases, the mechanical properties, like strength, stiffness and puncture resistance increase. The response of corrugated board to quasi-static crushing and energy absorption has been studied [133,134]; but no studies have been reported on the ballistic performance and blast

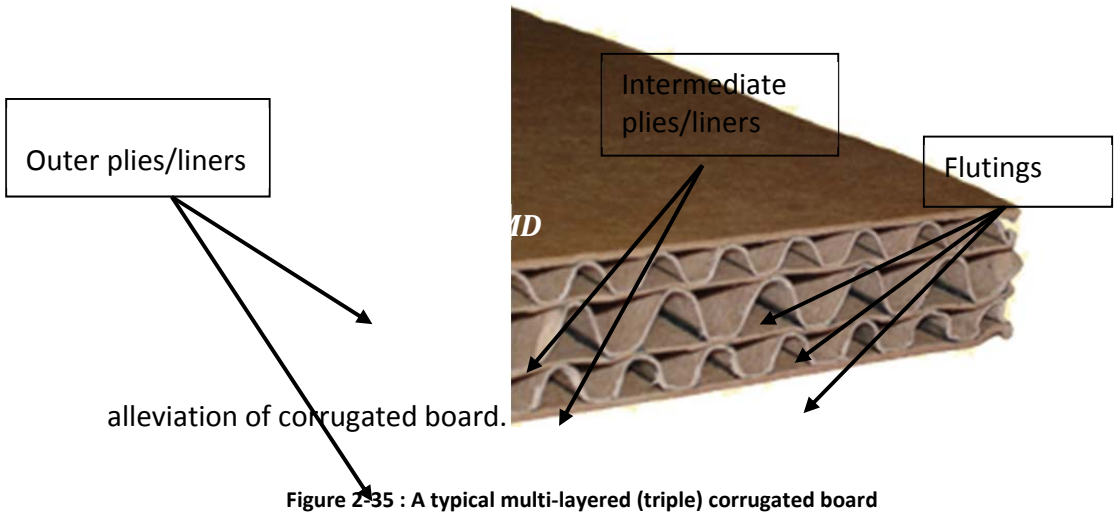

Figure 2-35 : A typical multi-layered (triple) corrugated board

2.2.4. Summary of considered energy absorbers

Based on the literature survey, there are numerous materials with potentially good energy absorbing characteristics Subsequently, based on cost, availability and on literature survey (§2.2.3) several materials are selected to be tested in quasi-static compression to quantify their energy absorption capabilities. Of these selectedmaterials, a second phase of selection was carried out to reduce the list down to those suitable for fragment impact (blast) tests. In both selection processes, cost and availability were key criteria, whereas energy absorbing capacities and the need to diversify the final material inventory are specific conditions applied in the second selection phase. Table 2.2 summarises the list of materials considered based on literature and indicates the materials chosen for quasi-static and fragment impact testing.

Table 2.2: Summary of materials considered from literature and the ones used for quasi-static and fragment-impact testing

Material	Advantages	Disadvantages	Verdict
FIBRE REINFORCED COMPOSITES	Some Dyneema available in BISRU	Fibre pullout and edge bulge during hole-sawing	**N/S**
FOAMS			
Metallic foams			
Aluminium Foam	Availability Cores require testing		**QS and BT**
Polymeric foams			
Corecell A-500 foam	Availability	Similar to M-80	**QS only**
Corecell M-80 foam	Availability	Similar to A-500	**QS and BT**
Polystyrene foam	Available in small quantities	Relative poor energy absorption	**QS only**
Polyurethane 80 foam	Availability	Polyurethane 200 already selected	**QS only**
Polyurethane 200 foam	Availability	Two batches used	**QS and BT**
RG 5565 EVA foam	Energy absorption ability	Availability	**QS only**
WOOD			
Balsa wood	More testing required on bare cores	Density inconsistent between sheets	**QS and BT**
HONEYCOMBS			
Aluminium honeycomb	More testing required on bare cores		**QS and BT**
CERAMIC MATERIALS	High energy absorption capacity	Availability	**N/S**
MR and ST FLUIDS	Still require more testing	Cost and Availability	**N/S**
LATTICE STRUCTURES (TRUSSES)	More testing required on bare cores	Manufacturability	**N/S**
CORRUGATED BOARD	Not reports on fragment impact	Availability	**QS only**

*__N/S__ means 'Not Selected', **QS** denotes Quasi-Static testing whilst **BT** denotes Blast Testing

.

3. EXPERIMENTAL DETAILS

This chapter outlines the details of the experiments which have been conducted for this study. Blast experiments are conducted on mild steel plates on a ballistic pendulum, which results in capping of the front plate and damage to the rear plate due to impact by the fragment. Energy absorbing materials, which are initially tested in quasi-static compression, are then subjected to impact from the fragments when placed in front of the rear plate. The size and kinetics of the fragment (mass and speed) are noted and the subsequent damage to the absorbers and the plates is observed and analysed.

3.1. Setup for blast testing

The blasts tests are conducted in a blast chamber located in the BISRU laboratories at the University of Cape Town. These tests are undertaken with the minimum charge mass of 7g (6g base charge + 1g lead charge) of PE4 and a maximum charge mass of 11g. The blast chamber can safely contain detonations of a PE4 charge of up to 75g. The experiments are carried out on a ballistic pendulum.

3.1.1. The ballistic pendulum

The test rigs which are used in the blast experiments – before and after the inclusion of energy absorbers – are assembled on the front end of a ballistic pendulum, shown schematically on Figure 3-1. The ballistic pendulum comprises the test rig, an I-beam and counter-masses attached to the rear end of the pendulum. The pendulum is suspended from the ceiling by means of four steel wires with turn buckles and hooks as shown in Figure 3-2. The counter-

masses are weighted to counter the mass of the test rig such that the mass acting through each wire is approximately equal. The time period of the pendulum, which is the time taken for one oscillation cycle to be complete is determined by perturbing the pendulum horizontally and, as it begins to swing, a stopwatch is used to measure the time taken for ten (10) oscillations to be completed; after which, the stopwatch is stopped. The time reading is divided by 10 to find the average time period. The time period (T) found in this study is ***3.41s***.

When the explosive charge is detonated in close proximity to the front of the rig, impulse from the explosion is imparted to the exposed area of the blast loaded plate and transmitted into the entire ballistic pendulum. To determine the impulse, the total mass and the initial velocity of the pendulum are required. The initial velocity of the pendulum is obtained from the maximum horizontal forward and backward distance of swings of the pendulum. This velocity is calculated from the measured back and front maximum displacements, traced by a pen attached on the lower side of the rear end of the pendulum. Knowing the maximum horizontal swings and the damping constant of the swinging pendulum, the initial velocity of the pendulum can be computed. The initial velocity and the total mass of the pendulum are used to compute the initial momentum of the pendulum which equals the impulse from the blast, as shown in Eq. 3-1.

$$I = \left(p_{pend}\right)_0 = M\dot{x}_0 \qquad \text{Eq. 3-1}$$

Where : I = Impulse, $\left(p_{pend}\right)_0$ = Initial momentum of the pendulum,
M = Mass of pendulum, $\dot{x}_0$ = Initial velocity of the pendulum

Details of the method used to determine the initial velocity of the pendulum are given in Appendix C.

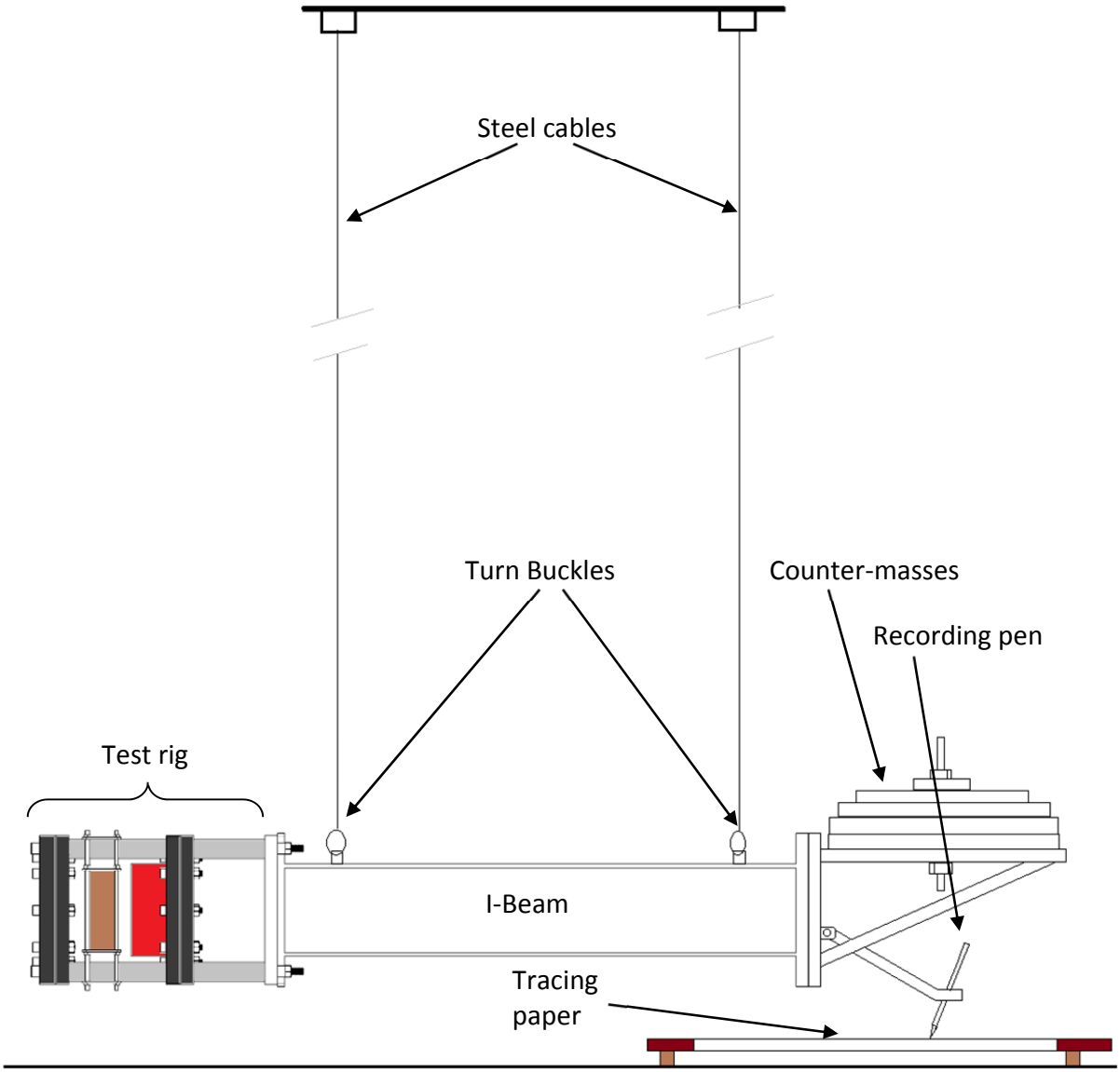

Figure 3-1: Schematic showing setup on the ballistic pendulum

Figure 3-2: Photograph showing set-up of the ballistic pendulum

3.1.2. Experimental rig arrangement

The blast experiments are carried out in two setups. In the first, two clamped test plates are assembled and between them is a speed-trap assembly. In the second setup, the rear plate is clamped in a slightly modified frame which accommodates a containment tube which serves the purpose of housing and locating the energy absorbers which are placed in front of the rear test plate.

3.1.2.1. System without energy absorbers

In the initial phase of the blast experiments, a mild steel plate, 244mm x 244mm, of thickness 1.6mm and of exposed diameter 106mm is clamped between two clamping plates. This clamped rig would be connected to a similarly clamped secondary rig – comprising of two clamping plates – by four spacer rods, each of length 110mm. This is connected to a ballistic pendulum. The speed trap assembly is placed at a fixed distance of 50mm from the front plate. The plates are consequently at an initial separation of 150mm.

The front plate is separated from a cylindrical PE4 charge by a 13mm thick polystyrene foam pad which fits snugly into the front clamp at a diameter of 106mm. Figure 3-3 shows a CAD schematic and a dimensioned view of the test rig that is attached to the rest of the pendulum assembly before energy absorbers are included. The 50mm distance between the front plate and the speed trap assembly is kept constant for all the tests conducted.

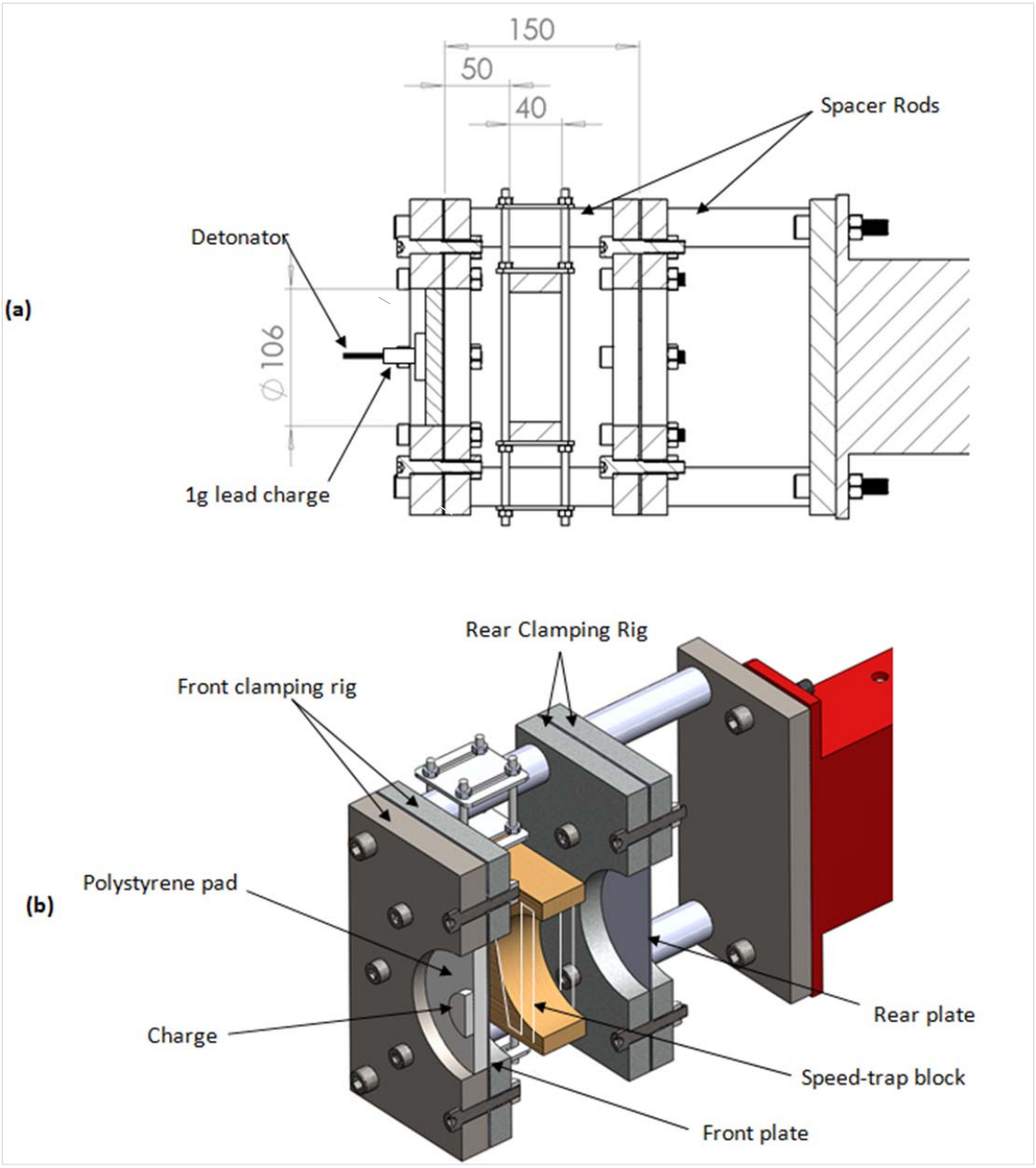

Figure 3-3: (a) Dimensioned view and (b) CAD schematic of the experimental arrangement without energy absorber

3.1.2.2. System with Energy Absorbers

After the initial phase of the experiments are carried out without energy absorbing materials, a slightly modified rig is used on the pendulum to accommodate the energy absorbing materials. For the second set-up, the front clamp frame is maintained as previously described whilst the front most clamping plate of the rear clamping rig is replaced by a threaded plate onto which a mild steel tube of length 75mm is fastened. The tube has an inner diameter which is equal to the exposed plate diameter (106mm) and has an outer diameter of 150mm. Slightly longer spacer rods (150mm as compared to 110mm) are used to separate the two plates to fit both the speed trap assembly and the blast tube between the two test plates.

In both cases, the spacer rods which connect the rear clamp frame to the rest of the pendulum allow the deflection of the rear plate to be unconstrained. In essence, the setup of the rig, as shown in the sectioned dimensioned assembly and CAD schematic in Figure 3-4 is the same as the setup used for the first phase of the experiments except that the plate separation is now 190mm from 150mm and the containment tube which houses the energy absorbers is incorporated into the setup. Details of the components which are used during the tests and their corresponding masses are shown on Table 3.1.

***Note**: As shown in Figure 3-3, the plate separation for the system with no absorbers commences at 150mm and the increases to 190mm when the containment tube is added and thus absorbers are added. The reason to increase this distance is because a shorter containment tube to house thinner absorbers (minimum thickness of 20mm) was initially planned, but due to early findings the a longer containment tube had to be made and thus the separation distance had to be increased. To *validate* the decision of increasing the separation distance, a few further tests are undertaken with no absorbers but using the setup shown in Figure 3-4 (with a separation of 190mm) to investigate whether there is a changed effect after increasing the separation distance. Further details are outlined in §3.5.

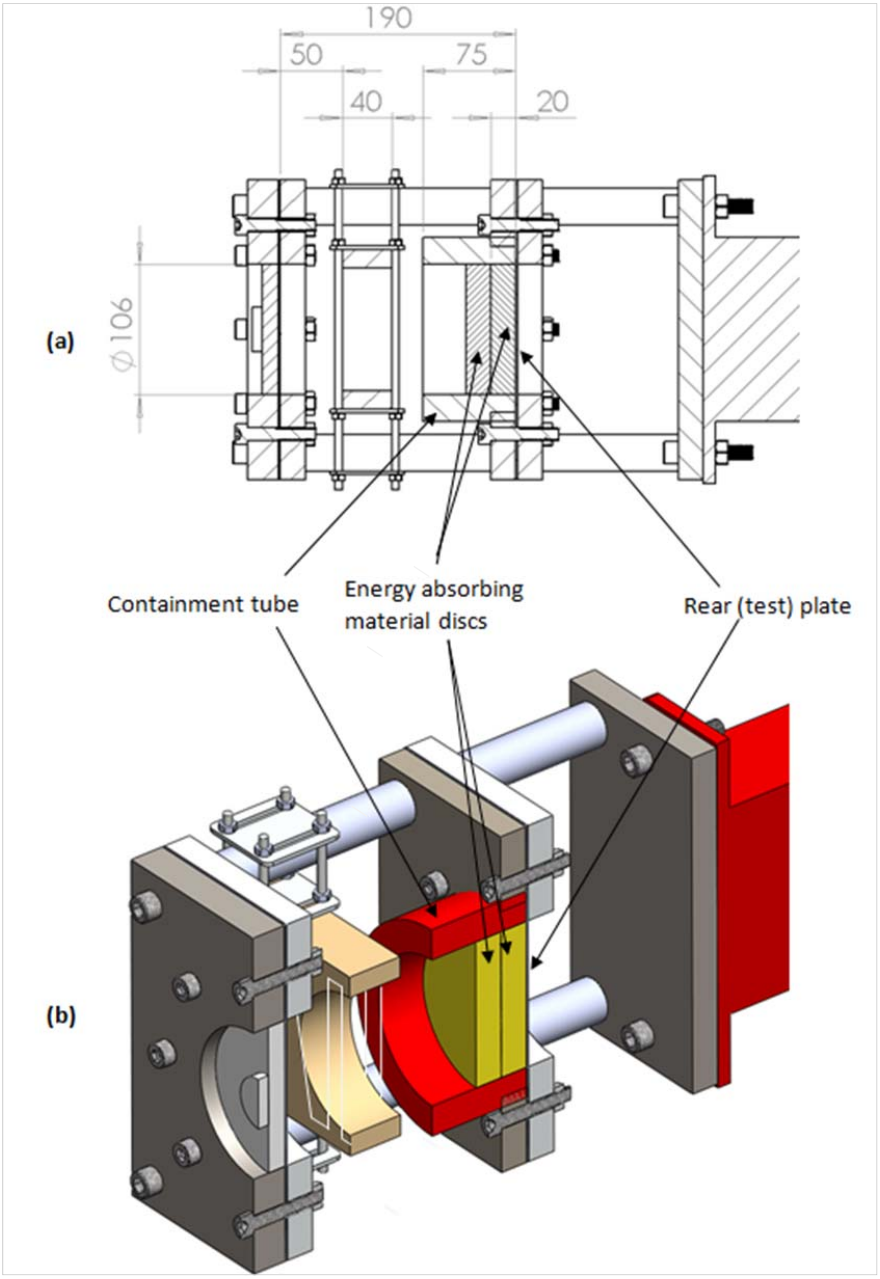

Figure 3-4: (a) Dimensioned view and (b) CAD schematic of the experimental arrangement with energy absorbers

Table 3.1: Mass detail of components of the test rig

Component	***Mass (kg)***	***Quantity***	***Mass (kg)***
Front clamp plate of the front clamping rig	9.48	1	9.48
Rear clamp plate of the front clamping rig	7.64	1	7.64
110mm Spacer Rod*	0.55	8	4.36
150mm Spacer Rod**	0.74	4	2.96
Speed Trap Assembly	1.40	1	1.4
Speed Trap Circuit box	0.24	1	0.24
M12 threaded rods	0.08	4	0.3
Front clamp plate of the rear clamping rig (unthreaded)*	7.70	1	7.7
Rear clamp plate of the rear clamping rig	7.70	1	7.7
Front clamp plate of the rear clamping rig (threaded)**	6.24	1	6.24
Threaded tube**	4.72	1	4.72
Test plate (average)	0.69	2	1.38
Back plate	8.98	1	8.98
M10 nut	0.02	16	0.3
M10 bolt	0.06	16	0.88
M12 bolt	0.09	8	0.72
TOTAL TEST RIG MASS (INITIAL TESTS WITH NO ABSORBERS)*			**51.08**
TOTAL TEST RIG MASS (TESTS WITH ABSORBERS)**			**54.86**

*In the initial phase with no absorbers, eight 110mm spacer rods are used with unthreaded clamps for all testing rigs (visual details in Figure 3-3)

**In the phase with energy absorbers, four 150mm spacer rods replace four of the 110mm spacer rods. The front unthreaded clamp of the rear clamping rig is replaced by a threaded one onto with the threaded tube is fastened for the containment of the absorbers (visual details in Figure 3-4)

3.1.3. Speed Trap System

In each of the tests, the speed of the fragment released from the front plate and flying towards the rear plate is required as part of the quantification of the characteristics of the fragment. A speed trap system is used to capture two distinct points in time in the motion of the fragment at two fixed points in its path. With the distance between the two points known, the speed can be determined. Initially, an infra-red system was designed and deployed for this purpose. However, the system presented problems and failed to consistently work. A wire-break system was used instead, which, in principle, is similar to one successfully used by Nurick et al. [16,29,30]. Further details of the infra-red system and its shortcomings are discussed in Appendix A.

3.1.3.1. Wire-break speed trap system

The speed of the fragment is captured through a simple wire-break electic circuit system which makes use of two meshes of ‘fuse wire’ that can is easily broken. The wooden block assembly, shown in Figure 3-5, is held in position on spacer bars by an arrangement of aluminium fasters and brackets. The wooden frame has two wires, each woven tautly around nails into a mesh covering a section of the opening on either side of the 40mm thick wooden block. The thickness of the wood serves as the constant separation distance between the two wire meshes. For each mesh, the ends of the break-wire are wound around a ‘banana plug’ pin that is located on the wooden frame on either side of the 100mm-diameter centrally located hole – as shown on the assembly shown in Figure 3-5.

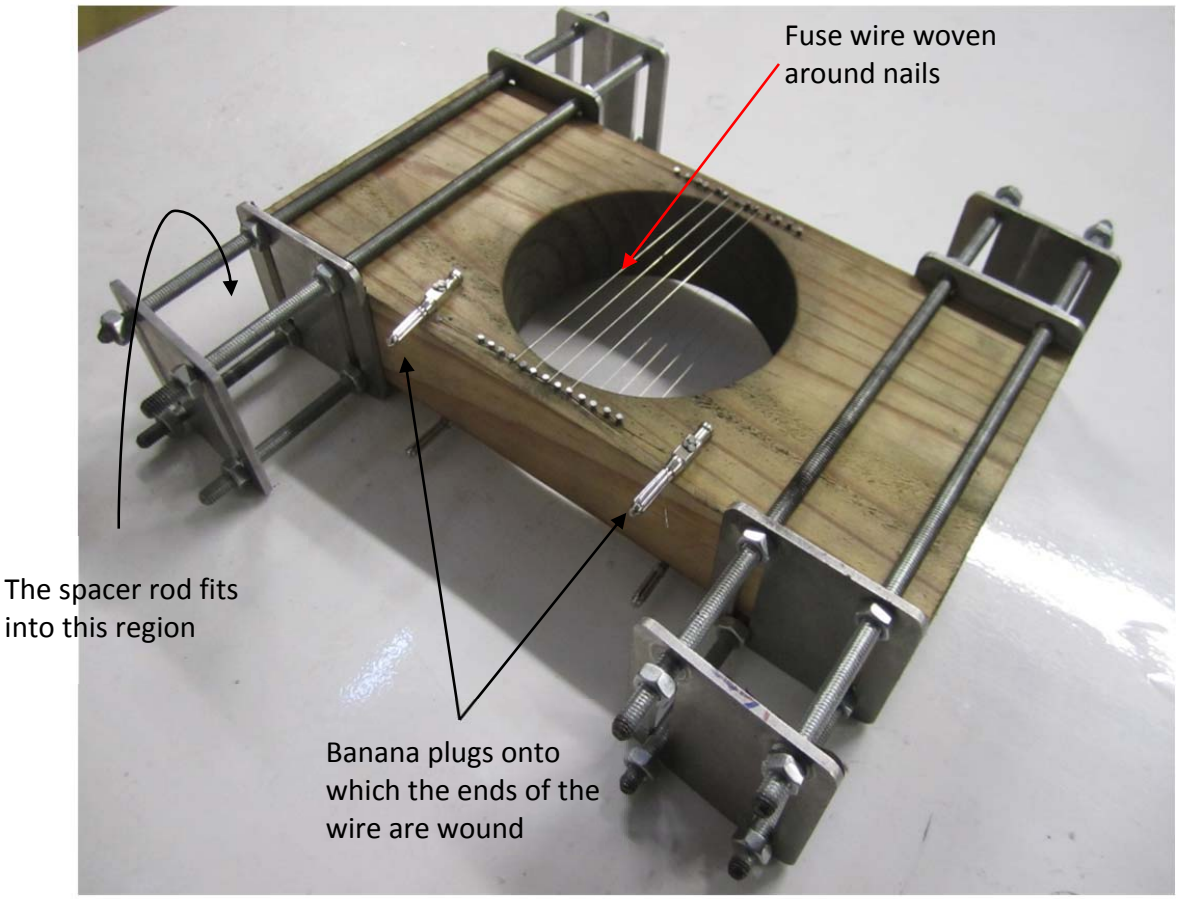

Figure 3-5: Photograph of the speed trap wooden block assembly

The circuit box – consisting of a power supply connected to a circuit board in a closed plastic container – as shown in Figure 3-6a, is located on the I-beam of the ballistic pendulum. The battery cells, which are connected in series, send current through two resistors connected in parallel. The circuit board inside the container is attached to a 'slab' of Ethyl-Vinyl Acetate foam to prevent or reduce any vibrations generated during the blast loading from being transmitted through the I-beam and consequently disrupting or damaging the circuit and its components.

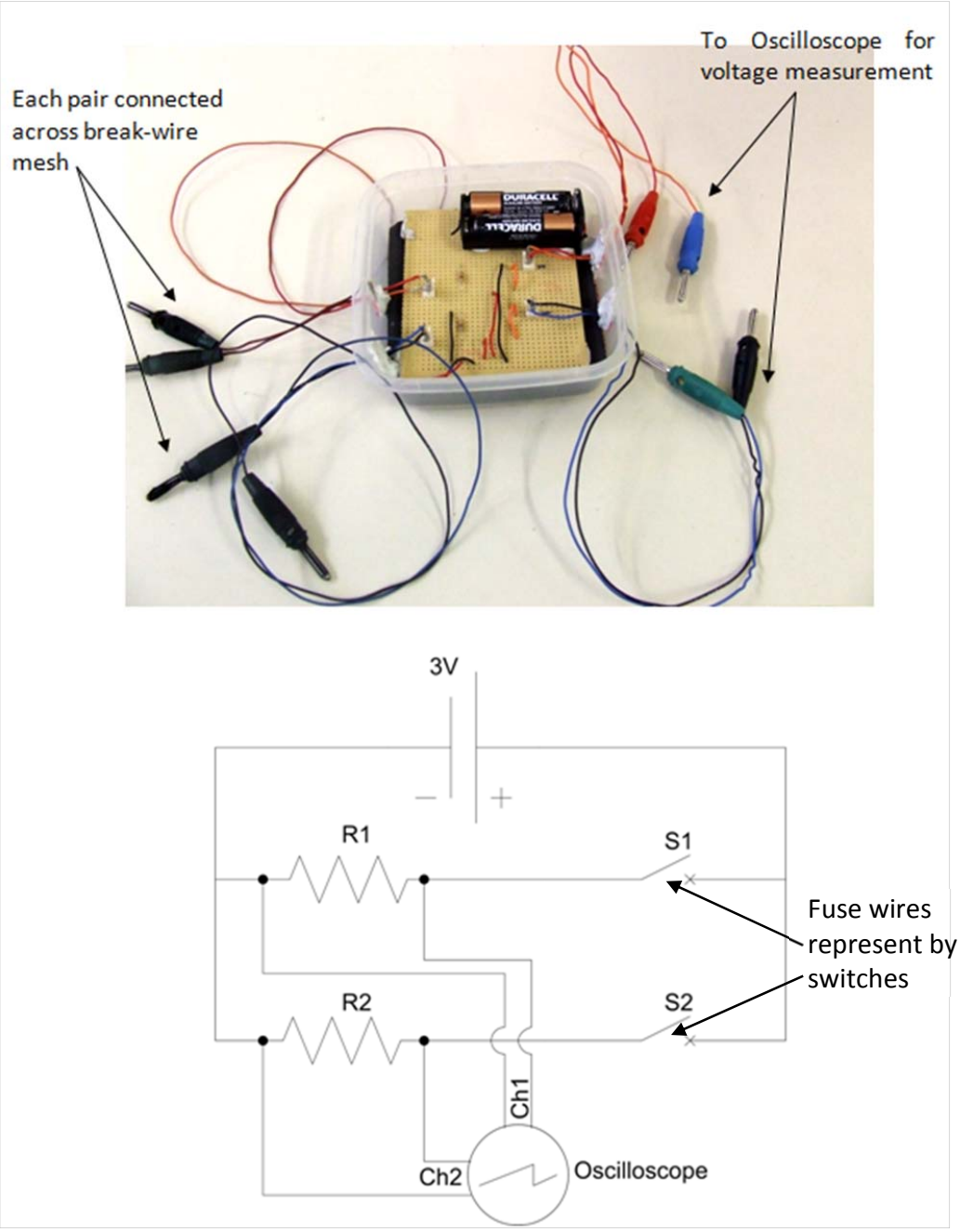

Figure 3-6: (a) Speed trap circuit box and (b) circuit diagram showing the connections between the circuit box and oscilloscope

These break-wires act as switches; denoted as S1 and S2 in the circuit schematic in Figure 3-6b. Each break wire is connected to a 10kΩ resistor. The entire setup is powered by a 3V DC supply. The voltage across each of the 10kΩ resistors is measured through two channels of a digital oscilloscope.

As each mesh is broken by a passing fragment, the switches can be regarded as open, and the voltage measured across the respective resistor drops from 3V to 0V. Both the voltage drops are captured on the oscilloscope and the difference in time between the drops is used to calculate the average speed of the fragment, since the distance between the meshes is known as 40mm. The formula for computing the average speed of the fragment in each case is shown in Eq. 3-2.

$$v_f = \frac{\Delta x_{mesh}}{\Delta t} = \frac{0.04}{\Delta t} \qquad \text{Eq. 3-2}$$

Where : v_f = Speed of the fragment, Δx_{mesh} = Distance between the two wire meshes, Δt = Time between the two mesh breaks (obtained from the oscilloscope)

3.2. Explosive charge details

For the blast tests conducted in this study, plastic explosive PE4, which is commonly known as Component 4 (C4) in other geographical regions, is used. PE4 can be moulded easily into a desired shape and size. For the experiments, the explosive is moulded into cylindrical shapes in three distinct diameters – 27mm, 36mm and 43mm. The minimum charge mass is 7g, while the maximum is 11g – each charge mass comprises 1g lead charge inserted into a cylindrical base charge. It thus follows that a charge of 7g is made of 6g base charge plus 1g lead charge. For each charge diameter used, an increasing charge mass results in an increase in the height of the cylindrical charge. The properties of PE4 are shown in Table 3.2. A typical setup of the base explosive used in the study is shown in Figure 3-7. The dot on the charge is the centre of the charge, where the detonator and lead charge are attached.

Table 3.2: Properties of PE4

Constituents	RDX grade B (88%), Plasticiser (11%) , Pentaerythritol di-oleate (1%) [135]
Mean density	1.59 mg/m^3 [135]
TNT Equivalence	1.37 (for deformation effects) [136]
	1.09-1.21 (for target plate acceleration effects) [136]
	≈1.3 (effective equivalence) [136,137]
Detonation velocity	8027 ± 180 m/s [135]

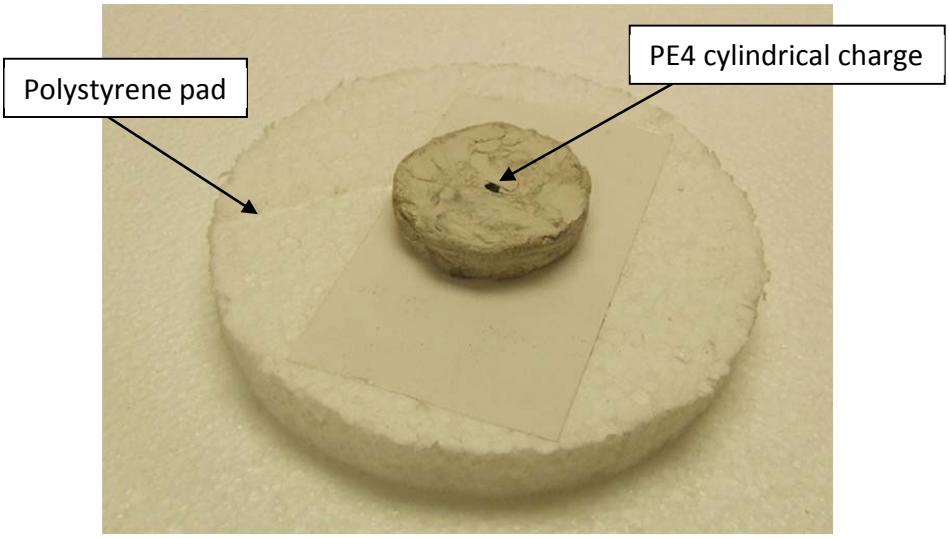

Figure 3-7: Photograph showing the PE4 explosive charge setup used in the blast experiments

3.3. Test plate details

In each of the blast tests, two parallel plates are used – the front plate as the source of the fragment and the rear plate as the target onto which the fragment travels impacts. The plates are made of mild steel and have a thickness of 1.6mm and an exposed circular area of 106mm diameter.

For each of the sheets of mild steel from which the test plates are cut, six dog-bone tensile test specimens are also cut. Each of the six specimens is subjected to quasi-static tensile testing at a different cross-head speed, hence displacement rate, ranging from 5mm/min to 100mm/min. Six sheets are used for the test plates which are used in the blast tests, resulting in thirty-six (36) tensile test. All thirty six specimens were tested but one specimen failed outside the gauge length and that specimen was ignored – leaving 35 tests to be analysed. A graph of engineering stress vs. engineering strain with results for specimens from one of the sheets is shown in Figure 3-8. The remaining results can be found in Appendix B.

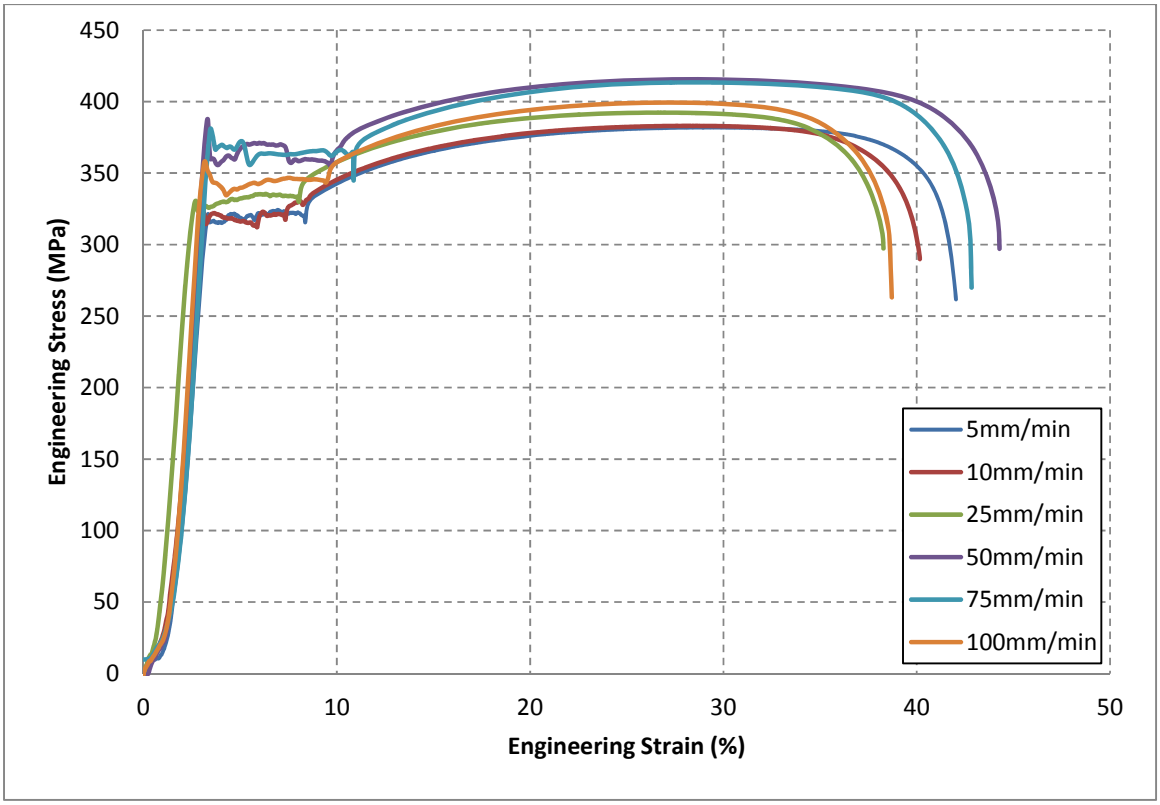

Figure 3-8: Engineering stress vs. strain curves for specimens taken from one of the sheets of mild steel (Sheet 1)

Mild steel is known for its strain rate sensitivity, meaning that it behaves differently at different strain rates. The Cowper-Symonds equation [138] is used to relate the dynamic yield stress, which is the yield stress that is observed at a certain strain rate, and static yield stress, which is the yield stress of the material at zero strain rate.

$$\frac{\sigma_0^1}{\sigma_0} = 1 + \left(\frac{\dot{\varepsilon}}{D}\right)^{1/q} \qquad \text{Eq. 3-1}$$

Where: σ_0= static yield stress, σ_0^1 = dynamic yield stress, $\dot{\varepsilon}$ = strain rate, D & q are material constants.

Table 3.3 shows properties of mild steel as found from tensile tests conducted on the dog bone specimens and literature.

Table 3.3: Selected properties of mild steel

Density	7870 kg/m^3 [139]
Average static yield strength (MPa)	288.2*
Ultimate tensile strength (MPa)	375.9*
Elongation at failure (%)	34.1*
D (s^{-1})	40.4 [138]
q	5 [138]

*Obtained from uniaxial quasi-static tensile tests

3.4. Energy absorbing materials

After the initial phase of the blast experiments, involving impacting an unprotected rear plate by a blast-induced fragment, energy absorbing materials are placed in turn in front of the rear plate. Six materials are chosen for the purpose of blast testing. Factors such as availability, ease of manufacture, specific energy absorbed during quasi-static compression were considered (see §2.2.4.). ALPORAS aluminium foam, aluminium honeycomb, balsa wood, Corecell M80 foam, Divinycell (PVC) H200 foam and rigid polyurethane 200 foam were the six materials used in the blast experiments. Before the final materials were selected, a total of eleven unique materials were initially considered and tested – aluminium honeycomb (≈80kg/m3) Corecell A-500 foam, corrugated board, polystyrene foam, rigid polyurethane 80 foam and RG-5565 Ethylene-vinyl acetate foam complete the list of eleven materials considered.

3.4.1. Material characterisation of the energy absorbers

During quasi-static compression, all the energy absorbing materials are crushed at different crosshead speeds. The materials are cut into rectangular prisms or cubes. In most cases the difference in dimensions of the quasi-static compression specimens is due to the difference in default thicknesses of the materials as some test samples are outsourced at small thicknesses as they were provided at no cost and suppliers only offer the test samples at smaller sizes (RG-5565 EVA foam at 10mm thickness, Corecell M80 foam at 15mm and Corerecell A-500 foam at 13mm thickness). After Corecell M80 foam had been selected as one of the materials to be used for the blast tests, it was re-tested in quasi-static compression with a new height of 20mm.

In some cases, materials were available within the BISRU laboratories from previous studies and had already been cut into certain sizes and could only be compressively tested as is – the aluminium honeycomb of density 79.4kg/m^3 was already cut to a mean thickness of approximately 150mm. The materials which are initially subjected to quasi-static compression are shown on Figure 3-9.

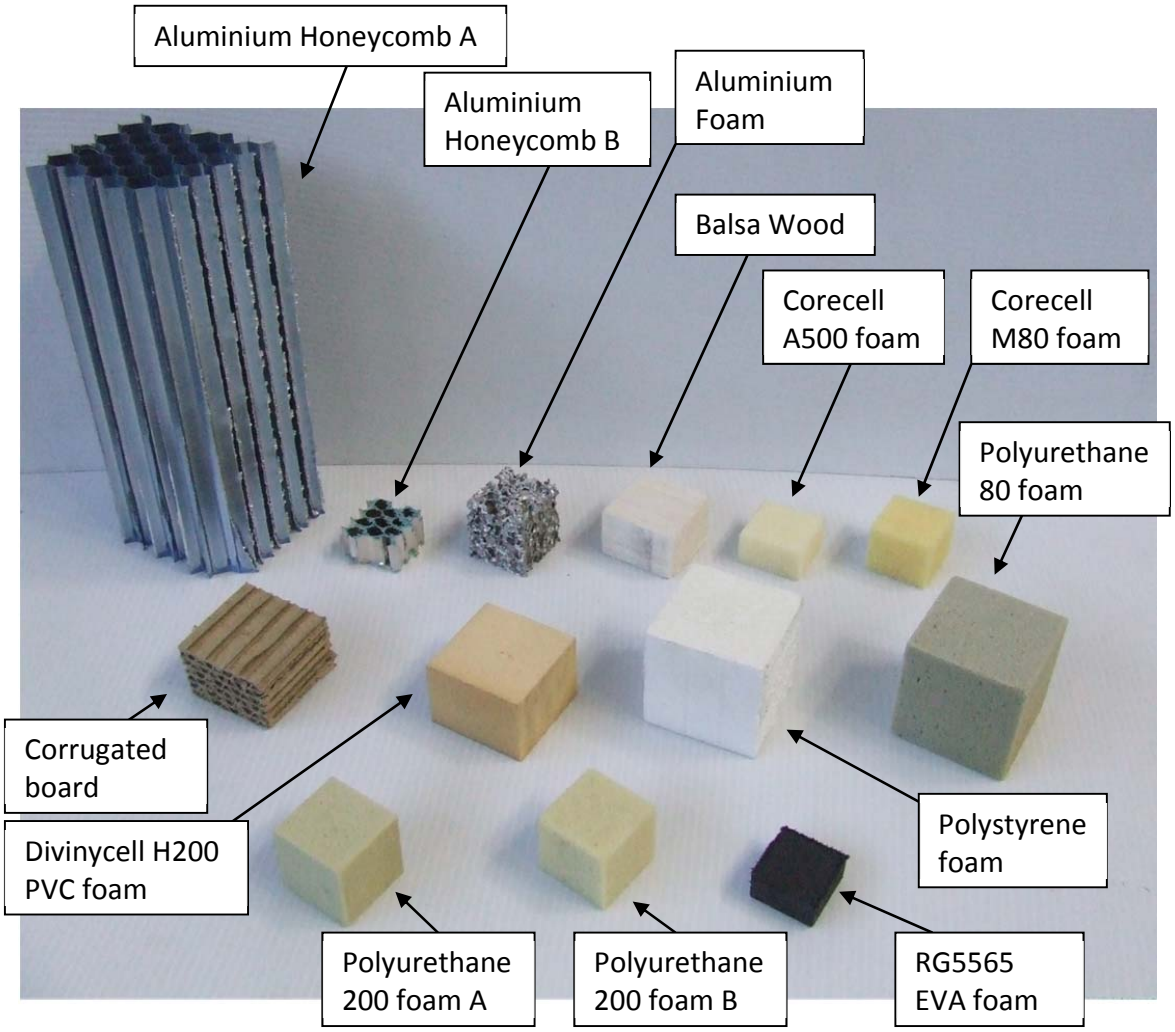

Figure 3-9: Photograph of all specimens subjected to quasi-static testing

For the quasi-static compression tests, the discrepancies, which may be due to the difference in volumes of the materials, are accounted for by considering not just cumulative energy absorbed but also the energy absorbed per unit mass and per unit volume during the compression cycle. Table 3.4 shows the details of the quasi-static specimens.

Table 3.4: Mean dimensions, masses and densities for compression specimens

Material 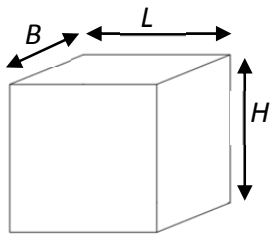	**Mean Specimen size** **B x L x H** *(mm x mm x mm)*	**Mean Density** $\overline{\rho^*}$ *(kg/m^3)*	**Mean Specimen mass** $\bar{m}$ *(g)*
Aluminium foam	25.3 x 25.4 x 25.2	229.7	3.72
Aluminium honeycomb A	57.4 x 57.9 x 150.8	79.4	39.77
Aluminium honeycomb B	25 x 25 x 13	103.4	0.84
Balsa Wood	30 x 30 x 19.7	77.3	1.37
Corecell A-500 foam	25.5 x 25.5 x 13	94.6	0.80
Corecell M-80 foam	25.5 x 25.4 x 15.3	85.8	0.85
Corrugated Board (loaded in Z-axis)	34.7 x 34.8 x 23.5	81.0	2.30
Divinycell H200 PVC foam	35.4 x 36 x 25.2	185.6	5.96
Polystyrene foam	40 x 40.2 x 39.1	44.2	2.78
Polyurethane 80 foam	40 x 40.3 x 40.1	78.0	5.04
Polyurethane 200 foam A	24.7 x 24.7 x 25.4	191.0	2.96
Polyurethane 200 foam B	24.8 x 24.7 x 24.4	191.3	2.86
RG 5565 EVA foam	20.5 x 20.45 x 10	324.4	1.36

Four specimens of each materials were subjected to four crosshead speeds (2, 10, 20 and 40mm/min) except for the first aluminium honeycomb tested (referred to as Aluminium honeycomb A) which was tested at two speeds of 10mm/min and 20mm/min. The loaded area is denoted by the area $B \times L$,shown on Table 3.4, meaning that the initial gauge is the height H of the specimen. Graphical results showing compressive stress against strain for each of the materials subjected to a speed of 10mm/min are shown on Figure 3-10.

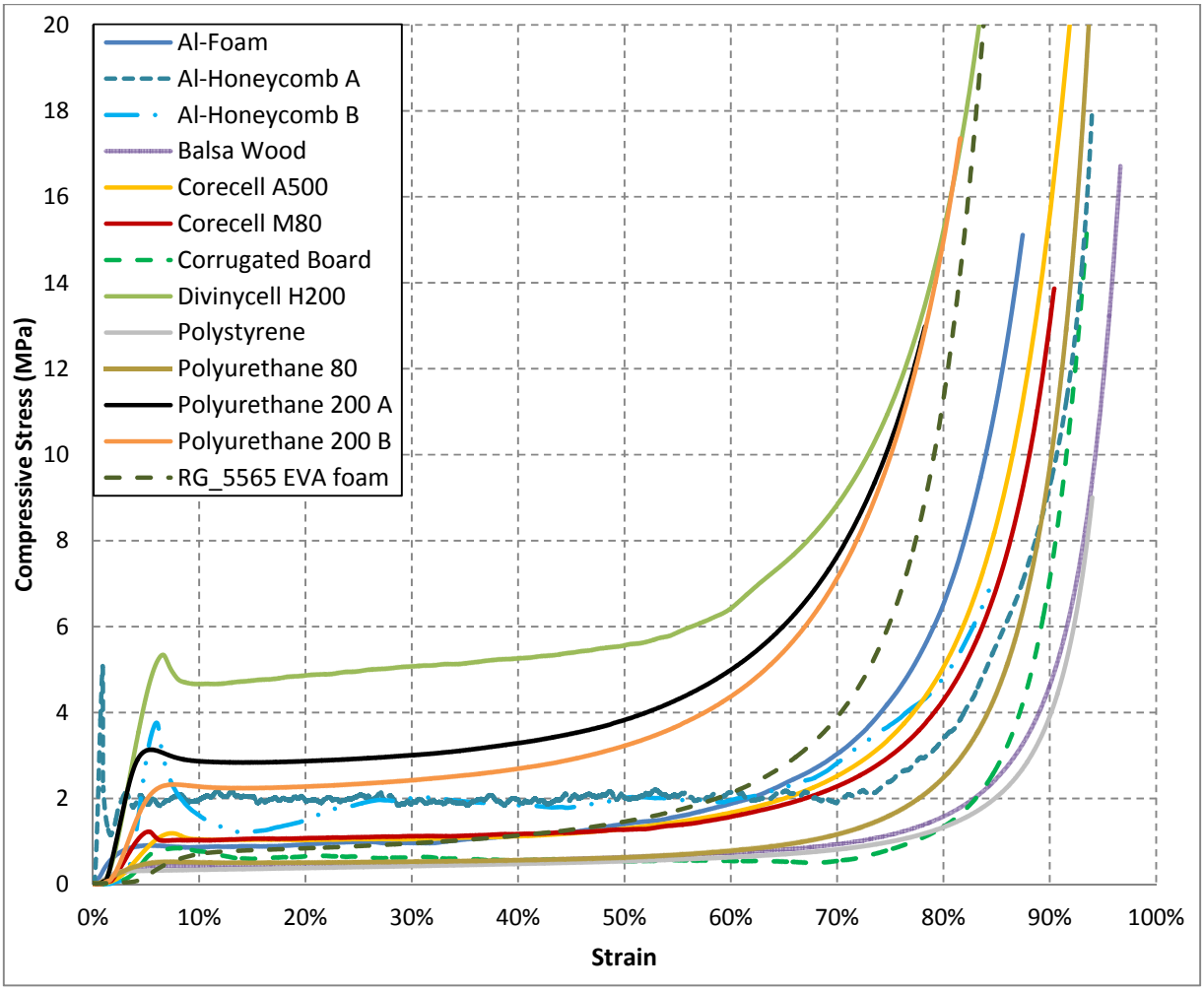

Figure 3-10: Compressive stress vs. Strain for all materials tested quasi-statically (cross-head speed = 10mm/min)

An important factor after the compression tests, when choosing the materials to be used in the blast tests, is the energy absorption capbility of the materials. The energy absorption efficiency method shown in §2.2.3.2 can be used to find the densification strain for each material based on the stress-strain data from the quasi-static compression tests.

For Divinycell H200 foam, Figure 3-11 shows how the energy absorption efficiency relates to compressive stress, when both are plotted against compressive strain. Using the energy absorption efficiency method, the onset strain of densification is the strain at which the energy absorption efficiency is maximum. As it can be observed in Figure 3-11, the densification strain is 0.6 or 60%. The stress against strain for all the other tested materials can be found in Appendix B. The summarised results from the quasi-static compression tests on the various energy absorbing materials are listed in Table 3.5.

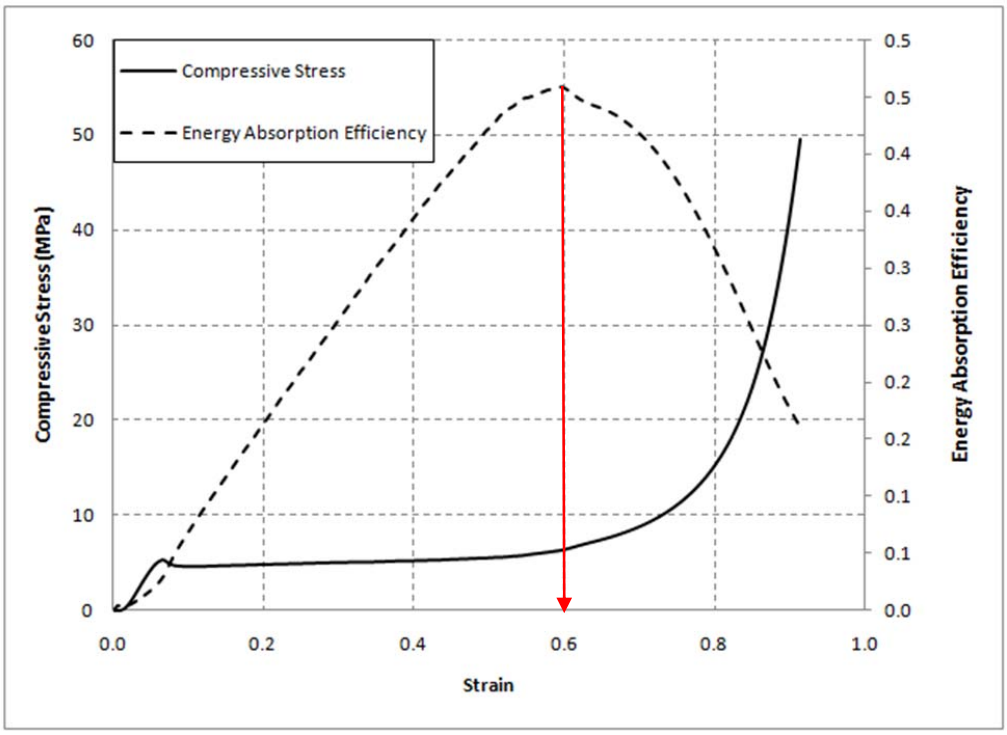

Figure 3-11: Stress and energy absorption efficiency against strain for Divinycell foam compressed at 10mm/min

Table 3.5: Results on materials subjected to quasi-static compression testing

Material	**Strain at Peak load**	**Onset Strain of densification**	**Plateau Stress**	**Energy Absorbed until densification starts**	
	ε_{pk} %	ε_d %	σ_{pl} MPa	Mass SEA MJ/kg	Volumetric SEA GJ/m^3
Aluminium foam	3.5	54	1.0	163.0	34.3
Aluminium Honeycomb A	0.9	70	2.0	34.1	2.8
Aluminium honeycomb B	5.9	59	1.9	1194.4	127.1
Balsa Wood	2.5	65	0.6	251.7	19.8
Corecell A-500 foam	6.4	55	1.1	726.2	67.7
Corecell M-80 foam	4.4	54	1.1	702.6	62.4
Corrugated Board	6.3	70	0.6	17.4	1.39
Divinycell H200 foam	6.3	60	5.0	510.6	95.2
Polystyrene foam	1.5	64	0.5	108.0	4.5
Polyurethane 80 foam	5	55	0.6	49.9	4.5
Polyurethane 200 foam A	4.8	53	3.0	531.3	101.1
Polyurethane 200 foam B	7.2	52	2.4	447.0	81.9
RG 5565 EVA foam	7.5	52	1.0	337.6	109.3

*The materials chosen for the blast tests are highlighted in green

3.4.2. Energy absorbers used in blast testing

From the materials which were tested in quasi-static compression, ALPORAS aluminium foam (relative density 8.5%), aluminium honeycomb (relative density 3.8%), balsa wood, Corecell M80 foam (henceforth simply referred to as Corecell foam), Divinycell H200 PVC foam (henceforth referred to as Divinycell foam), and rigid polyurethane 200 foam (henceforth referred to as polyurethane foam) were chosen as energy absorbers in the blast tests as shown in Figure 3-12.

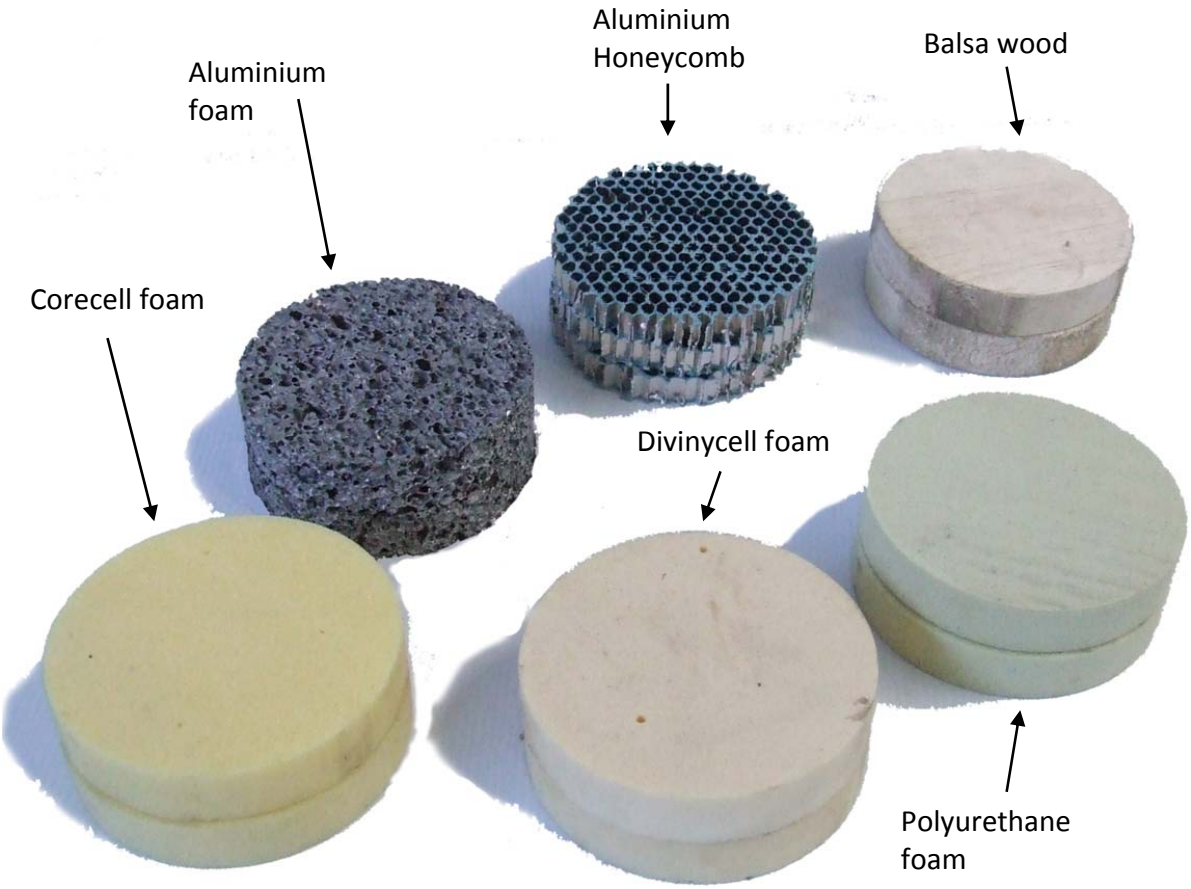

Figure 3-12: Photograph of all the materials used as energy absorbers during blast tests (40mm thick specimens shown)

The energy absorbers are all cut from their respective parent materials as discs with diameters of 106mm, which is equal to the plate diameter, to fit snugly into the containment tube which is threaded onto the rear clamping rig. Aluminium foam is milled into 106mm diameter discs, and the other materials are cut using a hole-saw which has an internal diameter of 107mm and are then machined to an approximate diameter of 106mm. Table 3.6 summarises all the stacking arrangements to achieve each of the nominal thicknesses at which the energy absorbing materials are tested during the blast tests.

Table 3.6: Summary of all the energy absorbing material layer arrangements for each nominal thickness

Energy absorbing material	**Layering for total thickness**			
	40mm			**60mm**
Aluminium foam	1 x 40mm			Not tested at 60mm
Aluminium honeycomb	3 x ~13mm			Not tested at 60mm
Balsa wood	2 x 20mm			3 x 20mm
Corecell M-80 foam	2 x 20mm			Not tested at 60mm
Divinycell H200 foam	2 x 20mm			3 x 20mm
Polyurethane 200 foam	1 x 40mm*	2 x 20mm*	4 x 10mm*	3 x 20mm

*More description of the tests on 40mm thick polyurethane foam is given in §3.5.3.

3.5. Experimental plan for the blast tests

All blast tests were undertaken with two mild steel plates of an exposed circular region of 106mm diameter and a thickness of 1.6mm. The blast from the charge placed in front of the front plate ejects a fragment from the central region of the plate which flies towards the rear plate, on which impact from the fragment occurs.

3.5.1. Tests with no energy absorbers

The initial blast tests were carried out whit no energy absorber between the front and rear plates. The initial plate separation distance is set at 150mm, and cylindrical charges of three diameters (27mm, 36mm and 43mm) and increasing masses (7g to 11g, respectively) are used to eject fragments from the front plate.

The blast tests with no energy absorbers were also carried out at a 190mm plate separation distance for the following reasons: For tests in which energy absorbing materials being are used to protect the rear plate, the **preliminary plan** was to use a **minimum absorber thickness of 20mm**, increasing to 40mm whilst the plate separation remains 150mm. As tests with energy absorbers commenced, the Corecell foam with a thickness of 40mm was subjected to a fragment released by a blast from a 7g charge of 36mm diameter. It was observed that the fragment perforated the absorber and caused substantial rear plate deflection (12.68mm). Based on this observation, the new **minimum energy absorber thickness** was chosen as **40mm**, with an increase to 60mm. A longer containment tube was thus required, and for the tube and the speed trap assembly to fit between the front and rear clamp rigs, the spacer rod between the two rigs was increased such that the plate separation increased from 150 to 190mm. Validation tests were then carried out at a plate separation of 190mm when **no energy absorber** was present to investigate whether increasing the separation from 150mm to 190mm had an insignificant effect on the damage caused by the fragments on the rear plate. The details of blast tests undertaken with no energy absorbers are shown in Table 3.7.

Table 3.7: Details of parameters governing blast tests which occur with no energy absorbers

Plate separation (mm)	150mm and 190mm*
Charge diameter (mm)	27mm, 36mm & 43mm
Charge mass (g)	7g ⟶ 11g

3.5.2. Effect of the thickness of the energy absorbing materials

For **all** tests carried out with the energy absorbers, 190mm is the fixed plate separation distance. All six materials (discussed in §3.4.2) are initially tested at a thickness of approximately 40mm and the fragments are induced by charges of 36mm diameter with charge masses ranging from 7g to 11g. In the first series, the different materials are analysed individually on how they respond to increasing speeds of fragments; in addition, they are compared with each other with regards to their respective protective performances of the rear plate. Aluminium foam is made by a single 40mm thick disc. The approximate 40mm thickness of aluminium honeycomb is formed by stacking three layers of honeycomb with thickness of approximately 13mm. For each of balsa wood, Corecell foam, Divinycell foam and polyurethane foam, two discs which are nominally 20mm thick are stacked on each other for this thickness.

In a subsequent series of tests, three of the materials (balsa wood, Divinycell foam and polyurethane foam) are tested at 60mm thickness by stacking three layers of 20mm thick discs on each other in front of the rear plate. Table 3.8 lists the details of the parameters which govern the series of tests conducted on 40mm and 60mm thick energy absorbers whilst the charge diameter is maintained at 36mm.

Table 3.8: Parameters for series of blast tests carried out with 40mm & 60mm thick absorbers (36mm charge diameter)

40mm thick energy absorbers	**Energy absorbers tested**	Aluminium foam, aluminium honeycomb, balsa wood, Corecell foam, Divinycell foam, Polyurethane foam
	Charge diameter (mm)	36mm
	Charge mass range (g)	7g ⟶ 11g
60mm thick energy absorbers	**Energy absorbers tested**	Balsa wood, Divinycell foam, Polyurethane foam
	Charge diameter (mm)	36mm
	Charge mass range (g)	7g ⟶ 11g

3.5.3. Effect of different layering arrangements of the energy absorbing materials

In one parametric test, the charge diameter is maintained at 36mm to investigate how a material responds to fragment impact if its thickness remains the same, but the arrangements of the same thickness are varied. 40mm thick polyurethane foam is tested at three varying layering arrangements for this series of tests – a single 40mm thick disc, two 20mm thick disc and four 10mm thick discs. The plan of the series of tests to investigate the effects of altering the layering arrangement of 40mm thick polyurethane foam is tabulated in Table 3.9.

Table 3.9: Details of series of tests to investigate effects of different layering arrangements of energy absorbers

Effects of different layering arrangements	
Description	Fragments released by use of 36mm charge and increasing in mass (from 7g to 11g) on three arrangements of the same effective thickness to see the protective effects of having the same thickness made of one, two and four layers of discs of an energy absorber.
Materials tested	Polyurethane foam
Layer arrangement	1 x 40mm disc 2 x 20mm discs 4 x 10mm discs

3.5.4. Effects of size and speed of a fragment

A final parametric series of tests is conducted to investigate the effect the subjecting a protected plate to impact from fragments of different sizes and different impact speeds but with the impact kinetic energies being close to a nominal value. Balsa wood, Divinycell foam and polyurethane foam are placed in front of the rear plate. The details of the parametric test are outlined in Table 3.10.

Table 3.10: Details of plan of series of tests to investigate effects of different size and speed of a fragment

Effects of different size and speed of fragments	
Description	A fragment is released for each of the three charge diameters (27, 36 and 43mm) and the speeds are such that the impact kinetic energies are within close numerical range. This is to investigate the effects of impact from different sized fragments on plate damage.
Materials tested	Balsa wood
	Divinycell foam
	Polyurethane foam
Energy absorber thickness	40mm *(comprised of two stacked 20mm thick discs for all three materials)*

3.5.5. Repeat tests

During blast tests, some of the tests are repeated once or a number of times. One of the reasons for the *repeat tests* is that in the initial phase of the blast tests, the need to check the reproducibility of readings of the speed of the fragment through the speed trap circuit necessitated conditions being repeated and the speed variations being observed. *Repeat tests* are also carried out because it is noted that tearing of the rear plate is sometimes observed at fragment kinetic energies at which tearing is not expected; usually because the fragment impacts the rear plate with is edge and consequently slices the plate rather than impacting the plate by its face. Figure 3-13 is a photograph showing the face region and edge of a typical fragment in the study.

It was observed that kinetic energy of a fragment is an unpredictable parameter in that the range of kinetic energy of fragments released by a charge of a certain mass and diameter can be more than 1000J. Consequently, in some of the tests conducted, *repeat tests* were carried out to account for this uncertainty in an attempt to observe the response of the rear plate at certain fragment kinetic energies.

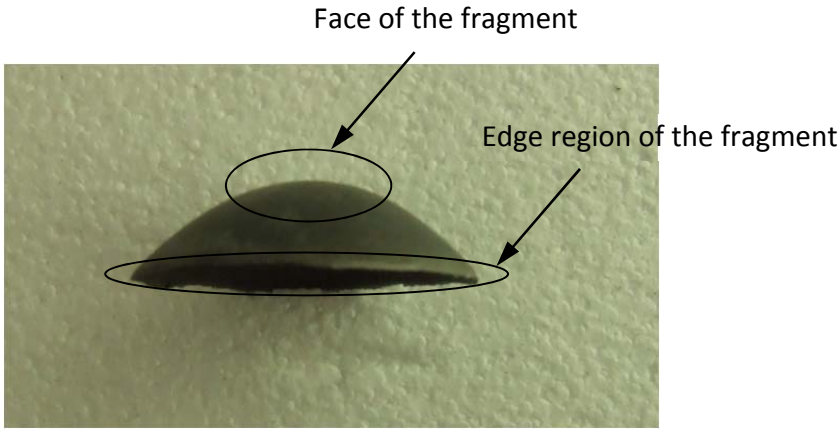

Figure 3-13: Side view photograph of a typical fragment in the study – showing face and edge region

3.6. Measurements and Test notations

Before, during and after the blast tests, a number of parameters were measured and notes created to describe the different tests and their respective conditions. This subsection describes the parameters and how they have been measured and calculated, and showing how the different test notes were used.

3.6.1. Determining the speed of the fragment

As discussed in §3.1.3, a wire-break method of calculating the speed of the fragment was used in the study. As a fragment breaks the mesh closest to the front plate, Channel 1 of the oscilloscope records a drop in voltage through the 10kΩ resistor in the circuit branch which is completed by that wire mesh (see Figure 3-6). Channel 2 responds similarly by measuring the drop in the other 10kΩ resistor as the second mesh is broken. An extracted plot of the signals from the two oscilloscope channels from one of the tests is shown in Figure 3-14. The **horizontal axis** represents the time in microseconds (μs) and the **vertical axis** represents the voltage across each of the resistors in volts (V). Channel 2 gets vertically offset for clarity when measuring the difference in the times for the fragment to break the fuse-wire meshes.

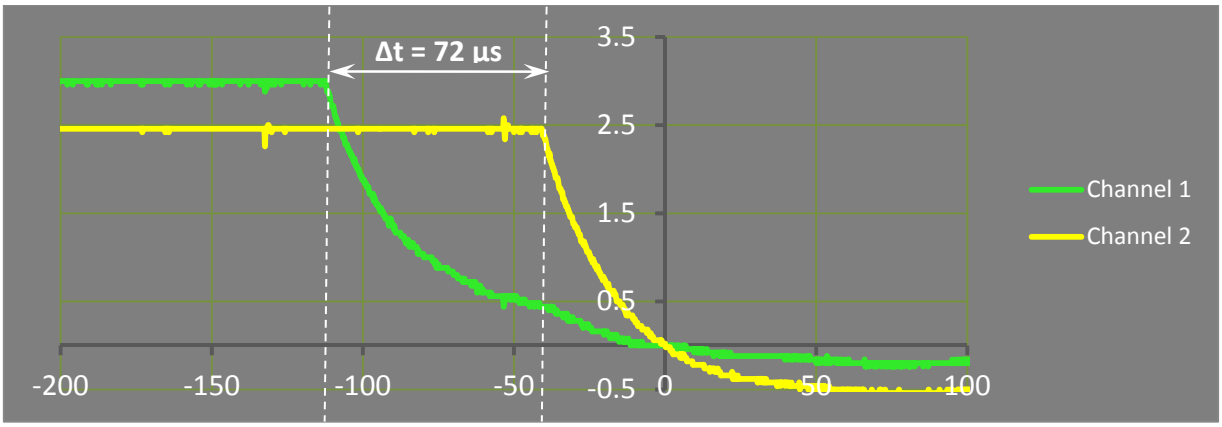

Figure 3-14: Typical oscilloscope voltage drop signals for the tests conducted during the study

3.6.2. Fragment diameter

Depending on the orientation of impact between the fragment and the rear plate, there were observed crumpled, shredded fragments, or fragments which remained fused to the rear plate, that maked it impossible to measure the average diameter of the fragment. *For the different states in which fragments are recovered after impact in this study, reference can be made to §4.2*. In cases where the fragment comes into contact with the rear plate with its face and does

not undergo considerable secondary deformation or fusion to the rear plate, it is recovered and it is possible for its average diameter to be measured.

Since the fragment was observed to not be perfectly circular, the span between opposite points on its edges is measured for two or three orientations (depending on the circularity of the fragment) and an average span is calculated and recorded as the diameter of the fragment. Figure 3-15 shows a typical measurement of the diameter of a fragment where the diameter of the fragment is the mean of measurements D_1, D_2 and D_3.

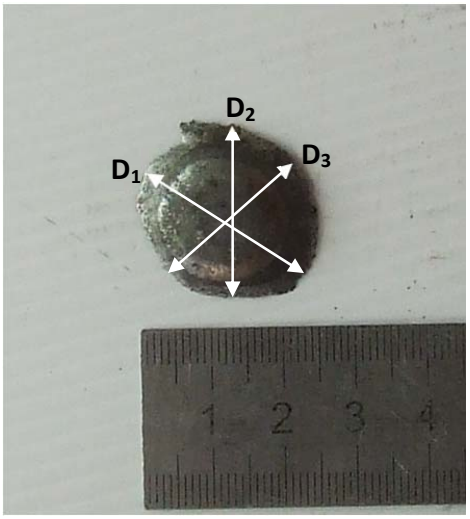

Figure 3-15: Typical measurement of the diameter of the a fragment (ruler shown, in mm, is for scale)

3.6.3. Measuring the mass of the fragment

The mass of the fragment in each test was required to compute the momentum and kinetic energy of the fragment. Following each test, if a fragment was recovered, without being wedged within an energy absorber or without being fused to any section of the rear plate, then it is weighed and its mass is noted. However, if the fragment cannot be weighed due to being fused to the rear plate, or when it is wedged tightly within an energy absorber, then the mass of the front plate is measured after the test and the difference between the original plate mass and the mass after the test is taken as mass of the fragment which got ejected the front plate, as described in Eq. 3-2. This is possible because each plate is weighed individually before the tests commence.

$$m_f = m_{fp0} - m_{fp1} \qquad \text{Eq. 3-2}$$

where : m_f= Fragment mass, m_{fp0}= Initial front plate mass, m_{fp1}= Final front plate mass

3.6.4. Rear plate maximum deflection

In all cases where the rear plate has some permenant deflection or by inelastic deflection with some minor tearing, the maximum deflection is measured. The term ‘midpoint deflection’ is not used because the measured deflection is not always observed at the centre of the exposed plate area. Measurements weres carried out mechanically by the use of a height gauge. An area on the plate just outside the area exposed to impact is used at a datum surface (representing zero deflection) where the height gauge is zeroed. The maximum height reading on a point on the exposed area of the plate is the noted as the ‘rear plate maximum deflection’.

3.6.5. Material loss from the energy absorber

When an energy absorber was inserted in front of the rear plate, material is lost in some form from the absorber, due to perforation of the energy absorber,. The material loss is calculated from the difference between the initial mass of an energy absorber and the final measured mass of an impacted absorber. It is *important* to note that the mass of each absorber had **not** been measured before impact, but the mass of one reference energy absorber (for each material) was used as the datum.. From Figure 3-16, the material loss can be represented as:

$$Material\ lost\ (\%) = \frac{m_{a0} - m_{a1}}{m_{a0}} \times 100 \qquad \text{Eq. 3-3}$$

Where: m_{a0} = mass of absorber before impact, m_{a1} = mass of absorber after impact

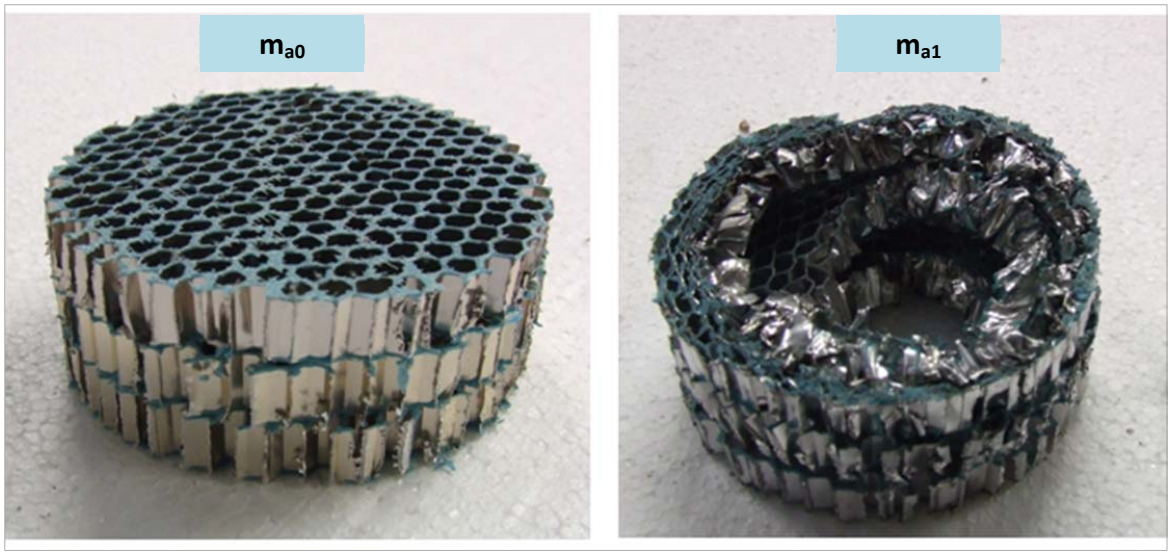

Figure 3-16: Typical initial and post-impact states of an aluminium honeycomb energy absorber

3.6.6. Notation used to describe the blast tests

Each test that was undertaken is represented by a specific test description which shows the material used as the energy absorber (if any), the thickness of the absorber, the charge diameter, charge mass and the order showing where the specific test is the first, the second, third etc. in the case of repeated tests.

Table 3.11: Notations used to describe the name of the energy absorber used for the various blast tests

Energy absorber	Abbreviated notation
No Absorber	NA
Aluminium foam	AL
Aluminium honeycomb	AH
Balsa wood	BA
Corecell M-80 foam	CM
Divinycell H200 foam	DV
Polyurethane 200 foam	PU

As shown in §3.5, and specifically in Table 3.9, polyurethane foam is also tested in three different arrangements of 40mm thickness to investigate the effects of varying the layering arrangements of an absorber on the plate damage. One 40mm thick disc, two 20mm thick discs and four discs of 10mm thickness are used. The special description of these thickness arrangements is **40S** and **40Q** for the **s**ingle and **q**uadruple layered polyurethane foam respectively. The double-layered polyurethane foam is not given any special description for the thickness value as it is the batch that is compared to the other materials, and thus is a datum.

Two examples of tests conducted and the interpretations of their respective descriptions are shown below:

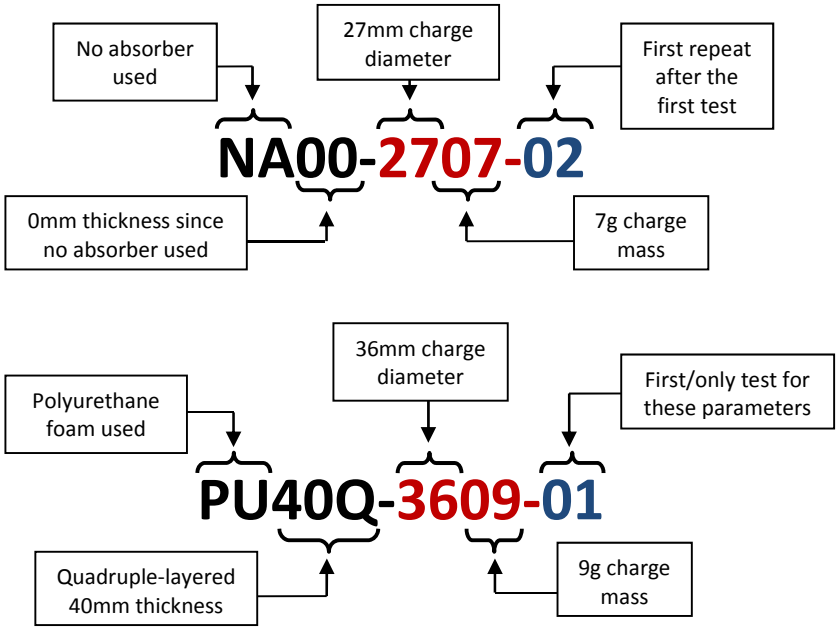

4. EXPERIMENTAL OBSERVATIONS AND RESULTS

From the blast tests a number of observations are made through simple visual means and through measurements. In this section, the results and observations made on the front plate, fragment, rear plate, and energy absorbers are discussed. A total of 107 blast tests were conducted in the study.

4.1. Front plate

The blast tests are conducted at three charge diameters; 27mm, 36mm and 43mm. For all three charge diameters, it is observed that the minimum charge mass at which a fragment can be released is 7g. The progressive increase in the charge mass from 7g to 11g is observed to cause a transition in failure of the front plate from a simple central hole with associated fragment fragment to a plate which shows petalling failure after the fragment has been discharged. At a charge mass of 11g (or 10g when charge diameter is 27mm), the front plate fails by petalling; the plate material wraps around the rear clamping plate, as shown in Figure 4-1, making it difficult to remove the test plate from the clamping plate. Tests are not undertaken at charge masses greater than 11g.

Figure 4-1: Front test rig, with test plate exposed to a blast from an 11g, 36mm charge; showing how the petalled test plate wraps around the rear clamping plate

The range of momentum and kinetic energy of the fragments are limited by the amount of mass of PE4. Figure 4-2 shows the evolution of the post-capping state of the front plate from the minimum charge mass to the maximum for fragments generated by a 27mm diameter charge.

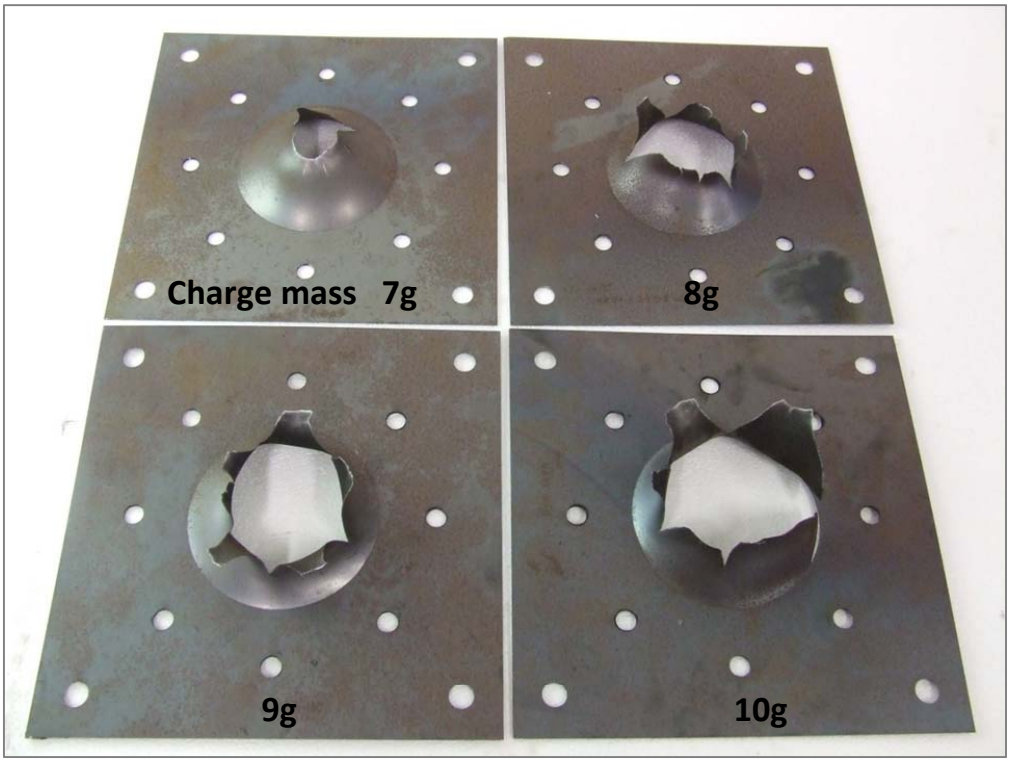

Figure 4-2: Photograph showing the failure of the front plates when charge mass increases for 27mm charge diameter (for tests NA00-2707-02, NA00-2708-01, NA00-2709-01 and NA00-2710-01)

The evolution of front plate failure for the charge diameters 36mm and 43mm are shown in Figure 4-3 and Figure 4-4. As the charge diameter is increased, the size of the opening in the front plate also increases. The failure evolution for plates subjected to charges of diameter 36mm and 43mm is observed to be similar to the failure observed for a charge diameter of 27mm.

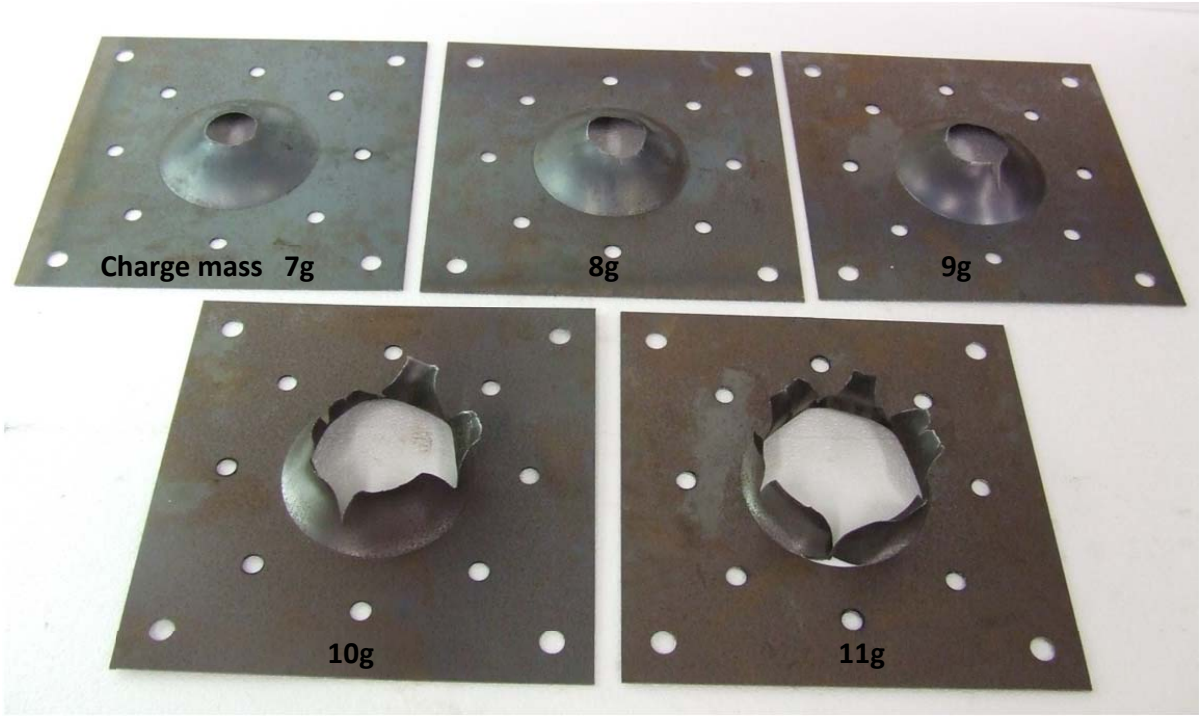

Figure 4-3: Photograph showing the failure of the front plates when charge mass increases for 36mm charge diameter (for tests NA00-3607-02, NA00-3608-01, NA00-3609-02, NA00-3610-01 and NA00-3611-01)

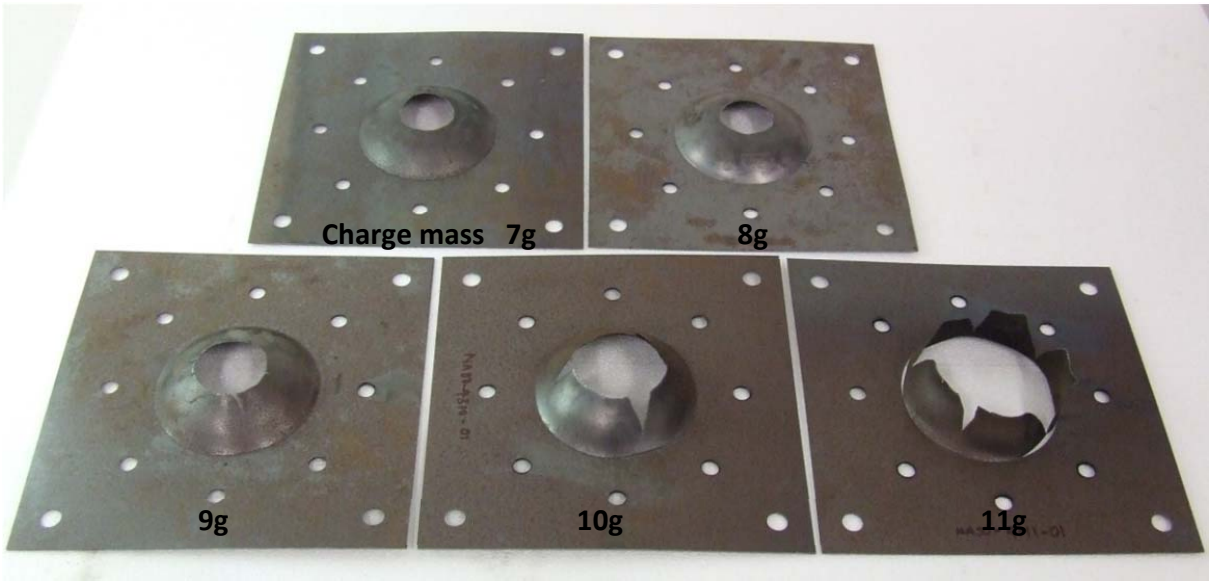

Figure 4-4: Photograph showing the failure of the front plates when charge mass increases for 43mm charge diameter (for tests NA00-4307-02, NA00-4308-01, NA00-4309-01, NA00-4310-01 and NA00-4311-01)

4.2. Fragment characteristics

The release of the fragment and its speed, mass, diameter and orientation of motion are independent of whether there are energy absorbers protecting the rear plate or not. Of all the test variables applied to this study, the **input** parameters governing the release of the fragment are the charge diameter and charge mass. Table 4.1 lists the average diameter and mass, minimum and maximum speeds of the fragments for charges of different diameters.

Table 4.1: Summarised details of the released fragments from the blast tests

Charge diameter (mm)	**27**	**36**	**43**
Average fragment diameter $\bar{d}_f$ (mm)	25.73	34.04	40.08
Average fragment mass $\bar{m}_f$ (g)	4.11	8.41	12.59
Minimum fragment speed $(v_f)_{min}$ (m/s)	322.6	312.5	243.9
Maximum fragment speed $(v_f)_{max}$ (m/s)	666.7	740.7	500.0

In the post-impact state, some of the fragments are observed to have an insignificant change of diameter with a slightly flattened face (*state A* in Figure 4-5). This occurs as a fragment impacts the rear plate with its face and rebounds from the plate or if it fails to perforate the energy absorber. In some cases, the skewed or spinning orientation of the fragment is such that it crumples after impact (State B). Fragments are also observed to be released from the front plate as multiple-piecefragments (State C). In rare conditions, the fragment gets fused to a section of the rear plate (State D) and in other cases it was observed that the fragment gets slightly shredded or bent outwards from the edge (State E). After each test, the fragment is hot when it is handled.

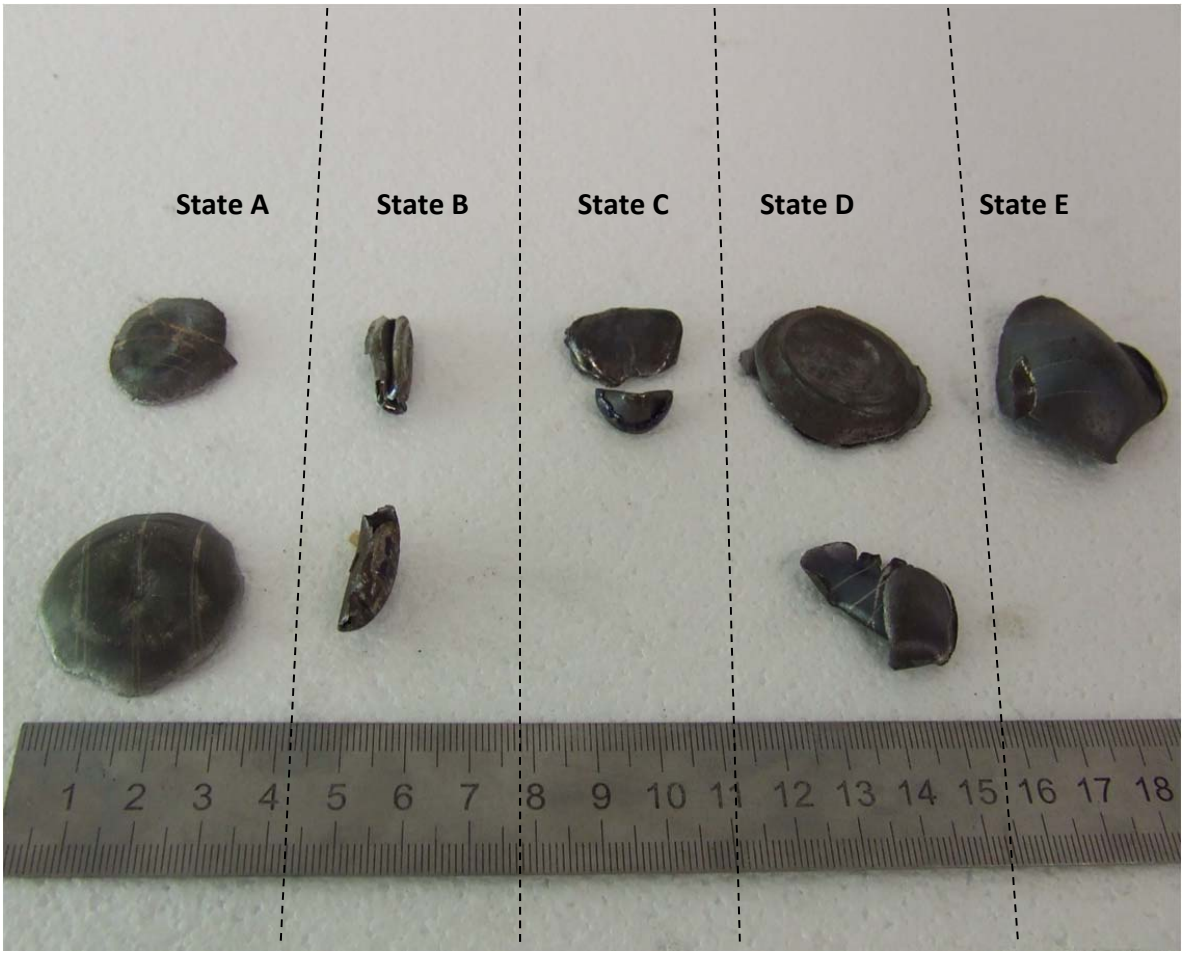

Figure 4-5: Various states of the fragments after impact with the rear plates (ruler, in mm, is added for scale)

4.3. General observations on rear plate failure

The rear plate is observed to fail in various ways, depending on the orientation of the fragment, the diameter and speed of the fragment, and the thickness and type of the energy absorber placed in front of the plate. It is important to note that the observations in this study are generalised to define the classes of the failure modes observed on the rear plate.

4.3.1. Inelastic deflection (Mode I)

This kind of failure is observed for impacts where the fragments have relatively low kinetic energy. In most cases, the deflection profile suggests that the fragment impacts the plate on its smooth rounded front rather than its edge. The plate deformation is characterised by a simple inelastic deflection and is characteristic of localised impulsive loading – inner dome superimposed on a global dome. The fragment does not always impact the middle of the exposed area of the rear plate and hence maximum deflection is not always observed at the centre of the plate. Figure 4-6 shows one of the plates which exhibited simple inelastic deflection after fragment impact.

Figure 4-6: Photograph of a rear plate which fails by simple inelastic deflection (Mode I) after fragment impact

4.3.2. Inelastic deformation with thinning around the centre (Mode Itc)

Thinning (similar to the failure mode reported by Nurick and Radford [19] as Mode Itc) is sometimes observed around the edge of the impact region, inaddition to the inelastic deflection of the plate. Two principal thinning patterns are observed in the impact plates; perimetral and chordal thinning.

4.3.2.1. Perimetral thinning

This type of failure is observed when the fragment kinetic energy is higher than the energy at which the rear plate fails by simple inelastic deflection. In addition to Mode I failure, thinning is observed in a perimetral region around the point of impact – as shown on the plate in Figure 4-7. As per Mode I failure, this failure mode suggests impact from the fragment on its face side rather than its edge. It is important to note that although in the literature [19] Mode II*c refers to *"inelastic deformation with partial thinning around the centre"*; in this study the term is not limited to the 'centre' because impacts can occur off-centre of the plate.

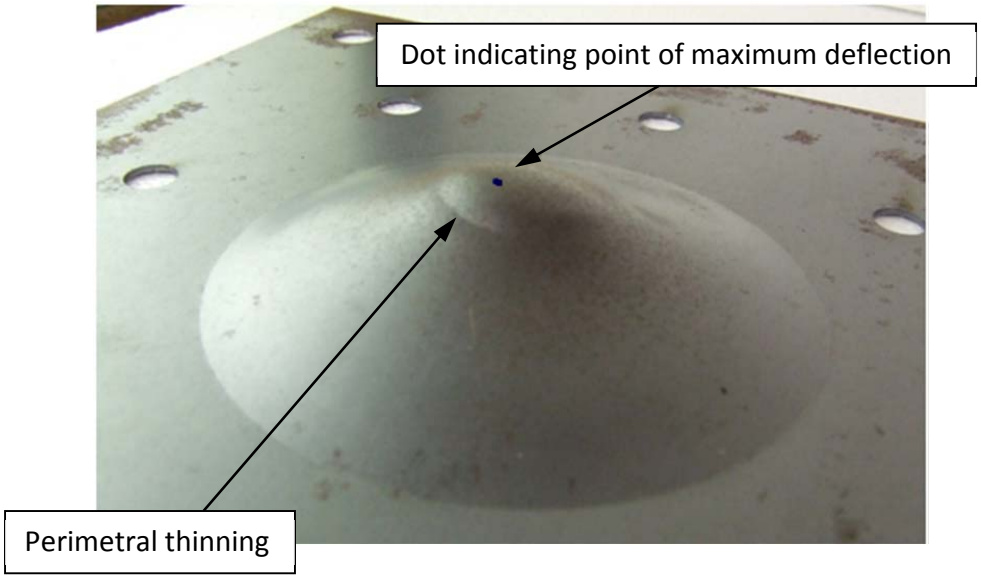

Figure 4-7: Photograph showing typical inelastic deflection with thinning around the impact region

4.3.2.2. Chordal thinning

The observed cases of perimetral thinning suggest face-impact of the fragment around the point of maximum deflection. However, thinning is also observed in an almost linear pattern, not surrounding the point of measured maximum deflection, but adjacent to the point, similarly to a chord through the centre of a circle – hence the suggested term 'chordal thinning'. This kind of thinning suggests that the impact from the fragment occurs in a slicing mode – in other words, the rear plate is impacted by the edge of the fragment instead of its face. The photograph shown in Figure 4-8 shows a plate where chordal thinning is observed.

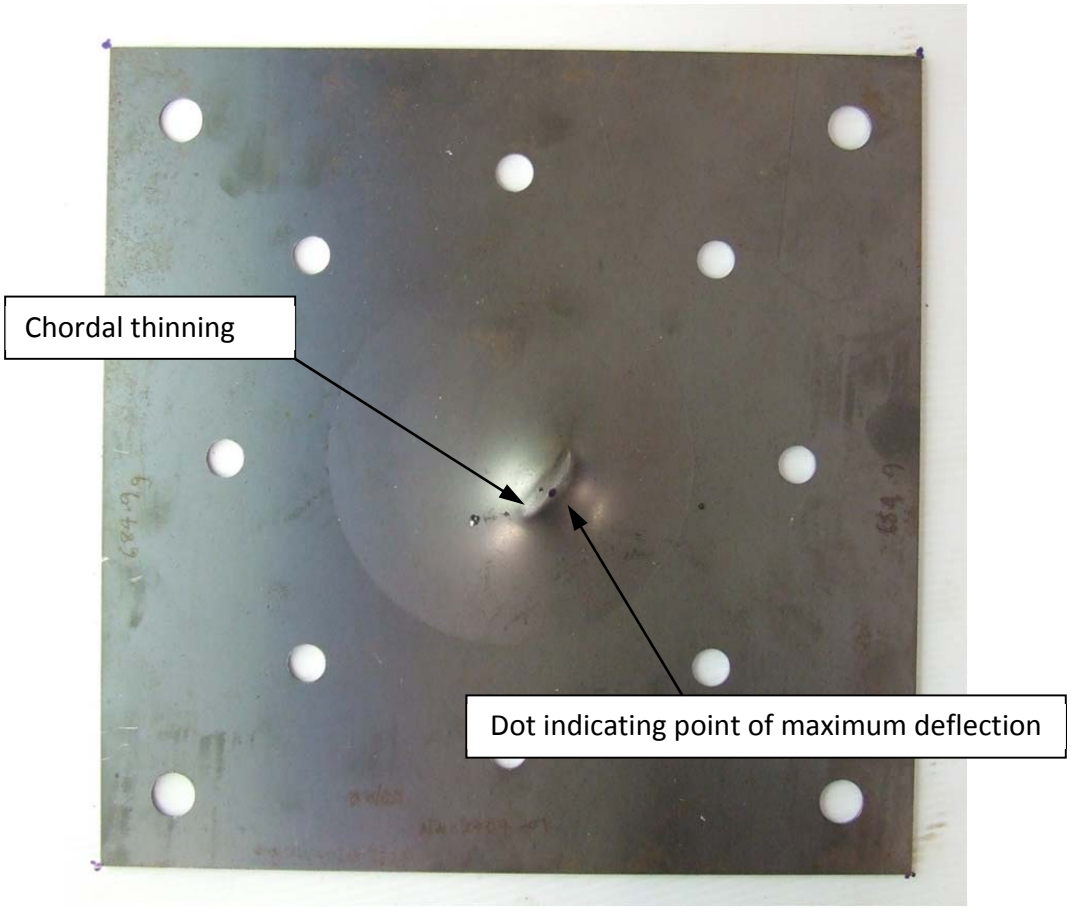

Figure 4-8: Photograph of a rear plate showing failure by inelastic deflection with chordal thinning

*4.3.3. Inelastic deflection with partial tearing (early Mode II*c)*

4.3.3.1. Perimetral small partial tearing

When the failure of the plate goes beyond thinning, partial tearing is observed, where a small perimetral section of the plate is observed to tear around the region where the fragment strikes the rear plate. In such a case of tearing, it is still possible to measure the maximum deflection of the plate as it is an early stage of Mode II*c.

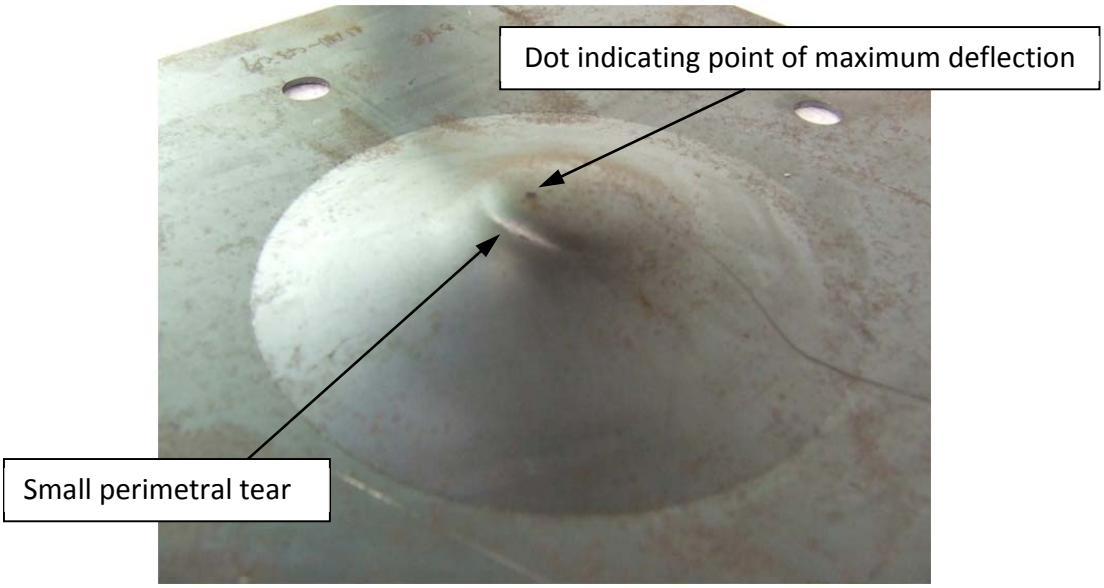

Figure 4-9: Photograph of a rear plate showing failure by inelastic deflection with perimetral partial tearing (charge diameter = 36mm)

4.3.3.2. Chordal small partial tearing

As discussed in the observations in §4.3.1.2., it is also noted that impact occurs by slicing from the edge of the fragment. Beyond chordal thinning, the rear plates are observed to fail by chordal tearing under slicing impact of the fragment. In certain cases, due to the adjacent occurrence of chordal tearing, it is possible to measure maximum deflection. Figure 4-10 shows two of the rear plates in which chordal partial tearing was observed and maximum deflection could be measured. In Figure 4-11, a case where the fragment impact occurs at a rear plate eccentricity and the manner of chordal tearing makes it impossible to measure the maximum deflection.

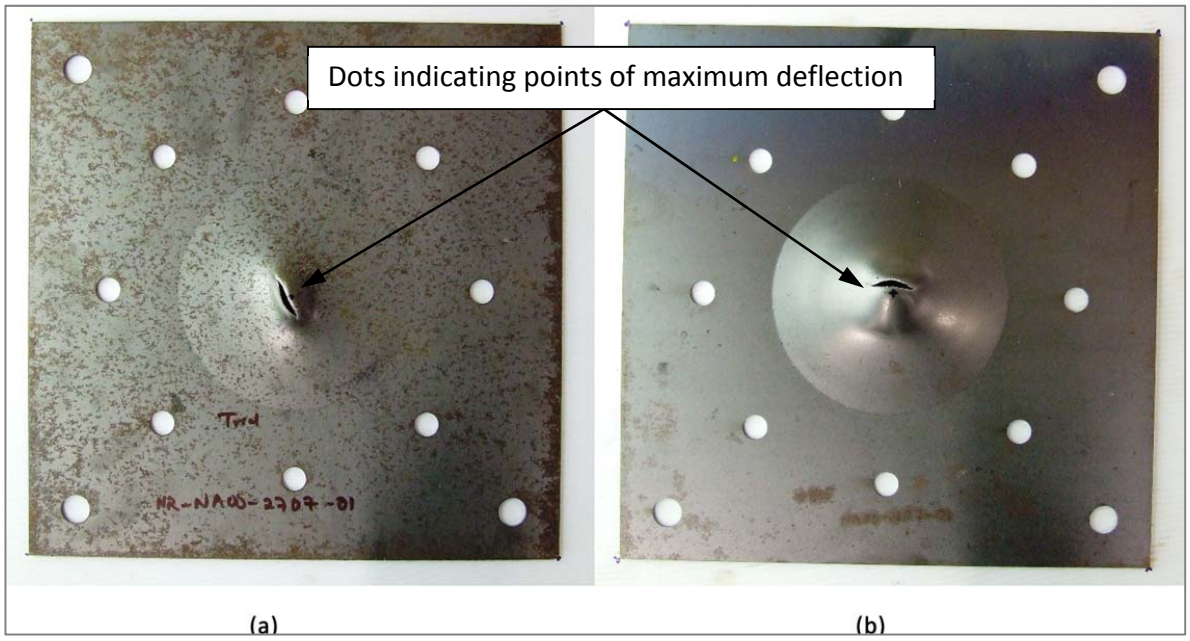

Figure 4-10: Photograph of inelastic deflection with chordal small partial tearing observed on rear plates, (a) when subjected to 27mm diameter charge, and (b), charge diameter is 36mm

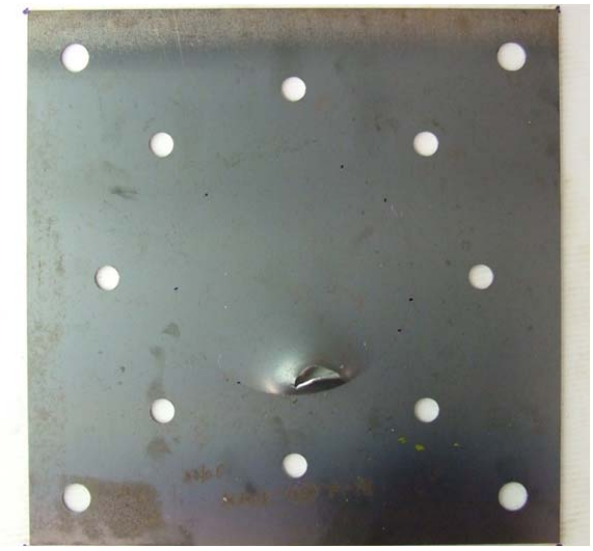

Figure 4-11: Photograph of rear plate showing eccentric chordal partial tearing with little inelastic deflection. The maximum deflection cannot be defined in such a case (charge diameter = 43mm)

*4.3.4. Inelastic deflection with large partial tearing (advanced Mode II*c)*

At the different charge diameters (27mm, 36mm and 43mm) and in some of the energy absorbers (40mm thick balsa wood, Corecell foam and Divinycell foam), as the mass of PE4 is increased, observations change from partial tearing to a large section of the area around the point of impact observed to have been torn – still a case of Mode II*c but at an advanced state – as observed for a charge mass exceeding 7g for 27mm charge diameter (with no energy absorbers). In most cases where this failure mode is observed, the fragment will have perforated the plate instead of rebounding. Large tearing of the back plate is not only observed along with fragment perforation, but in rare cases it is also observed along with the fragment fusing to the section of the plate which is largely torn. A typical observed large partial tearing of the rear plate because of perforation and large tearing occurring along with fragment fusion are shown in Figure 4-12 (a and b respectively). The observed large tearing on the rear plate is an undesirable aftermath of the impact since it means that, unless the fragment remains fused to the plate, perforation by the fragment occurred.

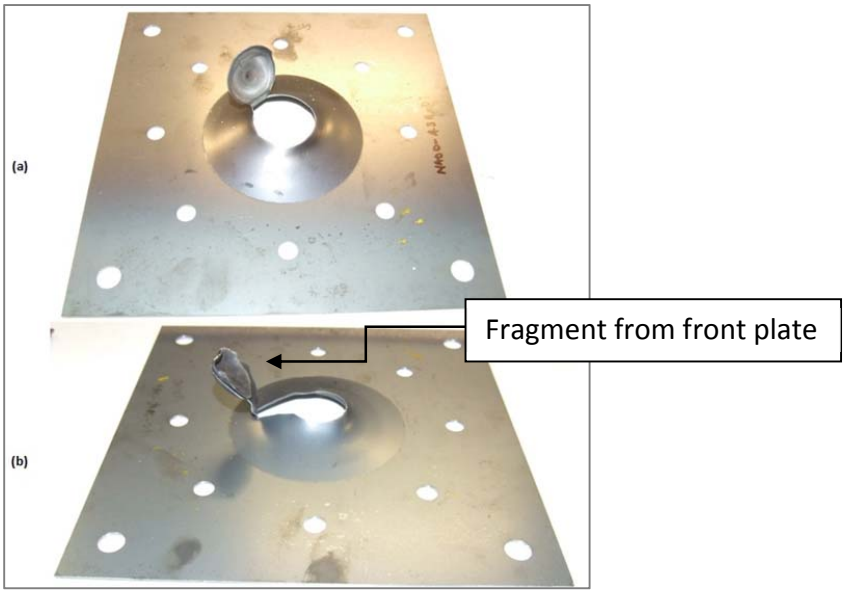

Figure 4-12: Photograph of large tearing of the rear plate (a) because of fragment perforation and (b) because of fusion of fragment onto the rear plate

4.3.5. Inelastic deflection with full tearing of central region (Mode IIc)

In certain cases of the largest charge masses tested (10g for 27mm diameter charge and 11g for 36mm diameter charge), the rear plate is observed to exhibit large permanent deflection with subsequent capping (full tearing). In cases where this phenomenon is observed, it is accompanied either by separate post impact motions of the fragment from the front plate and a torn fragment from the rear plate **or** by fusion of the fragment from the front plate with the fragment from the rear plate – henceforth referred to as the *secondary cap*. In essence, in such cases, a fragment that is capped from the front plate results in secondary capping on the rear plate. Two plates, on which the complete tearing occured, are shown in Figure 4-13. It is also important to note that the term Mode IIc, as used to define the failure of the rear plate, does not constrain the failure to the centre, as reported in literature. As it can be observed in Figure 4-13a, the secondary capping phenomenon occurs slightly off-centre.

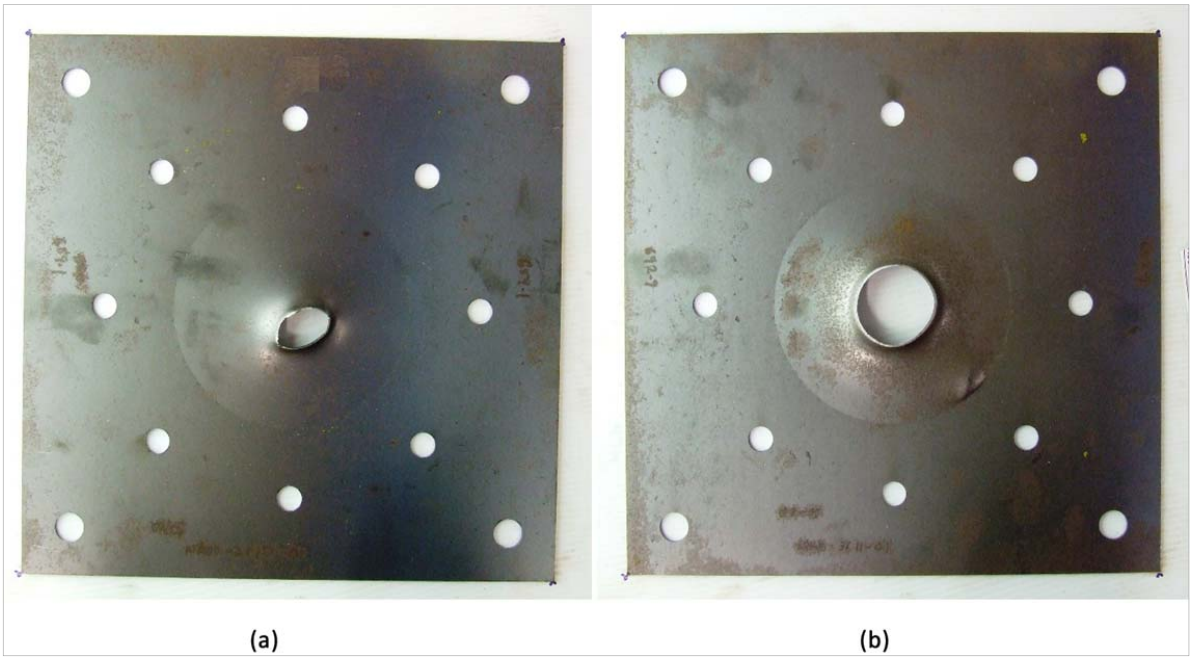

Figure 4-13: Photograph of rear plates which have undergone secondary capping failure

4.4. Tests with no energy absorbers protecting the rear plate

When no energy absorbers are used to protect the rear plate, it is noted that in most of the cases, small or large partial tearing is observed on the rear plate. A summary of all the results for the series of tests carried out with no energy absorber is listed in Table 4.2. For 36mm charge diameter, all plates show some level of tearing. In some cases, the tearing is minimal and the deflection can be measured. For large partial tearing or full rear plate tearing, the deflection is not measured.

The charge mass required for tearing the rear plate is not always at the highest end of the charge mass range. This could be possibly attributed to inconsistent material properties of mild steel and due to the fact that the fragment does not always fly towards the rear plate in translation, but with spinning in some cases. For charge diameters of 27mm and 36mm, full tearing is observed on the rear plate at the charge masses of 10g and 11g respectively, with the fragment remaining fused to the section of the rear plate which is fully torn. The observation of

fusion of the fragment to the rear plate is reminiscent of the observations by Nurick and Bryant [39] on square tubes subjected to localised loading at capping on one of the faces. The phenomenon of the fragment fully tearing a section of the rear plate can be referred to as ‘secondary capping’ since ‘primary’ capping occurs on the front plate due to the localised blast. For a charge diameter of 43mm, large tearing occurred for charge masses exceeding 9g.

Table 4.2: Summary of results for tests in which no energy absorbers are used

	Test Description	Impulse (Ns)	Fragment speed (m/s)	Fragment momentum (Ns)	Fragment kinetic energy (J)	Rear plate deflection (mm)
27mm charge diameter	NA00-2707-T1	15.7	444.4	1.9	414.8	12.31
	NA00-2707-01	14.4	370.4	1.4	267.5	8.67
	NA00-2707-02	14.4	434.8	1.7	378.1	10.28
	NA00-2707-03	13.9	476.2	1.8	419.5	Partial tear*
	NA00-2707-04	15.4	322.6	1.0	169.1	7.45
	NA00-2708-01	15.5	625.0	2.8	878.9	Large tear
	NA00-2708-02	16.4	666.7	2.5	844.4	Large tear
	NA00-2709-01	16.0	666.7	2.5	844.4	Large tear
	NA00-2710-01	17.4	588.2	2.5	726.6	Secondary cap
36mm charge diameter	NA00-3607-01	13.9	400.0	3.2	637.6	15.7
	NA00-3607-02	14.7	322.6	2.7	430.3	10.38
	NA00-3608-T1	16.0	465.1	3.8	887.0	Large tear
	NA00-3608-01	15.3	434.8	3.8	820.4	19.24
	NA00-3609-01	16.7	N/A	N/A	N/A	Large tear
	NA00-3609-02	17.7	476.2	4.3	1020.4	Large tear
	NA00-3609-03	18.9	408.2	3.3	676.4	14.52
	NA00-3610-01	19.8	555.6	4.1	1125.5	Large tear
	NA00-3611-01	19.6	645.2	4.8	1560.9	Secondary cap
	NA00-3611-02	22.0	526.3	4.8	1260.4	Large tear
43mm charge diameter	NA00-4307-01	13.9	N/A	N/A	N/A	No impact
	NA00-4307-02	14.0	243.9	2.9	356.9	Partial tear*
	NA00-4308-01	16.9	322.6	3.8	619.1	10.61
	NA00-4308-02	16.8	281.7	3.7	521.7	5.73
	NA00-4309-01	18.0	377.4	4.8	904.2	16.45
	NA00-4310-01	19.5	476.2	6.0	1428.6	Large tear
	NA00-4311-01	21.9	500.0	6.5	1612.5	Large tear

* These partial tears are not accompanied by noticeable inelastic deflection as they occur when the fragment slices the rear plate at an near the boundary of the exposed area and simply induces a localised opening on the plate

4.5. Tests with the rear plates protected by energy absorbers

The energy absorbing materials are placed in front of the rear plate to mitigate the damage from the blast-induced fragment. The manner in which the various materials fail under impact is observed to vary. It is generally noticed that after the fragment penetrates or perforates the absorber, the mass of the material decreases, suggesting that there is a loss of material in some form. For all the energy absorbers, there is no apparent relationship between the size of the opening on the impact/entry face of the absorber and the charge mass used to eject the fragment. The opening size on the entry face appears to depend solely on the *normal projected* area of the fragment as it strikes the absorber; traces of soot from the blast are observed on the entry face and tunnel bored by the penetrating fragment. The exit opening is generally observed to be larger than the entry opening and increases with increasing charge mass – which generally is also increasing fragment speed.

4.5.1. Tests with 40mm thick energy absorbers protecting the rear plate

In the first series of tests where rear plates are protected by 40mm thick absorbers against fragment impact, charges of 36mm diameter are used at increasing charge masses to eject fragments. The resulting impact response of the energy absorbers and the mass fraction of the absorber material which is lost due to impact are observed.

4.5.1.1. Aluminium foam

When the aluminium foam is subjected to impact by the fragments, it is observed that a compressed plug in the path of the fragment's motion is sheared from the foam disc. The exit opening of the absorber material is observed to get wider as the kinetic energy of the fragment is increased. A post-impact photograph of typical failure and perforation of 40mm thick aluminium foam is shown Figure 4-14 – the sheared and compressed plug can be observed next to the fragment. Previous investigations on impact of aluminium foam structures do not mention plugging failure. However this is the plugging failure mode discussed for intermediately thick plates under projectile impact by Zukas [63].

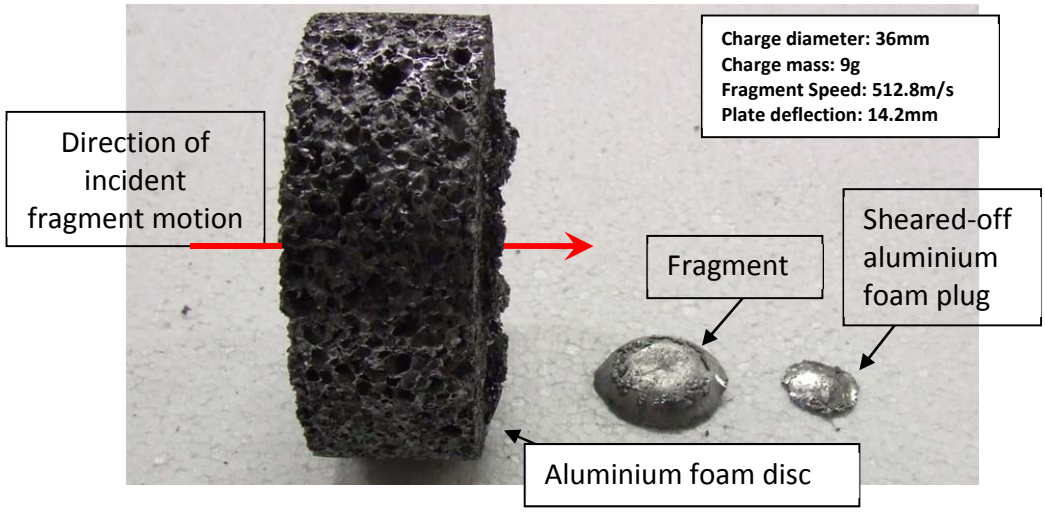

Figure 4-14: Post impact for of aluminium foam under impact from a fragment released from the front plate by a 36mm diameter charge (showing sheared-off foam plug)

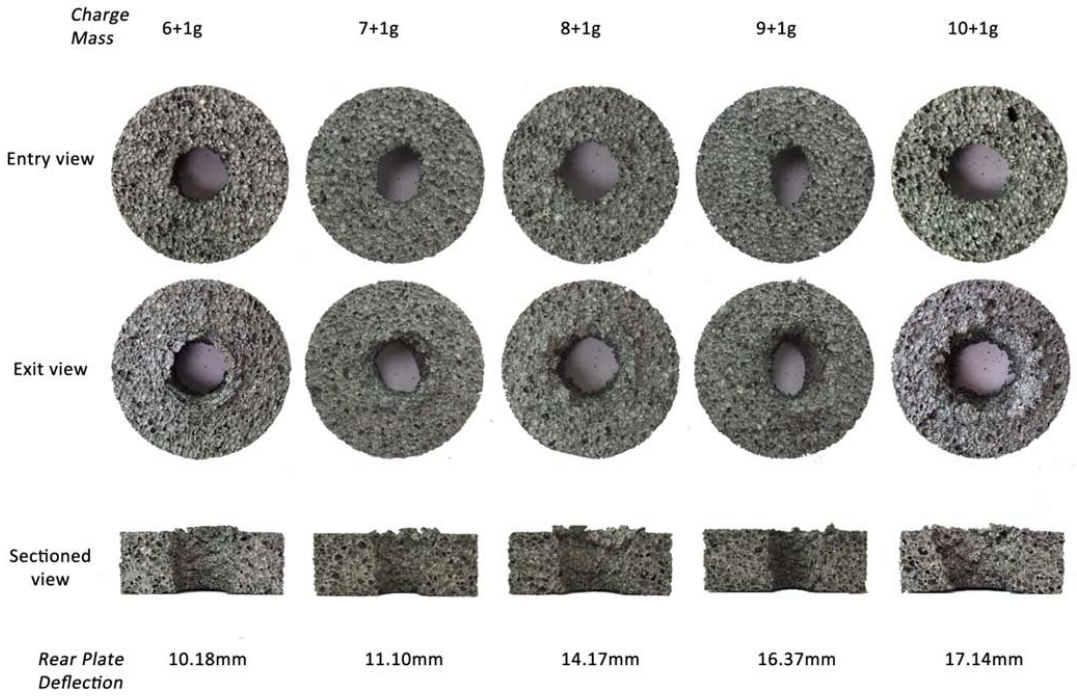

Figure 4-15: Entry, Exit and Sectioned views of 40mm thick aluminium foam subjected to increasing charge masses at 36mm charge diameter

For the 40mm thick aluminium foam, Figure 4-15 shows the entry, exit and sectioned views for fragment impacts corresponding to increasing charge masses. A summary of the results for the tests conducted on the aluminium foam is listed in Table 4.3. For the absorber subjected to impact by a fragment released by a 10g (9+1g) charge, the small material loss (0.4%) may be

attributed to the smaller entry and exit opening because of a slightly skew fragment impact which can be observed in Figure 4-15. For all the aluminium foam energy absorbers tested, the mean material loss was 5.7%.

Table 4.3: Summary of results for tests conducted with aluminium foam energy absorbers of 40mm thickness

Test Description	Impulse (Ns)	Fragment speed (m/s)	Fragment momentum (Ns)	Fragment kinetic energy (J)	Rear plate deflection (mm)	Material Lost From Absorber (%)
AL40-3607-01	13.6	392.2	3.3	645.9	10.18	4.3
AL40-3608-01	15.1	434.8	3.5	765.6	11.11	5.1
AL40-3609-01	16.6	512.8	4.4	1117.7	14.17	12.6
AL40-3610-01	18.9	606.1	5.0	1506.0	16.37	0.4
AL40-3611-01	21.7	666.7	5.9	1955.6	17.14	6.3

4.5.1.2. Aluminium honeycomb

The thickness of aluminium honeycomb energy absorbers is approximately 40mm as each is formed by stacking three layers of honeycomb of approximately 13mm thickness. After fragment impact, it is observed that the opening in each of the three layers gets wider from the front layer to the rear. The aluminium honeycomb is also observed to bend as it fails. With an increasing charge mass, the honeycomb has an increasing level of bending, particular on the layer of honeycomb through which the fragment exits. A post-impact photograph of 40mm thick aluminium honeycomb is shown in Figure 4-16 with details of the test also indicated. Remnants of the lost honeycomb material were not recoverable after impact.

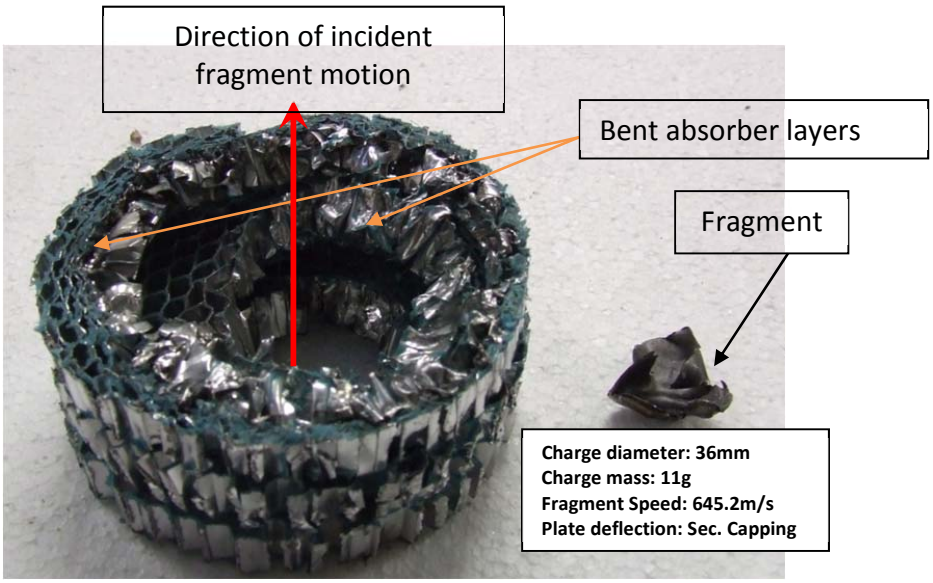

Figure 4-16: Post impact state of aluminium honeycomb showing bending of the absorber layers and increasing opening from entry side to exit side

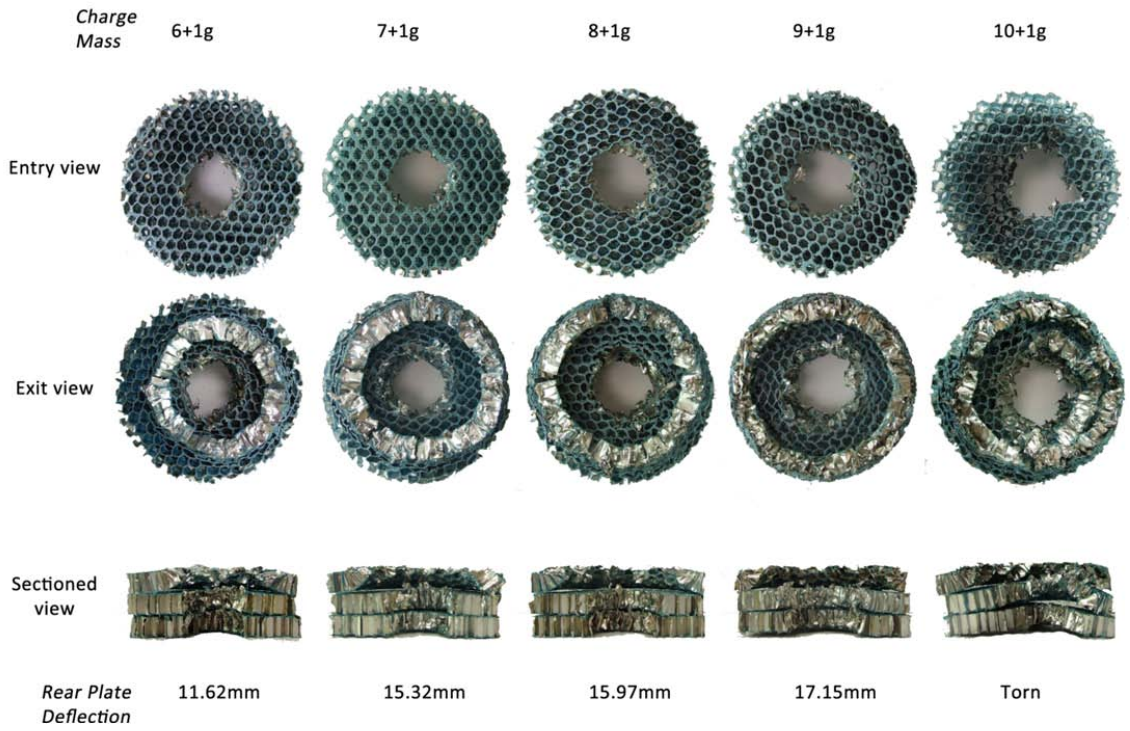

Figure 4-17: Entry, Exit and Sectioned views of 40mm thick aluminium honeycomb subjected to increasing charge masses at 36mm charge diameter

Figure 4-17 shows the impacted aluminium honeycomb energy absorbers; entry, exit and sectioned views. As it can be noted, the aluminium honeycomb which is subjected to the largest charge mass undergoes extensive bending and the greatest material loss (9.4%). The mean material loss was found to be 7.5%. The bending and the material loss in the honeycomb are not reported in previous studies as honeycomb cores under localised impact are usually prevented from bending by the bend-resistant face sheets, as in the case of the impact investigation on honeycomb sandwich panels by Fatt and Park [100]. The results of the tests conducted on the aluminium honeycomb are summarised in Table 4.4. As charge mass increases, there appears to be a general increase in the fraction of the absorber material lost, particularly in the exit layer.

Table 4.4: Summary of results for tests conducted with aluminium honeycomb energy absorbers of 40mm thickness

Test Description	Impulse (Ns)	Fragment speed (m/s)	Fragment momentum (Ns)	Fragment kinetic energy (J)	Rear plate deflection (mm)	Material Lost From Absorber (%)
AH40-3607-01	13.9	370.4	2.9	541.8	11.62	7.0
AH40-367.5-01	15.1	370.4	2.9	530.2	13.11	4.8
AH40-3608-01	15.7	512.8	4.2	1078.2	15.32	7.5
AH40-3609-01	15.5	526.3	4.5	1191.1	15.97	7.8
AH40-3610-01	20.5	571.4	4.6	1306.1	17.42	8.7
AH40-3611-01	20.9	645.2	5.1	1644.1	Secondary cap	9.4

4.5.1.3. Balsa wood

Balsa wood energy absorbers are cut from sheets of wood which are 1000mm long, having a nominal thickness of 20mm and width ranging from 100mm and 105mm depending on the sheet. After impact, small pieces of wood from the part of the energy absorber in the path of the fragment are observed within the containment tube. As charge mass increases, in addition to complete perforation of the absorber material, it is noted that there was cracking and loss of wood material along the grain on the rear face of the energy absorber, as shown in Figure 4-18 where the fragment was ejected by 11g PE4 of diameter 36mm. The wood material is lost in small chunks which are not compressed. The entry opening is generally smaller than the exit opening in all cases. The entry, exit and sectioned views of balsa wood after impact are shown in Figure 4-19.

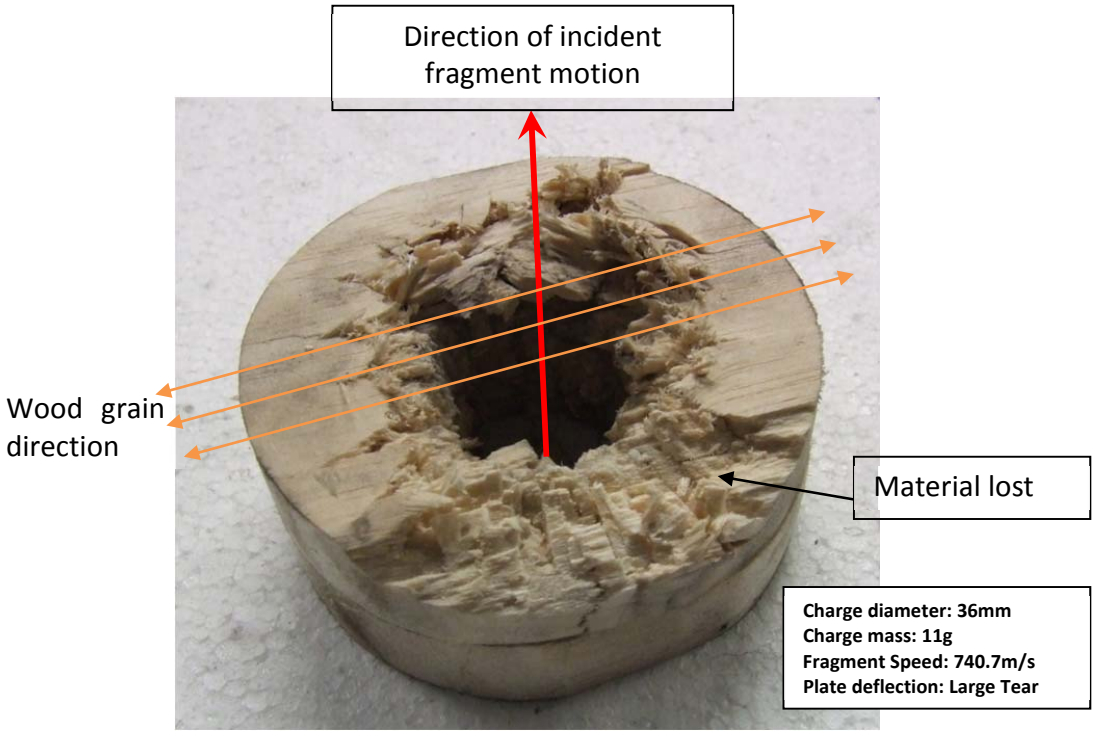

Figure 4-18: Post-impact state of 40mm thick balsa wood, showing material loss along the wood grain on the exit surface

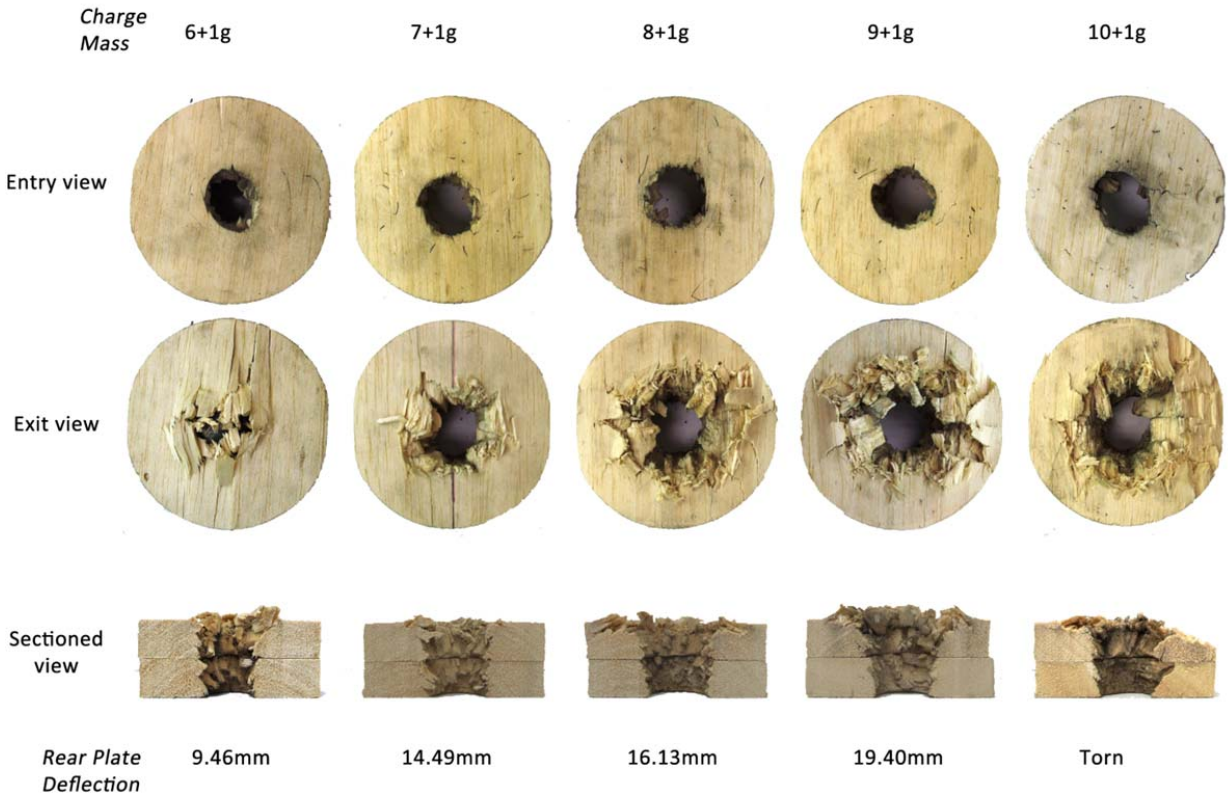

Figure 4-19: Entry, Exit and Sectioned views of 40mm thick balsa wood subjected to charges of 36mm diameter

Cracking along the wood grain on the exit face is observed at 7g charge mass, where the fragment is at the onset of perforation (ballistic limit). Perforation of the wood occurs at all larger charge masses. Extensive loss of the wood was also observed, at larger charge masses, on the disc of wood that is closest to the rear plate. A summary of the results for the 40mm thick balsa wood is shown in Table 4.5. It can be noticed that Balsa wood undergoes material loss of up to 30.2% at a charge mass of 10g, with a mean material loss of 17.6% across all the balsa wood tested.

Table 4.5: Summary of results for tests conducted with balsa wood energy absorbers of 40mm thickness

Test Description	Impulse (Ns)	Fragment speed (m/s)	Fragment momentum (Ns)	Fragment kinetic energy (J)	Rear plate deflection (mm)	Material Lost From Absorber (%)
BA40-3607-01	13.3	363.6	2.7	489.3	9.46	19.9
BA40-367.5-01	15.0	444.4	3.7	811.9	13.66	8.8
BA40-3608-01	15.1	512.8	4.1	1038.8	14.49	4.3
BA40-3609-01	17.7	512.8	4.3	1091.4	16.13	27.3
BA40-3610-01	18.2	N/A*	N/A*	N/A*	18.49	30.2
BA40-3610-02	19.3	689.7	5.8	1997.6	19.40	17.9
BA40-3610.5-01	20.2	588.2	5.2	1522.5	Large Tearing	10.9
BA40-3610.5-02	20.6	571.4	5.3	1523.3	Large Tearing	13.9
BA40-3611-01	21.6	740.7	2.7	2332.0	Large Tearing	25.4

*A temporary malfunction of the speed trap circuit was the reason that speed of the fragment could not be measured

4.5.1.4. Corecell foam

Corecell foam is observed to lose some of its material during fragment perforation with some of the remnants being recoverable. Like other energy absorbers, traces of soot from the blast are observed on the foam. **Unlike other** energy absorbers tested, after perforation by the fragment, sections of the Corecell foam tunnel through the foam and on the exit face of the absorber become hardened in touch and darkened with noticeable discolouration in Figure 4-20. This suggests that in addition to soot deposited by the blast, there is possible **scorching** of the energy absorber by the hot fragment

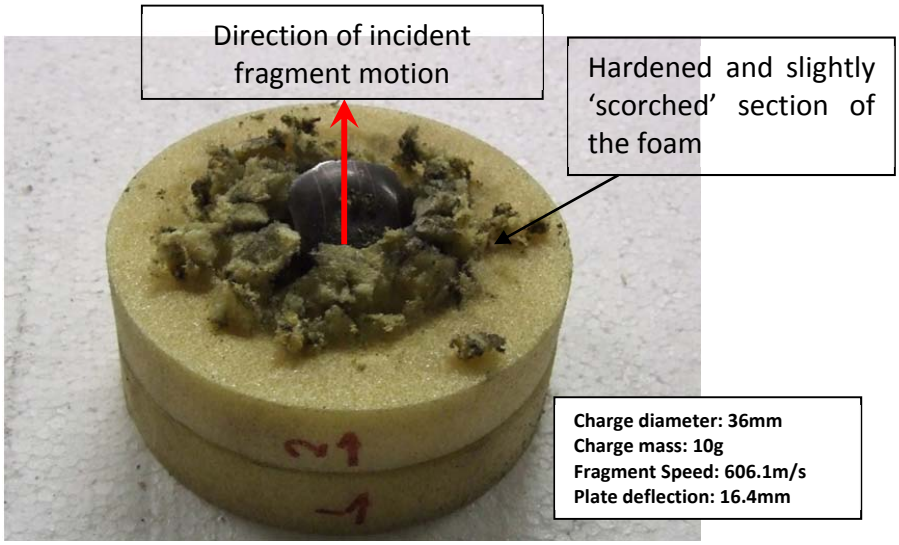

Figure 4-20: Corecell foam of 40mm thickness after impact - showing darkening of foam material in the fragment's path

As observed in all the other energy absorbing materials, the entry opening size remains constant at increasing charge masses. However, on the exit face, damage, change of form and texture of the foam are more pronounced and the exit opening widens as the charge mass, and consequently the fragment speed, increases. Entry, exit and sectioned views of Corecell foam after impact are shown in Figure 4-21.

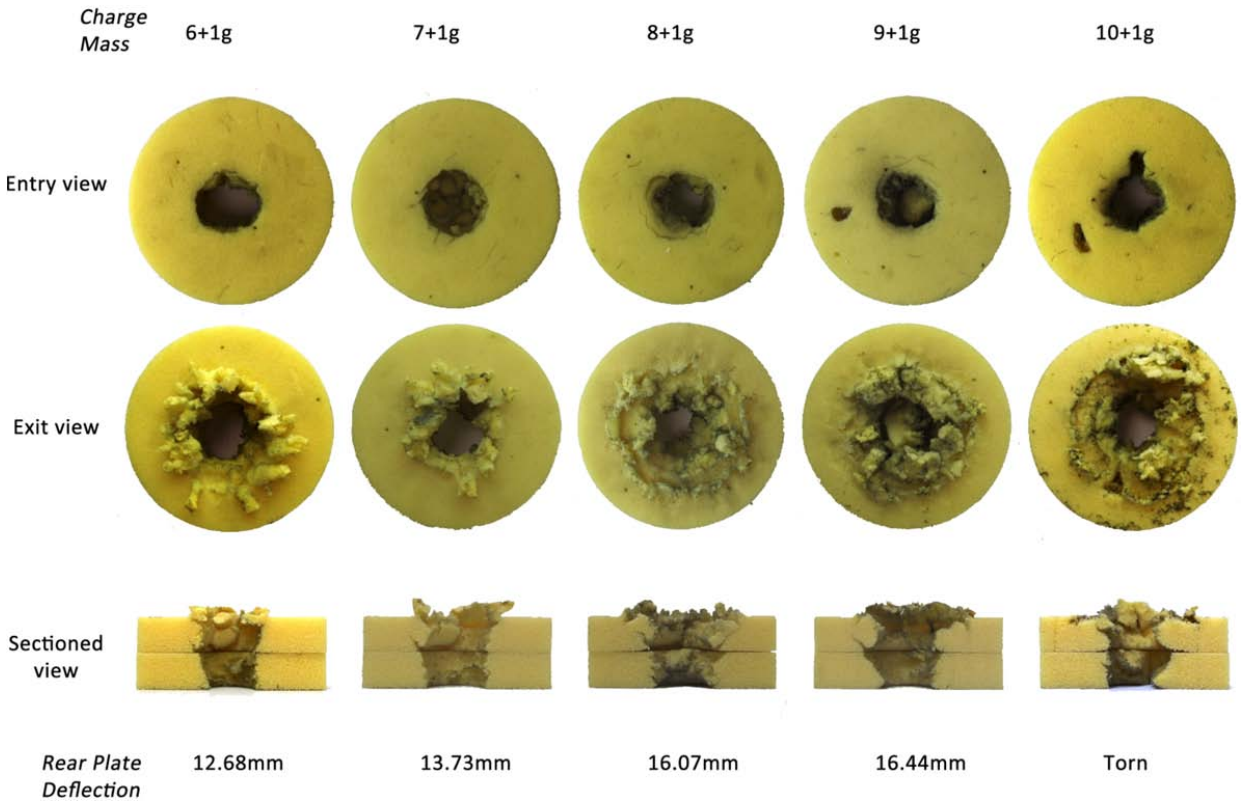

Figure 4-21: Entry, Exit and Sectioned views of 40mm thick Corecell foam subjected to increasing charge masses at 36mm charge diameter

For charge masses greater than 7g, an increase in the exit face deformation and scorch marks caused by either the increasing incident fragment speed and rebound speed (from the rear plate) or the interaction of the hot fragment with the exit face is observed, as shown in Figure 4-21. Not all the Corecell foam absorbers which were tested are included in Figure 4-21 since there are repeat tests for the charge mass of 8g. The results of all the tests on Corecell foam are summarised in Table 4.6. There is generally low to moderate material loss (3.7% - 13.8% with a mean material loss of 7.8%) after impact, and the highest material loss is observed in the impact corresponding to the largest charge mass (11g).

Table 4.6: Summary of results for tests conducted with Corecell foam energy absorbers of 40mm thickness

Test Description	Impulse (Ns)	Fragment speed (m/s)	Fragment momentum (Ns)	Fragment kinetic energy (J)	Rear plate deflection (mm)	Material Lost From Absorber (%)
CM40-3607-01	N/A	400	3.1	624.0	12.68	7.7
CM40-3608-01	14.4	476.2	4.2	997.7	17.93	5.8
CM40-3608-02	15.8	487.8	4.2	1035.1	15.95	3.7
CM40-3608-03	16.4	506.3	4.3	1097.3	Large Tearing	8.9
CM40-3608-04	16.0	408.2	3.4	687.2	13.73	5.6
CM40-3609-01	18.1	540.5	4.1	1110.3	16.07	11.1
CM40-3610-01	19.5	606.1	4.4	1322.3	16.44	6.0
CM40-3611-01	21.4	666.7	6.7	2222.2	Large tearing	13.8

4.5.1.5. Divinycell foam

Divinycell foam, which is made from PVC, shows more resistance to fragment motion in both incident penetration and rebound from the plate. In a number of cases, as the energy absorber is removed from the containment tube after impact, it is noted that the fragment is mildly or tightly wedged within the material. An example of one of the Divinycell foam energy absorbers with a wedged fragment is shown in Figure 4-22. Slight darkening due to the blast soot is also observed on the entry face of the absorber and through some portion of the tunnel formed by the fragment.

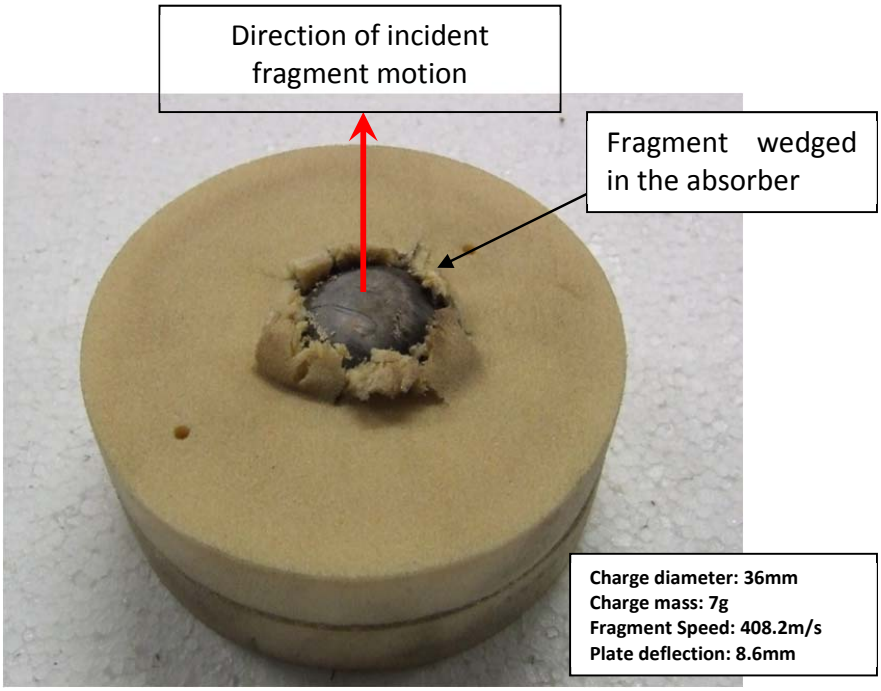

Figure 4-22: Photograph of a post impact state of 40mm thick Divinycell foam, showing the fragment wedged in

On the entry face of the absorber, there is observed cracking and subsequent fracture in a perimetral pattern around the tunnel formed by the fragment. This is noticeable in Figure 4-23 where a shear crack is propagated through the thickness of the disc, i.e. conical plug failure. The fracture prevalence and propagation is also observable (even though to a lesser extent) at the second of the two stacked 20mm thick absorber discs. This observation is similar to the core cross-cracking observed by Kepler [118] in sandwich panels with Divinycell H80 foam cores subjected to impact by an indenter. Figure 4-24 shows the entry, exit and sectioned views of the 40mm thick Divinycell foam under impact for increasing charge masses.

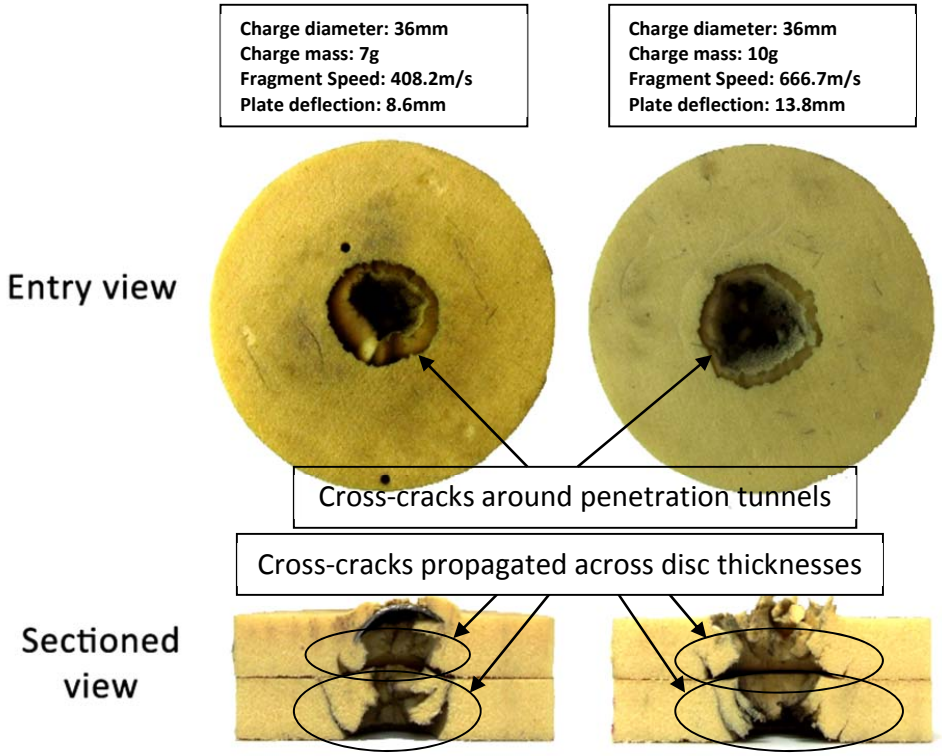

Figure 4-23 : Entry and Sectioned views of 40mm thick Divinycell foam, showing cross-cracks propagated through the thickness of the each foam disc

It is also observed that there is considerable hardening of Divinycell foam after impact in and around the region in which impact occurrs, with a particular prevalence near the exit face of the absorber. This could be a result of densification of the foam material due to the perforation and subsequent outward compression of the walls as the fragment penetrates. The results listed in Table 4.7, where the foam shows little material loss after impact (ranging between 2.1% and 9% with the mean material loss being 4.5%), are for Divinycell foam.

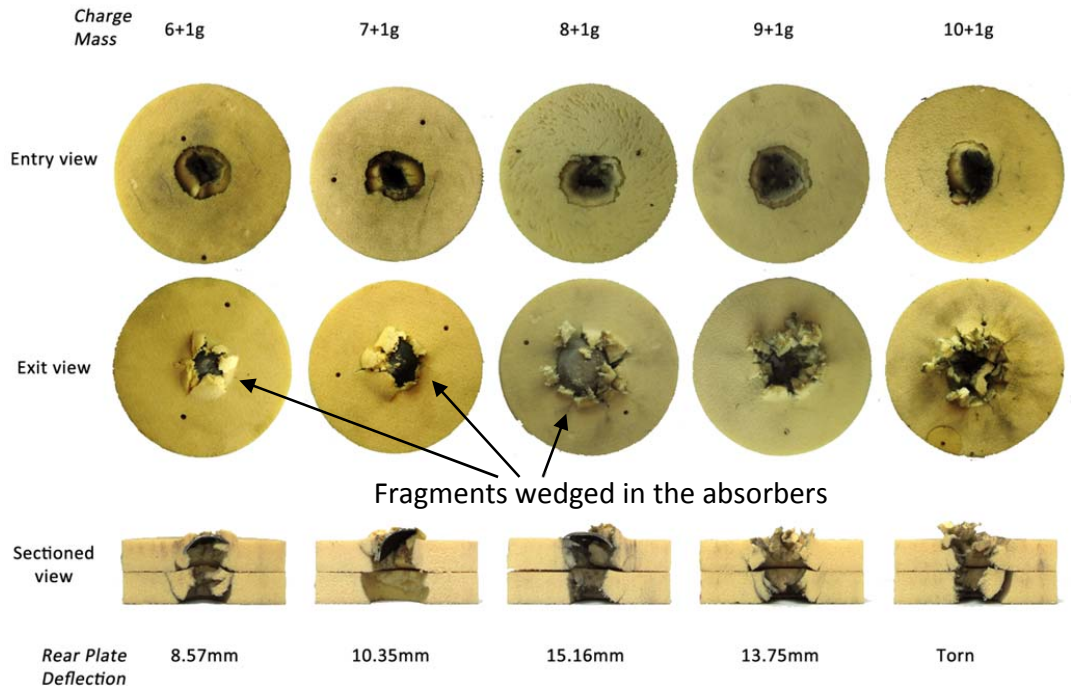

Figure 4-24: Entry, Exit and Sectioned views of 40mm thick Divinycell foam subjected to increasing charge masses at 36mm charge diameter

Table 4.7: Summary of results for tests conducted with Divinycell foam energy absorbers of 40mm thickness

Test Description	Impulse (Ns)	Fragment speed (m/s)	Fragment momentum (Ns)	Fragment kinetic energy (J)	Rear plate deflection (mm)	Material Lost From Absorber (%)
DV40-3607-01	13.6	408.2	3.1	641.4	8.57	2.5
DV40-3608-01	15.6	571.4	4.6	1322.4	13.77	3.7
DV40-3608-02	16.7	370.4	3.3	610.4	10.35	2.1
DV40-368.5-01	16.4	476.2	4.1	968.3	12.75	3.1
DV40-3609-01	16.5	540.5	4.9	1329.4	15.16	5.3
DV40-3610-01	19.4	645.2	6.1	1956.3	16.53	7.0
DV40-3610-02	18.5	666.7	5.7	1911.1	13.75	2.9
DV40-3611-01	21.2	714.3	6.1	2168.4	Large Tearing	9.0

4.5.1.6. Polyurethane foam

As observed in the other polymeric foams and balsa wood, the rigid polyurethane foam shows traces of soot from the blast as witnessed on the entry face of the absorber. Under impact, the foam material crushes and turns to powder as shown in Figure 4-25. The phenomenon is reminiscent of observations made by Zaretsky [96] on flexible polyurethane foam subjected to projectile impact.

In contrast to Divinycell foam which tends to render the fragment wedged during incident or residual motion, polyurethane foam provides limited restraint on the motion of the fragment; as the fragment is readily found outside the containment tube after a test – this suggests that the fragment perforates the absorber and thereafter rebounds from the rear plate and travels back through the already-formed tunnel. Entry, exit and sectioned views of the impacted polyurethane foam for increasing charge masses are shown in Figure 4-26.

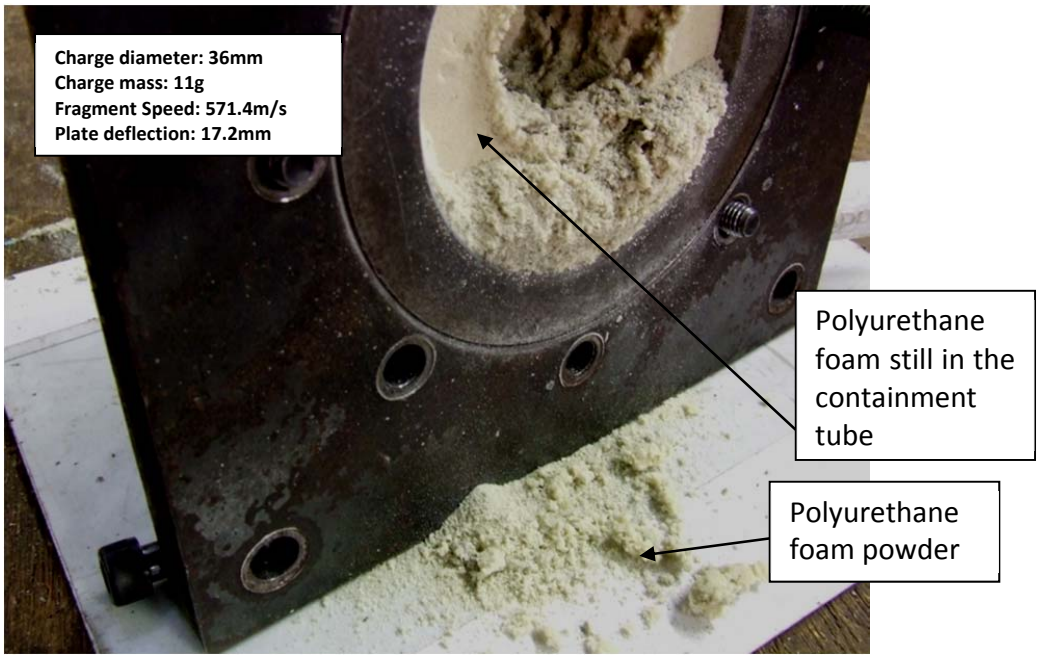

Figure 4-25: Photograph showing post-impact state of polyurethane foam while it is still in containment tube, showing powderised material

Polyurethane foam, when subjected to impact by fragments released at increasing charge masses, shows an increasing opening size at the exit face of the absorber. The entry opening, similarly to the other materials, does not appear to be affected by the speed of the incoming fragment. At a thickness of 40mm, along with aluminium foam, polyurethane is the only energy absorber which, when placed in front of the rear plate, no tearing is observed after impact on the plate at any of the charge masses. Tabulated summaries of impact tests on 40mm thick polyurethane foam are listed on Table 4.8. Inferred from the table, at a thickness of 40mm, polyurethane foam shows the highest level of material loss when compared to the other materials with the average material loss of 19.2% after impact by the fragment.

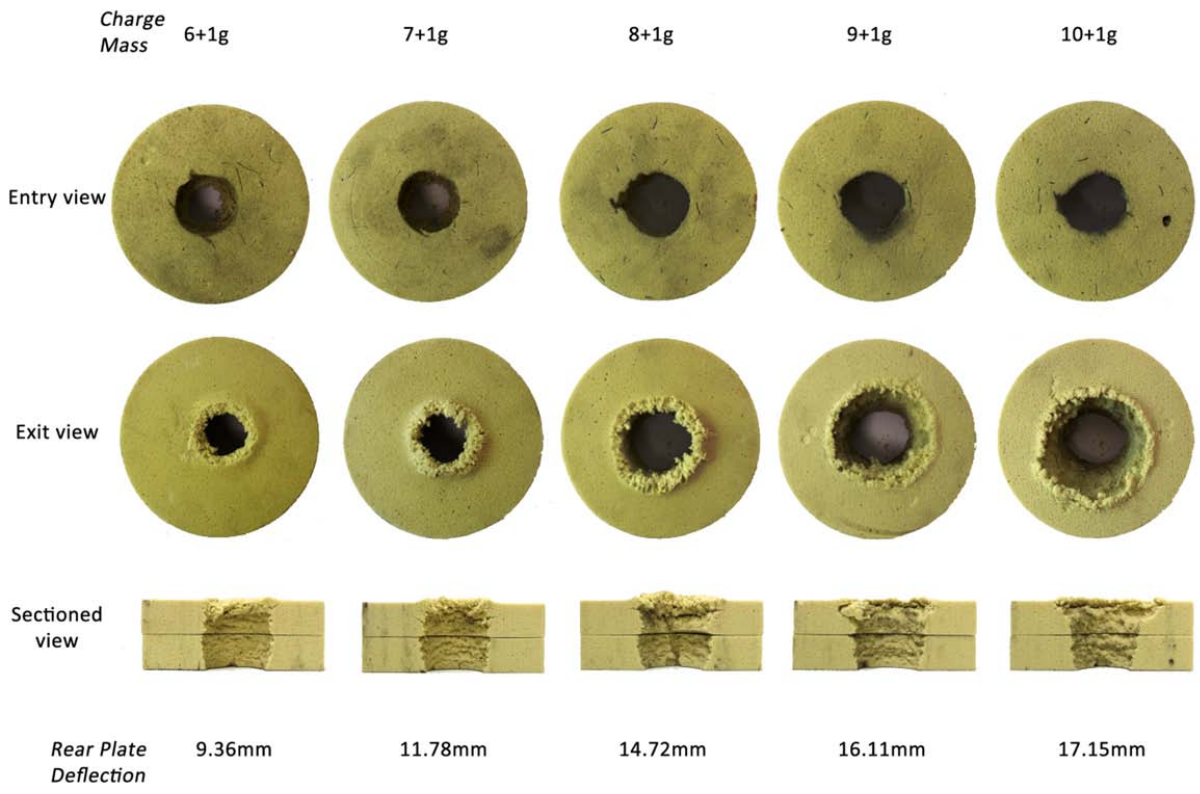

Figure 4-26: Entry, Exit and Sectioned views of 40mm thick polyurethane foam subjected to increasing charge masses at 36mm charge diameter

Table 4.8: Summary of results for tests conducted with polyurethane foam energy absorbers of 40mm thickness

Test Description	Impulse (Ns)	Fragment speed (m/s)	Fragment momentum (Ns)	Fragment kinetic energy (J)	Rear plate deflection (mm)	Material Lost From Absorber (%)
PU40-3607-01	13.9	370.4	3.1	576.1	9.36	19.3
PU40-3608-01	15.8	444.4	3.9	870.1	11.78	12.6
PU40-3609-01	17.1	487.8	4.4	1069.6	14.72	19.0
PU40-3610-01	20.6	526.3	4.6	1214.7	16.11	20.0
PU40-3611-01	21.3	571.4	4.6	1312.7	17.15	22.8
PU40-3611-02	21.8	606.1	5.0	1506.0	16.84	21.6

4.5.1.7. Summary

The experimental results and observations of the 40mm thick energy absorbers has been outlined with key differences among each failure pattern noted. Comparative photographs, showing entry, exit and sectioned views for the energy absorbers tested at 40mm thickness and at charge masses 7g and 11g are shown in Figure 4-27 and Figure 4-28 respectively.

The least amount of material loss was observed for Divinycell foam whilst polyurethane foam loses a largest fraction of its original material in a conversion to a powder form. Aluminium honeycomb bends during impact and exhibits moderate material loss. Corecell foam exhibits relatively extensive scorch marks, particularly on its exit face. A compressed plug is ejected by the fragment from aluminium foam by shearing during impact. Balsa wood loses a large fraction of its original mass whilst brittle cracking can be noticed in some of the balsa wood. Cracking and material loss in the balsa wood occurs along the grain direction, which is particularly noticeable on the exit face of the energy absorber.

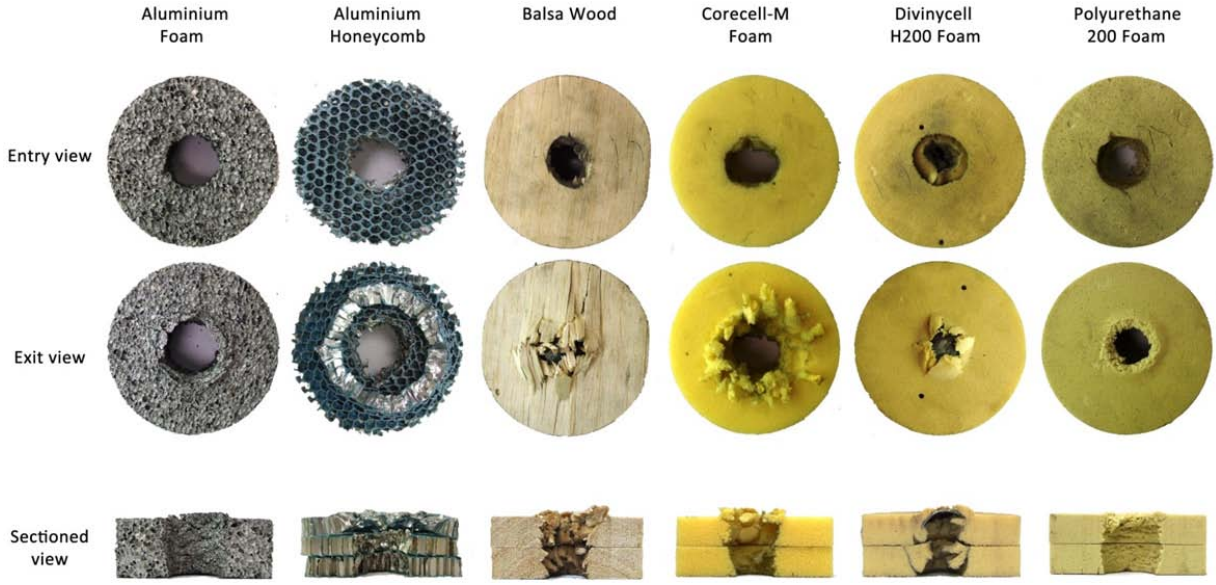

Figure 4-27: Entry, Exit and Sectioned views of the 40mm thick energy absorbers subjected to impacts from fragment released by 7g charge masses at 36mm charge diameter

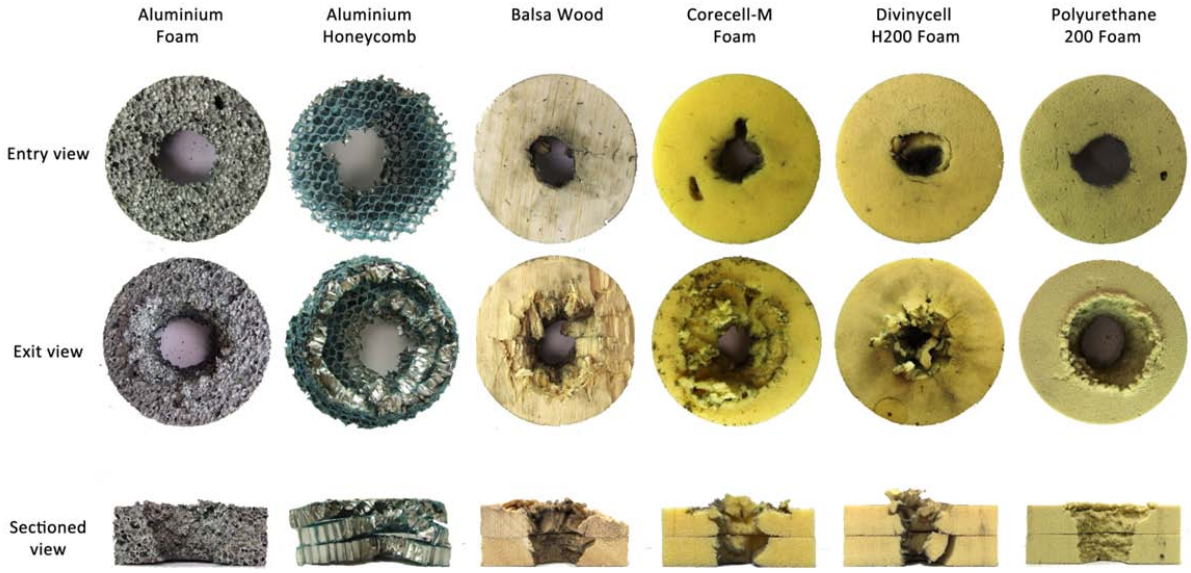

Figure 4-28: Entry, Exit and Sectioned views of the 40mm thick energy absorbers subjected to impacts from fragment released by 11g charge masses at 36mm charge diameter

In all the energy absorbing materials tested, extensive change of texture and wider opening of the absorber is observed on the exit face, similar to general observations of targets perforated by bullets or other projectiles, where the exit surface exhibits larger material loss, wider opening or more extensive deformation. A tabulated summary of the failure patterns of each of the energy absorbing materials tested at 40mm thickness is shown in Table 4.9.

Table 4.9: Summary of the general failure patterns of the energy absorbing materials (observed at 40mm thickness)

Energy absorbing material	Failure pattern	Material loss
Aluminium foam	Compressed foam plug sheared off by fragment	Low
Aluminium honeycomb	Bending of absorber layers during perforation, which gets more extensive at higher charge masses	Moderate
Balsa wood	Cracking along grain on exit face at lower charge masses and loss of wood on exit face at higher charge masses	High
Corecell foam	Discolouration and scorching on perforation tunnel and exit face	Moderate
Divinycell foam	Hardened and densified. Cross-crack shear failure observed, as well as occasionally wedged fragment	Low
Polyurethane foam	Powdering of foam material in the path of the penetrating/perforating fragment	High

Interim analyses on the relationship between kinetic energy of the fragment and maximum deflections of the rear plates protected by 40mm energy absorbers suggest that Divinycell foam provides the best protection (particularly at impact kinetic energies exceeding 700J) to the rear plate as the smallest deflection is observed on the rear plate. Balsa wood appears to be the absorber of which the protective performance of the rear plate lies closest to the average of all tested materials. Polyurethane shows a different trend as it exhibits the greatest impact

mitigation at lower fragment kinetic energies (less than 700J) and progressively decays to one of the poorest impact mitigations at the highest end of the kinetic energy regime (at 1300J) possibly because of a lesser strain rate sensitivity when compared with the other energy absorbing materials.

4.5.2. Tests with 60mm thick energy absorbers protecting the rear plate

Following the interim analyses of results observed on 40mm thick energy absorbers (as discussed in the summary in §4.5.1.7), three materials – balsa wood, Divinycell foam and polyurethane foam – are chosen for tests at a thickness of 60mm for a range of charge masses of 7g to 11g at a constant charge diameter of 36mm. The tests on the 60mm thick energy absorbers is carried out to investigate the effects of increasing the thickness of the energy absorber on the rear plate response and the response of the energy absorber material.

The failure mechanism for each material is similar to the observed failure at a thickness of 40mm. It should be noted that at 7g charge mass, the fragment fails to perforate the thickness of any of the 60mm thick energy absorbing materials. At this charge mass, however, transient deflections of the rear/free face of the absorbers appear to be responsible for the observed deflections of the rear plate. Summarised details of the impact tests on the 60mm thick energy absorbers are tabulated in Table 4.10.

Table 4.10: Summary of results for tests conducted on balsa wood, Divinycell foam & polyurethane foam of 60mm thickness

BALSA WOOD						
Test Description	**Impulse (Ns)**	**Fragment speed (m/s)**	**Fragment momentum (Ns)**	**Fragment kinetic energy (J)**	**Rear plate deflection (mm)**	**Material Lost From Absorber (%)**
BA60-3607-01	14.6	357.1	3.1	548.5	4.74	31.3
BA60-3608-01	16.6	425.5	3.6	766.9	9.86	20.7
BA60-3609-01	18.3	487.8	4.4	1070.8	14.17	14.9
BA60-3610-01	19.3	526.3	4.6	1205.0	16.25	24.1
BA60-3611-01	22.4	606.1	4.6	1395.8	15.45	13.0
BA60-3611-02	21.4	571.4	5.5	1583.7	14.99	18.1
DIVINYCELL FOAM						
Test Description	**Impulse (Ns)**	**Fragment speed (m/s)**	**Fragment momentum (Ns)**	**Fragment kinetic energy (J)**	**Rear plate deflection (mm)**	**Material Lost From Absorber (%)**
DV60-3607-01	14.6	339.0	2.9	488.4	1.67	1.1
DV60-3608-01	16.8	392.2	3.7	730.5	2.48	4.7
DV60-3609-01	18.6	425.5	3.8	805.8	5.46	~0
DV60-3610-01	20.1	512.8	4.7	1196.6	9.98	4.7
DV60-3611-01	22.0	540.5	5.1	1387.9	13.06	4.6
POLYURETHANE FOAM						
Test Description	**Impulse (Ns)**	**Fragment speed (m/s)**	**Fragment momentum (Ns)**	**Fragment kinetic energy (J)**	**Rear plate deflection (mm)**	**Material Lost From Absorber (%)**
PU60-3607-01	14.6	408.2	3.2	661.4	3.72	10.3
PU60-3607-02	15.2	312.5	2.6	405.3	1.25	5.2
PU60-3608-01	16.4	408.2	3.6	742.2	8.34	10.5
PU60-3609-01	19.1	444.4	4.2	937.3	10.45	18.2
PU60-3610-01	20.2	526.3	4.2	1113.6	11.42	13.8
PU60-3611-01	21.4	588.2	4.8	1417.0	13.79	14.4

For all the three types of energy absorbers tested at 60mm thickness, entry, exit and sectioned views showing the final state of the absorbers for 7g and 11g charge mass are shown in Figure 4-29 and Figure 4-30, respectively.

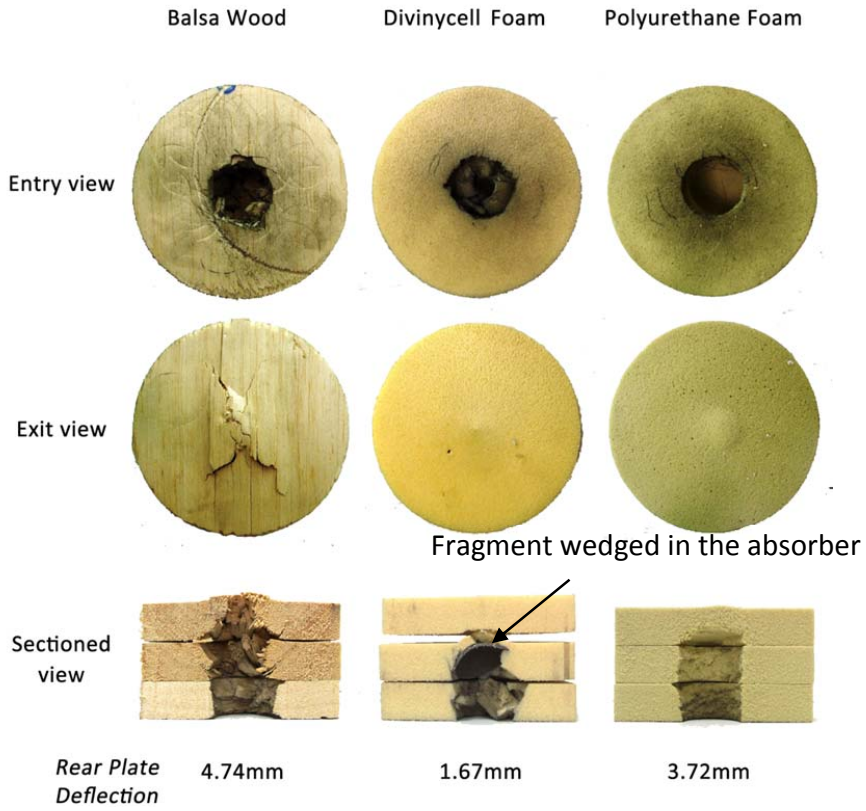

Figure 4-29: Entry, exit and sectioned views of 60mm thick energy absorbers subjected to fragment impact from 7g charge mass

For **balsa wood**, even though no perforation is observed at 7g charge mass, there is cracking of the rear face as it appears that the fragment is close to perforation. Perforation is observed at subsequent charge masses. At this thickness (60mm), balsa wood undergoes a high mean material loss of 20.4% which is close to the percentage loss observed at 40mm thickness (17.6%). The difference in material mass before and after impact for **Divinycell foam** at 9g charge is observed to be negligible (Table 4.10), whereas the mean material loss across all charge masses is 3%. The tendency of Divinycell foam to exhibit cross-crack shearing in the absorber layers and the occurrence of some fragments being wedged is also observed in the 60mm thick foam.

The powdering failure of **polyurethane foam** is apparent across the whole charge mass range. It undergoes a moderate-to-large mean material loss (12.1%), which is lower than its mean material loss at 40mm thickness (19.2%).

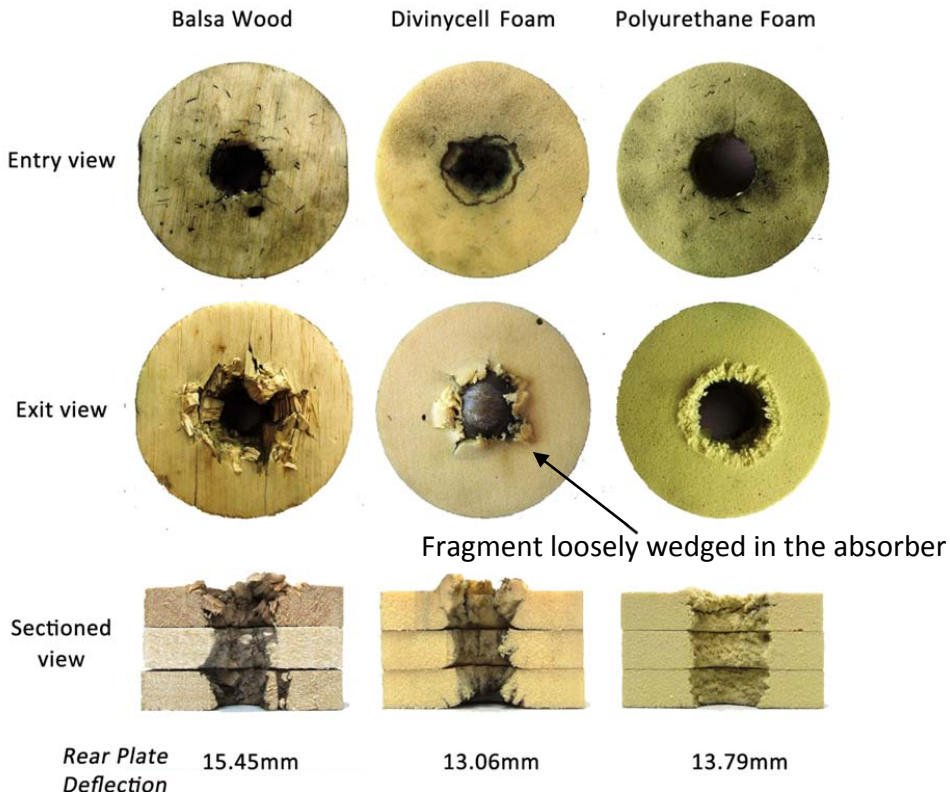

Figure 4-30: Entry, exit and sectioned views of 60mm thick energy absorbers subjected to fragment impact from 11g charge mass

4.5.3. Effect of varying the layering arrangements of energy absorbers

In this series of tests, polyurethane foam energy absorbers of 40mm thickness are tested at three different thickness combinations – a single 40mm disc, two 20mm discs and four discs of 10mm thickness. The charge diameter is maintained at 36mm diameter, but unlike the tests described in §4.5.1., this parametric series of tests is undertaken to investigate the fragment impact damage mitigation effect when changing the layering arrangement. In a study by Ronchietto et al. [140] on the impact response of axially stacked steel tubes, it was observed that there was an occurrence of two peak loads with a slightly greater mean crush load in the stacked arrangement compared to one peak load and smaller mean crush load for the one-tube arrangement. All the absorbers are tested at increasing charge masses from 7g to 11g. For the smallest charge mass (7g) and the largest (11g), the entry, exit and sectioned views for all three thickness arrangements, respectively, are shown in Figure 4-31 and Figure 4-32.

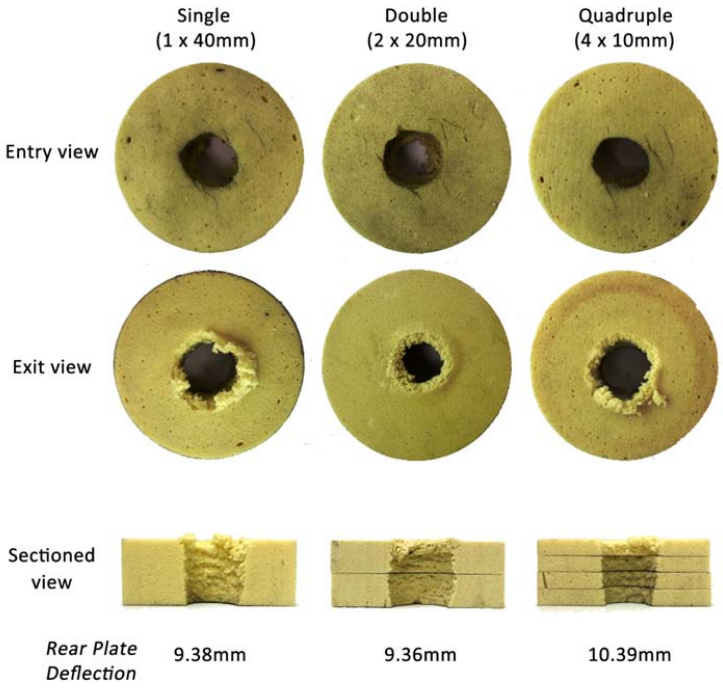

Figure 4-31: Entry, Exit and Sectioned views of 40mm thick single, double and quadruple-layered polyurethane foam subjected to 7g charge mass at 36mm charge diameter

For all the three layering arrangements, general absorber failure observations are similar to those of polyurethane foam discussed in §§4.5.1.6 and 4.5.2. The entry opening size is independent of the charge mass whereas the exit opening gets wider with increasing charge mass. Powdering failure is again observed for all the polyurethane foam arrangements. For the absorber comprising two 20mm thick polyurethane discs, the test data used for comparison with the other two layering arrangements is from the series of experiments of which the results are presented in §4.5.1.6, i.e. 40mm thick single layer.

For the multiple-layered setups (double and quadruple-layered arrangement), from front layer to the layer closest to the rear plate, each subsequent layer has a marginally wider opening than the preceding layer. Results pertaining to the investigations in which different combinations of the same thickness are investigated are listed in Table 4.11.

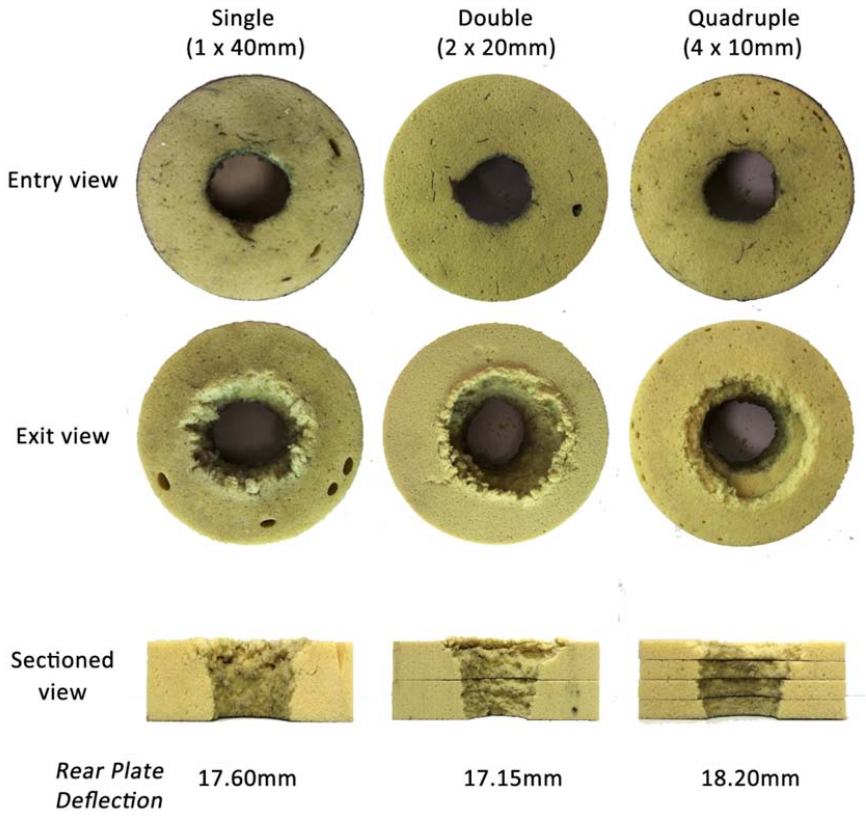

Figure 4-32: Entry Entry, Exit and Sectioned views of 40mm thick single, double and quadruple-layered polyurethane foam subjected to 11g charge mass at 36mm charge diameter

It was found that for all charge masses, the three layer arrangements of 40mm thick polyurethane foam provide comparable damage mitigation from the fragment – details of the analyses are discussed in §5.6. In the quasi-static tests of polyurethane foam, resultant graphs of which are shown in Appendix B (Figure B-16 and Figure B-17), it is observed that the peak stress (the 'yield' stress just before the plateau stress) is almost equal to the plateau stress. It is therefore justifiable that even if more layers are stacked together, the peak load that has to be overcome during failure of is almost equal to the plateau stress. This behaviour is a contrast to what can be expected for metallic materials like Aluminium honeycomb, where the peak stress is twice as much as the plateau stress (Figure B-7 and Figure B-8).

Table 4.11: Summary of results for tests conducted on 40mm thick single, double and quadruple-layered polyurethane foam

1 x 40MM POLYURETHANE FOAM DISC (SINGLE)						
Test Description	**Impulse (Ns)**	**Fragment speed (m/s)**	**Fragment momentum (Ns)**	**Fragment kinetic energy (J)**	**Rear plate deflection (mm)**	**Material Lost From Absorber (%)**
PU40S-3607-01	14.42	370.4	3.004	556.2	9.38	11.68
PU40S-3608-01	16.16	408.2	3.339	681.4	10.54	14.44
PU40S-3609-01	17.77	540.5	4.265	1152.7	15.16	16.90
PU40S-3610-01	20.35	555.6	4.561	1267.0	16.17	16.75
PU40S-3611-01	22.12	625.0	5.331	1666.0	17.6	16.57
2 x 20MM POLYURETHANE FOAM DISC (DOUBLE)*						
Test Description	**Impulse (Ns)**	**Fragment speed (m/s)**	**Fragment momentum (Ns)**	**Fragment kinetic energy (J)**	**Rear plate deflection (mm)**	**Material Lost From Absorber (%)**
PU40-3607-01	13.9	370.4	3.1	576.1	9.36	19.3
PU40-3608-01	15.8	444.4	3.9	870.1	11.78	12.6
PU40-3609-01	17.1	487.8	4.4	1069.6	14.72	19.0
PU40-3610-01	20.6	526.3	4.6	1214.7	16.11	20.0
PU40-3611-01	21.3	571.4	4.6	1312.7	17.15	22.8
4 x 10MM POLYURETHANE FOAM DISC (QUADRUPLE)						
Test Description	**Impulse (Ns)**	**Fragment speed (m/s)**	**Fragment momentum (Ns)**	**Fragment kinetic energy (J)**	**Rear plate deflection (mm)**	**Material Lost From Absorber (%)**
PU40Q-3607-01	14.29	384.6	2.996	576.2	10.39	10.26
PU40Q-3608-01	16.02	454.5	3.723	846.1	12.44	10.26
PU40Q-3609-01	18.31	425.5	3.323	707.1	11.17	12.34
PU40Q-3610-01	19.67	555.6	4.956	1376.5	16.67	11.15
PU40Q-3611-01	21.44	625.0	5.263	1644.5	18.2	17.40

*The findings for the double-layer arrangement are the same as the results of the series of tests discussed in §4.5.1.6

4.5.4. Effect of size and speed of a fragment

In this parametric series of experiments, three charge diameters (27mm, 36mm and 43mm) with different masses of charge are used to produce fragments of at different speeds and masses with mutually close kinetic energies.

A commonly observed trend for all the three present materials (balsa wood, Divinycell foam and polyurethane foam U is that the fragment released from a 27mm diameter charge causes the largest deflection, whilst the fragment ejected from a front plate subjected to a 43mm diameter charge shows the smallest rear plate deflection. This is attributed to the fact that the smallest charge diameter ejects the smallest fragment at the largest speed. Another factor is that the smallest fragment transmits its kinetic energy to the rear plate by the smallest contact area, translating to the greatest concentration factor of load transmission; whereas the largest fragment transmits the same kinetic energy through the largest contact area, which translates to a less concentrated loading. For each energy absorber, the material that is lost under fragment impact does not necessarily depend upon the size of the fragment because in some of the cases, full perforation occurs whereas only penetration occurs in others.

The two fragments released by 36mm and 43mm charge diameters, after impacting **balsa wood,** do not fully penetrate the energy absorber, although they partially emerge from the exit face, as is shown on the entry, exit and sectioned views of the absorber in Figure 4-33. The cracking observed on the exit face is similar to the observations discussed for balsa wood in §§4.5.1.3 and 4.5.2. A charge diameter of 27mm is noticed to cause full perforation.

The mean fragment kinetic energy for all three charge diameters was calculated as 489.9J with a mean (percentage) deviation* of 10.2%.

Expectedly, the balsa wood loses the least of its mass fraction at the smallest charge diameter (3.9%) but the largest at a charge diameter of 36mm (19.9%).

The fragment from the 27mm diameter charge impacts the energy absorber at a speed 487.8m/s and cause a rear plate deflection of 11.1mm whilst the fragment from a charge of 43mm diameter impacts the absorber at 270.3m/s and deflects the rear plate by 7.8mm.

***The mean deviation is computed as the ratio of the standard deviation of the sample to the *average* or *mean* of the data points in a data set or in a sample within the data set.**

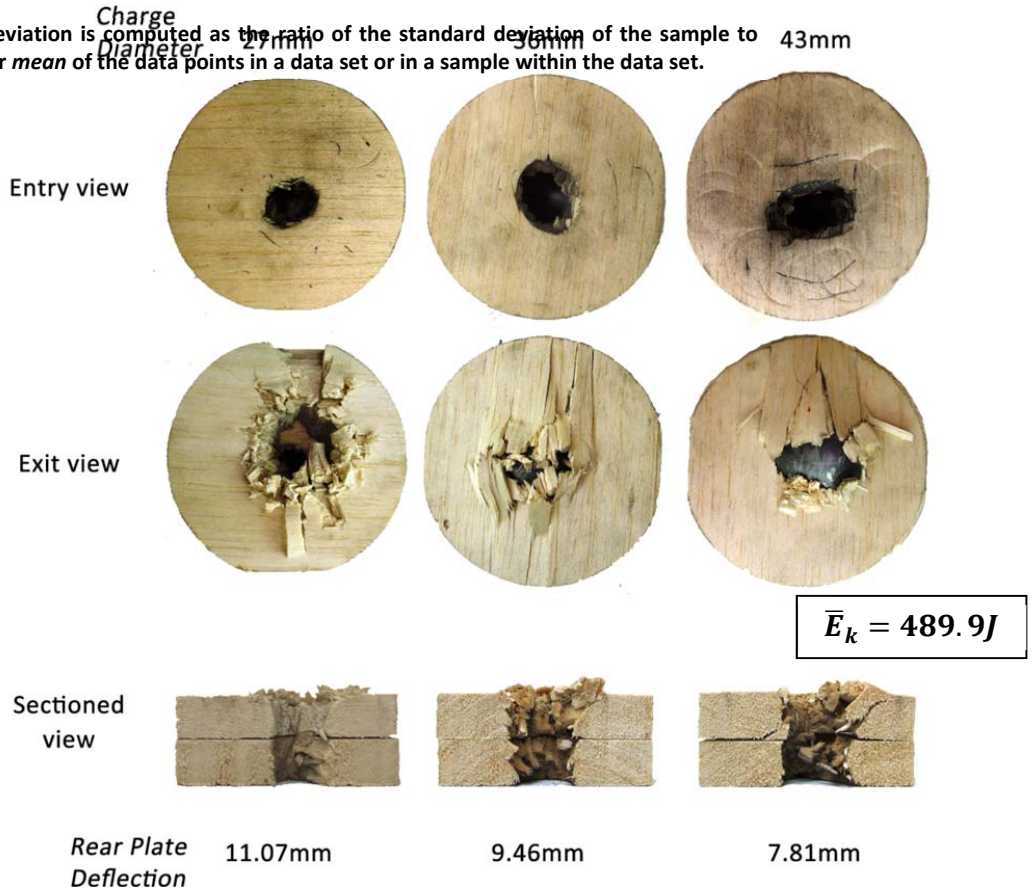

Figure 4-33: Entry, Exit and Sectioned views of 40mm thick balsa wood subjected to impact by fragments with similar kinetic energies (Charge diameter = 27mm, 36mm & 43mm)

For **Divinycell foam**, full perforation is only observed when the impact is from a fragment generated by a 27mm diameter charge that impacts the foam at 540.5m/s and imparts a rear plate deflection of 10.9mm as shown in Figure 4-34 and Table 4.12. A charge diameter of 36mm causes the fragment to be near the onset of perforation as it remains wedge just within the exit face. A charge diameter of 43mm generates a fragment at a speed of 294.1m/s which fails to perforate the foam, but due to the deflection of the exit face of the absorber, a deflection of 1.9mm is measured on the rear plate. When all the three fragment sizes are considered for Divinycell foam, the mean kinetic energy is 611.4J and the coefficient of variation is 7.5%.

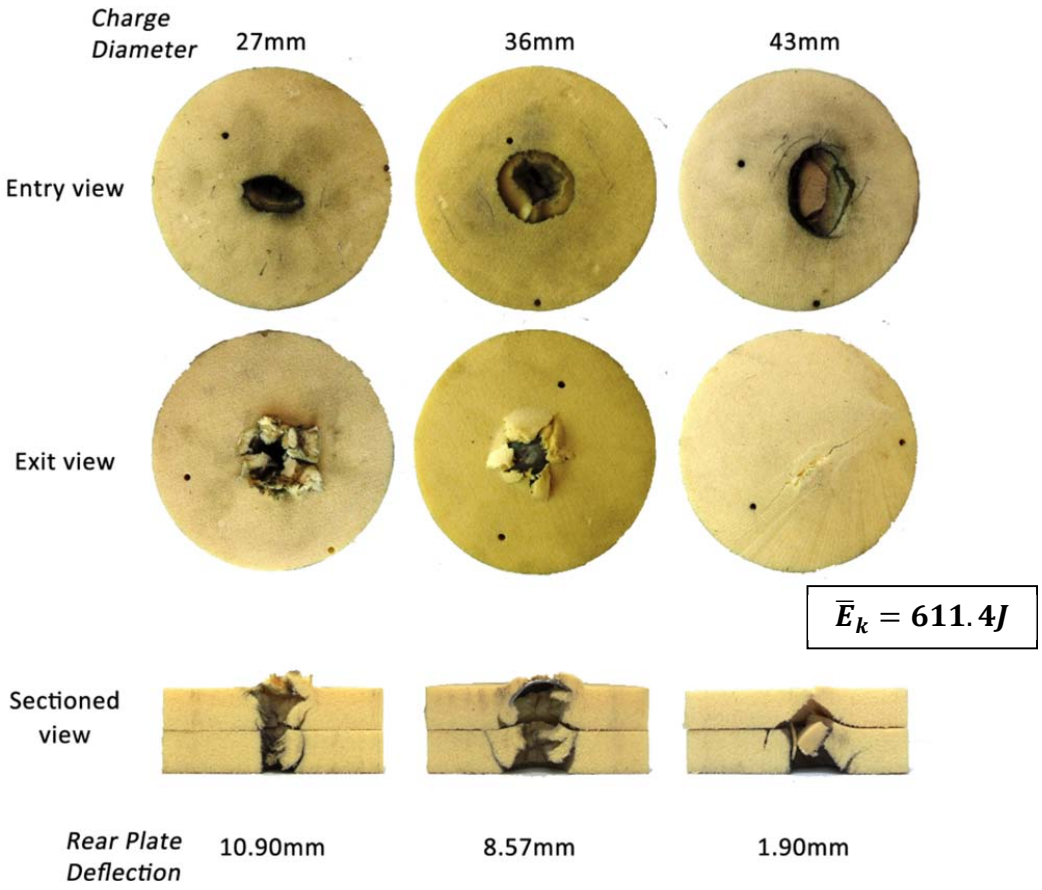

Figure 4-34: Entry, Exit and Sectioned views of 40mm thick Divinycell foam subjected to impact by fragments with close kinetic energies (Charge diameter = 27mm, 36mm & 43mm)

For **polyurethane foam**, as shown in the entry, exit and section view photographs in Figure 4-35, has the smallest fragment (from a 27mm charge diameter) and perforates the foam with an initial speed of 570.6m/s and the resulting rear plate deflection of 10.4mm. Full perforation, with powdering of the foam is also observed for the 36mm charge diameter test. Full perforation was not observed when the charge diameter was 43mm. The fragment in this case impacts the foam at a speed of 307m/s and causes a deflection of 7.9mm on the rear plate. The mean kinetic energy for the three fragments impacting polyurethane foam in this test series is 588.6J with a coefficient of variation of 4.5%. The collective summary of fragment kinetic energies and resultant rear plate maximum deflections for each charge diameter and all three materials is shown in Table 4.12.

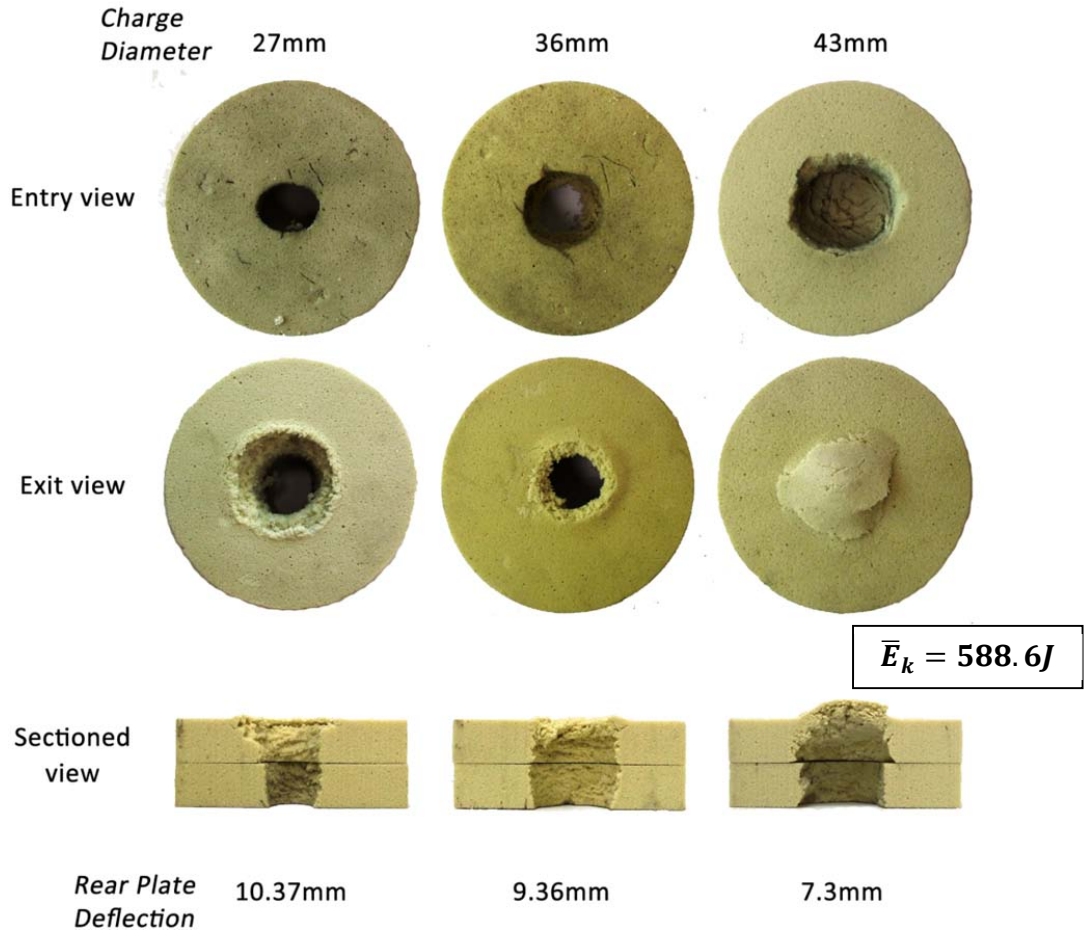

Figure 4-35: Entry, Exit and Sectioned views of 40mm thick polyurethane foam subjected to impact by fragments with close kinetic energies (Charge diameter = 27mm, 36mm & 43mm)

Table 4.12: Summarised results for the test series where balsa wood, Divinycell foam and polyurethane foam are subjected to impact from different sized fragments (for investigations on close kinetic energies)

BALSA WOOD						
Charge Diameter (mm)	**Impulse (Ns)**	**Fragment speed (m/s)**	**Fragment momentum (Ns)**	**Fragment kinetic energy (J)**	**Rear plate deflection (mm)**	**Material Lost From Absorber (%)**
27	15.9	500.0	2.2	545.0	Large tear	2.83
27	14.33	487.8	2.2	540.2	11.07	3.93
36	13.26	363.6	2.7	489.3	9.46	19.92
43	16.71	270.3	3.3	440.1	7.81	13.04
43	16.6	312.5	4.2	656.7	10.65	10.35
DIVINYCELL FOAM						
Charge Diameter (mm)	**Impulse (Ns)**	**Fragment speed (m/s)**	**Fragment momentum (Ns)**	**Fragment kinetic energy (J)**	**Rear plate deflection (mm)**	**Material Lost From Absorber (%)**
27	16.9	500.0	2.4	598.8	11.69	1.14
27	14.96	540.5	2.3	634.0	10.90	4.66
36	13.64	408.2	3.1	641.4	8.57	2.46
43	16.43	294.1	3.8	558.8	1.9	4.69
43	17.2	281.7	3.4	472.1	3.0	4.59
POLYURETHANE FOAM						
Charge Diameter (mm)	**Impulse (Ns)**	**Fragment speed (m/s)**	**Fragment momentum (Ns)**	**Fragment kinetic energy (J)**	**Rear plate deflection (mm)**	**Material Lost From Absorber (%)**
27	16.85	526.3	2.2	570.6	10.37	3.32
36	13.88	370.4	3.1	576.1	9.36	19.31
43	16.84	307.7	4.0	619.2	7.3	7.92
43	16.6	289.9	3.6	525.1	5.53	12.9

*Tests used for the parametric analysis are highlighted in green

In an attempt to match the kinetic energies of the different sized fragments to a common value, deviations between 4.5% and 10.2% in the measured kinetic energy were found. As a result of the complex loading mechanism due to the blast load, a considerable range is observed in the speeds of the ejected fragments for any given charge mass and charge diameter. The resulting determination of kinetic energies yields a wide variation and uncertainty; and due to this unpredictability of the release speed of the fragment, it is difficult to match the kinetic energies to one single value.

5. ANALYSIS AND DISCUSSIONS OF RESULTS

Impact from blast-induced fragments on mild steel plates – without and with the protection of energy absorbing cellular materials – has been investigated and the observations have been discussed in Chapter 4. In this section, the results are interpreted, analysed – particularly with the use of graphs – and discussed.

5.1. Effects of the blast on the front plate

5.1.1. Impulse from the blast

For all the blast tests carried out, before and after the inclusion of energy absorbers, three charge diameters are used, and for each test, the impulse imparted on the front plate is calculated based on the maximum traced swings (backward and forward) of the ballistic pendulum. For details on how the impulse in each case was computed, reference can be made to Appendix C. Figure 5-1 shows how impulse for the 27mm diameter charge changes with charge mass. Few tests are conducted at charge masses larger than 8g for this charge diameter.

For 8g charge mass, for example, the impulse from the different tests conducted ranges between 14.33Ns and 17.13Ns (a variation range of 2.8Ns with a coefficient of variation of 6%), which accounts for a reasonably narrow band of experimental variation. Even though there are only a few tests for charge masses beyond 8g, there is a general increase of impulse against charge mass. The trend line is generated using least squares method with an R^2 square of the correlation coefficien of less than 0.4.

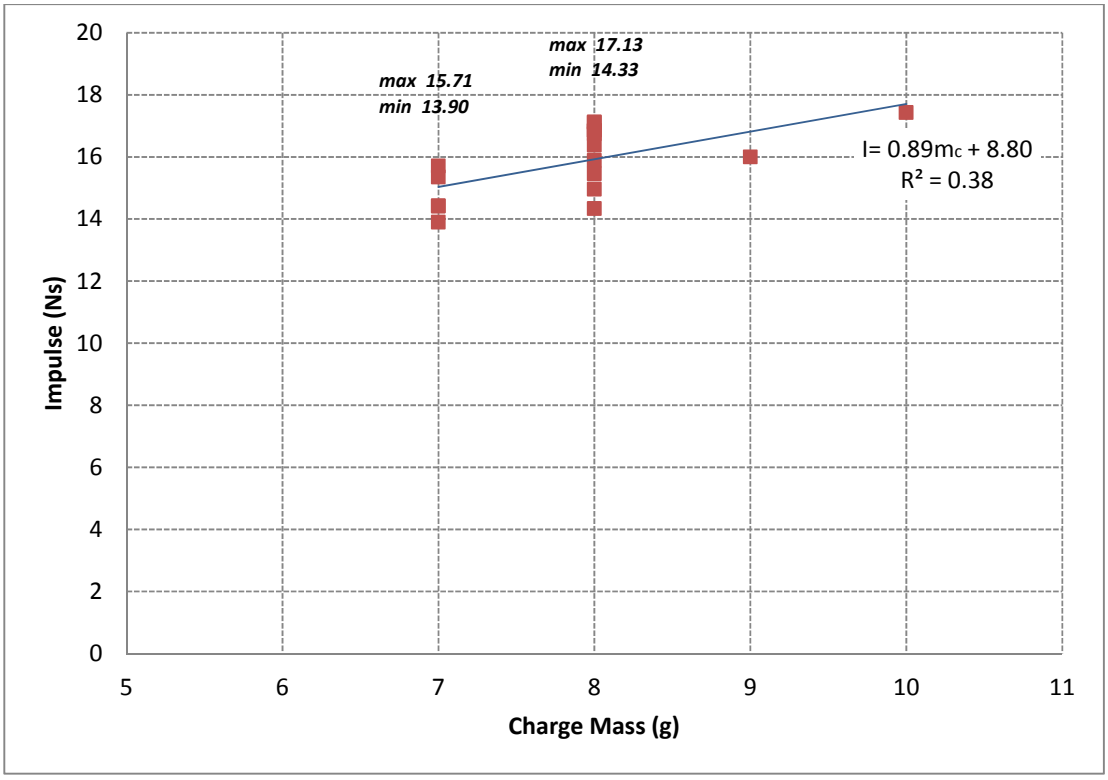

Figure 5-1: Impulse from the blast against varying charge mass for tests conducted using 27mm charge diameter

***The variation range is computed as the difference between the maximum data point value and the minimum data point value in a data set or in a sample within the data set.**

Figure 5-2 and Figure 5-3 show the impulse-charge mass relationships for tests conducted with charge diameters of 36mm and 43mm, respectively. The two generated trends exhibit similar slopes (1.83Ns/g and 1.82Ns/g). The presence of the relatively large amount of data points in Figure 5-2 is because most tests in the study were carried out at 36mm. The dotted bounding lines in Figure 5-2 are least squares trend lines running through the minimum and maximum impulse values in the plot (for each charge mass).

For the 36mm charge diameter, the widest impulse variation range for a given charge mass is observed at 9g (3.63Ns with a mean deviation of 5.8%). A linear least squares fit is generated with an R^2 correlation value of 0.93. Relatively few tests are conducted at a charge diameter 43mm. The impulse data points throughout the charge mass domain seem to fit closely to a linear trend fit with an R^2 value of 0.95.

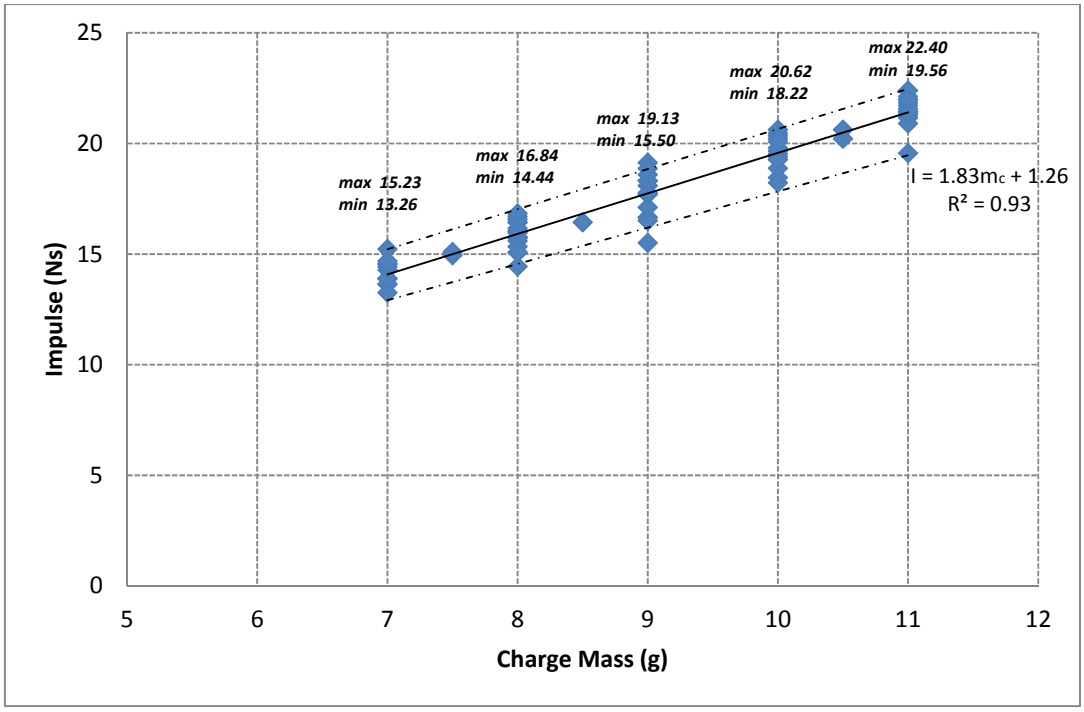

Figure 5-2: Impulse from the blast against varying charge mass for tests conducted using 36mm charge diameter

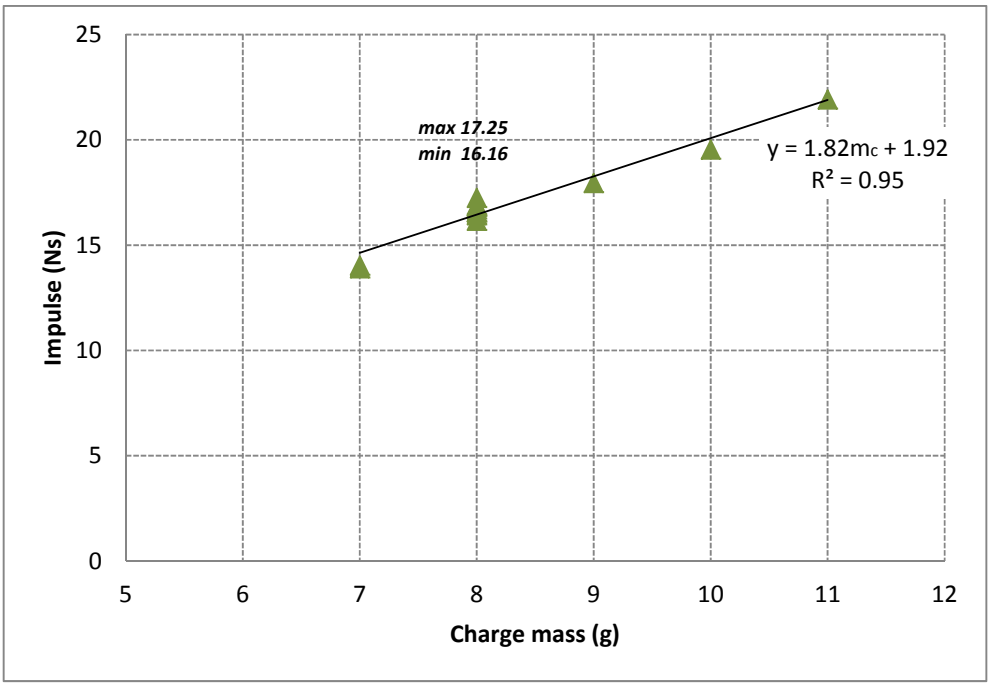

Figure 5-3: Impulse from the blast against varying charge mass for tests conducted using 43mm charge diameter

The three sets of data points from tests conducted at 27mm, 36mm and 43mm charge diameters are plotted together as shown in Figure 5-4. It appears that, within the tested charge mass domain (7g to 11g charge mass), all three charge diameters fall within a reasonably narrow range of impulse against charge mass. The distribution of data points in the plot suggests that there is no conclusive effect of the impulse generate by varying the charge diameter for any given charge mass. Furthermore, the slope of the trend line in the combined plot (1.76Ns/g) is close to that of tests conducted at 36mm and 43 charge diameters and there is a good fit of the trend line through all the data points with an R^2 value of 0.91.

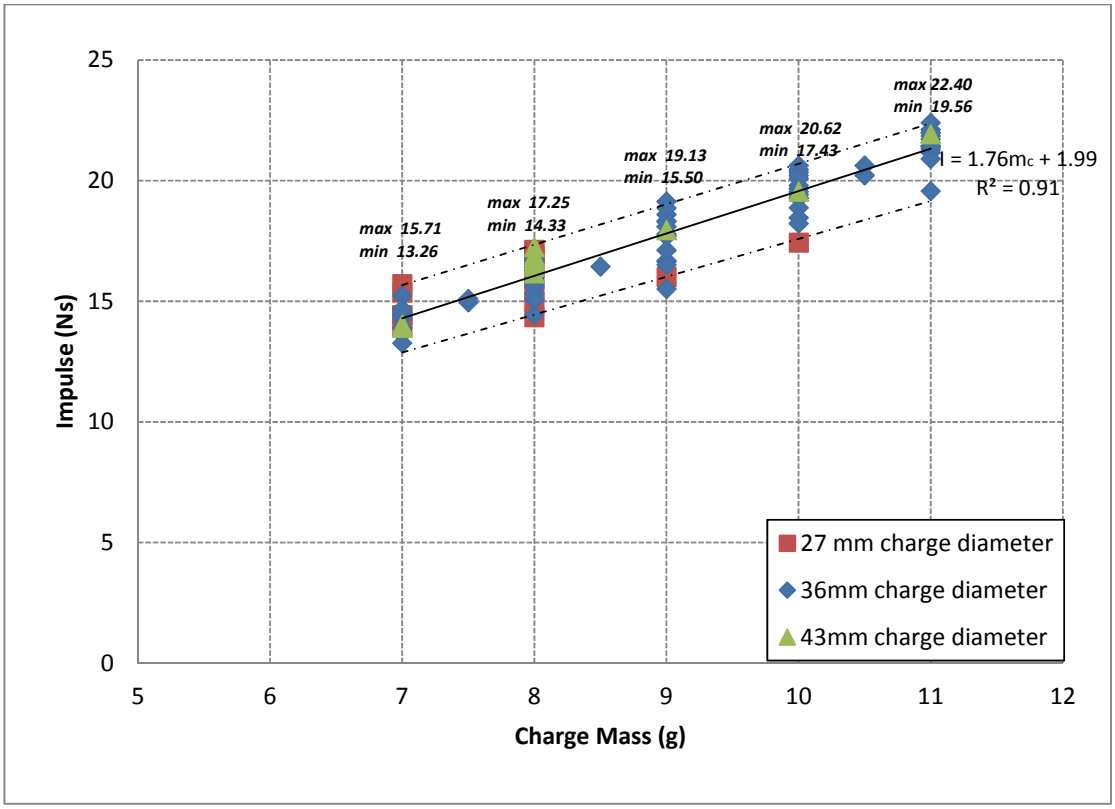

Figure 5-4: Impulse against varying charge mass for tests conducted using all three charge diameters

In their studies, Nurick and Radford [19] used charges of diameters 18mm, 25mm, 33mm and 43mm to subject circular mild steel plates of diameter 100mm and thickness 1.6mm to localised loading. From the data of impulse and charge mass for the combined different charge diameters, their investigation showed that despite the difference in charge diameters, the impulse from the blast is only dependent on the charge mass as all four diameters had data points which fell within a narrow band of experimental variation. Their linear relationship had an R^2 correlation value of 0.95 and is provided as Eq. 5-1.

$$I = 2.0m_c - 0.3128 \qquad \text{Eq. 5-1}$$

where : I= Impulse, m_c= mass of charge (in g)

The impulse-charge mass findings from the study by Nurick and Radford [19] confirm the charge-diameter independence of the relationship between impulse and charge mass which is found in this study. Furthermore, the slope from the combined data in this study (1.76) is acceptably close to the slope found in the data of Nurick and Radford [19] (2.0), which suggests some degree of repeatability.

5.1.2. Theoretical prediction of maximum front plate deflection just before capping

A relationship was presented by Rajendran et al. [5] to theoretically determine the maximum deflection of the front plate just before a cap fragment is generated by a localised blast load. The equation for determining this maximum deflection (δ_0) is:

$$\delta_0 = 2.47R_f\sqrt{\varepsilon_{fr}} \qquad \text{Recall Eq. 2-8}$$

where : R_f= Radius of the fragment, ε_{fr}= uniaxial fracture strain

If half of the average diameter of the fragment for each of the three charge diameters is taken as the radius of the fragment and the uniaxial fracture strain is taken as the average strain at fracture from the quasi-static tensile tests on mild steel, then the resulting maximum deflection before capping for each of the charge diameters is tabulated in Table 5.1. The predicted maximum front plate deflection before capping increases with increasing charge diameter.

Table 5.1: Table showing the theoretical prediction of maximum front plate deflection before capping

Charge diameter d_c (mm)	**27**	**36**	**43**
d_c/d ratio	0.25	0.34	0.41
Radius of fragment (mm)	12.87	17.02	20.04
Uniaxial fracture strain	0.341		
Maximum deflection before capping δ_0 (mm)	18.56	24.55	28.90

In their studies on localised blast loading of mild steel circular plates, three of the charge diameters that Nurick and Radford [19] used were 25mm, 33mm and 43mm to load plates of diameter 100mm and thickness 1.6mm to localised loading, where deformation and capping were reported. The corresponding d_c/d ratios for the given charge diameters were 0.25 for 25mm charge diameter, 0.33 for 33 mm diameter and 0.4 for 40mm charge diameter – similar to the ratios in this study. *d_c is the charge diameter and d is the plate diameter.*

The **measured** maximum plate deflection just before capping reported by Nurick and Radford [19] was 23mm for d_c/d=0.25, 29.6mm for d_c/d=0.33 and 28.5mm for d_c/d=0.4. Compared with the predicted maximum deflections before capping in this investigation, the present measured deflections were marginally larger for the first two d_c/d ratios, but for d_c/d=0.4, the two values are almost equal. The discrepancies in the predicted and measured values are possibly because the prediction formula used for this study does not explicitly account for the diameter, thickness and boundary conditions of the plate, which are important factors.

5.2. Kinetics of the fragment

When the fragment is released from the front plate, its velocity is measured before it impacts the rear plate or energy absorber. Since its post-test mass is also measured, kinetic parameters like momentum and kinetic energy can be calculated, and this can be used to quantify fragment impact.

5.2.1. Mass of the fragments

Figure 5-5 shows the distribution of fragment masses for each of the charge diameters. For some of the tests performed with all the three charge diameters, the fragment crumples or folds after impact with the rear plate, but the mass of the fragment can readily be measured as long as the fragment is recovered after the test or if the mass of the front plate is known before the test commences (§3.6.3). As expected, the mass of the fragment increases with increasing charge diameter, as the diameter of the fragment also increases with increasing charge diameter.

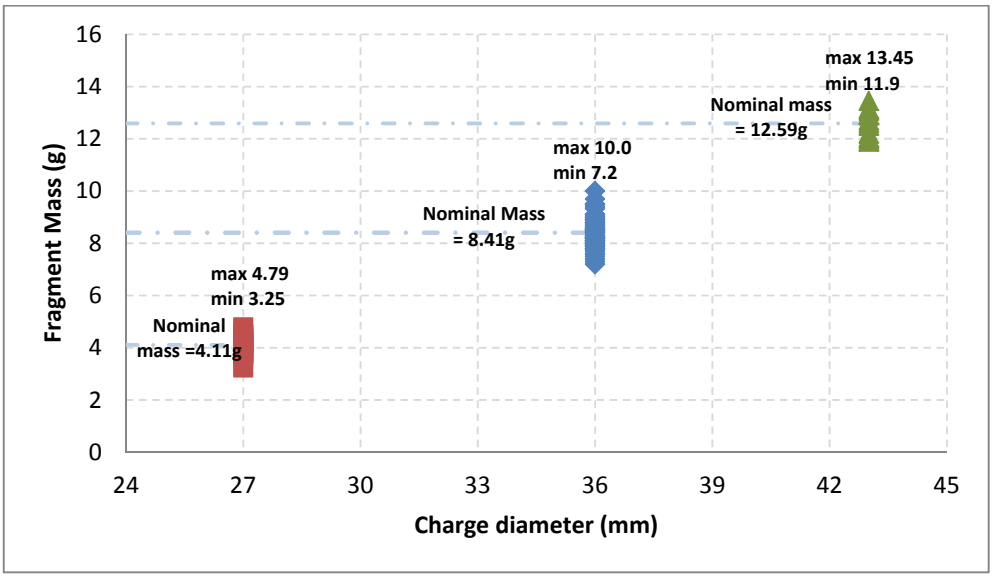

Figure 5-5: Measured fragment masses for all the fragments released by charges of the three tested diameters

The largest variation range of fragment mass for a given charge diameter is 2.8g within a coefficient of variation of 9.8% at 36mm charge diameter, whilst the fragment mass variation range for charge diameters 27mm and 43mm is 1.54g (with a coefficient of variation of 6.8%) and 1.55g (with a coefficient of variation of 4%), respectively. With the majority of the tests being carried out at a charge diameter of 36mm, a larger pool of data suggests that a wider range can be expected.

5.2.2. Speed of the fragments

The speed at which the fragments are released is noticed to increase as the charge mass increases. In the analysis of the mass of the fragment (§5.2.1.), it is noted that the mass of the fragment does not change by large amounts for a given charge diameter, even as charge mass varies. The speed, however, shows a greater amount of scatter within *distinct charge masses* for constant charge diameters. Figure 5-6 shows the fragment speed, plotted against charge mass for tests performed with the charge diameter kept at 27mm.

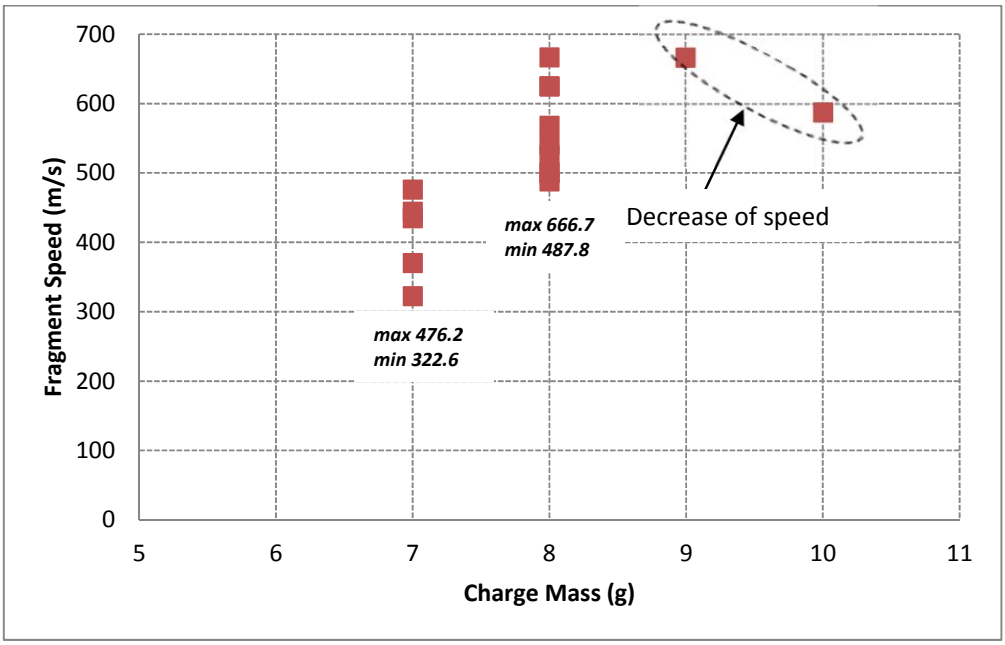

Figure 5-6: Speed of the fragment, plotted against charge mass for tests conducted at 27mm charge diameter

For charge diameter of 27mm, throughout the charge mass range, only 7g and 8g are the charge masses at which more than one test was carried out. This factor, coupled with the fact that the variation ranges of the fragment speeds for each of the two respective charge masses are 154m/s (with a coffecient of variation of 15%) and 179m/s (with a coefficient of variation of 11.6%), means that a least squares trend fit is a misleading factor and cannot be used to accurately describe the relationship between charge mass and fragment speed. An attempted linear fit through the points yields an R^2 value of 0.5 which translate to a relatively poor fit through the points. This is also the case because a decrease in speed is observed between the respective solitary data points corresponding to 9g charge mass and 10g, which is indicative of the large experimental variation in the determination of fragment speed.

The speeds measured for fragments released by **36mm diameter charges**, shown in Figure 5-7, are plotted from a larger pool of data points. There is considerable experimental variation. However, there is a clear increasing trend in the measured fragment speed as charge mass is increased from 7g to 11g.

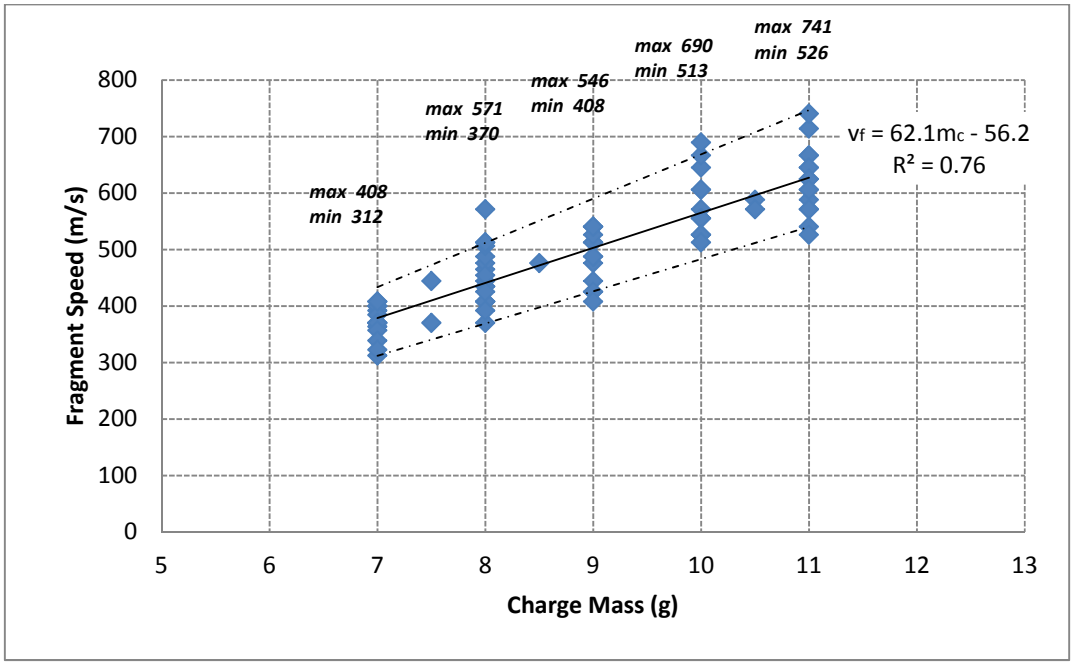

Figure 5-7: Speed of the fragment, plotted against charge mass for tests conducted at 36mm charge diameter

For a charge diameter of 36mm, the increasing relationship between fragment speed and charge mass in Figure 5-7 is approximated using a least squares linear trend, with and R^2 value of 0.76, by the expression for the speed as:

$$v_f = 62.13m_c - 56.2 \qquad \text{Eq. 5-2}$$

where m_c is the mass of the charge used (in *g*)

The dotted linear bounds are least squares trends running through the minimum and maximum values of fragment speeds for this range of charge masses. The variation range of fragment speeds for each charge mass appears to generally increase with increasing charge mass. At a charge mass of 7g, the variation range in fragment speed is 96m/s (with a coefficient of variation of 8.2%), and increases to 214m/s at 11g charge mass, with a coefficient of variation of 9.6%.

The fragment speed for **43g charge diameter** is measured for fewer data points than for the 36mm diameter. There appears to be less experimental variation and a clear increasing linear trend with an R^2 value of 0.94 (shown in Figure 5-8). The relationship between fragment speed and charge mass is given by Eq.5-3.

$$v_f = 73.4m_c - 290.1 \qquad \text{Eq. 5-3}$$

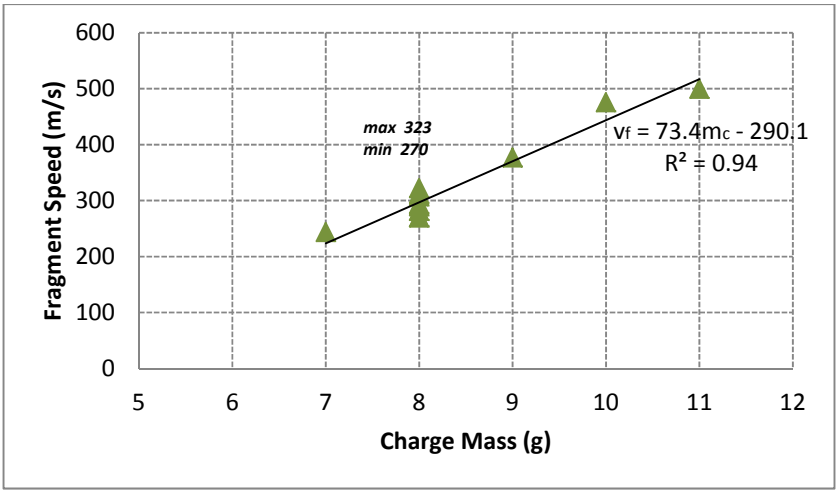

Figure 5-8: Speed of the fragment, plotted against charge mass for tests conducted at 43mm charge diameter

5.2.3. Momentum of the fragments

With the mass of each fragment known and the speed measured, linear momentum, or simply 'momentum' henceforth, can be computed and is defined as:

$$p = m_f v_f \qquad \text{Eq. 5-4}$$

where m_f is the mass of the fragment (in kg) and v_f is the speed of the fragment (in *m/s*)

The general relationship between the momentum of the fragment and charge mass is increasing. As per the analyses of impulse and fragment speed, there is a lack of data beyond 8g charge mass when the **charge diameter** is **27mm**, an inconclusive transition from 8g to 9g and a decrease in the value of momentum in the solitary data points from 9g to 10g. This experimental variation is why a trend line is not fitted through the data points; simply because it would not accurately depict the relationship between the momentum and charge mass, as shown on the graph in Figure 5-9.

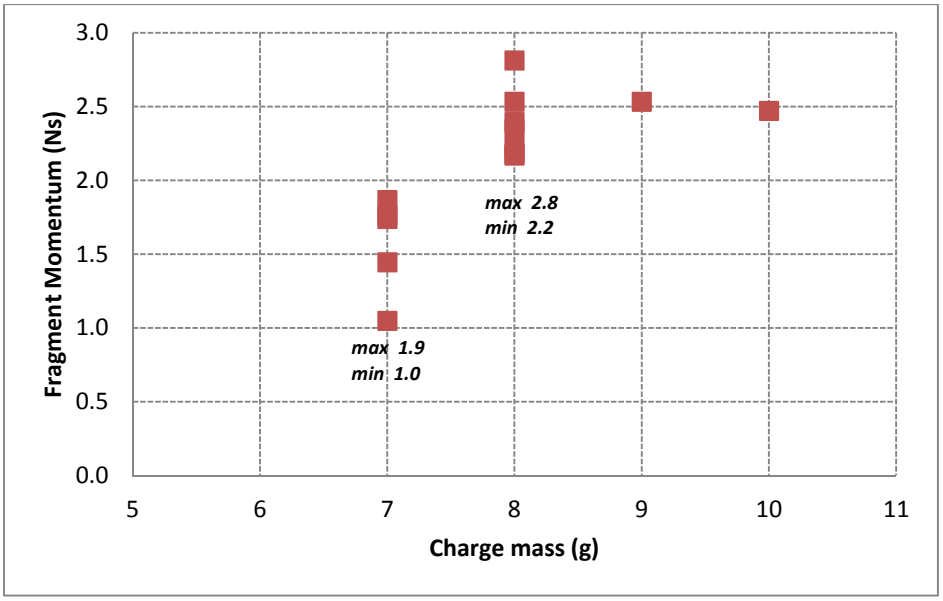

Figure 5-9: Momentum of the fragment against charge mass for tests conducted at 27mm charge diameter

As with fragment speed, there is a clear increasing relationship between the charge mass and the momentum when the charge diameters are **36mm** and **43mm** – as shown in Figure 5-10 and Figure 5-11, respectively. Experimental variation for the 36mm charge diameter accounts for the relatively wide range of momentum values for each charge mass, with an R^2 value of 0.75. The value of fragment momentum (p) as a function of charge mass at this charge diameter is expressed in Eq. 5-5.

$$p = 0.62m_c - 1.19 \qquad \text{Eq. 5-5}$$

Where : m_c is the mass of the charge used (in g)

The least squares linear fit in the case of a **charge diameter** of **43mm** shows a clear increase in momentum against charge mass and the trend fits well through the points with a R^2 value of 0.93. The momentum from the relationship is empirically given by Eq. 5-6

$$p = 0.97m_c - 4.0 \qquad \text{Eq. 5-6}$$

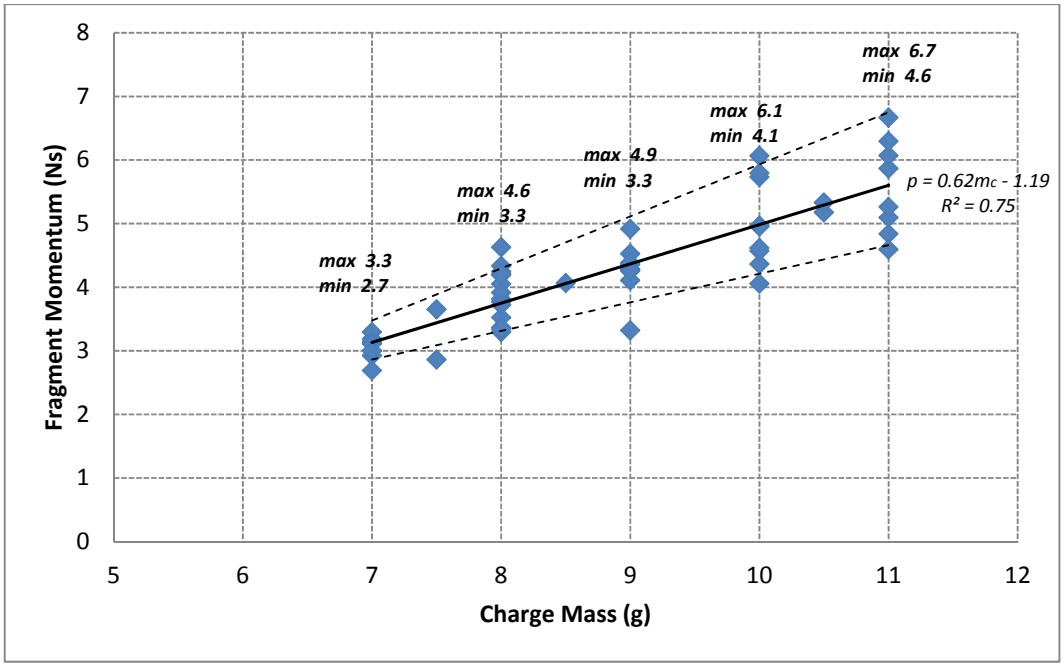

Figure 5-10: Momentum of the fragment against charge mass for tests conducted at 36mm charge diameter

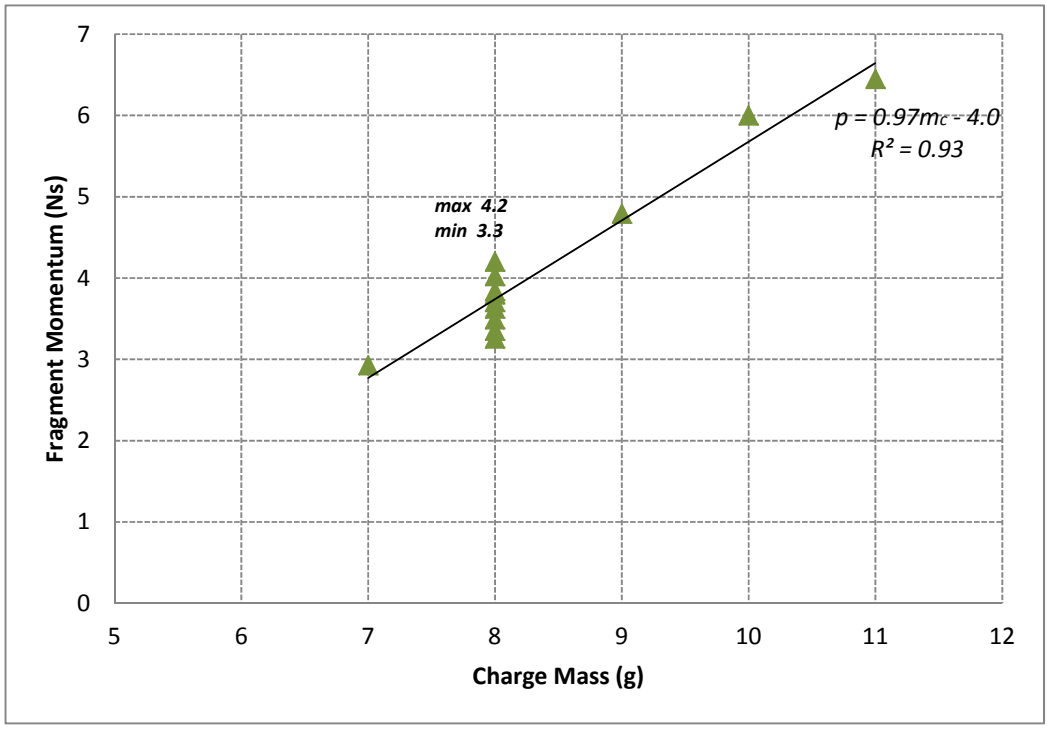

Figure 5-11: Momentum of the fragment against charge mass for tests conducted at 43mm charge diameter

5.2.4. Kinetic energy of the fragments

In a further analysis of the kinetics of the fragment, the kinetic energy of the fragment is also used which, like momentum, is a function of mass and speed of the fragment. Kinetic energy (E_k), however, is half the fragment speed more than momentum.

$$E_k = \frac{1}{2} m_f {v_f}^2 \qquad \text{Eq. 5-7}$$

Note: Based on Eq. 5-7, if the relationship between fragment momentum and charge mass is assumed to be linear, as in §5.2.3., logic dictates that the relationship between the kinetic energy and charge mass cannot be linear, but a quadratic trend, as shown in the idealised illustration in Figure 5-12. This is ideally when data points in the momentum-charge mass relationship are well defined and lying on the assumed linear trend line. The kinetic energy-charge mass relationships in this study are thus approximated by quadratic least squares fits.

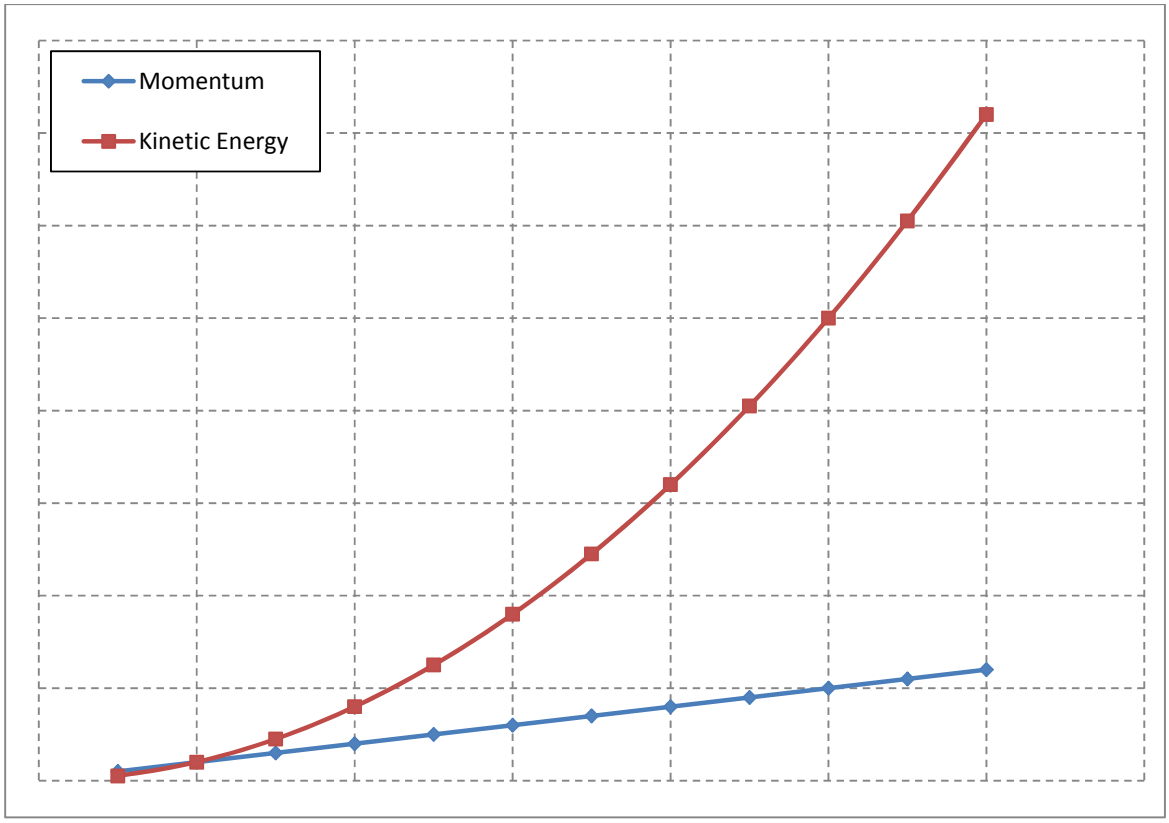

Figure 5-12: A generic ideal transition of trends from assumed momentum (linear) to a consequent kinetic energy trend

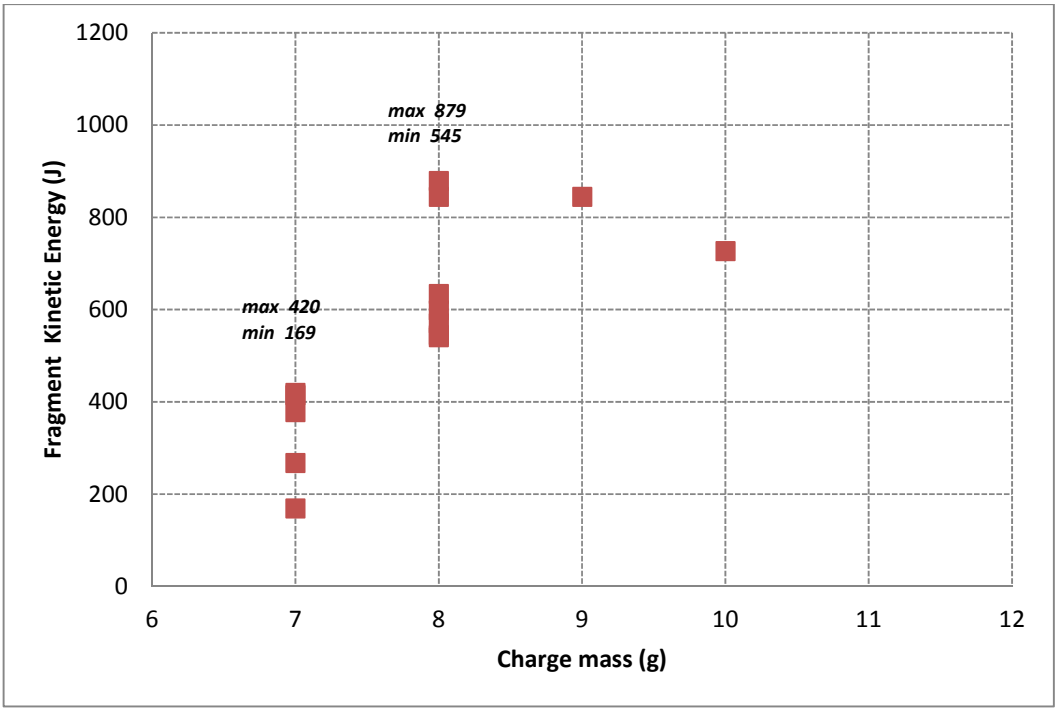

Figure 5-13: Kinetic energy of the fragment against charge mass for tests conducted at 27mm charge diameter

The kinetic energy of each of the fragments released from the plates by a **charge diameter** of **27mm** is shown in Figure 5-13. Similar to the analysis carried out on the speed and momentum of the fragment for the charge diameter of 27mm, the few data points which are beyond 8g charge mass make it impossible to conclude the exact in which the kinetic energy increases as charge mass increases. For this reason, a trend line is not plotted, although it is clear that increasing charge mass results in an increase in kinetic energy of the released fragment.

For the **charge diameter** of **36mm**, kinetic energy increases with increasing charge mass in a more apparent relationship, as shown in Figure 5-14. The considerable experimental variation in the speed of the fragment, as discussed in §5.2.2., and the fact that the speed is squared in the formula determining the kinetic energy ($E_k = \frac{1}{2} m_f {v_f}^2 = \frac{1}{2} p v_f$), results in a wide variation range in the values of the energy for each charge mass. At the minimum charge mass of 7g the variation range of kinetic energy is 256J within a coefficient of variation of 14.6%, and the variation range increases to 1072J at a charge mass of 11g with a relatively large corfficient of variation of 20.5%.

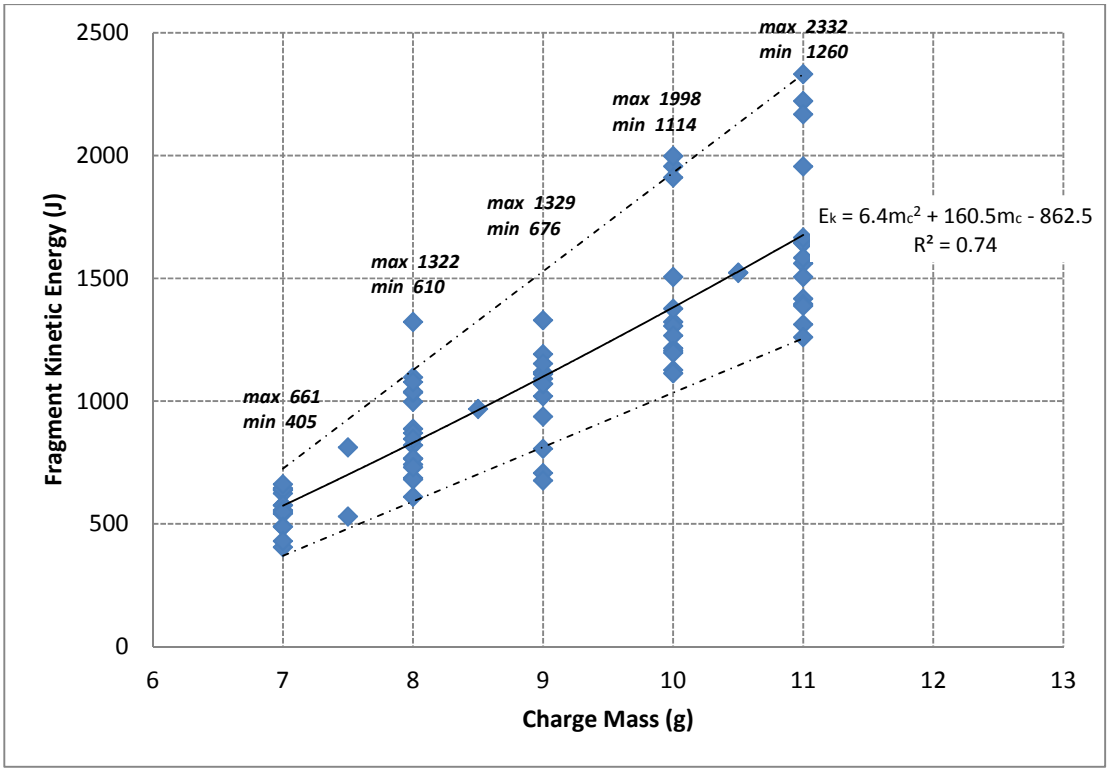

Figure 5-14: Kinetic energy of the fragment against charge mass for tests conducted at 36mm charge diameter

A quadratic trend is assumed for this increase in kinetic energy. The kinetic energy of the fragment, however, due to this scatter, is unpredictable for any given charge mass. For 11g, for example, the resulting released fragment can have a kinetic energy as little as 1260J or as much as 2332J. An R^2 value of 0.74 is a result of the experimental variation. The equation for the kinetic energy, as a function of charge mass is found to be:

$$E_k = 6.4{m_c}^2 + 160.5m_c - 862.5 \qquad \text{Eq. 5-8}$$

Where : m_c is the mass of the charge used (in g)

For a **charge diameter** of **43mm** a clear increasing trend of kinetic energy of the fragment against increasing charge mass is observed, as shown in Figure 5-15. A quadratic relationship appears to fit well through the data points with an R^2 value of 0.95. The equation relating fragment kinetic energy and charge mass is found and expressed in Eq. 5-9.

$$E_k = 22.1{m_c}^2 - 44.4m_c - 502.7 \qquad \text{Eq. 5-9}$$

Where : m_c is the mass of the charge used (in g)

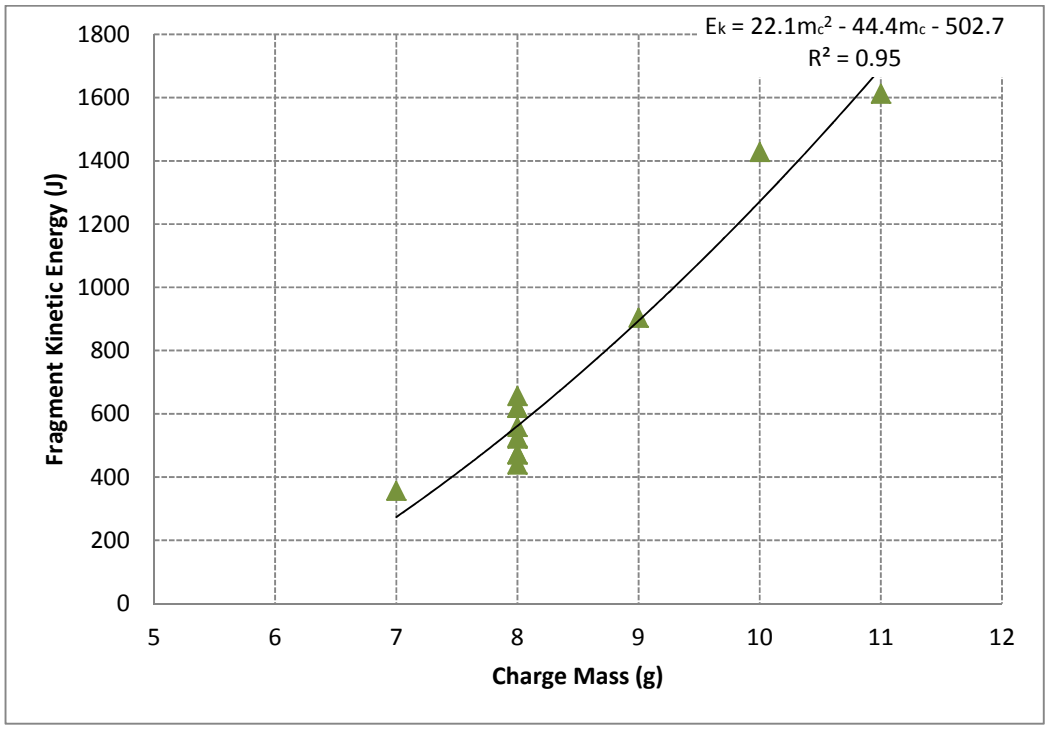

Figure 5-15: Kinetic energy of the fragment against charge mass for tests conducted at 43mm charge diameter

5.3. Damage to rear plate without energy absorbers

As discussed in the results (Chapter 4), damage to the rear plate is quantified through the mode of failure and the maximum deflection. The separation distance between the two plates was initially 150mm when there as no energy absorber protecting the rear plate and then it increased to 190mm when the rig is slightly modified to accommodate the energy absorbers. Additional tests without energy absorbers were carried out at a separation distance of 190mm to verify that the alteration of the separation by 40mm does not affect the plate failure.

5.3.1. Variation of plate separation distance without energy absorbers

Figure 5-16 shows how variation between the two plate separation distances affects the maximum rear plate deflection for all three charge diameters. The linear trends run through all the points within their respective charge diameters, regardless of the plate separation. The dotted lines enveloping each trend are offset 1.6mm (which is the plate thickness) vertically above and below the trend line. Each band represent an experimental variation zone in which there can be 90% confidence that any point inside that zone is within ±1 plate thickness of the least squares fit trend line [14].

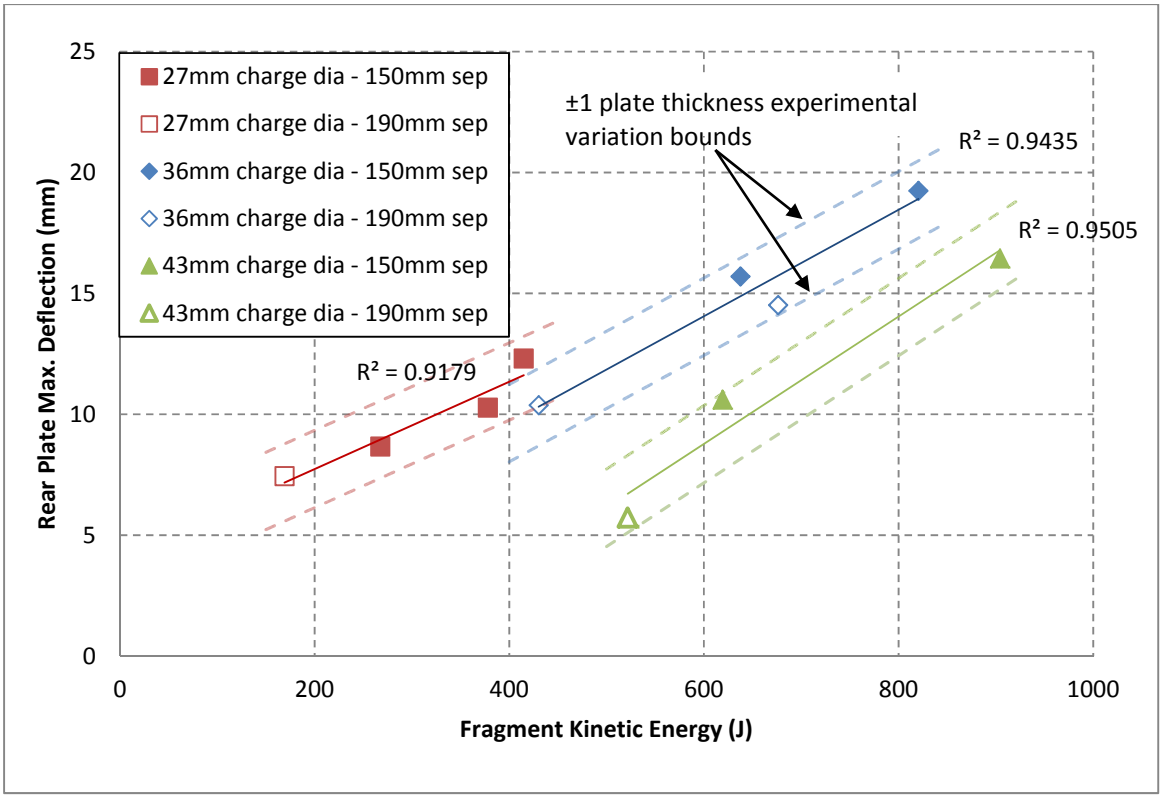

Figure 5-16: Rear plate deflection against fragment kinetic energy with no energy absorber at 150mm and 190mm plate separation

For all the three load diameters, the measured rear plate deflections from both separation distances lie within the 90% experimental variation bounds. Furthermore, the least squares linear trend line which runs through all the points in each of the three cases has a fit with R^2 values of 0.92, 0.94 and 0.95 for fragment impacts from the 27mm, 36mm and 43mm charge diameters respectively. Therefore, for all three load diameters and between the two plate separation distances, it appears that an increase of separation by 40mm is minor and has no significant effect on the response of the rear plate.

5.3.2. Rear plate tearing limits - no energy absorbers

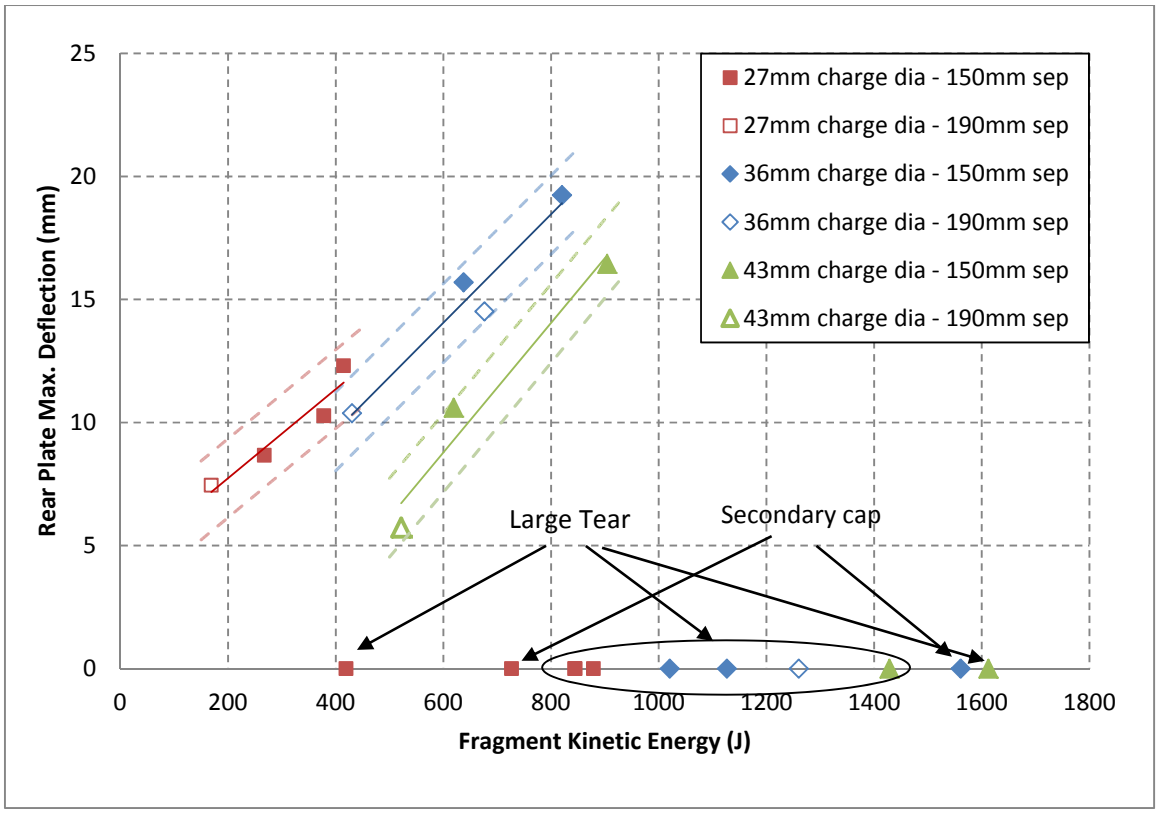

Figure 5-17: Rear plate deflection against fragment kinetic energy with no energy absorber - showing plate tearing points

For all three charge diameters, inelastic deflection evolves into small tearing when the charge mass is increased or when the fragment tends to strike the plate on its edge. A further increase in charge mass or edge-normal impact culminates in large tearing, where rear plate deflection cannot be measured. In some cases, full tearing of the rear plate occurs (secondary capping). Figure 5-17 shows the plate tearing points, in addition to the measured rear plate deflections, plotted against kinetic energy of the fragment for all three charge diameters.

For the case of fragment impact resulting from charges of 27mm diameter, the largest fragment kinetic energy at which rear plate deflection can be measured, with no absorber protecting the plate, is 415J; 820J for 36mm charge diameter and for the charge diameter of 43mm, 930J is the maximum fragment kinetic energy at which rear plate deflection can be measured.

Fragment kinetic energies which are greater than the aforesaid limits are observed to result in the fragment perforating the rear plate and consequently subjecting it to large or complete tearing such that it is not possible to quantify the plate damage by deflection.

5.3.3. Theoretical analysis

5.3.3.1. Dimensionless analysis – Zhao's response number

Zhao's response number uses dimensionless analysis to categorise the damage on a metallic beam or plate caused by an impact or any dynamically impinging load [65]. It is described as:

$$R_n = \left(\frac{l}{h}\right)^2 \left(\frac{\rho {v_0}^2}{\sigma_0}\right) = \left(\frac{R}{h}\right)^2 \left(\frac{\rho {v_f}^2}{\sigma_0}\right) \qquad \text{Recall Eq. 2-7}$$

Where : R_n= Zhao's Response number, l= half length of the plate, h= plate thickness, ρ= plate density, v_0= impact velocity, σ_0= static yield stress of plate

For this study, the impact velocity (v_0) is the velocity of the fragment (v_f) and the half length of the plate (l) is taken as the plate radius (R). Figure 5-18 shows the relationship between dimensionless rear plate deflection (δ/h ratio) and Zhao's response number for tests without energy absorbers, with all three charge diameters taken into account. From the graph in Figure 5-18 it is clear that the relationship between dimensionless deflection and the response number depends on the size of the impacting fragment. The equations for that relationship for the three charge diameters are shown in Table 5.2. For all tests without energy absorbers and where the rear plate deflection is measured, the applicable Zhao's response numbers are between **2000** and **6000**. It is also observable from the graph that for **all three** charge diameters, a Zhao's response number of about **6794** is the minimum number at which large tearing is observed for the plates struck. It appears that when the size of the fragment increases, the rate of increase of the deflection relative to the response number increases as

well. It can also be inferred that if the deflection of three plates struck by different sized fragments is equal, the response number is the highest for the plate struck by the smallest fragment and lowest for the plate struck by the largest fragment.

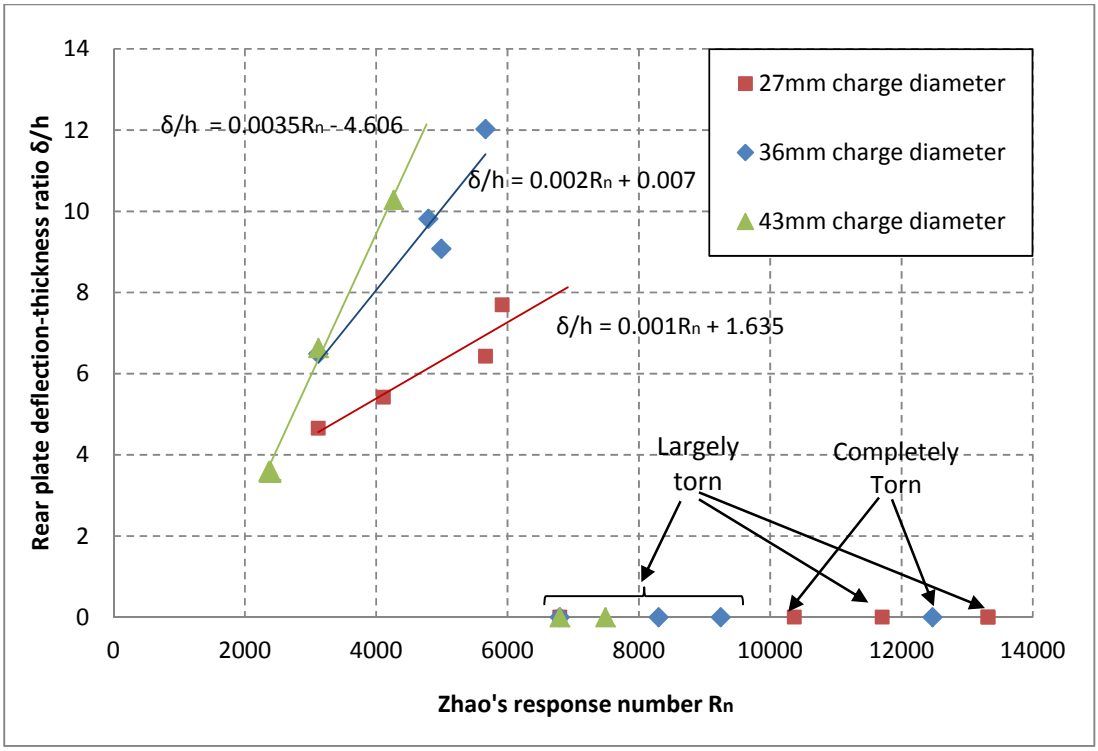

Figure 5-18: Rear plate deflection to thickness ratio against Zhao's Response number for tests with no absorbers

Table 5.2: Relationship between dimensionless deflection and Zhao's Response number for different fragments

Charge diameter (mm)	Average fragment diameter (mm)	Empirical relationship between dimensionless deflection and Zhao's Response number	
27	25.73	$\delta/_h = 0.001R_n + 1.635$	Eq. 5-10
36	34.04	$\delta/_h = 0.002R_n + 0.007$	Eq. 5-11
43	40.08	$\delta/_h = 0.0035R_n - 4.606$	Eq. 5-12

5.3.3.2. Theoretical prediction of rear plate deflection

For the experiments conducted in the absence of energy absorbers, the rear plate deflection is measured for those plates which are not subjected to large tearing or secondary capping. A theoretical prediction of determining the deflection of a plate subjected to impact by a projectile (fragment) was presented graphically by Baker et al. [3], as shown in Figure 2-23. The graphical relationship is found to be interpreted by Eq. 2-15.

$$\delta = \frac{{R_f}^2}{h}\left(0.5\frac{\rho_f v_f}{\sqrt{\sigma_p \rho_p}} - 0.034\right)$$ Recall Eq. 2-15

Where : δ = rear plate deflection, R_f= fragment radius, ρ_f= Fragment density,

v_f= fragment speed, h= plate thickness, σ_p= Plate yield stress, ρ_p= Plate density

In this study, $\rho_f = \rho_p = 7870 kg/m^3$ (Table 3.3)

$h = 1.6mm = 0.0016m$ (Nominal)

$\sigma_p = \sigma_0 = 288.2MPa$ (from uniaxial tests) (Table 3.3)

Table 5.3 lists the predicted rear plate deflections (using Eq. 2-15) and the measured deflections from the experiments. As it can be noticed, the predicted deflections are greater than the measured deflections by a substantial margin in which it is difficult to attribute the overestimated difference to experimental variation. The discrepancies in the prediction and the experimental measurement suggest that this method is not for the type of projectile impact as carried out in this study.

Table 5.3: Summary of predicted and measured rear plate deflection for tests carried out with no energy absorbers

Test Description	Fragment Radius	Fragment Speed	Predicted deflection	measured deflection
	(mm)	(m/s)	(mm)	(mm)
NA00-2707-T1	12.45	444.4	109.20	12.31
NA00-2707-01	13.00	370.4	98.62	8.67
NA00-2707-02	12.87	434.8	113.99	10.28
NA00-2707-04	12.87	322.6	83.67	7.45
NA00-3607-01	16.88	400.0	179.96	15.7
NA00-3607-02	16.98	322.6	145.75	10.38
NA00-3608-01	17.50	434.8	210.93	19.24
NA00-3609-03	17.06	408.2	187.81	14.52
NA00-4308-01	20.88	322.6	220.29	10.61
NA00-4308-02	19.89	281.7	173.58	5.73
NA00-4309-01	20.63	377.4	253.10	16.45

*Note: The theoretical analysis carried out in §§5.3.3.1. and 5.3.3.2. cannot be applied to the tests in which energy absorbers are present in front of the rear plate because the speed of the fragment that is used in Eq. 2-7 and Eq. 2-15 is the speed which the fragment strikes the plate. The energy absorbers decelerate the fragment to an unknown speed required for the equations.

5.3.3.3. Theoretical prediction of critical perforation energy

In §2.1.4.3., the BRL equation is referred to as a tool for predicting the energy (critical energy) beyond which a carbon steel target is perforated by an incoming flat head or hemispherical projectile or fragment [68]. The governing equation is described by:

$$E_c = 1.44 \times 10^9 . \left(d_f . h\right)^{1.5}$$ Recall Eq. 2-17

Where d_f = diameter of fragment/projectile, h = target thickness

If the diameter of the fragment is assumed to be the average fragment diameter as reported in §4.2, and the thickness of the target is 1.6mm, then for the three charge diameters, the comparison between the prediction of critical perforation energy and the reported maximum energy **before which** tearing is observed (§5.3.2.) is made in Table 5.4.

Table 5.4: Comparisons between the critical perforation energy prediction and maximum experimental energy reported before perforation

Charge diameter (mm)	Average fragment diameter (mm)	Maximum kinetic energy before large tearing/perforation (J)	Predicted critical perforation energy by BRL Equation (J)
27	25.73	414.8	380.4
36	34.04	820.4	578.9
43	40.08	930.0	739.4

The BRL relation underestimates the critical perforation in all three cases. It may be a conserved approach, however, Ohte et al [69] pointed out in their investigations that the BRL method is not the most accurate in predicting the critical energy.

5.4. Damage of rear plate protected by 40mm thick absorbers

All six materials – aluminium foam, aluminium honeycomb, balsa wood, Corecell foam, Divinycell foam and polyurethane foam – are tested at a thickness of 40mmwith a **36mm charge diameter**. In this first test series, each material is tested at increasing fragment kinetic energies and then its response is quantified and subsequently compared to the other materials at this thickness.

5.4.1. Aluminium foam

Figure 5-19 shows how much the rear plates deflects when aluminium foam is used to protect the plate. A linear trend is assumed and all the measured plate deflections across all the kinetic energies lie well within the one plate thickness bounds with an R^2 value of 0.93. As kinetic energy of the fragment increases, the rear plate deflection also increases. The slope of the least fit relationship is 0.006mm/J.

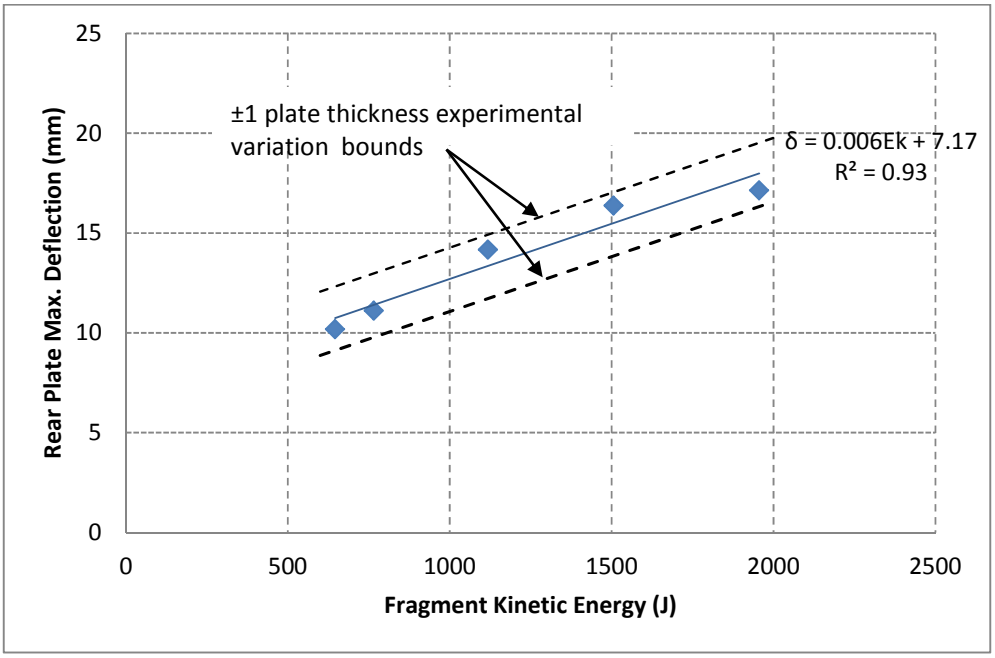

Figure 5-19: Rear plate deflection against fragment kinetic energy for tests with 40mm thick aluminium foam

5.4.2. Aluminium honeycomb

As discussed in §5.2.4., kinetic of the fragment can vary greatly and unpredictably within a given charge mass (Figure 5-14), and thus it can be noticed in the plot for aluminium honeycomb (Figure 5-20) that there appears to be a considerable jump in fragment kinetic energy from 542J to 1028J. Even though rear plate tearing occurs at 1644J of fragment kinetic energy, the remaining points, at which deflection can be measured, fit well within the one plate thickness band of a linear least squares fit with an R^2 value of 0.93. The honeycomb fails to prevent the rear plate from tearing when the kinetic energy of the fragment increases beyond 1300J.

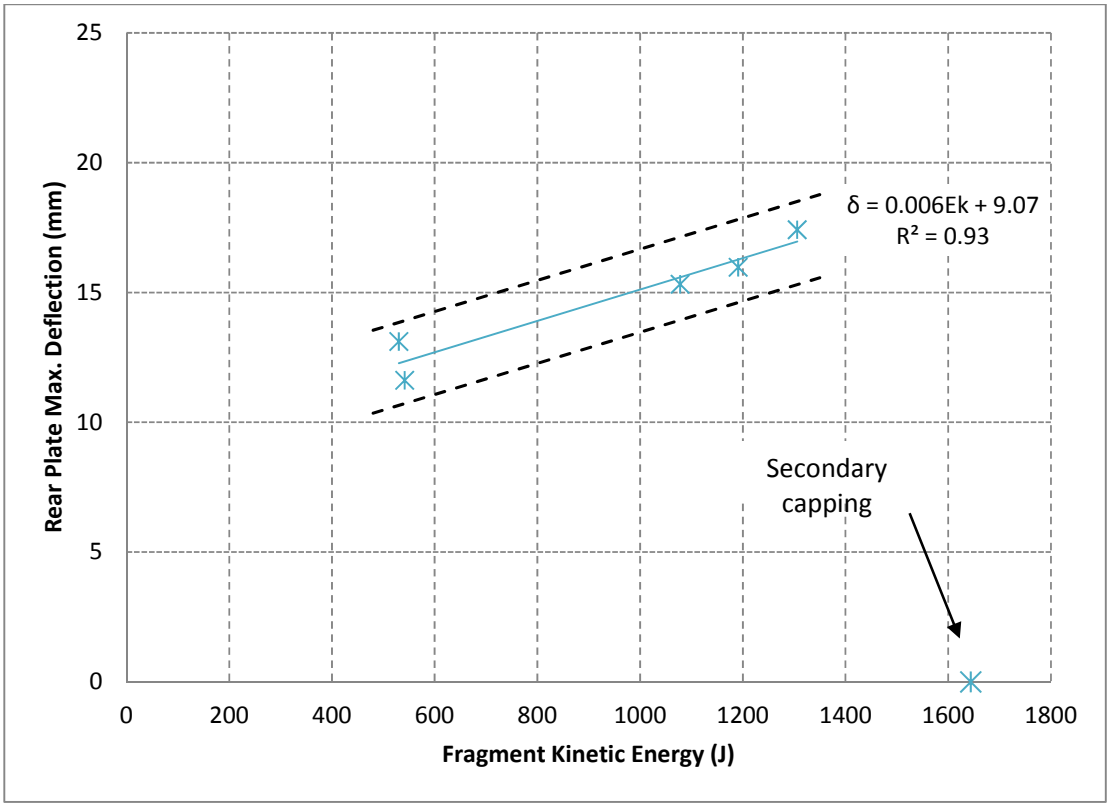

Figure 5-20: Rear plate deflection against fragment kinetic energy for tests with 40mm thick aluminium honeycomb

5.4.3. Balsa wood

For balsa wood, as shown in Figure 5-21, the rear plate deflection measurement points, can be related to fragment kinetic energy by a linear relationship, all lie within the one plate thickness variation of 1.6mm above or below the deflection profile represented by the linear least squares fit.

Between the two fragment kinetic energies of 1091J to 1998J in the deflection-energy trend, rear plate deflections of 16.1mm and 19.4mm are measured, however in the two cases in which the kinetic energy is 1522.5J and 1523.3J, the plate is observed to fail by large tearing, as also for the case for when the fragment kinetic energy is 2330J.

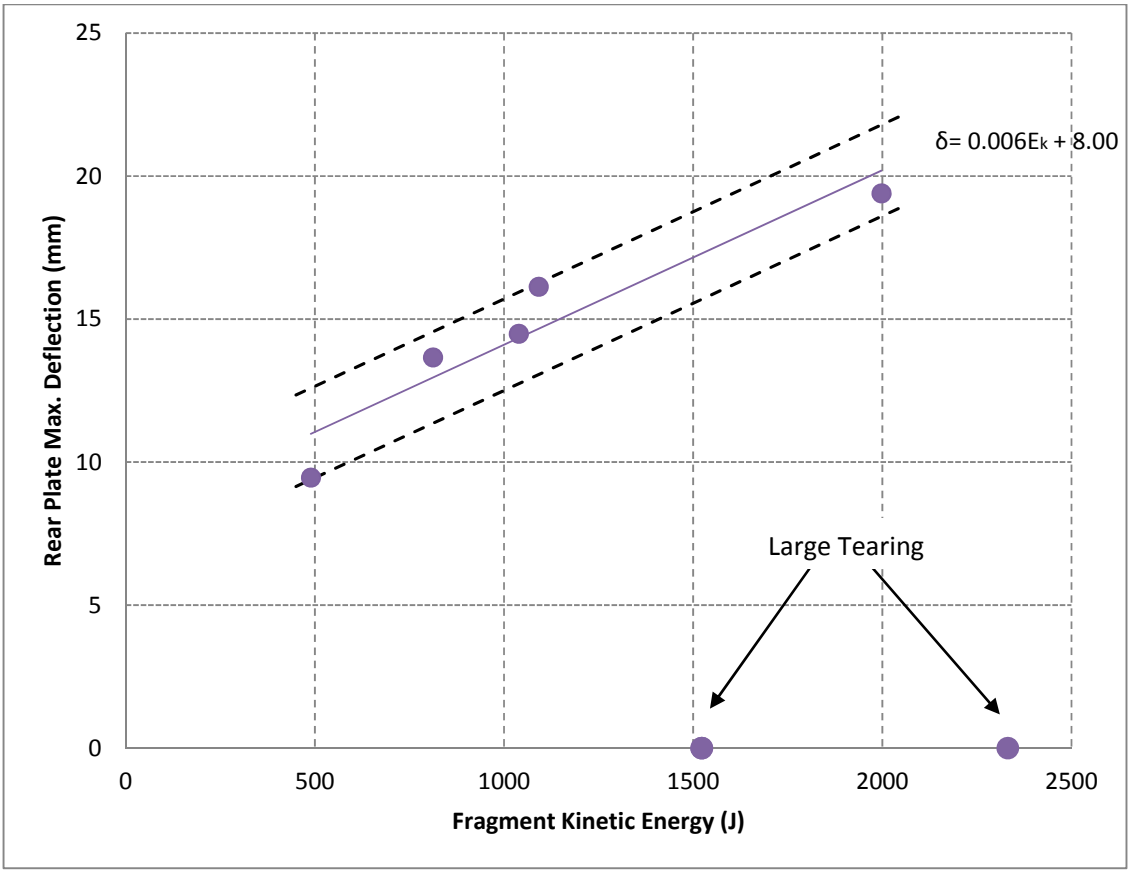

Figure 5-21: Rear plate deflection against fragment kinetic energy for tests with 40mm thick Balsa wood

5.4.4. Corecell foam

Corecell foam, of which the relationship between rear plate deflection and fragment kinetic energy is shown in Figure 5-22, appears to prevent large tearing in the rear plate until the fragment kinetic energy reaches 1322J, where the rear plate deflection is 16.44mm. Beyond 1322J, large tearing is observed. A point of experimental variation, however, is observed at 1097J where tearing of the rear plate is observed. Furthermore, for the data points corresponding to measurable deflections, the assumed linear relationship has a gradient of 0.005mm/J, with all the deflections lying within the one plate thickness of the least squares fit and an R^2 correlation of 0.92.

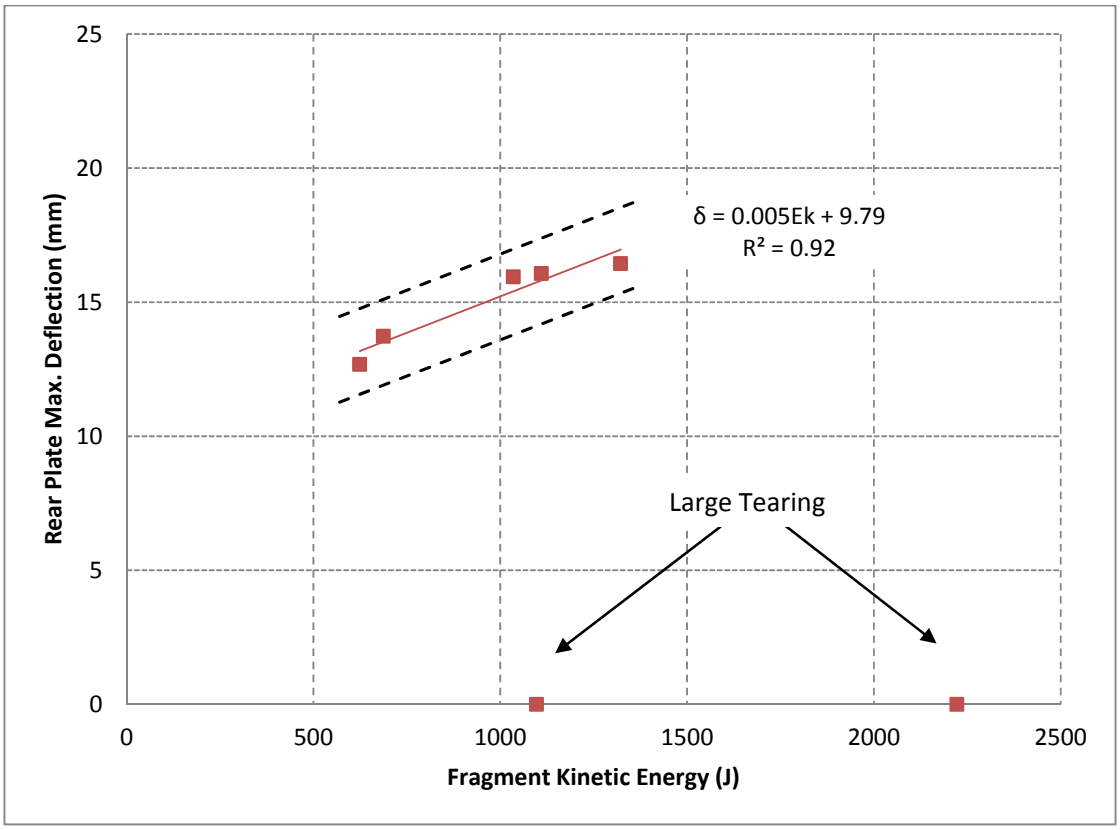

Figure 5-22: Rear plate deflection against fragment kinetic energy for tests with 40mm thick Corecell foam

5.4.5. Divinycell foam

Divinycell foam is observed to protect the rear plate from any tearing for all fragment impacts, the largest of which has an incoming fragment kinetic energy of 1956J, as is shown in Figure 5-23. The linear least squares trend has a computed slope of 0.004mm/J and yields an R^2 value of 0.73. Most of the data points for Divinycell foam lie within of the one plate thickness zone with an R^2 value of 0.73. It was observed that at a kinetic energy of about 2170J, the plate protected by 40mm thick Divinycell foam fails by large partial tearing.

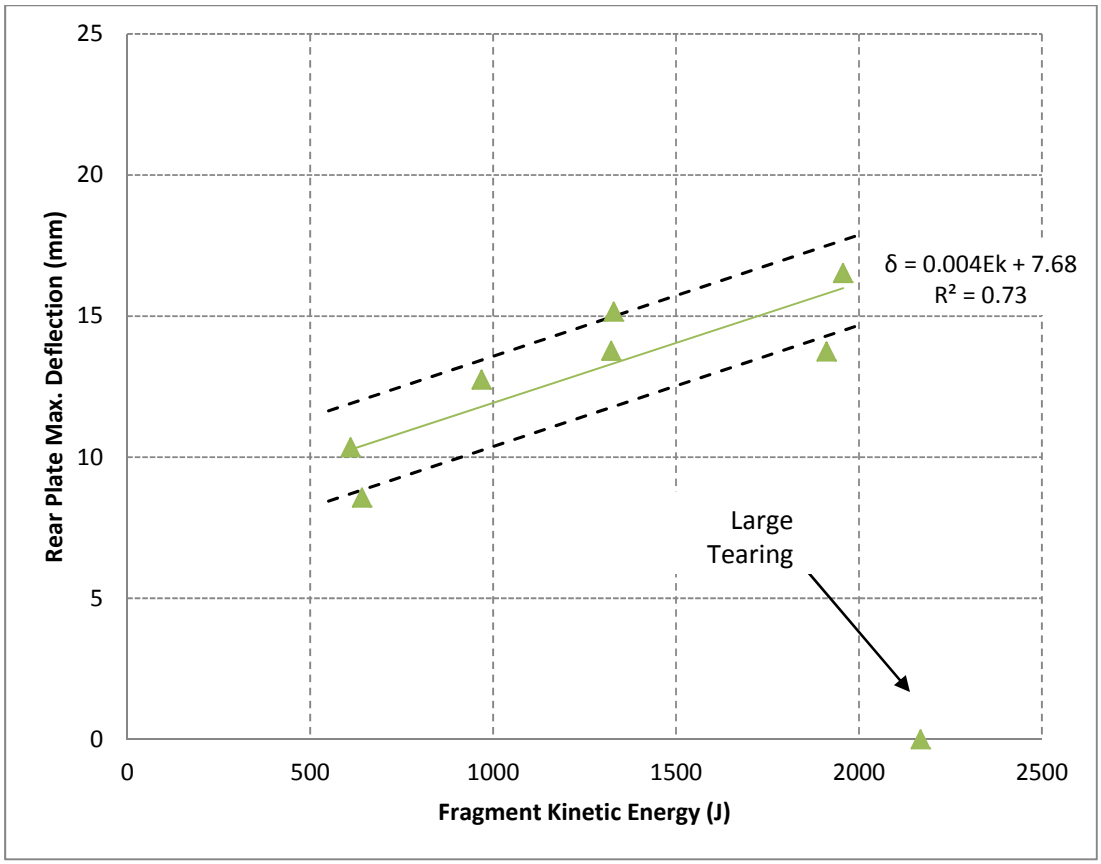

Figure 5-23: Rear plate deflection against fragment kinetic energy for tests with 40mm thick Divinycell foam

5.4.6. Polyurethane foam

Figure 5-24 is a graph showing varying the kinetic energy of the fragment affects the rear plate response when 40mm thick polyurethane foam is used. The slope of the assumed linear relationship is notably greater than that of the other five materials – 0.01mm/J compared to the second largest of 0.006mm/J. This suggests that at 40mm thickness, as the kinetic energy of the fragment increases, the level at which the polyurethane foam mitigates damage from the impact decreases at a greater rate than in the other materials. The points of the deflection-kinetic energy relationship of polyurethane foam lie well within the one plate thickness zone with an R^2 value of 0.99.

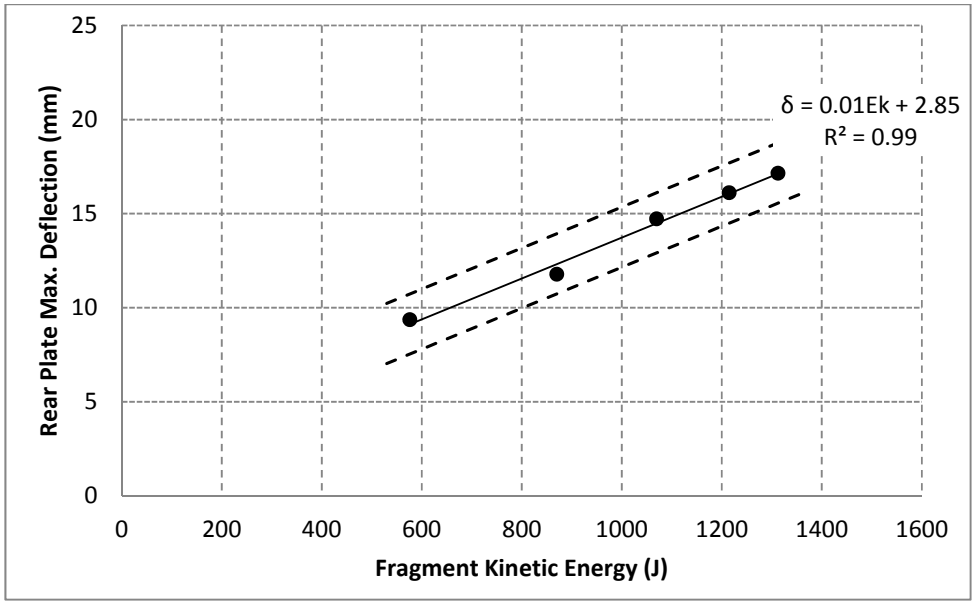

Figure 5-24: Rear plate deflection against fragment kinetic energy for tests with 40mm thick polyurethane foam

5.4.7. Summary

In the comparative plot, shown in Figure 5-25, it is notable that polyurethane foam, at lower fragment kinetic energies, exhibits protective performance which lies in the same zone as that of Divinycell foam, and at higher energies, its mitigation of plate deflection decreases to the zone of the mean trends of Corecell foam and aluminium honeycomb. In the same plot (Figure 5-25), the rear plate deflections – when the plates are protected by the energy absorbing materials – are comparatively plotted alongside the case where there are **no absorbers** to mitigate deflection from fragments generated by 36mm diameter charges.

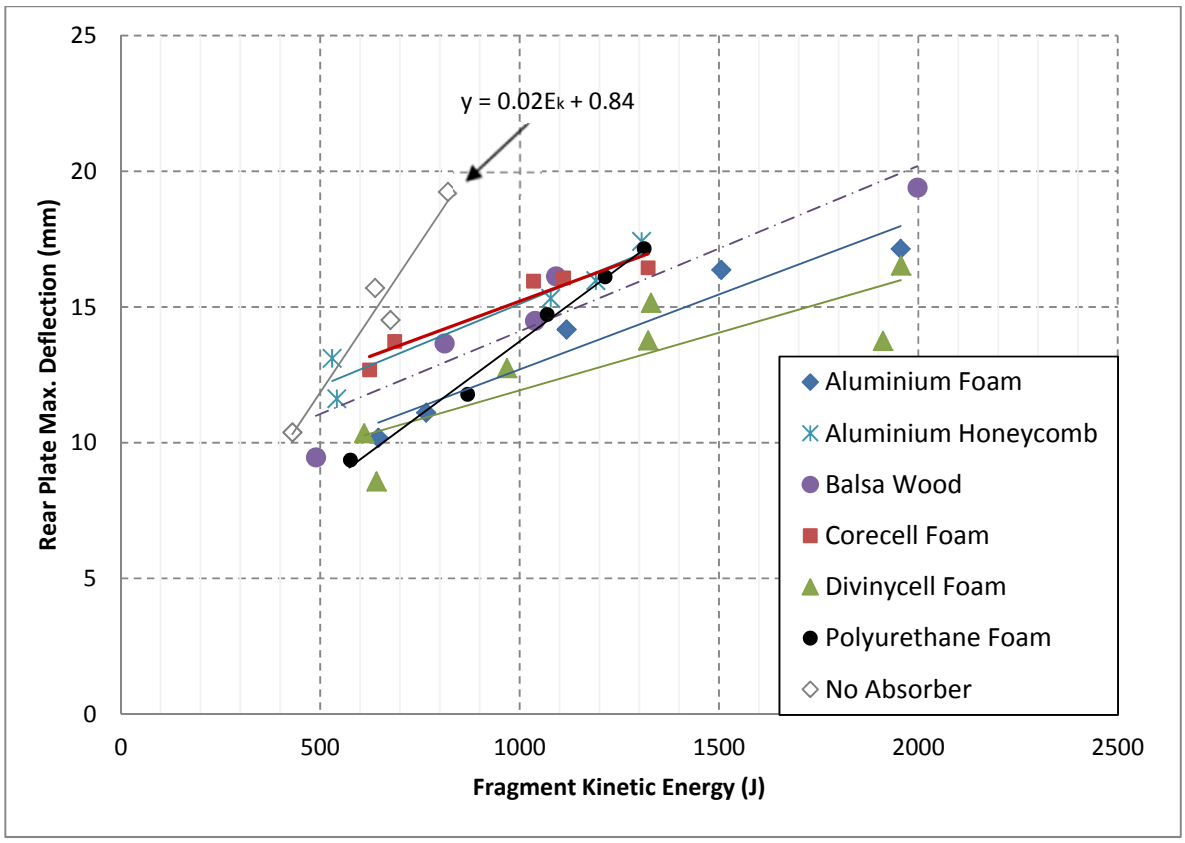

Figure 5-25: Comparative plot of rear plate deflection against fragment kinetic energy for all energy absorbers at 40mm thickness

At lower kinetic energies (around 600J) the impact mitigation provided by aluminium honeycomb and Corecell foam is close to the data when no energy absorber is used. The rest of the energy absorbers are better at reducing the rear plate deflection in this energy regime.

Moreover, for all the materials, in general, due to the shallow slopes of their deflection-energy profiles, compared to that when no energy absorber is present (0.02mm/J), it is apparent that as the kinetic energy of the fragment increases, the extent to which energy absorbers mitigate plate deflection from the impact increases.

Based **purely** on the equations of the assumed linear relationships between rear plate deflection and kinetic energy and *not* the measured values of rear plate deflections,

Table 5.5 is generated to show the mean (calculated) decrease in rear plate deflection by each energy absorbing material compared to when no absorber is present. Since it is a comparison to the case where no absorbers are used, *this in only carried out in the kinetic energy domain where deflection is measured for no absorbers (between 430J and 820J)* because no fragments having a kinetic energy less than 430J were generated by the 36mm diameter charge; whereas beyond 820J, large tearing occurs when there is no absorber.

Table 5.5 can be taken as directly interpreted from the trends on the plot in Figure 5-25. The reason the kinetic energy values in the table jump from 430 to 650J is that based on the fragment kinetic energy, the minimum kinetic energy at which **all the materials** can be compared is 645J. The table also stops at a fragment kinetic energy of 820J, which the maximum energy at which deflection could be measured when there are no absorbers mitigating the fragment impact.

Table 5.5: Decrease in calculated mean rear plate deflections at fragment kinetic energy intervals for 40mm thick absorbers compared to when no energy absorber is present

Fragment Kinetic Energy (J)	**430**	**650**	**690**	**730**	**770**	**810**	**820**
Rear Plate Deflection for 'No Absorber' (mm)	10.30	15.14	16.02	16.90	17.78	18.66	18.88
Decrease in rear plate deflection (mm) *(projected by linear trend equations)*							
Aluminium Foam	-	4.39	5.05	5.71	6.37	7.03	7.20
Aluminium Honeycomb	-	2.17	2.81	3.45	4.09	4.73	4.89
Balsa Wood	-	3.17	3.80	4.44	5.08	5.71	5.87
Corecell Foam	-	1.83	2.50	3.16	3.83	4.49	4.66
Divinycell Foam	-	4.67	5.58	6.30	7.02	7.74	7.92
Polyurethane Foam	-	5.20	5.64	6.09	6.53	6.97	7.09

*Cells shaded in red indicated lowest decrease in deflection for the specific fragment kinetic energy, whereas cells shaded in green indicate highest decrease in deflection for the specific fragment kinetic energy

From

Table 5.5 and Figure 5-25 it can be inferred that Divinycell foam provides the highest level of mitigation beyond 700J. It is expected to decrease the deflection when by 7.9mm at a fragment kinetic energy of 820J compared to when no absorber is present. It is followed by aluminium foam, and balsa wood. Corecell foam and aluminium honeycomb appear to provide the least mitigation, whereas polyurethane foam, as previously stated, has a steeper deflection profile which translates to its impact mitigation effect being better than that of Divinycell foam at the lowest fragment kinetic energy and degrading with increasing fragment kinetic energy.

5.5. Damage of rear plate protected by 60mm thick absorbers

In the second test series, Balsa wood, Divinycell foam and polyurethane foam are tested at a thickness of 60mm where the charge mass is increased from 7g to 11g while the charge diameter is maintained at 36mm. The tests are undertaken to investigate the effects of increasing the thickness of an energy absorber on the rear plate damage. Figure 5-26 is a graph of **balsa wood** at 60mm thickness, where rear plate deflection is plotted against kinetic energy of the fragment. The linear least squares trend fit through the 60mm thick balsa wood deflection-kinetic energy relationship yields an R^2 value of 0.78 owing to experimental variation.

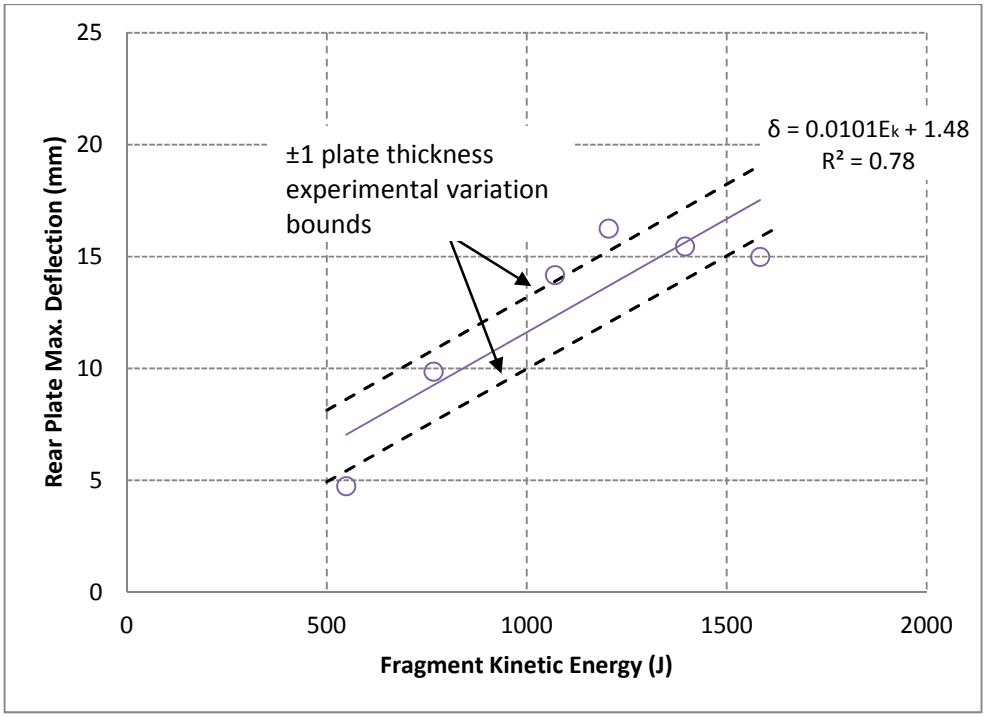

Figure 5-26: Rear plate deflection against fragment kinetic energy for tests with 60mm thick Balsa wood

The impact mitigation provided by the 60mm thick balsa absorber is compared to the same material (balsa wood) tested in the first 40mm thickness series, see Figure 5-27. It is apparent that the mitigation of damage provided by the 60mm balsa wood is considerably greater than that of 40mm thick balsa wood at the lower fragment kinetic energies (about 550J). The 60mm thick balsa wood, however, has a steeper rear plate deflection profile (slope of 0.01mm/J) than the 40mm thick counterpart (0.06mm/J) and consequently it is notable that at the largest fragment kinetic energy that the *60mm thick balsa wood* is subjected to (about 1500J), its mitigation of damage is observed to have decreased to be on par with the 40mm thick energy absorber. As the sectioned photographs of the balsa wood in Figure 5-27 show, at the lowest fragment kinetic energies, 40mm thick balsa wood is perforated whereas significantly less

damage occurs for the 60mm thick balsa wood where no perforation occurs. Around 1500J, the 60mm thick balsa wood undergoes perforation; the damage on the 40mm thick wood is progressively greater as well. The plots and photographs suggest that the additional 20mm disc (for the 60mm thick wood) does not improve the damage mitigation provided by 40mm thick balsa wood beyond a fragment kinetic energy of 1500J although more damage is observed at the exit face of the 40mm thick absorber.

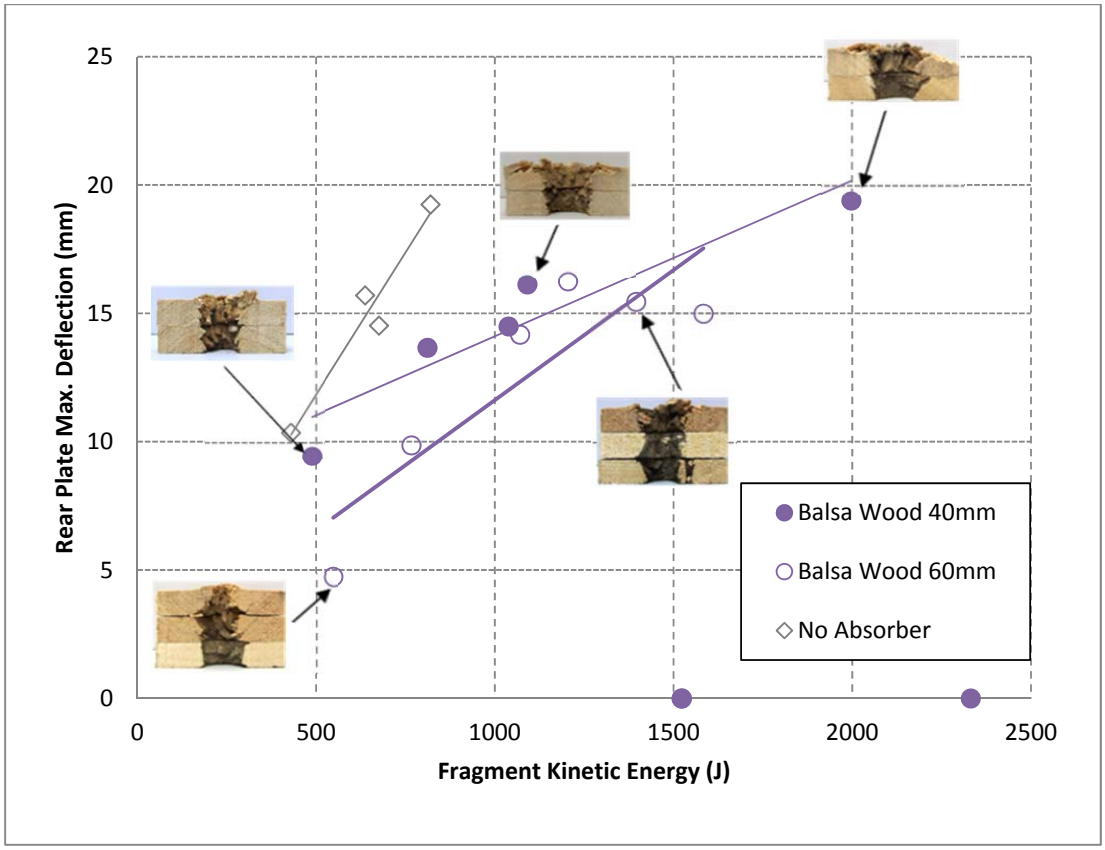

Figure 5-27: Change in rear plate deflection against kinetic energy when Balsa wood thickness increases to 60mm

Divinycell foam, which was also tested at 60mm thickness, shows a better linear fit of rear plate deflection against kinetic energy of the fragment, as shown in Figure 5-28 – all five data points fall within the one plate thickness variation interval. The 0.013mm/J slope of the Divinycell foam least squares fit is similar to that of 60mm thick balsa wood. The trend runs through the data points with an R^2 value of 0.96.

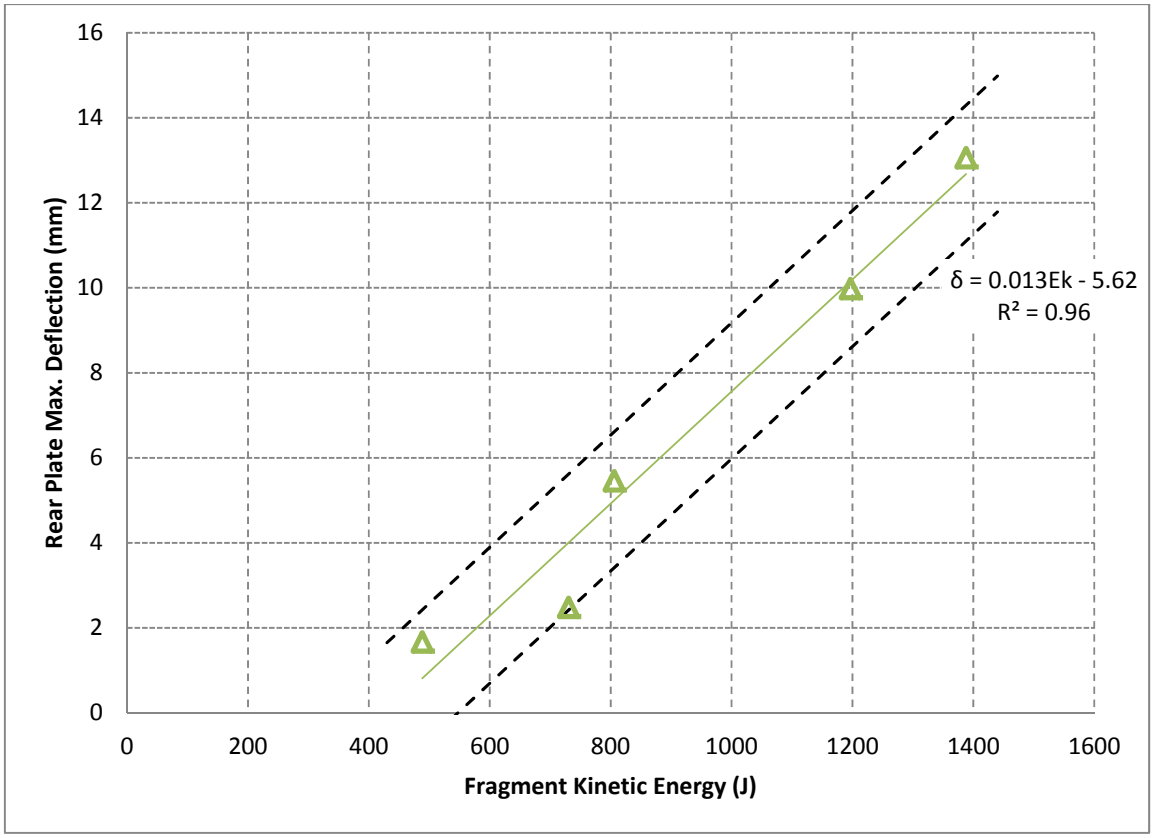

Figure 5-28: Rear plate deflection against fragment kinetic energy for tests with 60mm thick Divinycell foam

When compared to Divinycell foam at 40mm, as shown in Figure 5-29, it can be noticed that the slope of the deflection-energy trend of 60mm thick Divinycell foam is significantly higher. Although at lowest fragment kinetic energies it is clearly better to increase the thickness to 60mm in order to increased damage alleviation, at higher impact energies (between 1300J and 1400J), the mitigation effects of the material at the two thicknesses is comparable. The sectioned photographs of the impacted Divinycell foams shown in the graph affirm the advantage of the additional 20mm disc at lower kinetic energies as fragment penetration only occurs to a depth of approximately 40mm for the 60mm thick foam, compared to the 40mm thick Divinycell foam, in which the fragment emerges at the exit surface, even though it remains wedged in the absorber. Between 1300J and 1400J, the post-impact state of the 40mm thick foam remains visually similar to the state at the lowest kinetic energy; however at 60mm

thickness, the damage on the absorber is increased as the fragment perforates the 60mm thickness and remains loosely wedged at the exit face (even though in the sectioned photograph, it is not observed because of the sectioning process which removes the fragment). At this higher kinetic energy regime, the progressive damage on the 60mm thick Divinycell foam is high and its protective performance of the rear plate becomes comparable with that of the 40mm thick foam at the same kinetic energy regime.

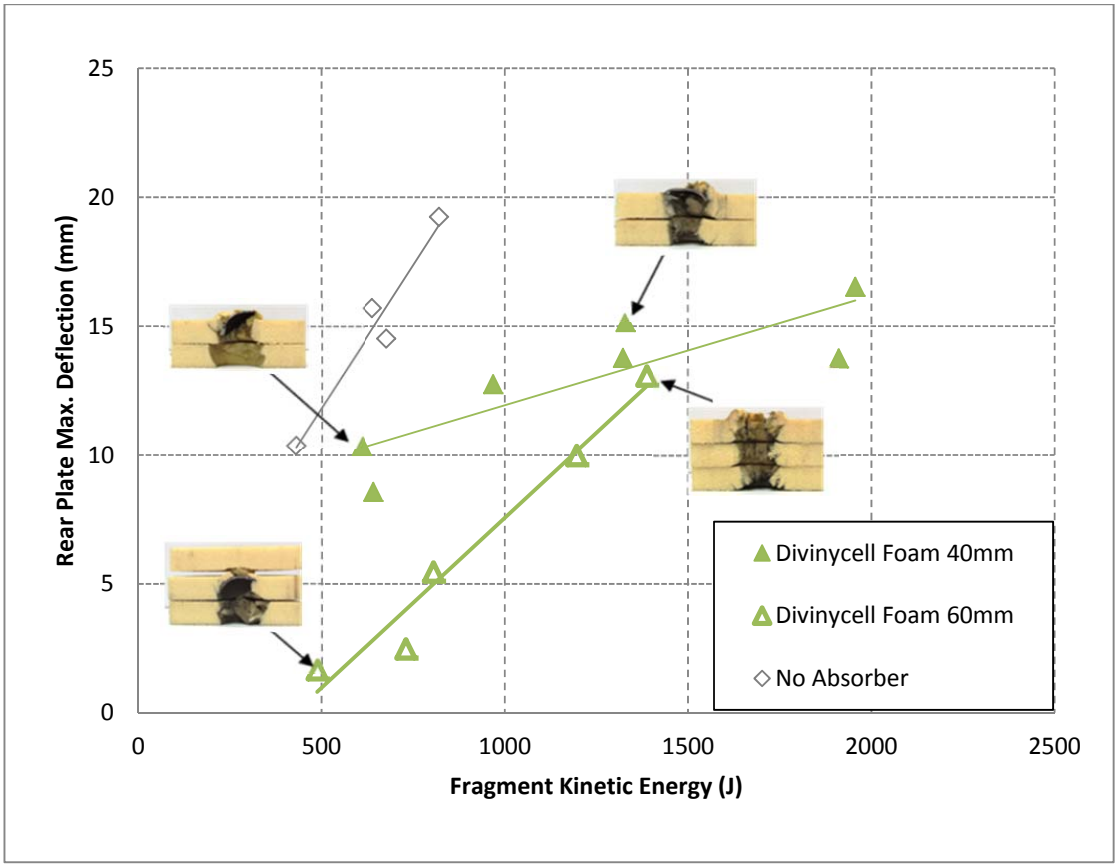

Figure 5-29: Change in rear plate deflection against kinetic energy when Divinycell foam thickness increases to 60mm

For **polyurethane foam** of 60mm thickness, shown in Figure 5-30, the data points are moderately scattered about the mean least squares fit when rear plate deflection is plotted against fragment kinetic energy. The slope of the fit, 0.013mm/J, is also very comparable with the slopes of the other two materials tested at this thickness (balsa wood and Divinycell foam) and fits through the data with an R^2 value of 0.9.

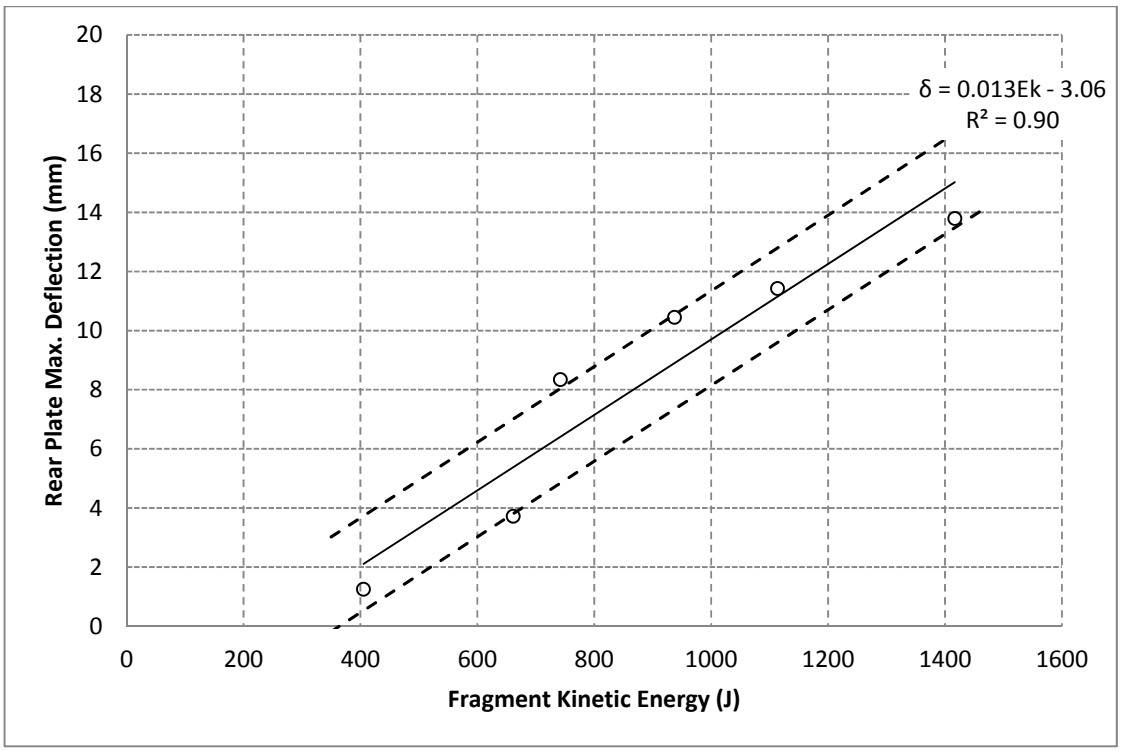

Figure 5-30: Rear plate deflection against fragment kinetic energy for tests with 60mm thick polyurethane foam

When the 60mm thick polyurethane foam is compared to the rear plate protection provided by the 40mm thick counterpart, it is apparent that at the lowest fragment kinetic energies of the respective thicknesses, less damage is observed at 60mm thickness, as penetration only occurs to ≈45mm depth whereas the 40mm thick absorber is fully perforated, as shown in the comparative plot in Figure 5-31. In the comparative plot, it is also observed that the slope of the 60mm thick foam fit is greater, however in the tested kinetic energy regime; the two trends are still offset from each other even at their highest respective fragment kinetic energies. The

sectioned photographs show that that both absorbers are perforated at their high fragment kinetic energy regimes but there is more damage in the exit face of the 40mm thick foam than in the exit face of the 60mm thick foam. This suggests that even though the extra damage alleviation of the 60mm thick foam, compared to the 40mm thick foam, decreases as kinetic energy of the fragment kinetic energy increases, the 60mm thick foam remains less damaged than the 40mm thick foam and still provides extra mitigation at the highest fragment kinetic energies. The fact that the polyurethane material in both thicknesses turns to powder upon fragment impact relatively unrestrained motion of the fragment may be attributed to the two thicknesses showing more parallel responses to increasing fragment kinetic energy. However, in the drop impact investigations of paper honeycomb sandwich panels by Wang [101] it was found that the advantage of increasing the thickness of the core of the panel was diminished with further increase in thickness until the advantage effectively disappeared. This could be a possible justification of the faster deterioration of 60mm thick absorbers, compared 40mm thick counterparts.

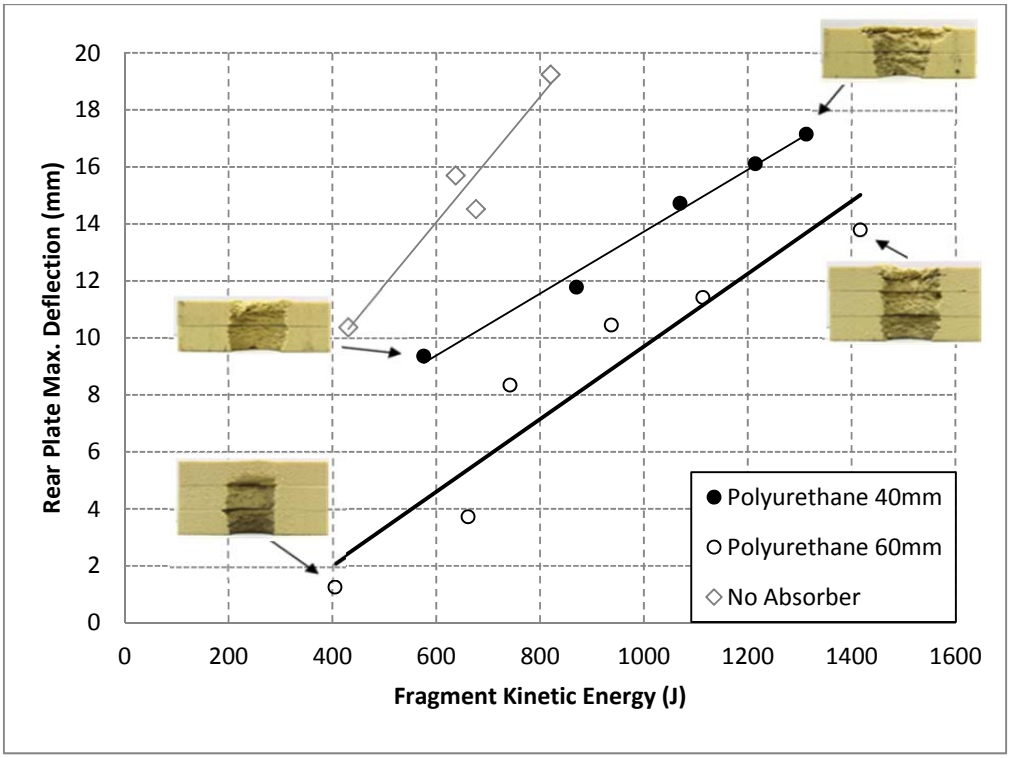

Figure 5-31: Change in rear plate deflection against kinetic energy when polyurethane foam thickness increases to 60mm

The comparative plot of the three 60mm thick materials, shown in Figure 5-32, indicates a clear distinction of the trends of the tested materials. Based on the trends which are clearly offset from each other and almost mutually parallel in slope, Divinycell foam provides the highest level of alleviation with polyurethane foam as the second best, and balsa wood being the material that decreases the rear plate damage the least.

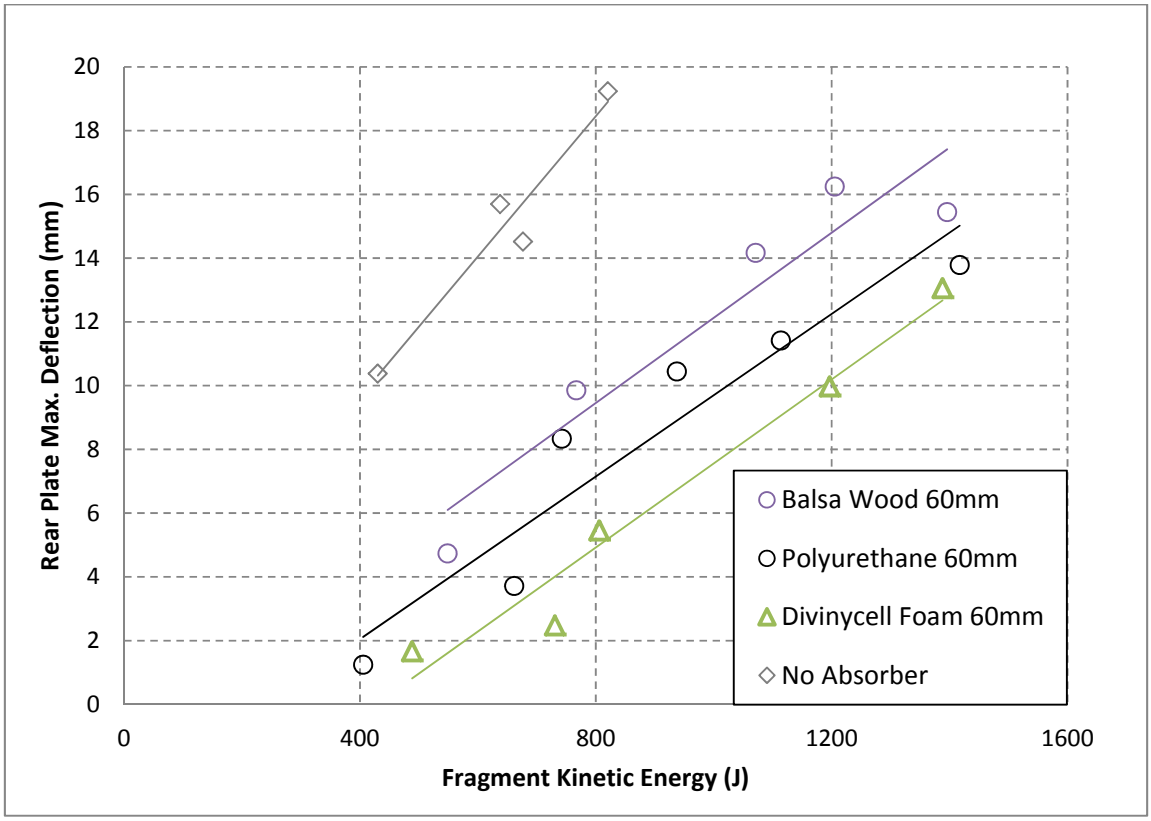

Figure 5-32: Comparative plot of rear plate deflection against kinetic energy for the 60mm thick energy absorbers

5.6. Effect of varying layering arrangements of energy absorbers

In this parametric study, polyurethane foam is also cut into single 40mm thick discs, two 20mm thick discs, as well as four 10mm discs investigate the effect of changing the thickness arrangement in alleviating fragment impact. Figure 5-33 shows a graph with data from all three arrangements plotted on one system of axes, where rear plate deflection is plotted against kinetic energy of the fragment. All three profiles are compared to the condition in which no energy absorber is used. A single least squares linear fit is run through the deflection-kinetic energy points in all three layering arrangements. It is evident that the linear fit and the ±1 plate thickness bounds describe the trend of the all the point well. All the points fall well within the 90% experimental variation interval with an R^2 value of 0.95. It can thus be inferred that, when the points are analysed holistically, all three thickness arrangements provide indistinguishable alleviations against fragment impact; there are no significant effects on the rear plate damage if any of the three configurations is used.

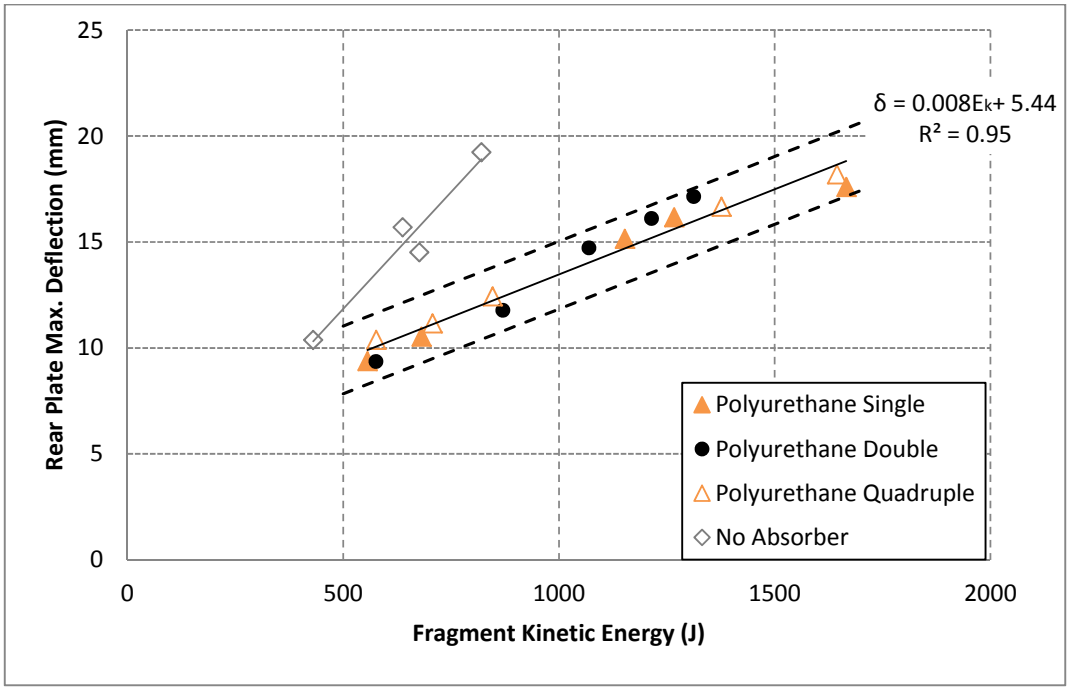

Figure 5-33: Graph of rear plate deflection plotted against fragment kinetic energy, of the various polyurethane foam layering arrangements

5.7. Effect of size and speed of a fragment

Balsa wood, Divinycell foam and polyurethane foam of 40mm thickness are subjected to tests from three charge diameters (27mm, 36mm and 43mm) with different masses of explosive are used to induce fragments of at different speeds and masses with mutually close kinetic energies. Figure 5-34 is the resulting plot in the test series. For each of the three materials tested, the three fragment diameters are not synchronised to the exactly the same fragment kinetic energy. As inferred from analysis on how charge mass affects kinetic energy (§5.2.3), determining kinetic energy for known charge masses is an unpredictable effort because of the substantial energy variation ranges. The plot in Figure 5-34, therefore shows the different sized fragments at close kinetic energies.

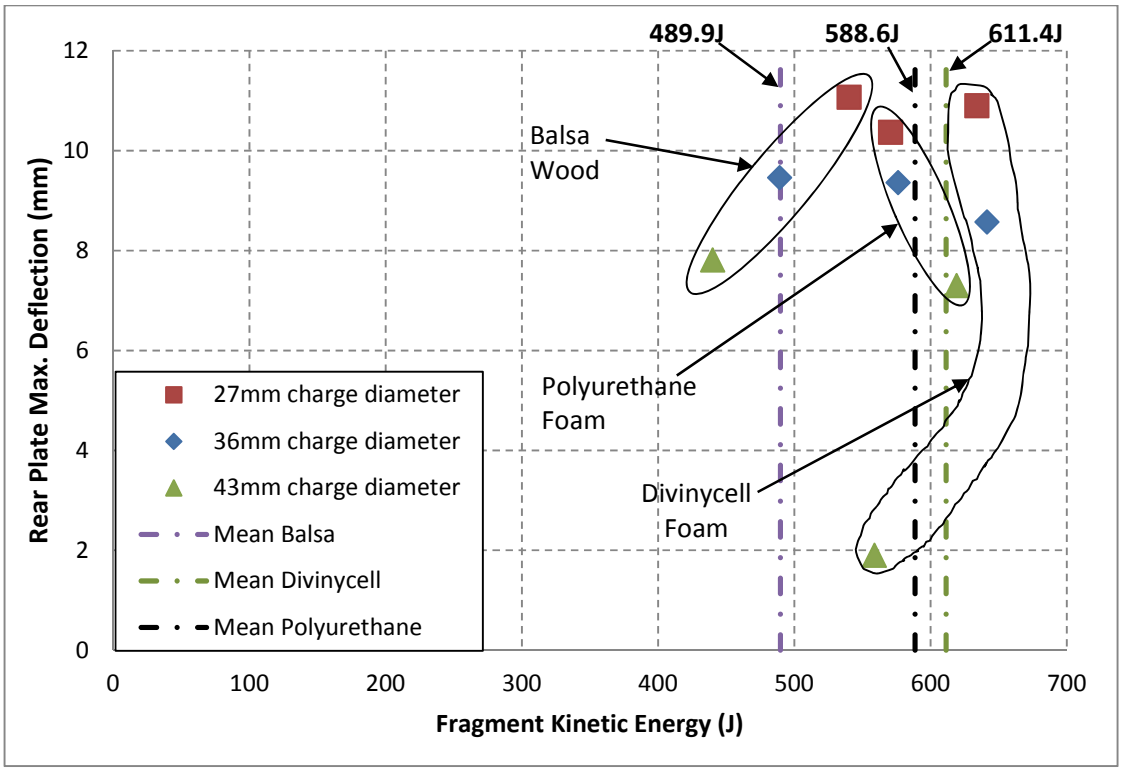

Figure 5-34: Graph showing rear plate deflection under impact from difference sized fragments with close kinetic energies

The fragments which are impacted against balsa-wood-protected rear plates are at the largest energy variation range (100J) where the mean kinetic energy is 489.9J, whereas the best case of synchronising the kinetic energies is evident in polyurethane foam (49J) with a mean kinetic energy of 588.6J. In all three cases the common observation is that fragments released from charges of 27mm result in the highest rear plate deflection whilst those released by 43mm diameter charges impart the lowest deflection.

When the three materials are compared with each other, Divinycell foam shows the largest progressive damage as fragment size decreases. When the fragment is released by a 43mm charge, the rear plate deflection is 1.9mm, which increases by 6.7mm (352% increase) when the charge diameter is 36mm and rises by a further 2.3 (27% increase) when the charge diameter is reduced to 27mm.

6. CONCLUSIONS

The use of various cellular materials to alleviate damage (on a rear plate) from a blast-induced fragment has been comprehensively studied in this project. Capping (Mode IIc) is induced by mean of a localised blast load on a circular front plate (diameter 106mm and thickness 1.6mm). The resulting mass, diameter and speed of the released fragment are measured. The damage caused by the fragment on a rear plate is observed. Various energy absorbers are placed in front of the rear plate and their protective performances of the rear plate are noted and reported. From the experimental plan, the execution, the resulting observations and findings, analyses and discussions, the following conclusions are thus drawn:

6.1. Applicable charge mass range for capping failure

For the three charge diameters used in this study (27mm, 36mm and 43mm), the minimum charge mass is 7g and the maximum is 11g. The front plate only fails in a capping mode of failure (Mode IIc) when the charge mass is at least 7g. As the mass is increased to 11g, capping occurs with petalling failure on the front plate in a way that the petals wrap around one of the clamp frames and thus makes it difficult to loosen the plate from the clamping rig. Due to this limitation of the range of charge masses, there is also a limit in the minimum and maximum values of the momentum and kinetic energy at which the fragments are released from the front plate.

6.2. Effect of charge parameters on impulse

The impulse that is imparted on the front plate, and hence the entire pendulum, is generated by the detonation of the charge. When each of the charge diameters is considered in isolation, there is an expected increasing relationship between charge mass and impulse. When all the

three charge diameters are considered collectively, they all lie within a narrow band of a linear relationship between charge mass and impulse. The consequent governing relationship is:

$I = 1.76m_c + 1.99$

From the observed relationship, it can thus be concluded that the impulse generated by the blast is not dependent on the charge diameter, but on the charge mass.

6.3. Fragment characteristics

6.3.1. Diameter and mass of released fragments

The methods of measuring the diameter and mass of each fragment are well described in §§3.6.2--3.6.3. The size of the fragment (diameter and mass) is dependent on the charge diameter in that it increases as the charge diameter increases. There is, however, no conclusive relationship that exists between charge mass and either fragment mass or fragment diameter. For the charge diameters 27mm, 36mm and 43mm, the respective average fragment masses are 4.11g, 8.41g and 12.59g whilst the average diameters of the fragments are 25.73mm, 34.04mm and 40.08mm respectively.

6.3.2. Effect of charge mass on speed of fragment

From the analyses carried out on the relationship between charge mass and the speed of the fragment, it can be conclusively stated that the speed of the released fragment increases with an increase in charge mass. The limited number of data points for charge masses above 8g when charge diameter is 27mm, coupled with the fact that there is a decrease in speed from charge mass of 9g to 10g, makes it impossible to fit a satisfactory linear squares fit to describe the relation between charge mass and fragment speed (see Figure 5-6). For charge diameters of

36mm and 43mm, linear least squares trends are used to describe the increasing relationship between charge mass and speed of the fragment.

For all the charge diameters, it is however noticeable that the speed of the fragment for any given charge mass has a **significant variation range**, with the variation range being as much as 214m/s (with a mean deviation of almost 10%) for the charge mass of 11g and charge diameter of 36mm. It can be concluded that, although there is an increasing relationship between charge mass and speed of fragment, the speed of the fragment for any given charge mass is unpredictable.

6.3.3. Momentum and kinetic energy of fragment

With the mass of the fragment being in a narrow band of values for each charge diameter and the relationship between charge mass and fragment being an increasing one, effect of charge mass on the momentum ($p = m_f v_f$) of the fragment is also observed to be increasing. A linear least squares fit satisfactorily describes the relationship.

The consequent relationship between fragment kinetic energy and charge mass is estimated by a quadratic least squares fit since mathematically, kinetic energy should increase in a quadratic manner (if a linear increase is assumed between charge mass and fragment speed) since kinetic energy is proportional to the square of the speed of the fragment ($E_k = ½m_f v_f^2$) .

6.4. Observed failure of the rear plate

The region on the rear plate on which impact by the fragment occurs is not often dead-centre as impact can be slightly or substantially eccentric. Consequently, if only deflection is observed in the rear plate, the term ‘rear plate maximum deflection is used instead of ‘midpoint deflection’. The principal modes of failures of the rear plate which are noted are:

- **Inelastic deflection (Mode I)** – The region of impact is observed to fail this way, with the global and local dome profile reminiscent of plates under localised loading.
- **Inelastic deflection with thinning (Mode Itc)** – As the fragment rebounds back from the plate it may also leave a thinning around the perimetral region (due to impact from the face of the fragment) or chordal region (due to impact by the edge of the fragment).
- **Inelastic deflection with small partial tearing (early Mode II*c)** – As the fragment rebounds back from the plate it may also leave a partial tear around the perimetral region (due to impact from the face of the fragment) or chordal region (due to impact by the edge of the fragment).
- **Inelastic deflection with large partial tearing (advanced Mode II*c)** – This is observed when the fragment perforates through the rear plate by leaves large (but not complete) tearing around the region of impact.
- **Inelastic deflection with full tearing (Mode IIc)** – Observed when fragment deflects the rear plate and also tears a fragment from the rear plate, after which the fragment from the front plate either ricochets from or remains fused to the fragment from the rear plate. The phenomenon is referred to as *secondary capping*.

6.5. Damage on the rear plate with no energy absorbers

Two plate separation distances are used when no absorbers are protecting the rear plate 150mm and 190mm. In the wake of the analyses relating the measured rear plate deflection to the kinetic energy of the fragment, it can be concluded that the increase of the separation distance by 40mm has no notable effect on residual rear plate damage.

When there is no energy absorber protecting the rear plate, the maximum fragment kinetic energies beyond which the rear plate always fails by large tearing or secondary capping are 414.8J, 820.4J and 904.2J for the respective charge diameters of 27mm, 36mm and 43mm.

6.6. General response of energy absorbers to fragment impact

Aluminium foam, aluminium honeycomb B, balsa wood, Corecell M-80 foam, Divinycell (PVC) H200 foam and polyurethane 200 foam (A and B) are all used to protect the rear plate. A compressed plug is sheared off aluminium foam as the fragment perforates the material. Aluminium honeycomb layers bend as a fragment perforates through. Small chunks of wood are removed from the balsa wood absorber during failure and major loss of material or cracking occurs in the general orientation of the grain of the wood.

Corecell foam, in addition to being subjected to visible soot deposit, its texture and colour, after the fragment passes through the foam, suggests that it is partially scorched by the hot fragment. Divinycell, from which the least material mass fraction is lost, shows the highest plateau stress during quasi-static testing and also the highest perforation resistance during fragment impact. Cross-cracks originate from the entry surface of the foam and surround the tunnel and propagate through the thickness of each absorber disc obliquely. Some fragments are found tightly wedged in the Divinycell foam after impact. Polyurethane foam loses the highest fraction of its mass during fragment impact, when compared to the other materials (at 40mm thickness) and this occurs by crushing of the foam material to powder.

6.7. Damage on the rear plate with 40mm thick absorbers

When the materials are comparatively tested at 40mm thickness, Divinycell foam alleviates the most damage on the rear plate when the fragment kinetic energy exceeds 700J. Aluminium foam provides the second highest impact alleviation whilst balsa wood is the third and also mean ranked material for the range of materials tested. Aluminium honeycomb and Corecell foams are equally vulnerable against fragment impact and provide the least protected of the plate. Polyurethane provides a level of protection on par with Divinycell foam below 700J but it progressively diminishes to be comparable with the most vulnerable materials at highest kinetic

energies. Table 6.1 is a listed ranking of the 40mm thick energy absorbing materials based on the profiles of deflection vs fragment kinetic energy for the protected rear plates.

Table 6.1: Summary of the ranking of the protective performances of the various energy absorbers at 40mm thickness

Energy absorbing material	Rear plate damage alleviation level
Divinycell foam	1
Aluminium foam	2
Balsa wood	3
Aluminium honeycomb	4
Corecell foam	5
Polyurethane foam	Varying*

*At lower kinetic energies, polyurethane foam is on par with Divinycell foam but diminishes quicker than other materials as kinetic energy is increases and it ends up being on par with Corecell foam

6.8. Effect of thickness of the energy absorbing materials

Balsa wood, Divinycell foam, as well as polyurethane foam are tested at 60mm. For Balsa wood and Divinycell foam, it can be concluded that increasing the thickness from 40mm to 60mm improves the damage alleviation of the absorber at lower fragment kinetic energies but as kinetic energy increases, the improvement in damage alleviation decreases at becomes on par with the alleviation provided by 40mm thick absorbers at higher kinetic energies. The advantage of increasing the thickness of polyurethane foam always decreases with increasing kinetic energy but for the tested parameters increasing the thickness of polyurethane foam always increases the damage alleviation of the absorber.

6.9. Effect of varying layering arrangement of polyurethane foam

Single-layered, double-layered and quadrupled-layered polyurethane foam is tested at 40mm thickness. Increasing the layering arrangement means that as the number of layers increase, there is another peak stress (highest stress before plateau stress during quasi-static compression) to be overcome by the source of deformation, but it since the peak stress of polyurethane is almost equal to its plateau stress, unlike metals, increasing the layering arrangement **does not** significantly affect the protective performance of the energy when rear plate deflection is taken into account.

6.10. Effect of varying the fragment size while maintaining close kinetic energies

Fragments are released from the three charge diameters (27mm, 36mm and 43mm) such that their kinetic energies are within close numerical proximity of each other. For all three materials tested for this series (balsa wood, Divinycell foam and polyurethane foam at a thickness of 40mm), it can be concluded that given a kinetic energy, the highest damage is caused by the smallest sized fragment which has the highest speed; and conversely, the biggest fragment, which has the lowest speed, imparts the smallest damage on the rear plate.

6.11. Theoretical Analyses

For the three charge diameters, 27mm, 36mm and 43mm, the predicted maximum front plate deflections before capping occurs are 18.6mm, 24.5mm and 28.5mm which are reasonably close to measured values in literature.

Zhao's response number is used in a dimensionless analysis and it can be inferred from the relationship between dimensionless deflection (δ/h ratio) and the response number (R_n) that the largest damage is caused by the smallest fragment if the deflection of three plates impacted by three different fragments is equal. For the study, the minimum Zhao's response number required for large tearing of an unprotected plate is 6794, regardless of the size of the fragment.

Predicting the rear plate deflection when no energy absorbers are present by the use of the graphical relationship presented by Baker [3] is not applicable to this study. This is because the predicted values are found to be between nine (9) and thirty (30) times the measured deflection.

The BRL equation is used to predict the critical kinetic energies **beyond** which the released fragments from the three charge diameters cause large tearing on the rear plate and consequently perforate through the plate. At the charge diameters of 27mm, 36mm and 43mm the critical kinetic energy are predicted as 380.4J, 578.9J and 739.4J respectively. Experimentally it is found the maximum fragment energies before perforation for the three respective charge diameters are 414.8, 820.4 and 930J. Conclusively, the BRL equation underestimates the critical energy for perforation.

7. RECOMMENDATIONS

Based on the experimental scope, limitations, procedure, results, analyses and the drawn conclusions, the following recommendations are made:

- Material characterisation for the energy absorbers should be carried out at dynamic compression in addition to quasi-static compression to investigate the strain-rate sensitivity of the different energy absorbers.
- Different methods of achieving fragmentation like blasting a plate which has induced imperfections like grooves or simply accelerating a free projectile by a localised load should be employed to increase the range and minimise the variation of the release speed of fragments.
- Test plate materials which have more consistent properties (like Domex steel) should be used instead of mild steel to increase the consistency of both the characteristics of the fragment and the response of the rear plate.
- Investigations should be carried out to study the response of plates to multiple/repeated impact from fragments.
- The study should also be extended to investigating other classes of energy absorbing core materials like, ceramics, fibre composites and lattice structures.
- Constraining methods should be designed for location of energy absorbers to prevent motion of the energy absorbers during incident motion and rebound of fragments.
- Impact tests should be carried out on energy absorbers which are selected on a same-mass basis instead of same-thickness basis. This could include:
  - Different classes of materials having different thicknesses but synchronised masses and/or
  - Same class of materials which have different densities by which are set up such that their masses are the same, eg. Polyurethane 80 and Polyurethane 200.
- This study should be modelled using Finite Element Analysis (FEA) for further insights into capping and interaction of a fragment with an energy absorber and the rear plate.

8. REFERENCES

[1] JIEDDO COIC MID. *Global IED Monthly Summary Report.* Joint Improvised Explosive Device Defeat Organization (USA); 2012 .

[2] SIGAR. *Improvised Explosive Devices: Contracts for Culvert Denial Systems.* Special Inspector General for Afghanistan Reconstruction (USA); 2013 Report No.: SP-13-8.

[3] Baker WE, Kulesz JJ, Westine PS, Cox PA, Wilbeck JS. *A manual for the prediction of blast and fragment loadings on structures.* Southwest Research Institute: San Antonio, Texas; 1981 .

[4]Aviation Safety Network. ASN Aircraft accident Boeing 767-223ER N330AA Los Angeles International Airport, CA (LAX). 2006; Available at: http://aviation-safety.net/database/record.php?id=20060602-0. Accessed September 13, 2013.

[5] Rajendran R, Lee J. Blast loaded plates. *Marine Structures* 2009; 22(2): 99-127.

[6]Pike J. Explosives. 2012; Available at: http://www.globalsecurity.org/military/systems/munitions/explosives.htm. Accessed February/29, 2012.

[7] Wilkinson C, Anderson J. *An introduction to detonation and blast for the non-specialist.* Defence Science and Technology Organisation (Australia); 2003 .

[8] Baker WE. *Explosions in air.* Austin, Texas: University of Texas Press; 1973.

[9] Swisdak M. *Explosion Effects and Properties.Part I.Explosion Effects in Air.* White Oak, Maryland: Naval Surface Weapons Center; 1975.

[10] Kinney GF, Graham KJ. *Explosive shocks in air.* 2nd ed. Berlin: Springer-Verlag GmbH; 1985.

[11] Menkes S, Opat H. Tearing and shear failure in explosively loaded clamped beams. *Experimental Mechanics* 1973; 13: 480-486.

[12] Jones N. Plastic failure of ductile beams loaded dynamically. *Journal of Engineering for Industry* 1976; 98: 131.

[13] Nurick GN, Martin JB. The Measurement of the Response of Clamped Circular Plates to Impulsive Loading. In: *3rd Institute of physics conference on mechanical properties at high rates of strain.* London: 1984: 495-501.

[14] Nurick GN. An empirical solution for predicting maximum central deflections of impulsively loaded plates. *Mechanical Properties of Materials at High Rates of Strain* 1989: 457-464.

[15] Nurick GN, Martin JB. Deformation of thin plates subjected to impulsive loading—a review: Part i: theoretical considerations. *International Journal of Impact Engineering* 1989; 8(2): 159-170.

[16] Teeling-Smith RG, Nurick GN. The deformation and tearing of thin circular plates subjected to impulsive loads. *International Journal of Impact Engineering* 1991; 11(1): 77-91.

[17] Wierzbicki T, Nurick GN. Large deformation of thin plates under localised impulsive loading. *International Journal of Impact Engineering* 1996; 18(7): 899-918.

[18] Nurick GN, Gelman ME, Marshall NS. Tearing of blast loaded plates with clamped boundary conditions. *International Journal of Impact Engineering* 1996; 18(7-8): 803-827.

[19] Nurick GN, Radford AM. Deformation and tearing of clamped circular plates subjected to localised central blast loads. *Recent developments in computational and applied mechanics: A volume in honour of John B.Martin.International Centre for Numerical Methods in Engineering (CIMNE), Barcelona, Spain* 1997: 276-301.

[20] Wierzbicki T. Petalling of plates under explosive and impact loading. *International Journal of Impact Engineering* 1999; 22(9): 935-954.

[21] Wiehahn MA, Nurick GN, Bowles HC. Some insights into the mechanism of the deformation and tearing of thin plates at high strain rates incorporating temperature dependent material properties. In: *Proceedings of 6th International Conference on Structures under Shock and Impact (SUSI VI), Cambridge, UK.* 2000: 35-46.

[22] Bwalya KD. *The Response of Steel Plates to Repeated Blast Loads.* BSc. Eng. Thesis. University of Cape Town; 2004.

[23] Lee Y, Wierzbicki T. Fracture prediction of thin plates under localized impulsive loading. Part II: discing and petalling. *International Journal of Impact Engineering* 2005; 31(10): 1277-1308.

[24] Jacob N, Nurick GN, Langdon GS. The effect of stand-off distance on the failure of fully clamped circular mild steel plates subjected to blast loads. *Engineering Structures* 2007; 29(10): 2723-2736.

[25] Gupta N. Deformation and tearing of circular plates with varying support conditions under uniform impulsive loads. *International Journal of Impact Engineering* 2007; 34(1): 42-59.

[26] Gharababaei H, Darvizeh A. Experimental and Analytical Investigation of Large Deformation of Thin Circular Plates Subjected to Localized and Uniform Impulsive Loading#. *Mechanics based design of structures and machines* 2010; 38(2): 171-189.

[27] Chung Kim Yuen S, Nurick GN, Ranwaha N, Henchie T. The Response of Circular Plates to Repeated Uniform Blast Loads. *Key Engineering Materials* 2013; 535: 44-47.

[28] Nurick GN, Pearce HT, Martin JB. The deformation of thin plates subjected to impulsive loading. In: Bevilacqua L, Feijóo R, Valid R. (eds.) *Inelastic Behaviour of Plates and Shells.* Rio de Janeiro, Brazil: Springer Berlin Heidelberg; 1986: 597-616.

[29] Olson MD, Nurick GN, Fagnan JR. Deformation and rupture of blast loaded square plates—predictions and experiments. *International Journal of Impact Engineering* 1993; 13(2): 279-291.

[30] Nurick GN, Shave GC. The deformation and tearing of thin square plates subjected to impulsive loads—an experimental study. *International Journal of Impact Engineering* 1996; 18(1): 99-116.

[31] Jacob N, Chung Kim Yuen S, Nurick GN, Bonorchis D, Desai SA, Tait D. Scaling aspects of quadrangular plates subjected to localised blast loads—experiments and predictions. *International Journal of Impact Engineering* 2004; 30(8): 1179-1208.

[32] Chung Kim Yuen S, Nurick G, Verster W, Jacob N, Vara A, Balden V, Bwalya D, Govender R, Pittermann M. Deformation of mild steel plates subjected to large-scale explosions. *International Journal of Impact Engineering* 2008; 35(8): 684-703.

[33] Nurick GN, Olson MD, Fagnan JR, Levin A. Deformation and tearing of blast-loaded stiffened square plates. *International Journal of Impact Engineering* 1995; 16(2): 273-291.

[34] Nurick GN, Lumpp DM. Deflection and tearing of clamped stiffened circular plates subjected to uniform impulsive blast loads. In: Jones N, Brebbia C, Watson A, (eds.) Structures under Shock Impact IV: Computational Mechanics; 1996. p. 393-404.

[35] Chung Kim Yuen S, Nurick GN. Experimental and numerical studies on the response of quadrangular stiffened plates. Part I: subjected to uniform blast load. *International Journal of Impact Engineering* 2005; 31(1): 55-83.

[36] Langdon GS, Chung Kim Yuen S, Nurick GN. Experimental and numerical studies on the response of quadrangular stiffened plates. Part II: localised blast loading. *International Journal of Impact Engineering* 2005; 31(1): 85-111.

[37] Genson KW. *Vehicle shaping for mine blast damage reduction.* MS Thesis. University of Maryland; 2006.

[38] Chung Kim Yuen S, Langdon GS, Nurick GN, Pickering EG, Balden VH. Response of V-shape plates to localised blast load: Experiments and numerical simulation. *International Journal of Impact Engineering* 2012; 46: 97-109.

[39] Nurick GN, Bryant MW. Fragmentation damage as a result of an explosion. *Plasticity and Impact Mechanics* 1996: 484-498.

[40] Balden VH, Nurick GN. Numerical simulation of the post-failure motion of steel plates subjected to blast loading. *International Journal of Impact Engineering* 2005; 32(1): 14-34.

[41] Türkmen H, Mecitoğlu Z. Dynamic response of a stiffened laminated composite plate subjected to blast load. *Journal of Sound and Vibration* 1999; 221(3): 371-389.

[42] Zhu F, Zhao L, Lu G, Wang Z. Deformation and failure of blast-loaded metallic sandwich panels—Experimental investigations. *International Journal of Impact Engineering* 2008; 35(8): 937-951.

[43] Langdon GS, Nurick GN, Cantwell WJ. The response of fibre metal laminate panels subjected to uniformly distributed blast loading. *European Journal of Mechanics-A/Solids* 2008; 27(2): 107-115.

[44] Xue Z, Hutchinson J. Preliminary assessment of sandwich plates subject to blast loads. *International Journal of Mechanical Sciences* 2003; 45(4): 687-705.

[45] Marchand KA, Alfawakhiri F. *Facts for steel buildings: Blast and progressive collapse.* : American Institute of Steel Construction; 2004.

[46] Kanchibotla SS, Valery W, Morrell S. Modelling fines in blast fragmentation and its impact on crushing and grinding. In: Modelling fines in blast fragmentation and its impact on crushing and grinding. In: *Explo '99–A conference on rock breaking.* Kalgoorlie, Australia: The Australasian Institute of Mining and Metallurgy; 1999: 137-144.

[47] Hamdi E, Romdhane NB, du Mouza J, Le Cleac'h JM. Fragmentation energy in rock blasting. *Geotechnical and Geological Engineering* 2008; 26(2): 133-146.

[48] Kulatilake P, Qiong W, Hudaverdi T, Kuzu C. Mean particle size prediction in rock blast fragmentation using neural networks. *Engineering Geology* 2010; 114(3): 298-311.

[49] Hudaverdi T, Kuzu C, Fisne A. Investigation of the blast fragmentation using the mean fragment size and fragmentation index. *International Journal of Rock Mechanics and Mining Sciences* 2012; 56: 136-145.

[50] Crull MM. *Prediction of primary fragmentation characteristics of cased munitions.* Ft. Belvoir : Defense Technical Information Center; 1998 .

[51] Hutchinson MD. The escape of blast from fragmenting munitions casings. *International Journal of Impact Engineering* 2009; 36(2): 185-192.

[52] Glanville JP, Barnes I, Fairlie GE. Explicit Dynamics Simulation of the Natural Fragmentation of Cased Explosives. In: Explicit Dynamics Simulation of the Natural Fragmentation of Cased Explosives. In: *The First International Conference of Protective Structures.* 2010.

[53] Glanville JP, Barnes I. Numerical Simulation of the Natural Fragmentation of Cased Munitions. In: *15th International Symposium on Interaction of the Effects of Munitions with Structures (ISIEMS) 17 - 20 September 2013.* Potsdam, Germany: 2013.

[54] Tan H. Spalling and Fragmentation (part I). *iMechanica* 2008.

[55] Army U, Navy U, Force UA. *Structures to resist the effects of accidental explosions.* : US Government Printing Office; 1969.

[56] Wu C, Nurwidayati R, Oehlers DJ. Fragmentation from spallation of RC slabs due to airblast loads. *International Journal of Impact Engineering* 2009; 36(12): 1371-1376.

[57] Krivtsov AM. Computer simulation of spall crack formation. *Structural Dynamics–EURODYN* 1999; 99: 475-477.

[58] Ivanov A, Syrunin M, Fedorenko A, Tsoi A. Fragmentation of spherical shells under internal blast loading. *Strength of materials* 2001; 33(2): 150-156.

[59] Chung Kim Yuen S, Nurick GN. Modelling the deformation and tearing of thin and thick plates subjected to localised blast loads. In: Gupta N. (ed.) *Proceedings of the Eighth International Symposium on Plasticity and impact mechanics (IMPLAST 2003).* 2003: 729-739.

[60] Chung Kim Yuen S, Nurick GN. The Response of "Large" Square Tubes (Width/Thickness Ratio > 45) to Opposite Lateral Blast Loads Followed by Dynamic Axial Load. In: Reddy B, (ed.) : Springer Netherlands; 2008. p. 309-317.

[61] Bambach MR. Behaviour and design of aluminium hollow sections subjected to transverse blast loads. *Thin-Walled Structures* 2008 12; 46(12): 1370-1381.

[62] Jama HH, Bambach MR, Nurick GN, Grzebieta RH, Zhao XL. Numerical modelling of square tubular steel beams subjected to transverse blast loads. *Thin-Walled Structures* 2009; 47(12): 1523-1534.

[63] Zukas JA. *Impact dynamics: theory and experiment.* U.S. Army Research Ballistic Laboratory; 1980 Report No.: ARBRL-TC-02271.

[64] Johnson W. *Impact strength of materials.* : Edward Arnold Limited; 1972.

[65] Zhao Y. Suggestion of a new dimensionless number for dynamic plastic response of beams and plates. *Archive of Applied Mechanics* 1998; 68(7-8): 524-538.

[66] Duffey TA. *The large deflection dynamic response of clamped circular plates subjected to explosive loading.* : Sandia Corp., Albuquerque, N. Mex.; 1967.

[67] Symonds P, Wierzbicki T. Membrane mode solutions for impulsively loaded circular plates. *Journal of Applied Mechanics* 1979; 46: 58.

[68] Corbett G, Reid S, Johnson W. Impact loading of plates and shells by free-flying projectiles: a review. *International Journal of Impact Engineering* 1996; 18(2): 141-230.

[69] Ohte S, Yoshizawa H, Chiba N, Shida S. Impact Strength of Steel Plates Struck by Projectiles: Evaluation Formula for Critical Fracture Energy of Steel Plate. *Bulletin of JSME* 1982; 25(206): 1226-1231.

[70] Lu G, Yu TY. *Energy absorption of structures and materials.* : Woodhead Publishing; 2003.

[71] Alghamdi A. Collapsible impact energy absorbers: an overview. *Thin-Walled Structures* 2001; 39(2): 189-213.

[72] Hosseinipour S, Daneshi G. Energy absorbtion and mean crushing load of thin-walled grooved tubes under axial compression. *Thin-Walled Structures* 2003; 41(1): 31-46.

[73] Tasdemirci A. The effect of tube end constraining on the axial crushing behavior of an aluminum tube. *Materials & Design* 2008; 29(10): 1992-2001.

[74] Bodlani SB, Chung Kim Yuen S, Nurick GN. The Energy Absorption Characteristics of Square Mild Steel Tubes With Multiple Induced Circular Hole Discontinuities—Part I: Experiments. *Journal of applied mechanics* 2009; 76(4).

[75] Bodlani SB, Chung Kim Yuen S, Nurick GN. The Energy Absorption Characteristics of Square Mild Steel Tubes With Multiple Induced Circular Hole Discontinuities—Part II: Numerical Simulations. *Journal of applied mechanics* 2009; 76(4).

[76] Chung Kim Yuen S, Nurick GN. The Crushing Characteristics of Square Tubes With Blast-Induced Imperfections—Part I: Experiments. *Journal of applied mechanics* 2009; 76(5).

[77] Chung Kim Yuen S, Nurick GN. The Crushing Characteristics of Square Tubes With Blast-Induced Imperfections—Part II: Numerical Simulations. *Journal of applied mechanics* 2009; 76(5).

[78]ERG Duocel® Foam Energy absorption. Available at: http://www.ergaerospace.com/Energy-Absorbtion.html. Accessed June 10, 2012.

[79] Schonberg W. Protecting spacecraft against orbital debris impact damage using composite materials. *Composites Part A: Applied Science and Manufacturing* 2000; 31(8): 869-878.

[80] Dean J, Dunleavy C, Brown P, Clyne T. Energy absorption during projectile perforation of thin steel plates and the kinetic energy of ejected fragments. *International Journal of Impact Engineering* 2009; 36(10): 1250-1258.

[81] Shim VPW, Tan VBC, Tay TE. Modelling deformation and damage characteristics of woven fabric under small projectile impact. *International Journal of Impact Engineering* 1995; 16(4): 585-605.

[82] Goldberg RK, Roberts GD, Gilat A. Implementation of an associative flow rule including hydrostatic stress effects into the high strain rate deformation analysis of polymer matrix composites. *Journal of Aerospace Engineering* 2005; 18(1): 18-27.

[83] Wambua P, Vangrimde B, Lomov S, Verpoest I. The response of natural fibre composites to ballistic impact by fragment simulating projectiles. *Composite Structures* 2007; 77(2): 232-240.

[84] Jolly MR, Bender JW, Carlson JD. Properties and applications of commercial magnetorheological fluids. *Journal of Intelligent Material Systems and Structures* 1999; 10(1): 5-13.

[85] Ahmadian M, Poynor JC. An evaluation of magneto rheological dampers for controlling gun recoil dynamics. *Shock and Vibration* 2001; 8(3): 147-155.

[86] Lee YS, Wetzel ED, Wagner NJ. The ballistic impact characteristics of Kevlar® woven fabrics impregnated with a colloidal shear thickening fluid. *Journal of Materials Science* 2003; 38(13): 2825-2833.

[87] Xue Z, Hutchinson JW. A comparative study of impulse-resistant metal sandwich plates. *International Journal of Impact Engineering* 2004; 30(10): 1283-1305.

[88] Yungwirth CJ, Wadley HN, O'Connor JH, Zakraysek AJ, Deshpande VS. Impact response of sandwich plates with a pyramidal lattice core. *International Journal of Impact Engineering* 2008; 35(8): 920-936.

[89] Liu H, Liu H, Yang J, Zhao S. Cantilever sandwich beams with pyramidal truss cores subjected to tip impact. *Science China Technological Sciences* 2013; 56(1): 181-187.

[90] Reid S, Peng C. Dynamic uniaxial crushing of wood. *International Journal of Impact Engineering* 1997; 19(5): 531-570.

[91] Atas C, Sevim C. On the impact response of sandwich composites with cores of balsa wood and PVC foam. *Composite Structures* 2010; 93(1): 40-48.

[92] Zhao H, Elnasri I, Girard Y. Perforation of aluminium foam core sandwich panels under impact loading—An experimental study. *International Journal of Impact Engineering* 2007; 34(7): 1246-1257.

[93] Hou W, Zhu F, Lu G, Fang D. Ballistic impact experiments of metallic sandwich panels with aluminium foam core. *International Journal of Impact Engineering* 2010; 37(10): 1045-1055.

[94] Wang E, Gardner N, Shukla A. The blast resistance of sandwich composites with stepwise graded cores. *International Journal of Solids and Structures* 2009; 46(18): 3492-3502.

[95] Colloca M, Dorogokupets G, Gupta N, Porfiri M. Mechanical properties and failure mechanisms of closed-cell PVC foams. *International Journal of Crashworthiness* 2012; 17(3): 327-336.

[96] Zaretsky E, Asaf Z, Ran E, Aizik F. Impact response of high density flexible polyurethane foam. *International Journal of Impact Engineering* 2012; 39(1): 1-7.

[97] Song B, Chen WW, Dou S, Winfree NA, Kang JH. Strain-rate effects on elastic and early cell-collapse responses of a polystyrene foam. *International Journal of Impact Engineering* 2005; 31(5): 509-521.

[98] Verdejo R, Mills N. Performance of EVA foam in running shoes. *The engineering of sport* 2002; 4: 580-587.

[99] Verdejo R, Mills N. Heel–shoe interactions and the durability of EVA foam running-shoe midsoles. *Journal of Biomechanics* 2004; 37(9): 1379-1386.

[100] Fatt H, Park K. Perforation of honeycomb sandwich plates by projectiles. *Composites Part A: Applied Science and Manufacturing* 2000; 31(8): 889-899.

[101] Wang D. Impact behavior and energy absorption of paper honeycomb sandwich panels. *International Journal of Impact Engineering* 2009 1; 36(1): 110-114.

[102] Palanivelu S, Van Paepegem W, Degrieck J, Reymen B, Ndambi J, Vantomme J, Kakogiannis D, Wastiels J, Van Hemelrijck D. Close-range blast loading on empty recyclable metal beverage cans for use in sacrificial cladding structure. *Engineering Structures* 2011; 33(6): 1966-1987.

[103] Lee M, Yoo Y. Analysis of ceramic/metal armour systems. *International Journal of Impact Engineering* 2001; 25(9): 819-829.

[104] López-Puente J, Arias A, Zaera R, Navarro C. The effect of the thickness of the adhesive layer on the ballistic limit of ceramic/metal armours. An experimental and numerical study. *International Journal of Impact Engineering* 2005; 32(1): 321-336.

[105] Sarva S, Nemat-Nasser S, McGee J, Isaacs J. The effect of thin membrane restraint on the ballistic performance of armor grade ceramic tiles. *International Journal of Impact Engineering* 2007; 34(2): 277-302.

[106] Qiao P, Yang M, Bobaru F. Impact mechanics and high-energy absorbing materials: review. *Journal of Aerospace Engineering* 2008; 21(4): 235-248.

[107] Harris B. *Engineering composite materials.* : Institute of metals London; 1986.

[108] Beckermann G. *Performance of hemp-fibre reinforced polypropylene composite materials* 2007.

[109] Kandan K, Russell B, Deshpande V, Fleck N. The blast resistance of Dyneema composite beams under shock loading. In: The blast resistance of Dyneema composite beams under shock loading. In: *ICCM International Conferences on Composite Materials.* 2011.

[110] Gibson LJ, Ashby MF. *Cellular solids: structure and properties.* : Cambridge university press; 1999.

[111] Avalle M, Belingardi G, Montanini R. Characterization of polymeric structural foams under compressive impact loading by means of energy-absorption diagram. *International Journal of Impact Engineering* 2001; 25(5): 455-472.

[112] Li Q, Magkiriadis I, Harrigan J. Compressive strain at the onset of densification of cellular solids. *Journal of cellular plastics* 2006; 42(5): 371-392.

[113] Banhart J. Manufacture, characterisation and application of cellular metals and metal foams. *Progress in materials Science* 2001; 46(6): 559-632.

[114] Park C, Nutt S. Strain rate sensitivity and defects in steel foam. *Materials Science and Engineering: A* 2002; 323(1): 358-366.

[115] Yasensky J, Christiansen EL. Hypervelocity Impact Evaluation of Metal Foam Core Sandwich Structures. 2007.

[116] Merrett RP. *Dynamic Response of Aluminium Foams.* MSc. Thesis. University of Cape Town; 2011.

[117] Karagiozova D, Nurick GN, Langdon GS, Chung Kim Yuen S, Chi Y, Bartle S. Response of flexible sandwich-type panels to blast loading. *Composites Science and Technology* 2009; 69(6): 754-763.

[118] Kepler J. Impact Penetration of Sandwich Panels at Different Velocities-An Experimental Parameter Study: Part I-Parameters and Results. *Journal of Sandwich Structures and Materials* 2004; 6(4): 357-374.

[119] Kepler J. Impact Penetration of Sandwich Panels at Different Velocities–An Experimental Parameter Study: Part II–Interpretation of Results and Modeling. *Journal of Sandwich Structures and Materials* 2004; 6(5): 379-397.

[120] Hou B, Zhao H, Pattofatto S, Liu J, Li Y. Inertia effects on the progressive crushing of aluminium honeycombs under impact loading. *International Journal of Solids and Structures* 2012; 49(19): 2754-2762.

[121] Chi Y, Langdon GS, Nurick GN. The influence of core height and face plate thickness on the response of honeycomb sandwich panels subjected to blast loading. *Materials & Design* 2010; 31(4): 1887-1899.

[122] Dharmasena KP, Wadley HN, Xue Z, Hutchinson JW. Mechanical response of metallic honeycomb sandwich panel structures to high-intensity dynamic loading. *International Journal of Impact Engineering* 2008; 35(9): 1063-1074.

[123] Nurick GN, Langdon GS, Chi Y, Jacob N. Behaviour of sandwich panels subjected to intense air blast–Part 1: Experiments. *Composite Structures* 2009; 91(4): 433-441.

[124] Srivastava A, Majumdar A, Butola BS. Improving the impact resistance performance of Kevlar fabrics using silica based shear thickening fluid. *Materials Science and Engineering: A* 2011; 529: 224-229.

[125] Browne AL, Mccleary JD, Namuduri CS, Webb SR. Impact performance of magnetorheological fluids. *Journal of Intelligent Material Systems and Structures* 2009; 20(6): 723-728.

[126] Ashby M. The properties of foams and lattices. *Philosophical Transactions of the Royal Society A: Mathematical, Physical and Engineering Sciences* 2006; 364(1838): 15-30.

[127] Wadley H, Dharmasena K, Chen Y, Dudt P, Knight D, Charette R, Kiddy K. Compressive response of multilayered pyramidal lattices during underwater shock loading. *International Journal of Impact Engineering* 2008; 35(9): 1102-1114.

[128] Xiong J, Vaziri A, Ma L, Papadopoulos J, Wu L. Compression and impact testing of two-layer composite pyramidal-core sandwich panels. *Composite Structures* 2012; 94(2): 793-801.

[129] Yin S, Wu L, Ma L, Nutt S. Hybrid truss concepts for carbon fiber composite pyramidal lattice structures. *Composites Part B: Engineering* 2012; 43(4): 1749-1755.

[130] Wadley H, Dharmasena K, Chen Y, Dudt P, Knight D, Charette R, Kiddy K. Compressive response of multilayered pyramidal lattices during underwater shock loading. *International Journal of Impact Engineering* 2008; 35(9): 1102-1114.

[131] McKown S, Shen Y, Brookes WK, Sutcliffe CJ, Cantwell WJ, Langdon GS, Nurick GN, Theobald MD. The quasi-static and blast loading response of lattice structures. *International Journal of Impact Engineering* 2008; 35(8): 795-810.

[132] Chung Kim Yuen S, Nurick GN, Theobald MD, Langdon GS. Sandwich panels subjected to blast loading. Dynamic Failure of Materials and Structures: Springer; 2010. p. 297-325.

[133] Wang Z. Energy absorption properties of multi-layered corrugated paperboard in various ambient humidities. *Materials & Design* 2011; 32(6): 3476-3485.

[134] Wang D. Energy absorption diagrams of multi-layer corrugated boards. *Journal of Wuhan University of Technology-Mater.Sci.Ed.* 2010; 25: 58-61.

[135] Chick MC, Learmonth LA. *Determination of shock initiation and detonation characteristics of PE4 in proof test geometries.* Department of Defence, Materials Research Laboratories; 1985 .

[136] Weckert S, Anderson C. *A preliminary comparison between TNT and PE4 landmines* 2006.

[137] Wharton R, Formby S, Merrifield R. Airblast TNT equivalence for a range of commercial blasting explosives. *Journal of hazardous materials* 2000; 79(1): 31-39.

[138] Cowper GR, Symonds PS. *Strain-hardening and strain-rate effects in the impact loading of cantilever beams.* ; 1957 .

[139]SSAB Tunnplat Dogal B500 Metal-coated Mild Steel. 2012; Available at: http://www.matweb.com/search/DataSheet.aspx?MatGUID=affca50c735d466ca3abc20e27a26d59. Accessed November 12, 2012.

[140] Ronchietto F, Chung Kim Yuen S, Nurick GN. Response of axially stacked square tubes to axial impact loads. *Latin American Journal of Solids and Structures* 2010; 6(4): 413-440.

APPENDICES

A. Appendix A – INFRA-RED SPEED TRAP CONCEPT

Before the wire-break speed trap system is deployed for this project, an infra-red light system is tried. In this system, an infra-red light emitter and a phototransistor (receiver) are placed diametrically opposite to each other, mounted in holes drilled on the wall of a the threaded tube separating the two test plates. An identical set of emitter and receiver are placed 40mm from the tube along the length of the tube. The tube is threaded at both ends and is fastened on to threaded clamps on both the front and rear clamping rigs.

Figure A-1: Threaded tube with two infra-red emitter-receiver pairs for velocity measurement

The light receiver works by a photoelectric effect, when the light emanating from the emitter falls on it, a potential difference is caused across it, which is dependent on the amount of light falling it, and thus current starts flowing. The voltage across the both the receivers would be measured through two channels on an oscilloscope. When an object like a fragment obscures the light on the first line of emitter-receiver pair, a drop in voltage on one channel can be captured and also for the second line of emitter and receiver. The initial assembled concept, showing two emitters and a D-subminiature male connector that links the receivers and emitters with power supply and the oscilloscope.

When this system is tried, it presents problems in that it fails to pick up the voltage drops which should theoretically be observed when the fragment passes through the two infra-red light gates. A number of reasons may be possible for this:

- The light from the emitter is fairly spread out, if only a small part of the fragment obscures the light, the voltage drop may be too slight to notice, particularly considering the fact that the voltage drop has to be captured at two points for the velocity to be measurable.
- As the fragment is released from the front plate, its motion is not always pure translation. Evidence of this can be found in the observations and results in Chapter 4 where the rear plate is sliced by the edge of the fragment. This suggests that the fragment may be subjected to spinning as it flies to the rear plate. This means that as it passes through a line of light, such may be the orientation of its spin that it doesn't adequately obscure both the lines of infra-red light.
- An added uncertainty of the motion of the fragment is the fact that in some cases, it does impact the rear plate at the central region, meaning that as the fragment is in motion it may completely be eccentric to the axis of the tube and thus may not obscure one or both of the lines of light.

B. Appendix B – MATERIAL CHARACTERISATION

B.1. Tensile tests on mild steel

Table B.1: : Detailed results of the quasi-static tensile tests performed on mild steel

Test #	Crosshead Speed	Strain rate	Elongation at failure	Dynamic Yield	Static Yield	UTS
	(mm/min)	($.s^{-1}$)	(%)	(MPa)	(MPa)	(MPa)
SHEET 1						
Test 1	5	0.00167	29.66	321.4	283.7	381.0
Test 2	10	0.00336	29.03	324.1	281.2	383.1
Test 3	25	0.0083	28.09	330.6	279.5	392.3
Test 4	50	0.01678	33.75	387.7	320.2	415.6
Test 5	75	0.02487	32.31	381.2	310.4	413.4
Test 6	100	0.03331	28.7	358.2	288.5	399.4
SHEET 2						
Test 1	5	0.00167	33.32	337.6	298.0	380.7
Test 2	10	0.00334	35.74	339.4	294.5	374.6
Test 3	25	0.00828	29.89	350.8	296.5	386.6
Test 4	50	0.01668	32.67	344.0	284.2	373.5
Test 5	75	0.0253	34.98	372.9	303.5	373.7
Test 6	100	0.0334	31.26	348.2	280.4094	381.8
SHEET 3						
Test 1	5	0.00167	30.95	314.7	277.8	360.1
Test 2	10	0.00333	35.65	336.2	291.7	370.0
Test 3	25	0.00835	VOID	VOID	VOID	VOID
Test 4	50	0.01669	36.08	344.8	284.8	369.1
Test 5	75	0.025	36.12	355.1	289.1	379.6
Test 6	100	0.03333	33.68	349.5	281.5	376.8
SHEET 4						
Test 1	5	0.00167	31.07	349.8	308.7	373.8
Test 2	10	0.00334	35.42	291.1	252.6	340.5
Test 3	25	0.00832	32.14	350.2	296.0	376.3
Test 4	50	0.01664	32.75	359.7	297.2	374.2
Test 5	75	0.02506	32.92	340.1	276.9	377.7
Test 6	100	0.03337	33.56	360.8	290.6	371.9

SHEET 5						
Test 1	5	0.00166	41.12	319.0	281.6	357.0
Test 2	10	0.00332	36.73	338.2	293.5	370.3
Test 3	25	0.00835	35.22	347.5	293.7	371.2
Test 4	50	0.01663	34.2	334.2	276.1	373.8
Test 5	75	0.02495	38.08	329.3	268.2	378.4
Test 6	100	0.03333	34.4	378.0	304.5	391.0
SHEET 6						
Test 1	5	0.00166	34.13	314.4	277.6	354.2
Test 2	10	0.00333	41.96	335.1	290.8	361.7
Test 3	25	0.00831	37.73	316.0	267.1	353.9
Test 4	50	0.01662	36.39	365.3	301.8	375.1
Test 5	75	0.025	38	345.4	281.2	371.5
Test 6	100	0.03328	37.18	352.8	284.1	373.0

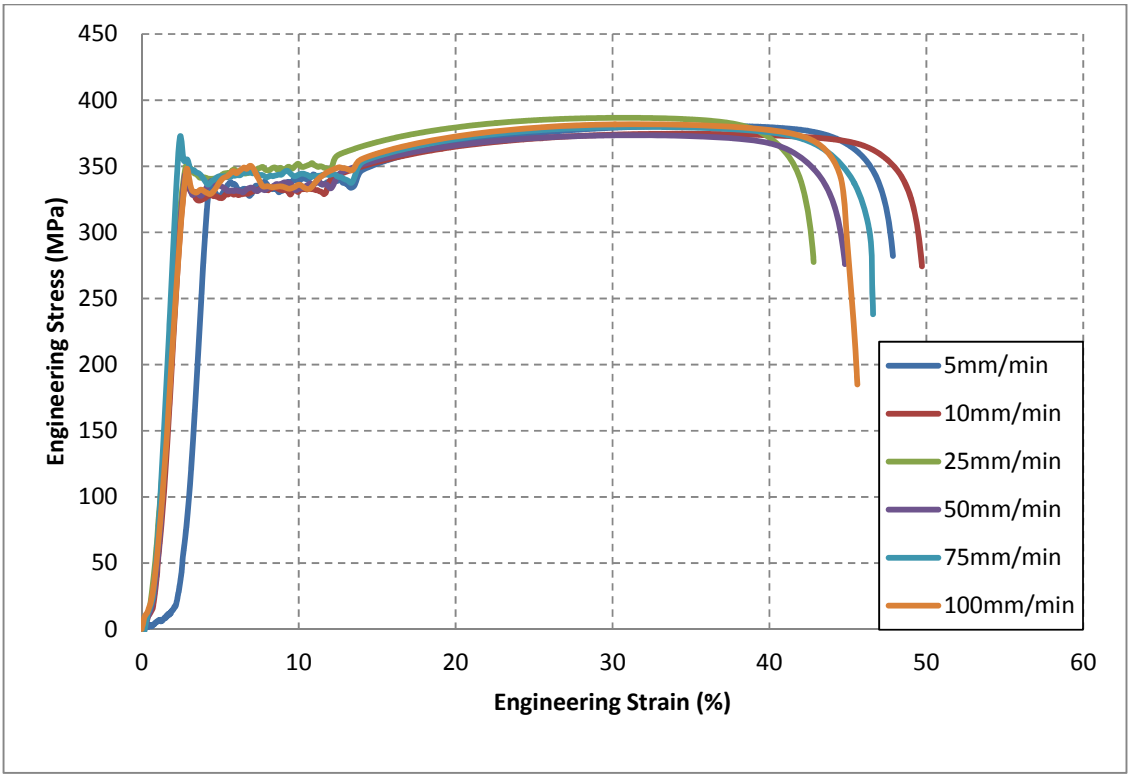

Figure B-1: Engineering Stress vs. Strain for all tests conducted on sheet 2 mild steel

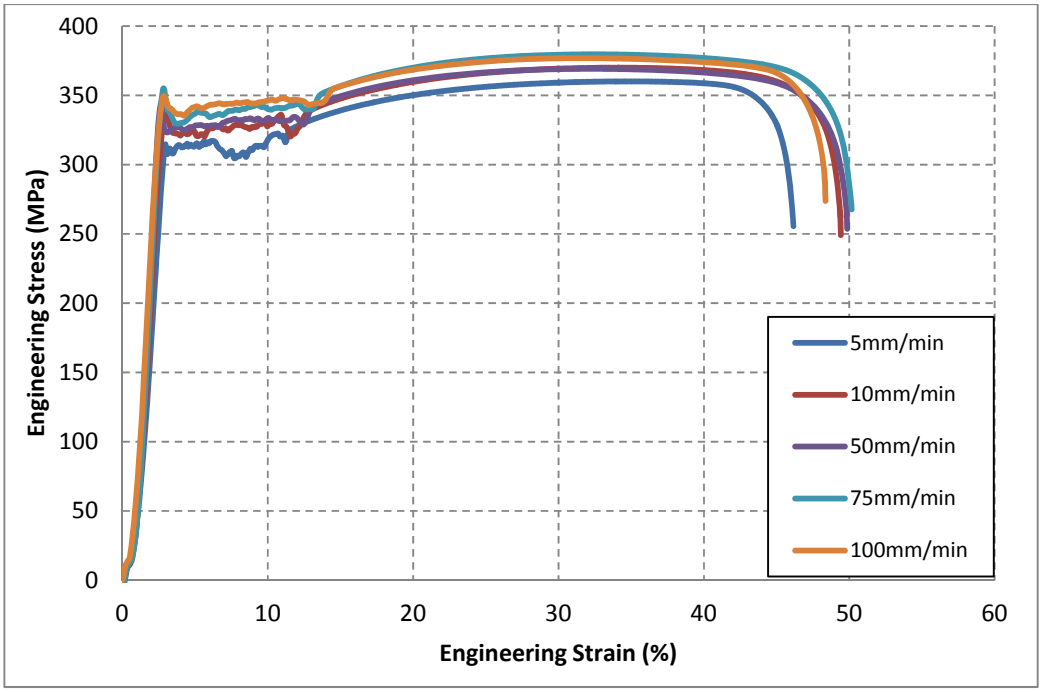

Figure B-2: Engineering Stress vs. Strain for all tests conducted on sheet 3 mild steel

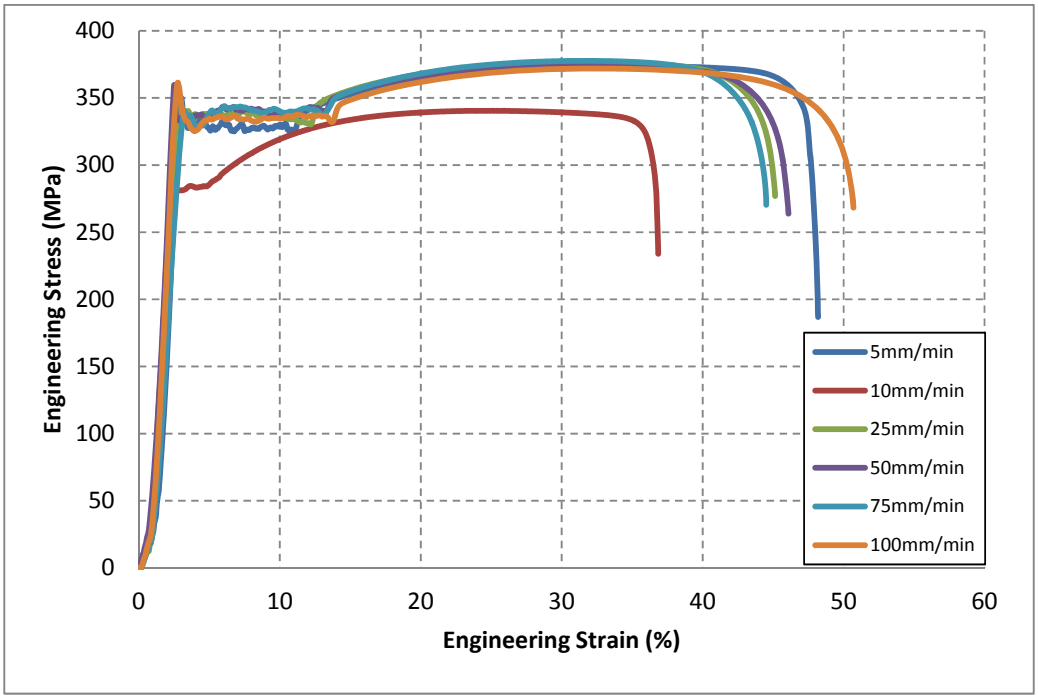

Figure B-3: Engineering Stress vs. Strain for all tests conducted on sheet 4 mild steel

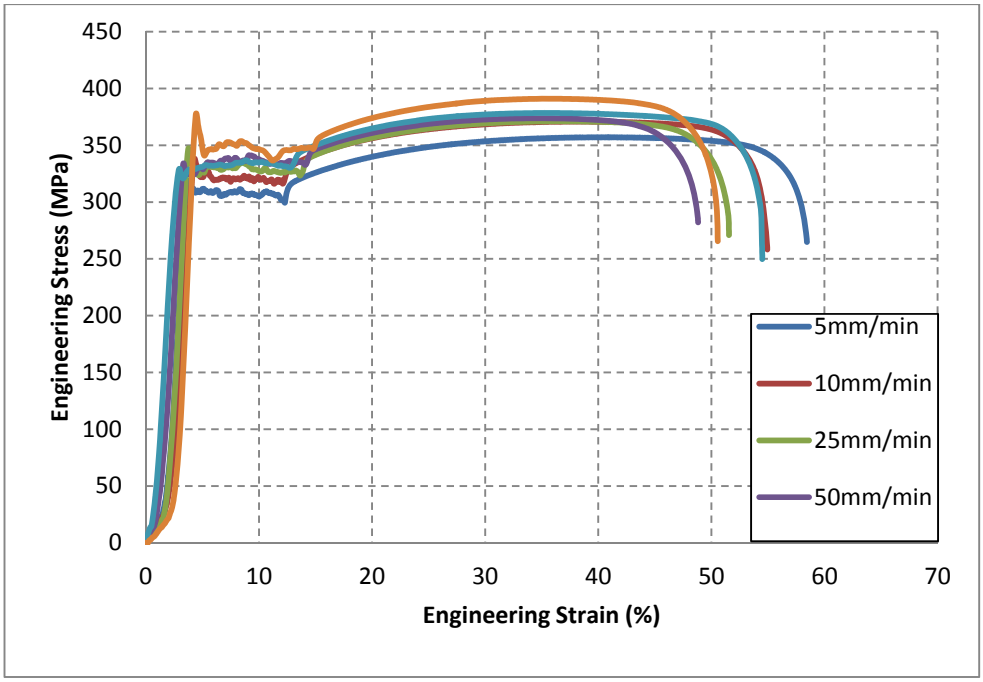

Figure B-4: Engineering Stress vs. Strain for all tests conducted on sheet 5 mild steel

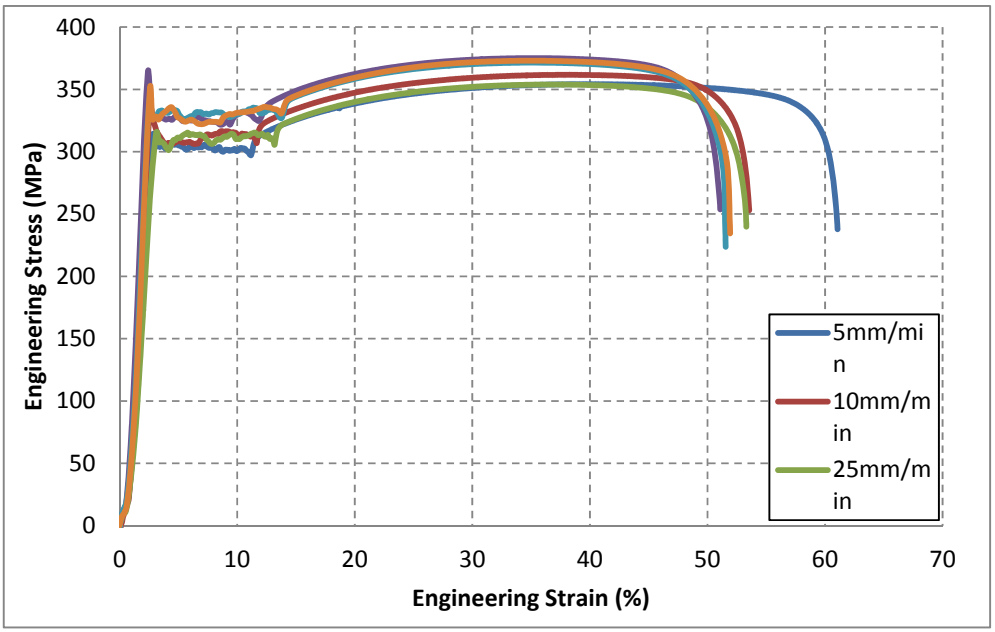

Figure B-5: Engineering Stress vs Strain for all tests conducted on sheet 6 mild steel

B.2. Quasi-static compression on energy absorbing materials

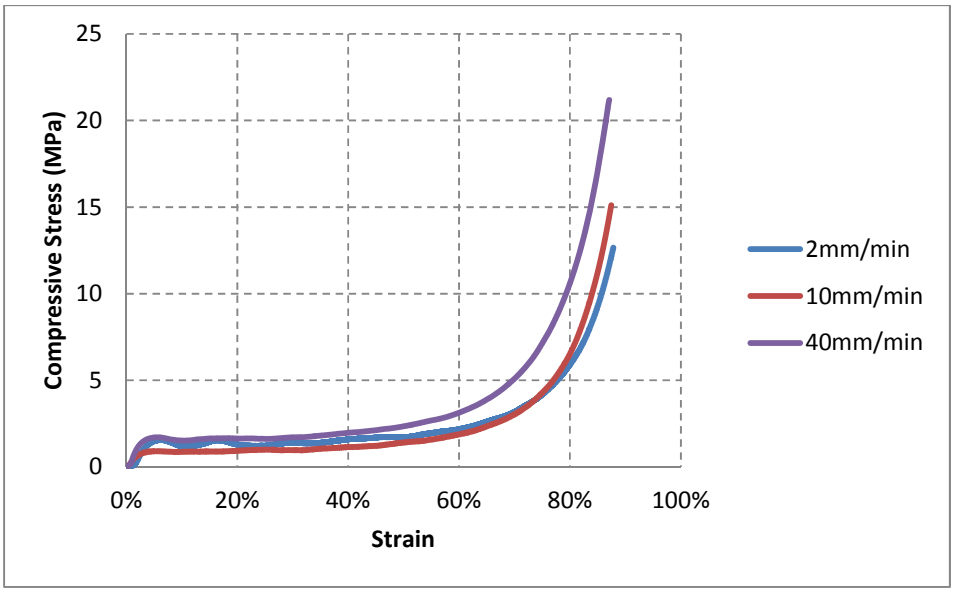

Figure B-6: Compressive stress vs. Strain for aluminium foam at different cross-head speeds

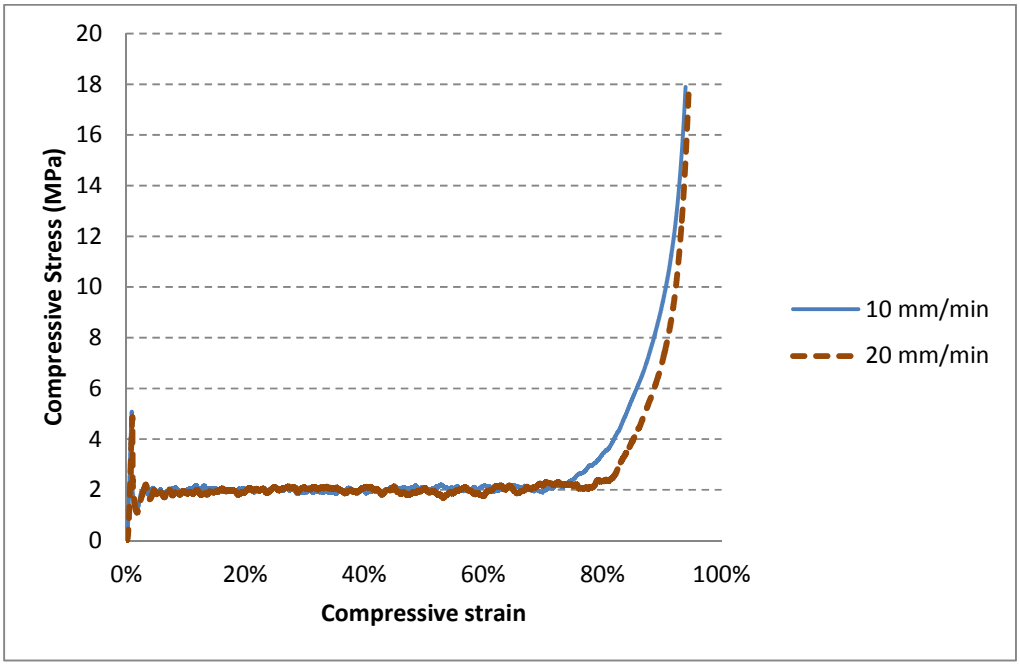

Figure B-7: Compressive stress vs. Strain for aluminium honeycomb 'A' at different cross-head speeds

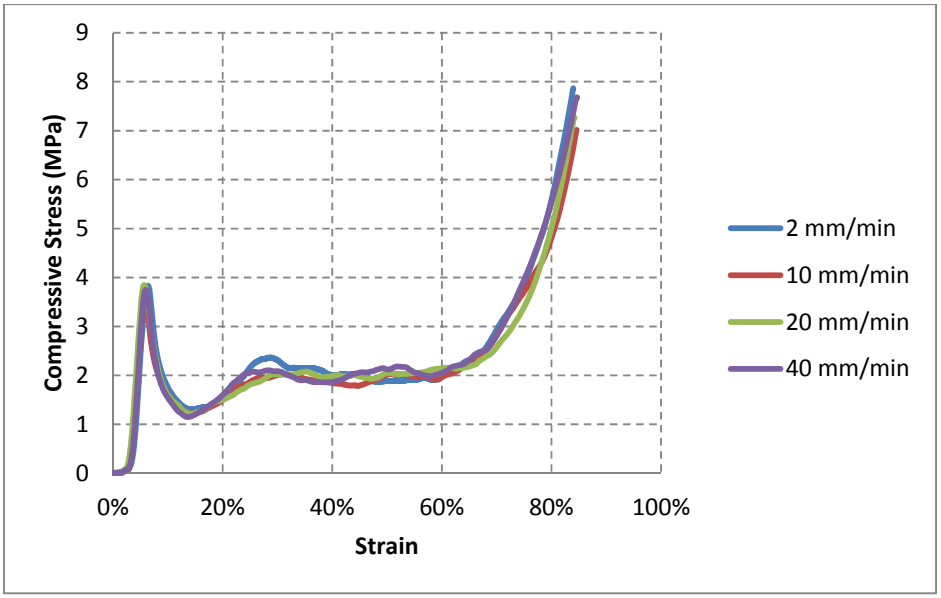

Figure B-8: Compressive stress vs. Strain for aluminium honeycomb 'B' at different cross-head speeds

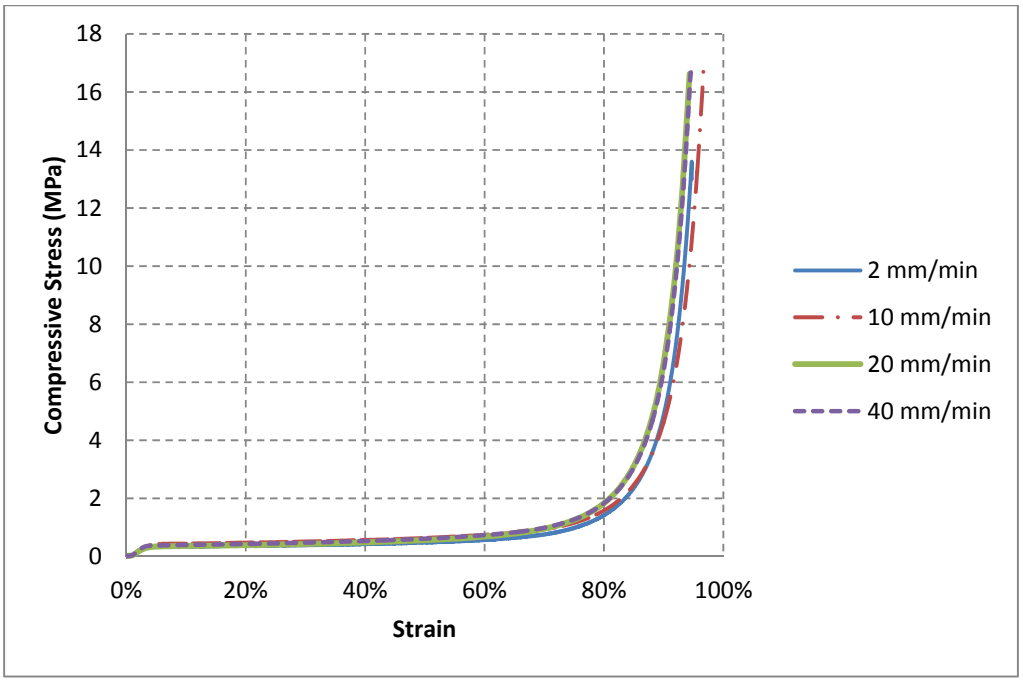

Figure B-9: Compressive stress vs. Strain for balsa wood at different cross-head speeds

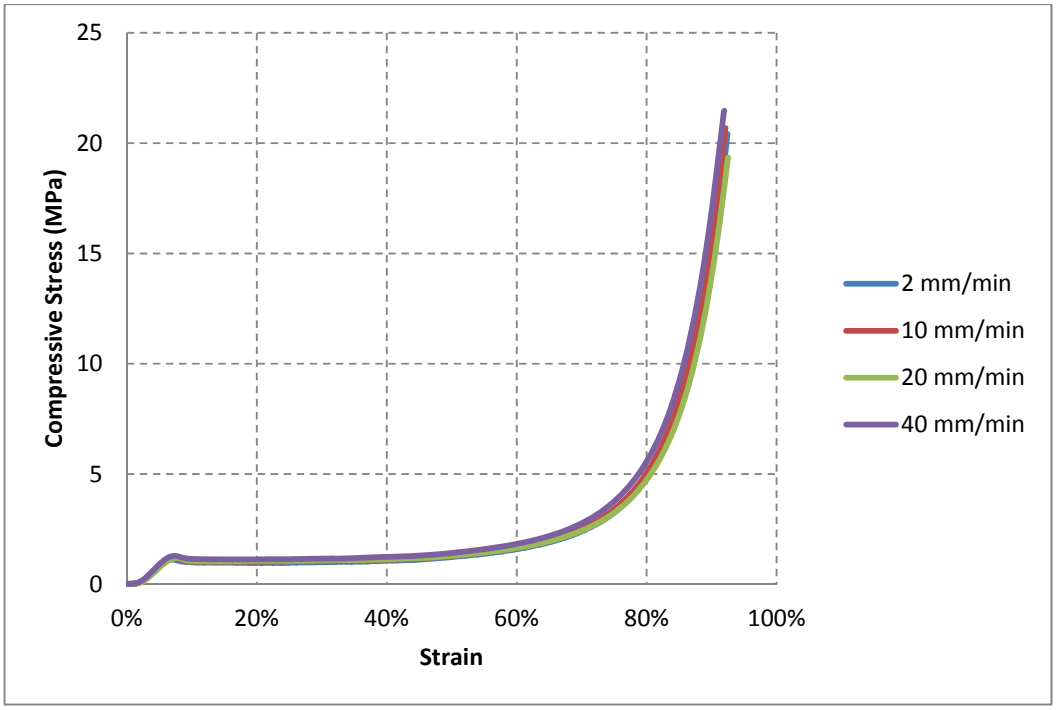

Figure B-10: Compressive stress vs. Strain for Corecell A500 foam at different cross-head speeds

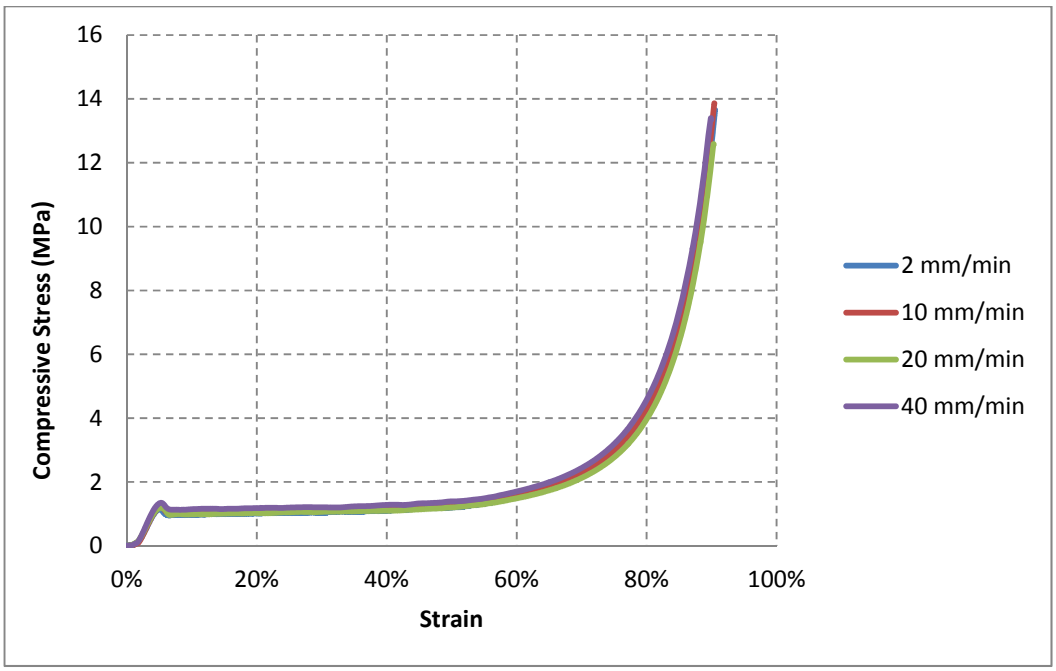

Figure B-11: Compressive stress vs. Strain for Corecell M80 foam at different cross-head speeds

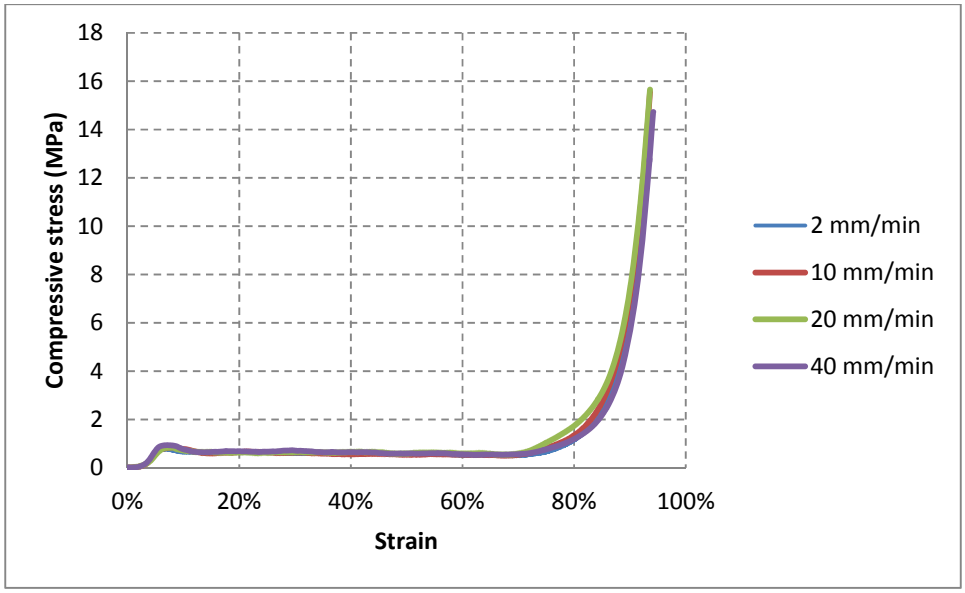

Figure B-12: Compressive stress vs. Strain for corrugated board at different cross-head speeds

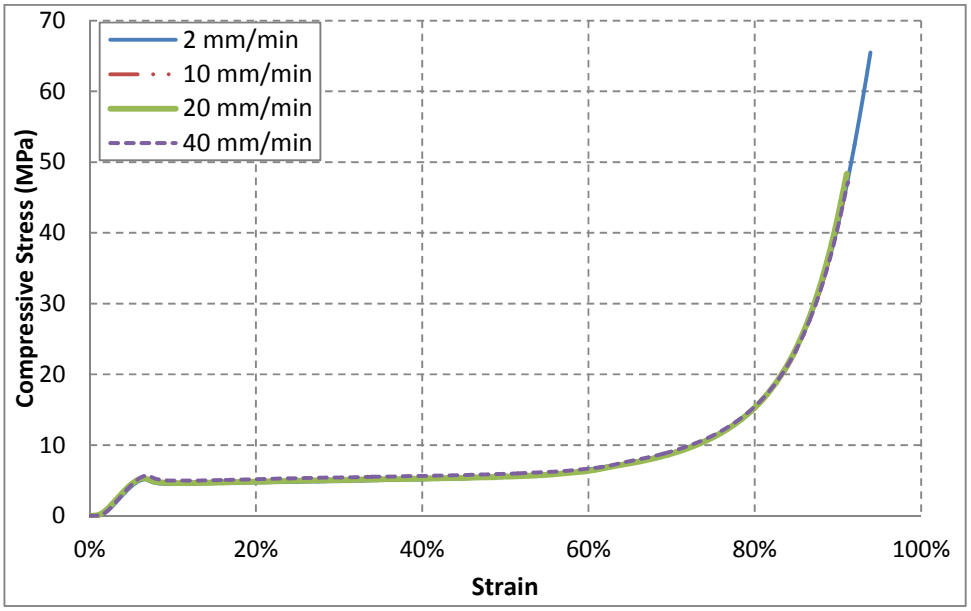

Figure B-13: Compressive stress vs. Strain for Divinycell H200 foam at different cross-head speeds

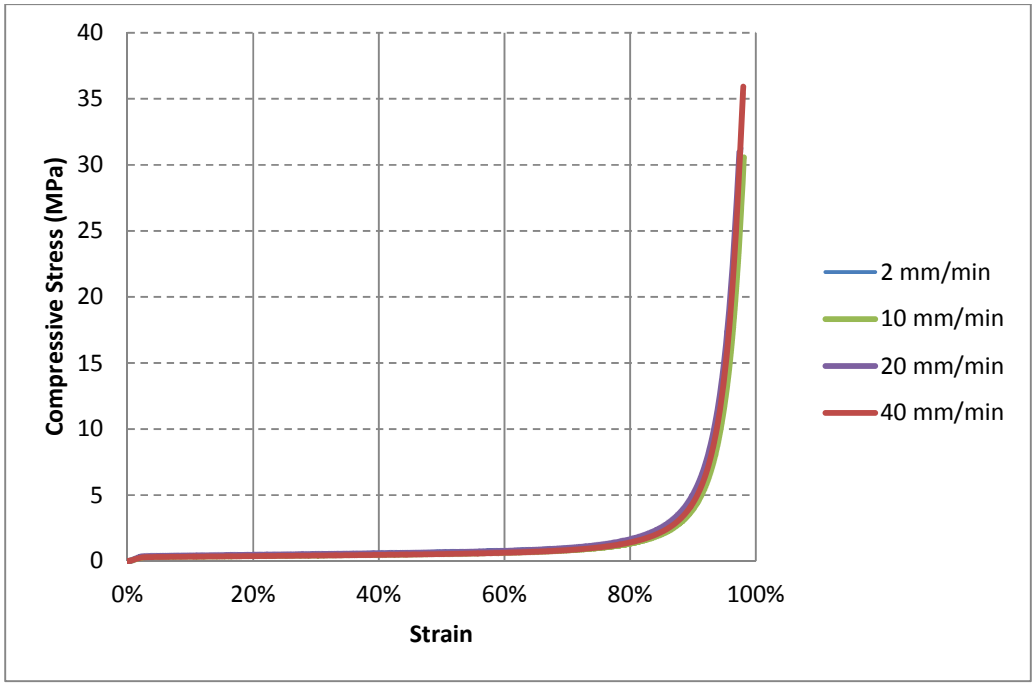

Figure B-14: Compressive stress vs. Strain for polystyrene foam at different cross-head speeds

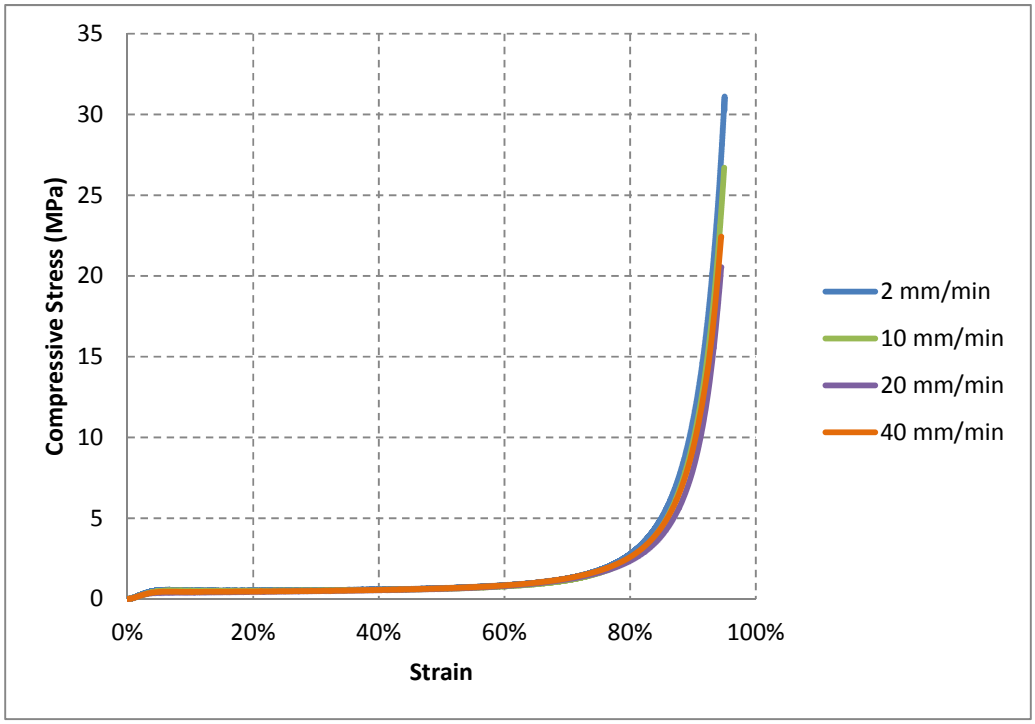

Figure B-15: Compressive stress vs. Strain for polyurethane 80 foam at different cross-head speeds

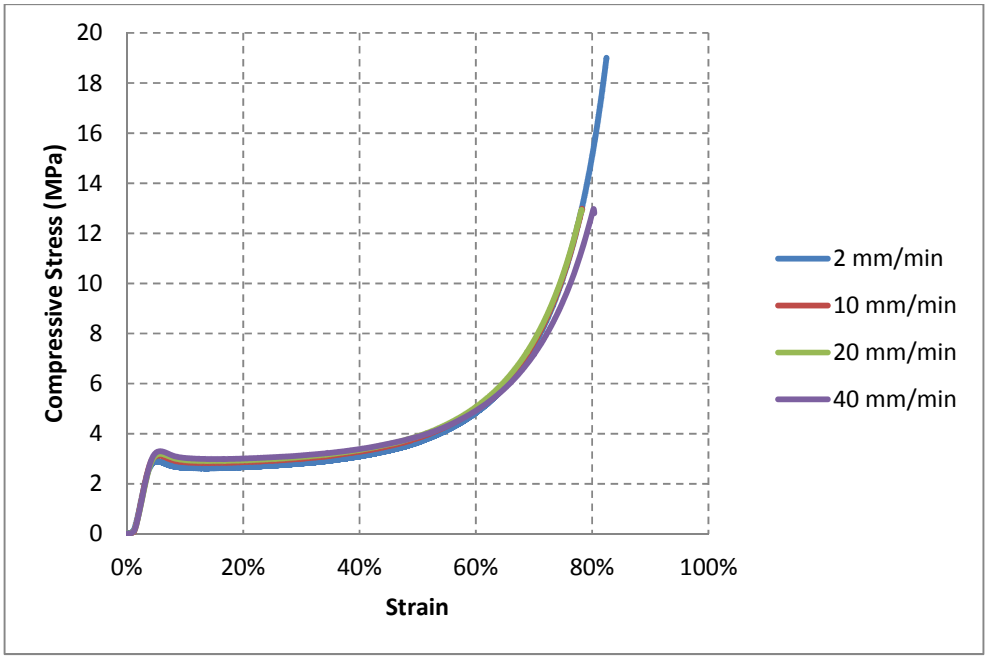

Figure B-16: Compressive stress vs. Strain for polyurethane 200 'A' foam at different cross-head speeds

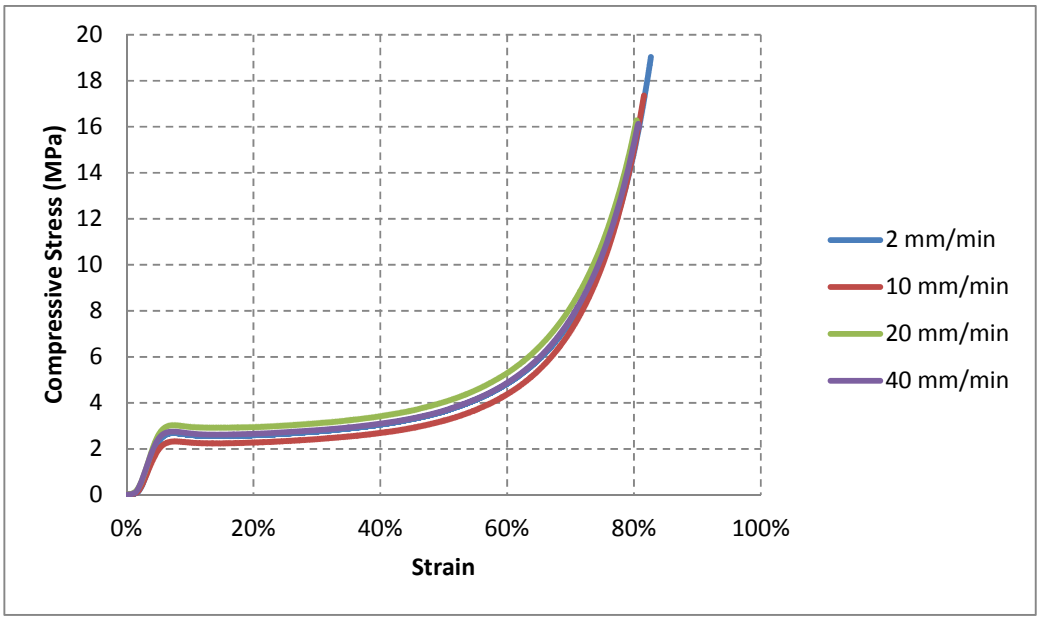

Figure B-17: Compressive stress vs. Strain for polyurethane 200 'B' foam at different cross-head speeds

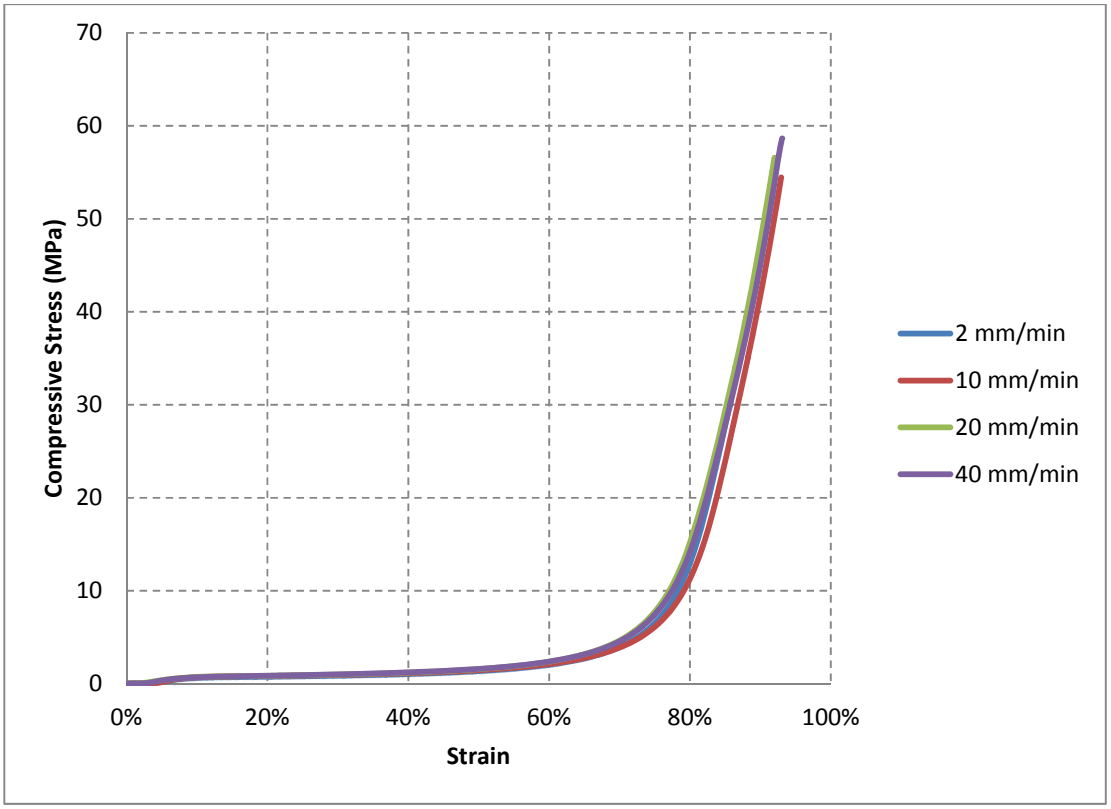

Figure B-18: Compressive stress vs. Strain for RG5565 EVA foam at different cross-head speeds

C. Appendix C – BALLISTIC PENDULUM THEORY

In this section, the theoretical approach that is used in working out of the initial velocity of the pendulum and hence impulse from the blast, in every test is shown.

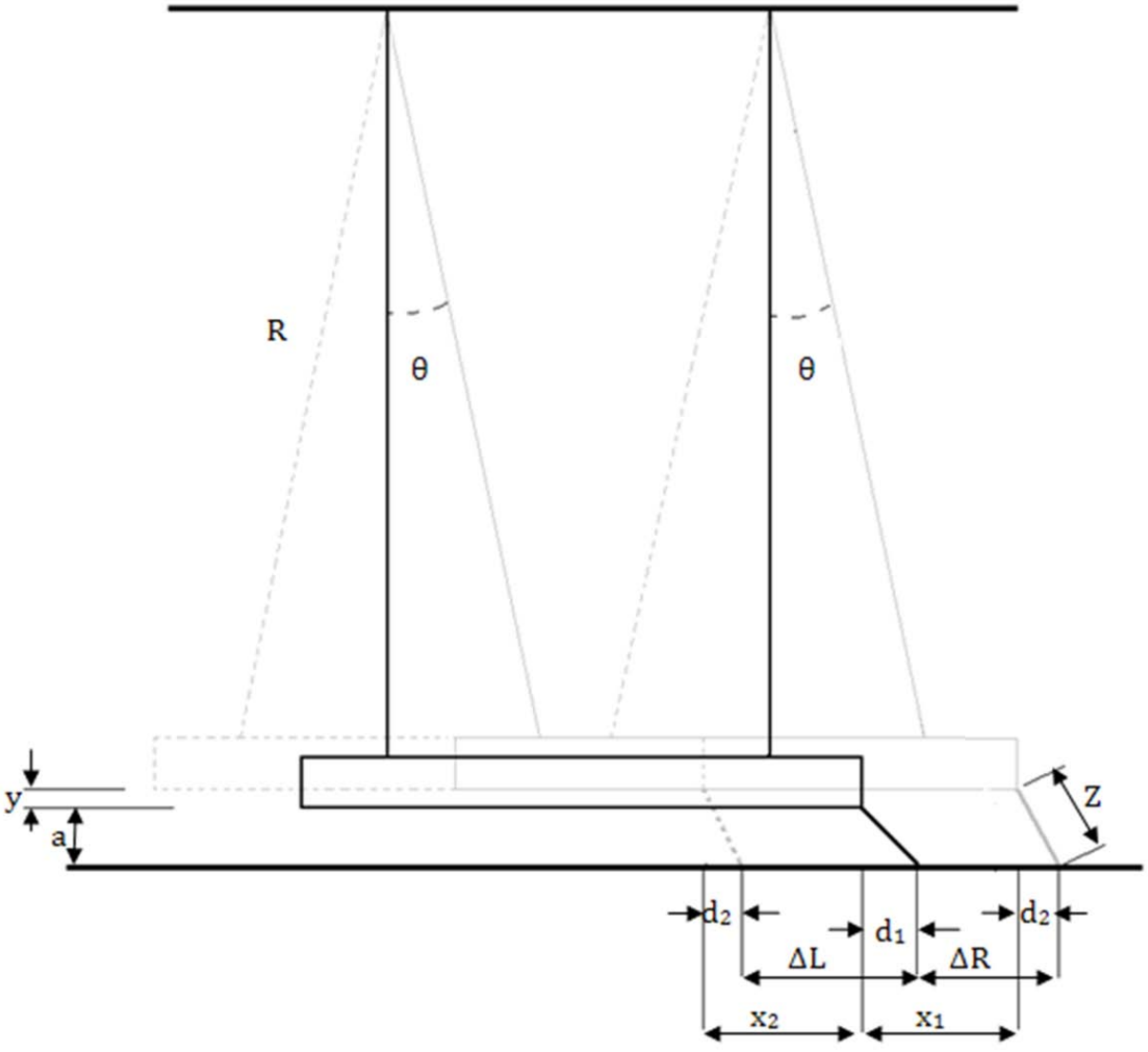

Figure C-1: Simplified geometry and key dimensions of the ballistic pendulum

Key: Pendulum at rest ——— Backward swing ——— Forward Swing - - - - -

In order to get the experimental impulse, initial velocity of the pendulum has to be known. For that, the maximum horizontal displacements (x_1 and x_2) in Figure C-1 have to be known. If viscous damping is to be assumed in the pendulum, the equation of motion of the pendulum can be expressed as:

$$\ddot{X} + 2\beta\dot{X} + {\omega_n}^2 X = 0 \qquad \text{Eq. C-1}$$

With : $\beta = \frac{C}{2M}$, $\omega_n = \frac{2\pi}{T}$ and $\omega_d = \sqrt{{\omega_n}^2 - \beta^2}$

C is the damping coefficient, M is the total mass of the pendulum and T is its time period. The solution to the above equation (Eq. C-1) is:

$$X = \frac{e^{\beta.t}\dot{x}_0 \sin(\omega_d t)}{\omega_d} \qquad \text{Eq. C-2}$$

Where: $\dot{x}_0$ is the initial velocity of the pendulum and *t* is an arbitrary time

Let x_1 be the horizontal displacement at *t = T/4*

and x_2 be the horizontal displacement at *t = 3T/4*

If these values are substituted into Eq. C-2, they give

$$X_1 = \frac{\dot{x}_0 T}{2\pi} e^{-0.25\beta T} \qquad \text{Eq. C-3}$$

And

$$X_2 = \frac{\dot{x}_0 T}{2\pi} e^{-0.75\beta T}$$ Eq. C-4

Therefore:

$$\frac{x_1}{x_2} = e^{0.5\beta T}$$ Eq. C-5

If Eq. E-5 is rearranged, the damping constant can thus be given as:

$$\beta = \frac{2}{T} \ln\left(\frac{x_1}{x_2}\right)$$ Eq. C-6

And from Eq. C-3:

$$\dot{x}_0 = \frac{2\pi}{T} . x_1 . e^{0.25\beta T}$$ Eq. C-7

The impulse of the pendulum can thus be defined as :

$$I = M\dot{x}_0$$ Eq. C-8

However, x_1 and x_2 are not known by simple tracing or visual means (Figure C-1). This is because the support of the recording pen is hinged on the pendulum and as the pendulum sways and consequently changes in its vertical position, the support of the pen moves about its hinge. This thus means that the horizontal displacements of the pendulum (x_1 and x_2) and the horizontal displacements of the tip of the pen (ΔR and ΔL) are.

Referring to Figure C-1, the distance between the hinge of the support of the pen and the tip of the pen at equilibrium is given by:

$$d_1 = \sqrt{Z^2 - a^2} \qquad \text{Eq. C-9}$$

When the pendulum is at the maximum displacement:

$$d_2 = \sqrt{Z^2 - (a + y)^2} \qquad \text{Eq. C-10}$$

The angle θ is small, and for small angles:

$x_1 = R\theta$ and $y = \frac{R\theta}{2}$

$$\therefore y = \frac{{x_1}^2}{2R} \qquad \text{Eq. C-11}$$

Substituting this into Eq. C-10 yields:

$$d_2 = \sqrt{Z^2 - \left(a + \frac{{x_1}^2}{2R}\right)^2} \qquad \text{Eq. C-12}$$

From Figure C-1, it is apparent that:

$$x_1 = \Delta R + d_1 - d_2$$ Eq. C-13

and also that

$$x_2 = \Delta L - d_1 + d_2$$ Eq. C-14

If the values of d_1 and d_2 (from Eq. C-9 and Eq. C-12) are substituted into Eq. C-13 and Eq. C-14, the following equations are formed:

$$x_1 = \Delta R + \sqrt{Z^2 - a^2} - \sqrt{Z^2 - \left(a + \frac{{x_1}^2}{2R}\right)^2}$$ Eq. C-15

And

$$x_2 = \Delta L - \sqrt{Z^2 - a^2} + \sqrt{Z^2 - \left(a + \frac{{x_1}^2}{2R}\right)^2}$$ Eq. C-16

The value of x_1 in Eq. C-15 is solved using iterative methods whilst x_2 in Eq. C16 is solved based on the value of x_1.

The details of the Pendulum are listed in Table C.1:

Table C.1: Details of dimensions and masses of the ballistic pendulum

Parameter	**Value**
Z (mm)	215
a (mm)	154
R (mm)	2960
Time Period T (s)	3.41
I-Beam mass (kg)	32.96
TEST RIG MASS (INITIAL WITH NO ABSORBERS) (details, see §3.1.2) (kg)	51.08
TEST RIG MASS (TESTS WITH ABSORBERS) (details, see §3.1.2) (kg)	54.86
Counter-mass (kg)	51.72
TOTAL PENDULUM MASS (INITIAL WITH NO ABSORBERS) (kg)	135.74
TOTAL PENDULUM MASS (TESTS WITH ABSORBERS) (kg)	139.52

D. Appendix D – CHALLENGES IN THEORETICAL ANALYSIS

It was planned in the study to determine the **energy required for deforming a plate** from an impulsive load like fragment impact (Eq. 2-10) and compare it to the kinetic energy of the fragment before impacting the plates, which could be used to find energy absorbed by the energy absorber.

$$E_{def} = \pi h \int_0^R \frac{{\sigma_0}^1}{(1-\nu+\nu^2)^{1/2}} \left(\frac{\partial w_i}{\partial r}\right)^2 r dr$$ Recall Eq. 2-10

Where ${\sigma_0}^1$ = dynamic yield stress, ν = poisson's ration of the plate, w_i is an arbitrary plate deflection, $w_i = \delta.\gamma(r)$ and δ is the maximum/midpoint deflection and $\gamma(r)$ is the shape function of the plate deflection profile.

To get the energy required for deformation (Eq. 2-10) requires the knowledge of the dynamic yield stress of the impacted plate material. As discussed in §2.1.4.2., and as shown in Eq. 2-12, the iterative solution of the dynamic yield stress requires the knowledge of impulse from the impact of fragment on the plate.

$$\frac{I^4 96421.8^2}{{\sigma_0}^1}\left[\frac{{\sigma_0}^1}{\sigma_0} - 1\right]^{-10} = 1600$$ Recall Eq. 2-12

Where: I = Impulse from the load, σ_0 = static yield stress

Therefore, it follows that the parameters to be used in the energy analyses are dependent on impulse from the fragment. For cases when there are no energy absorbers protecting the rear plate, it is found that the impulse from the fragment cannot be solved as shown in Eq. 2-13,

because, whilst the impact velocity of the fragment is **known**, the rebound velocity (which, because of the rebounding of fragments, is **not** zero) is not known.

$$I = m_f \left[\left(\overrightarrow{v_f}\right)_0 - \left(\overrightarrow{v_f}\right)_1 \right]$$ Recall Eq. 2-13

Where $\left(\overrightarrow{v_f}\right)_0$ = impact velocity of the fragment, $\left(\overrightarrow{v_f}\right)_1$ = its rebound velocity **(unknown)**

Additionally, for cases where an energy absorber protect the rear plate, the impulse imparted by the fragment on the plate cannot be solved, because, besides the fact that the rebound velocity is not known, the impact velocity of the fragment is also **not known** because, the energy absorber decelerates the fragment from a known release velocity to an unknown velocity just as the fragment impacts the rear plate.

E. Appendix E – DRAWINGS

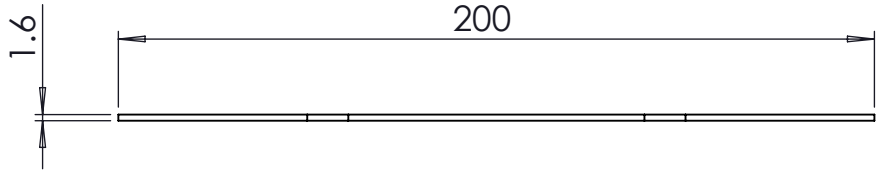

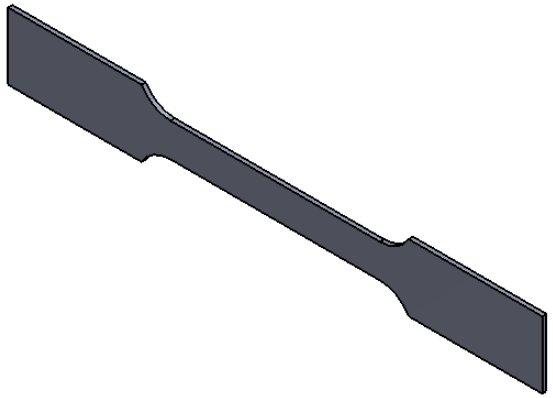

Note: Specimen should be cut from the same parent sheet as the test plate material

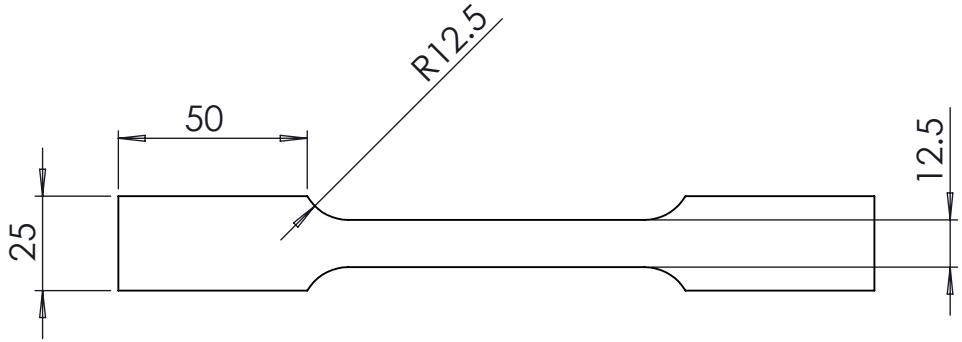

SolidWorks Student Edition.
For Academic Use Only.

A4 Landscape	University of Cape Town Department of Mechanical Engineering				
	Title: Mild Steel Tensile Specimen				
Quantity: 6	Part Finish	Date: 2013/05/28	Scale: 1:2	Sheet1	of 1
Material: Mild Steel	Drawn By: Nzudzanyo Ranwaha			Drawing Number	

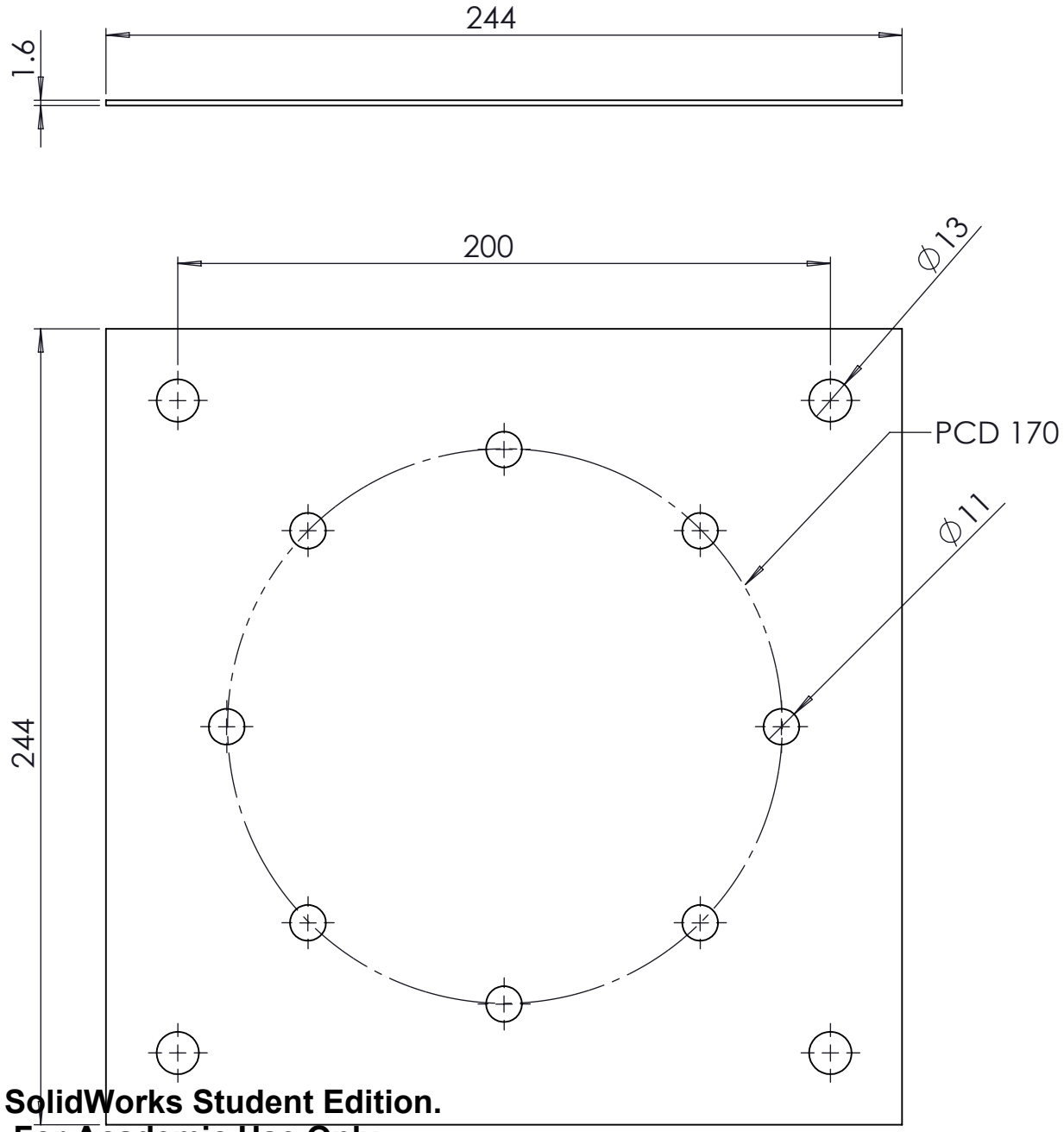

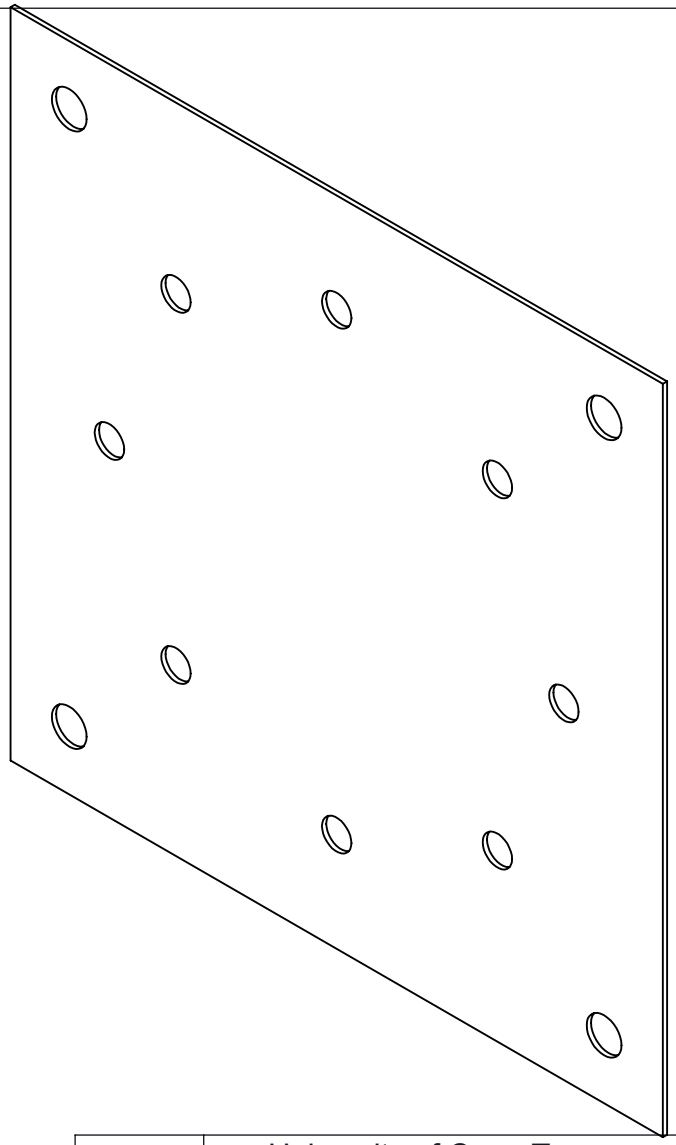

SolidWorks Student Edition.
For Academic Use Only.

A4 Landscape	University of Cape Town Department of Mechanical Engineering				
	Title: 1.6mm thick Test Plate				
Quantity: 200	Part Finish	Date: 2013/05/28	Scale: 1:2	Sheet1	of 1
Material: Mild Steel	Drawn By: Nzudzanyo Ranwaha			Drawing Number	

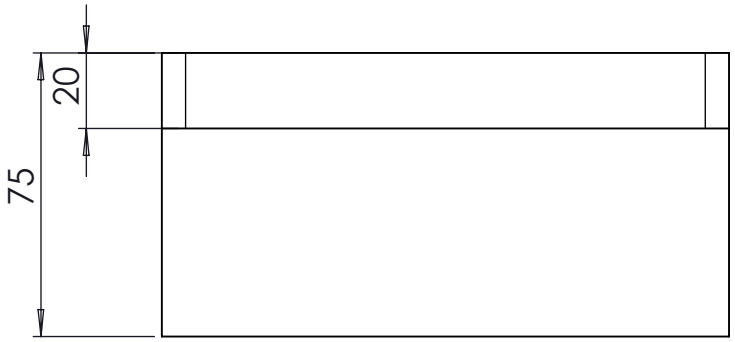

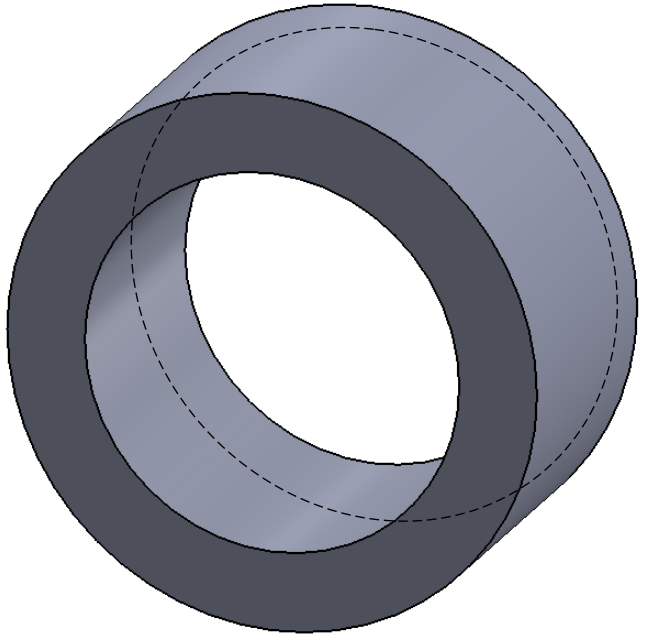

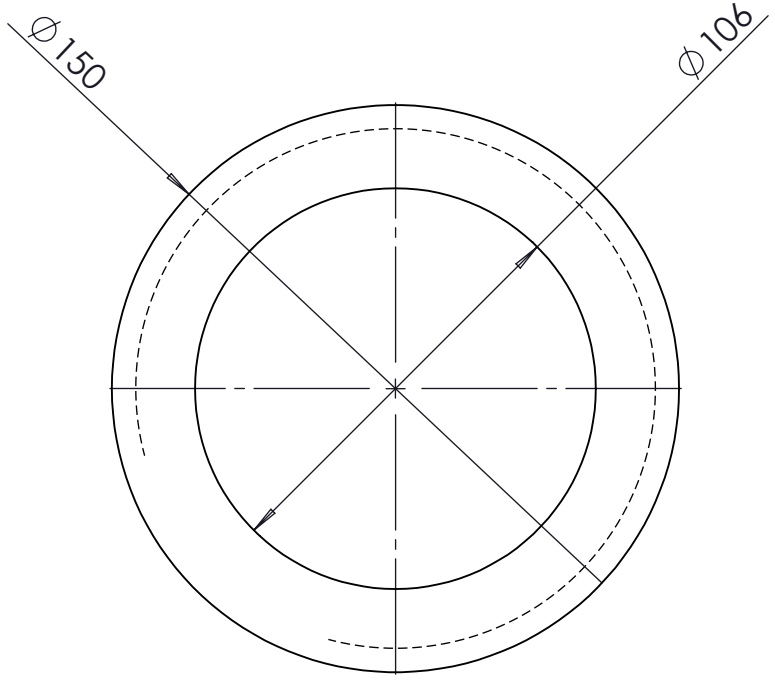

SolidWorks Student Edition.
For Academic Use Only.

A4 Landscape	University of Cape Town Department of Mechanical Engineering				
	Title: Energy absorber containment tube				
Quantity: 1	Part Finish	Date: 2013/04/17	Scale: 1:1	Sheet1	of 1
Material: Steel	Drawn By: Nzudzanyo Ranwaha			Drawing Number	

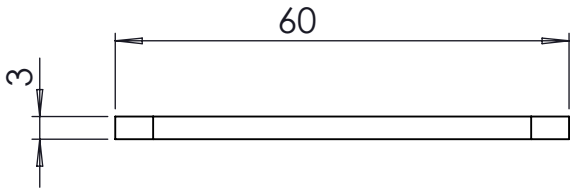

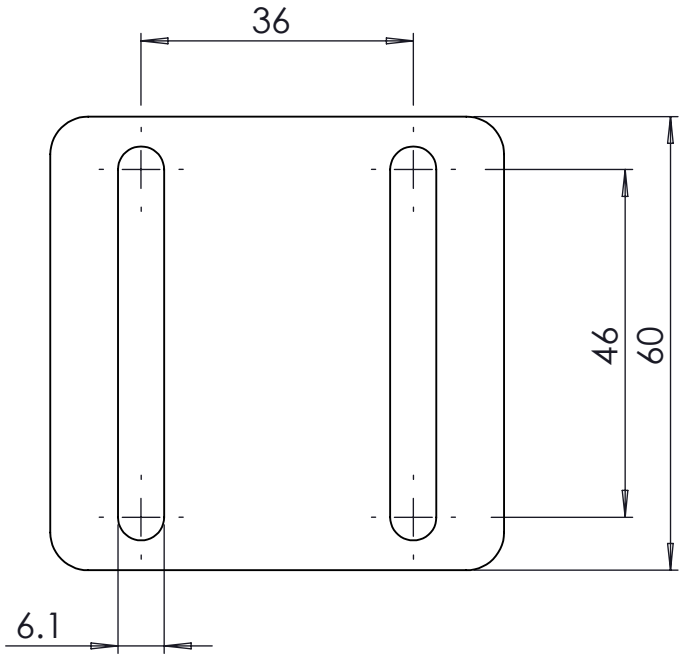

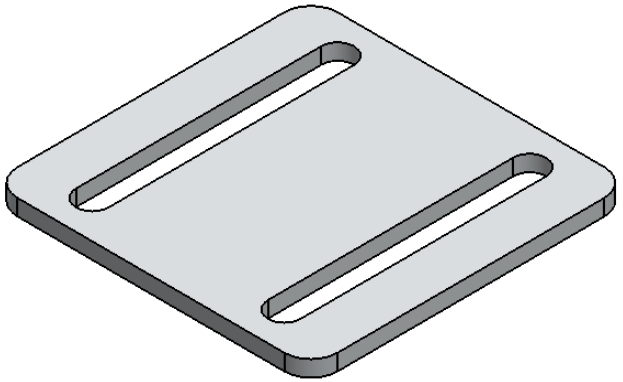

SolidWorks Student Edition.
For Academic Use Only.

A4 Landscape	University of Cape Town Department of Mechanical Engineering				
	Title: Aluminium Frame-Support Bracket				
Quantity: 8	Part Finish	Date: 2013/02/05	Scale: 1:2	Sheet1	of 1
Material: Aluminium	Drawn By: Nzudzanyo Ranwaha			Drawing Number	

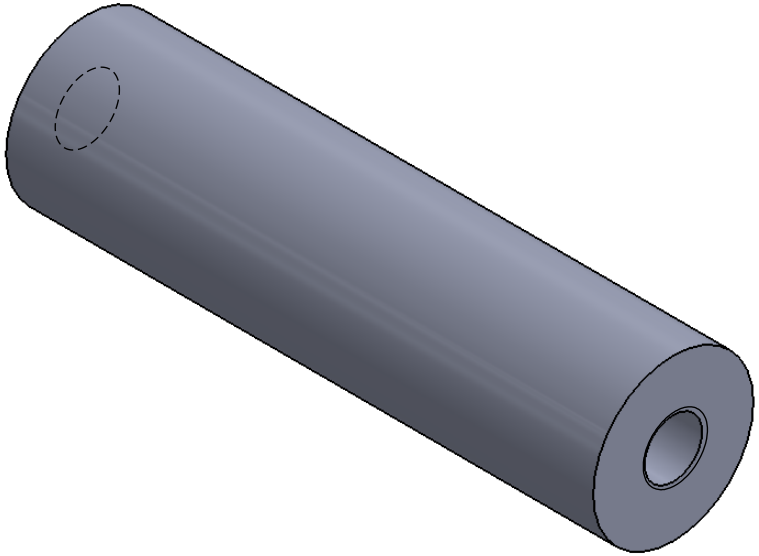

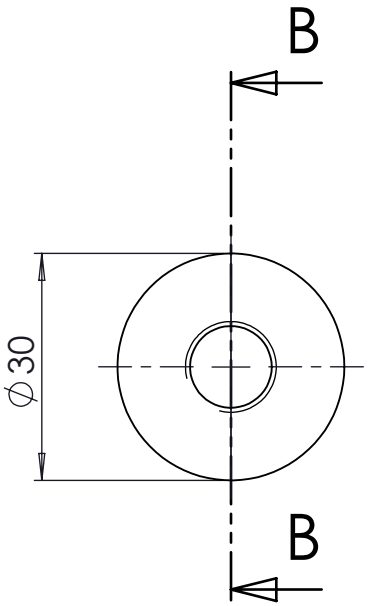

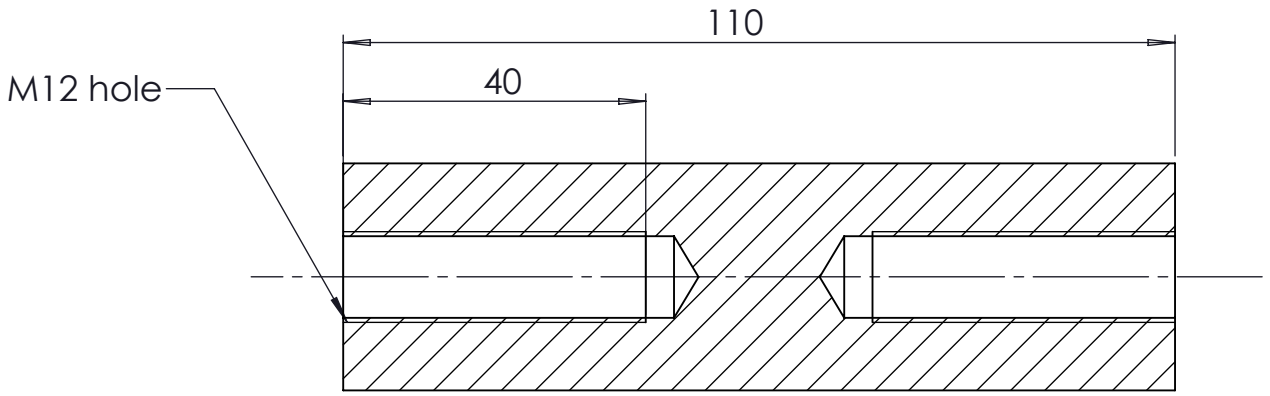

SECTION B-B

SolidWorks Student Edition.
For Academic Use Only.

A4 Landscape	University of Cape Town Department of Mechanical Engineering				
	Title: Spacer Rod 110mm				
Quantity: 8	Part Finish	Date: 2013/02/04	Scale: 1:1	Sheet1	of 1
Material: Steel	Drawn By: Nzudzanyo Ranwaha			Drawing Number	

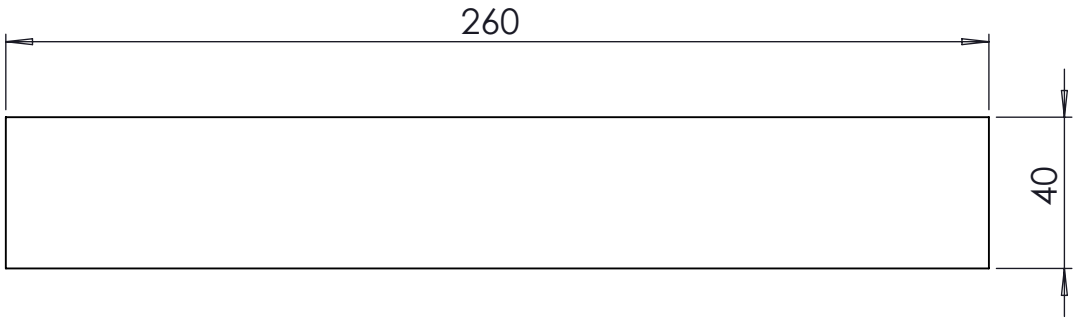

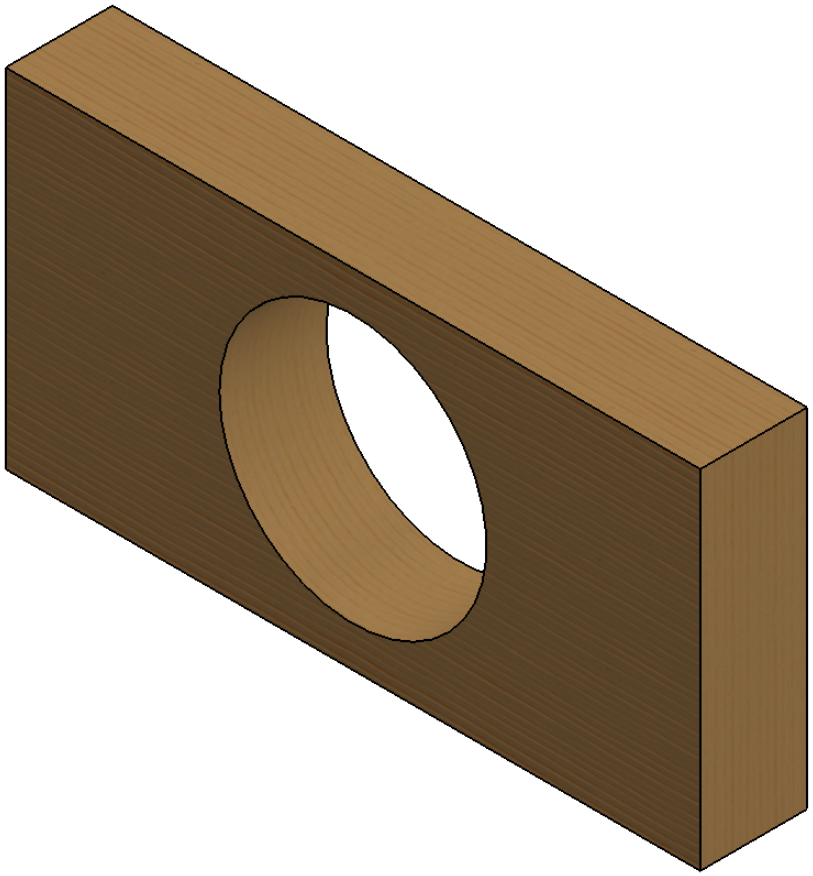

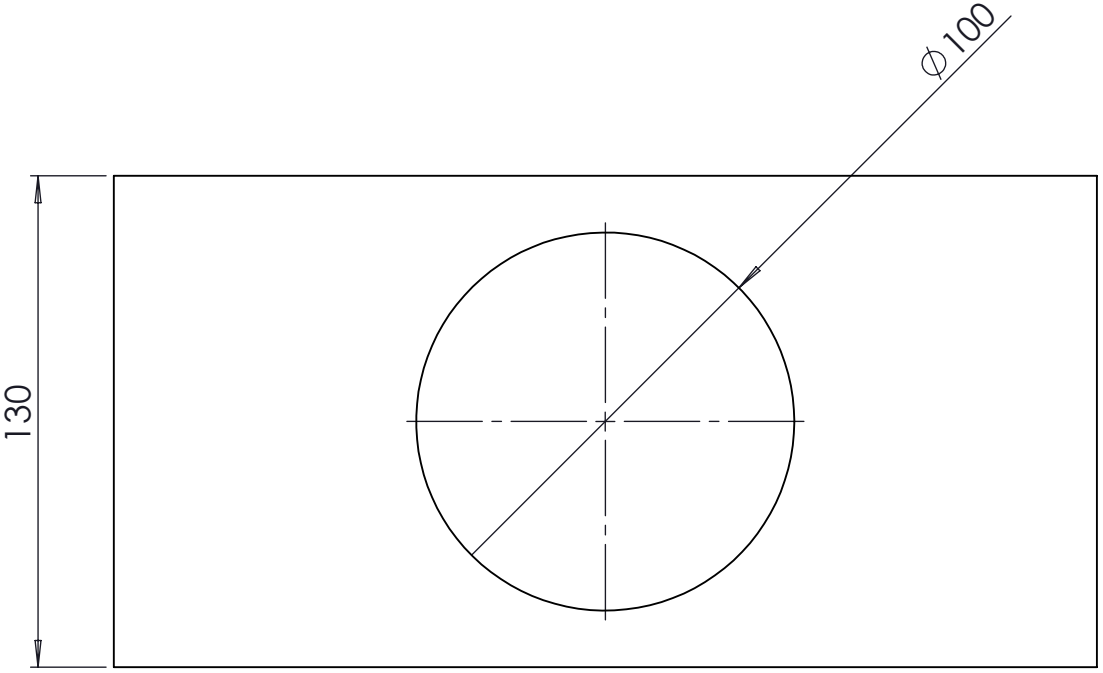

SolidWorks Student Edition.
For Academic Use Only.

A4 Landscape	University of Cape Town Department of Mechanical Engineering				
	Title: Speed Trap Wooden Frame				
Quantity: 3	Part Finish	Date: 2013/02/05	Scale: 1:2	Sheet1	of 1
Material: Wood	Drawn By: Nzudzanyo Ranwaha			Drawing Number	